IOWA STATE UNIVERSITY
Digital Repository

2018

Performance and stability of perovskite solar cells

S M Istiaque Hossain
Iowa State University

Follow this and additional works at: https://lib.dr.iastate.edu/etd

Part of the Electrical and Electronics Commons

Recommended Citation

Performance and stability of perovskite solar cells

by

S M Istiaque Hossain

A dissertation submitted to the graduate faculty

in partial fulfillment of the requirements for the degree of

DOCTOR OF PHILOSOPHY

Major: Electrical Engineering

Program of Study Committee:
Vikram L. Dalal, Major Professor
Rana Biswas
Jaeyoun Kim
Mani Mina
Farzad Sabzikar

The student author, whose presentation of the scholarship herein was approved by the program of study committee, is solely responsible for the content of this dissertation. The Graduate College will ensure this dissertation is globally accessible and will not permit alterations after a degree is conferred.

Iowa State University

Ames, Iowa

2018

DEDICATION

I would like to dedicate this work to my father Late Dr. Md. Tofazzal Hossain. I felt that I have lost everything when my father passed away in 2015 during my Ph.D. The only thing that kept me going is that I wanted to make him proud of me. Wherever he is, I hope he is proud of me. I also would like to dedicate this work to my wife Sabrina Sultana and my mother Ismotara Hossain. Without their support and sacrifice, I won't be the same person that I am today.

TABLE OF CONTENTS

vi

LIST OF FIGURES

Page

LIST OF TABLES

Page

NOMENCLATURE

I_{sc}	Short-circuit current
J_{sc}	Short-circuit current density
V_{oc}	Open-circuit voltage
FF	Fill factor
PCE	Power-conversion efficiency
R_s	Series resistance
R_{sh}	Shunt resistance
ETL	Electron transport layer
HTL	Hole transport layer
ITO	Indium Tin Oxide
PTAA	Poly (triaryl amine), Poly[bis(4-phenyl) (2,4,6- trimethylphenyl) amine]
PCBM	Phenyl-C61-butyric acid methyl ester
NiO	Nickel Oxide
PEDOT:PSS	Poly(3,4-ethylenedioxythiophene) poly(styrenesulfonate)
P_3HT	Poly(3-hexylthiophene-2,5-diyl)
MAI	Methylammonium iodide
PbI_2	Lead Iodide
FAI	Formamidium iodide
CB	Chlorobenzene
DMF	Dimethylformamide

DMSO	Dimethyl sulfoxide
CdS:In	Indium doped Cadmium Sulfide
ZnO:Al	Aluminum doped Zinc Oxide
SMU	Source Measure Unit
CV	Capacitance vs Voltage measurement
CF	Capacitance vs Frequency measurement
CFT	Capacitance-Voltage-Temperature measurement
QE	Quantum efficiency
EQE	External quantum efficiency

ACKNOWLEDGMENTS

Mohamed El-Henawey, and Dr. Ranjith Kottokkaran for their technical and non-technical supports. Their suggestions and guidance have helped to achieve my goal. I also would like to thank my lab mates and friends: Satvik Shah, Dr. Satyapal Nehra, Dr. Tanvir Muntasir, Behrang Bagheri, Harsh Gaonkar, Laila Parvin Poly, Nishtha Bhatnagar, Sabrina Stark and Dipak Paramanik.

Finally, I want to thank my wife Sabrina Sultana for being by my side during my Ph.D. Without your sacrifice and mental support, I would never be who I am today. I have no words to show my gratitude to my parents: my father Dr. Md. Tofazzal Hossain and my mother Ismotara Hossain. I can't express in words how much they have sacrificed to make me a better person.

I would also like to thank all my friends for making my stay in Ames a memorable one. I would like to thank the department stuffs and faculties at Iowa State University for all the technical supports.

Last but not the least, I would like to thank National Science Foundation (NSF) for supporting my work.

ABSTRACT

Perovskite solar cells have great potential not only as a high-efficiency and low-cost single junction solar cell, but also as a top cell (larger bandgap material) for tandem cells with either c-Si or CIGS solar cells. Perovskite as an active layer has a lot of fascinating photonic and electrical properties such a high absorption coefficient, low defect density, long diffusion lengths and low exciton binding energy. These properties have made perovskite an excellent choice for thin film solar cells. Given all exciting properties it also shows some very challenging characteristics such as hysteresis in light IV measurement, environmental instability, voltage evolution, self-degradation in dark and photon-induced degradation.

In the initial part of this work, we have optimized the power-conversion efficiency of a p-i-n structured solar cell and obtained an efficiency of about 18.5%, which is one of the best cells in the world on PTAA as hole transport layer using single-solution processed antisolvent technique.

For most part of this work, we have studied the detailed device physics to understand the photon-induced degradation of perovskite solar cells. We have developed a model based on generation and migration of ions. We have proposed a modified equivalent circuit model to understand the change in photovoltaic parameters during photon-induced degradation. The degradation in short-circuit current density can be modeled using a double-exponential model which explains both migration and generation of ions. The change in open-circuit voltage can be explained by two opposing components: open-circuit voltage increases due to migration from ions from perovskite-transport layers' interfaces towards bulk perovskite and decreases with increase in non-radiative recombination. These

factors can be considered with a dependent current source in parallel with the photo-generated current source and a dependent voltage source in series with the diode to have complete equivalent circuit for perovskite solar cells.

Finally, we have studied how different factors such as the transport layers, stoichiometry of perovskite (PbI_2 to MAI molar ratio), the biasing conditions at which the device is kept during photo-degradation, fabrication techniques of perovskite (Solution or Vapor) and perovskite grain size can affect the photon-induced degradation and dark-recovery. We have demonstrated that our model based on generation and migration of ions can explain these comparative studies completely.

For electrical characterization, we have calculated the dielectric constant of perovskite using capacitance spectroscopy and reported this value to be about 60, which suggests that perovskite has exciton binding energy of about 0.59 meV.

CHAPTER 1.   INTRODUCTION: ENERGY, SOLAR ENERGY AND PHOTOVOLTAICS

1.1 Energy

Energy is in the center of human civilization and its survival. The need for energy is very much correlated with the growth of human development. The amount of energy used per capita can define the development of a nation in terms of technology. For example, in the year of 2015 United states of America and China together have consumed about 42% of total energy consumed by the whole world. But, united states of America had only 4.5% of total world's population [1].

This energy consumption involves total energy harnessed by every energy source from every technological sector across all the countries accept energy harnessed from food and direct biomass burning [2]. But the challenging part is that with the development of human civilization there is a continuous increase in need for energy. But most of the non-sustainable energy sources (such as oil, natural gas, coal etc.) have finite capacity. In addition to that some of them have a huge detrimental effect on environment. So, there is need for energy sources which are sustainable and causes less environmental pollution. Renewable energy sources can be a solution to this problem although the costs of harnessing energy from these sources are still a little too high.

1.2 Renewable Energy

Renewable energy is a kind of energy that is harnessed from renewable resources such as wind, sunlight, tides, waves, geothermal heat etc. [3]. Most of the renewable sources of energy are sustainable and environment friendly. Renewable energy sources can provide long term solutions for energy crisis in the future.
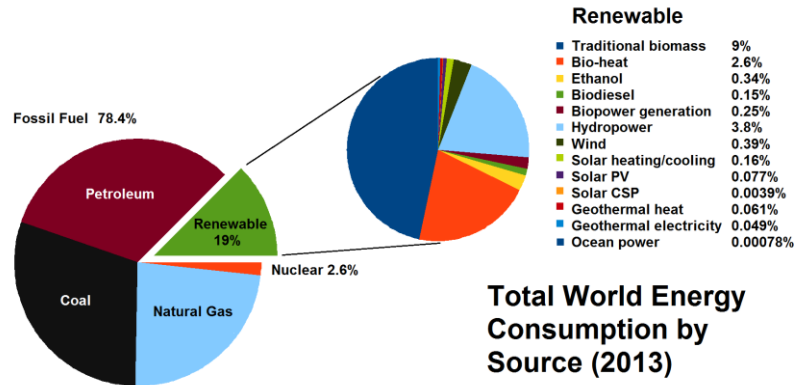
Figure 1.1: The world's energy consumption by source in 2012 [3]

In the year of 2012 only about 19% of the world's total energy consumption came from renewable sources of energy and the rest 81% was coming from combination of non-renewable sources of energy such as petroleum, coal, natural gas and nuclear energy. The main reason to extract energy from these non-renewable sources is that they are relatively inexpensive to extract energy from. More to that they can be stored or shipped from one place to another very easily. But most of these sources are no environment friendly. For instance, burning coal releases many toxic gases and pollutants in to the atmosphere. Mining coal is also one of the dangerous jobs in the world [4]. Also, these non-renewable sources of energy have limited capacity which means excessive use of them will result in running out of them. So, quest for renewable sources of energy getting huge attention day-by-day.

There are several sources of non-renewable energy available to us such as wind, sunlight, tides, waves, geothermal heat etc. There is a rapid increase in capacity over the years for different types of renewable energy sources [5]. Although wind and hydro power sources dominating during the early years, slowly other forms of renewable energies especially Solar PV is growing up in terms of capacity very rapidly.

1.3 Solar Energy

Solar energy comes from the sun to the earth as electromagnetic rays. Although only a small fraction of energy from the sun arrives the earth, that can be enough to fulfill the energy need of mankind. Solar energy is one of the most prominent sources of renewable energy and have already showed a great potential to be a prime source of energy in the future. The advantages of solar energy are:

- ❖ Solar energy is abundant in nature.

- ❖ Solae energy is mostly environmental friendly.

- ❖ The maintenance cost of solar panels is comparatively very low.

- ❖ This technology can have almost no noise pollution.

- ❖ It provides a very reliable source of energy.

- ❖ Solar power also provides energy security.

- ❖ Solar energy is also a sustainable source of energy.
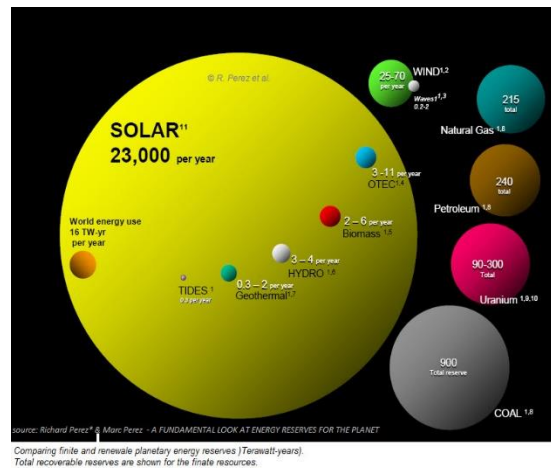
Figure 1.2: Potential for various energy sources and global energy consumption [7]

Figure 1.2 shows the actual potential of solar energy compared to other sources. The potential power that can be extracted from solar energy is about 2300 TW/year which is way

more compared to any other sources of energy. The total power consumed by the mankind is about 16 TW/year. So, efficient extraction of solar energy can be enough to fulfill all the energy need for mankind. But the actual picture regarding the portion of energy utilized from different sources in 2014 has been reported in figure 1.6. It shows that about 76% of total energy consumed was coming from non-renewable sources and the rest 24% was coming from renewable energy sources. If we analyze the breakdown of this 24% from renewable energy, we can see that only about 1.2% was coming from Solar PV [7].
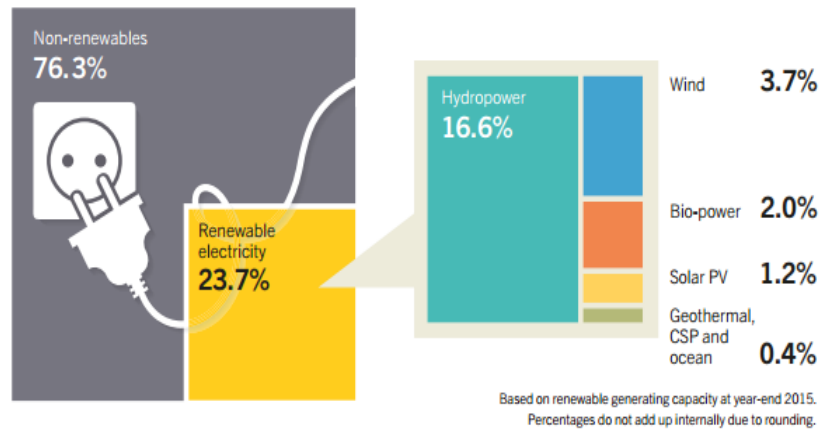
Figure 1.3: Renewable energy share from renewable sources in global energy consumption in 2014 [7]

From the discussion so far, we can see that Solar PV has huge potential to meet the global energy consumption, but there is reluctance to utilize Solar PV as the primary source of energy. The reason behind this can easily be understood from the comparison in cost per unit among different sources of energy [8]. The cost per unit for Solar PV is still high compared to other sources. Low extraction and power conversion efficiency attributes as a main reason behind high cost of Solar PV. For a given solar intensity the amount of power extracted from a solar panel is dependent of power conversion efficiency as well as the area of the solar panel. So, lower efficiency solar panels will need relatively larger area to extract same amount of

power. As the power conversion efficiency for solar panels still not very high it is comparatively more expensive. Also because of cloudy days and smaller day time can limit the amount of power that can be extracted from a given solar panel. So, storage of energy is becoming very important. So, we also need to make our energy storage and distribution more efficient. Also, the production cost of some state-of-the art solar panels is still very high.

But the encouraging sign for Solar PV is that the cost per unit power is going down exponentially over the years (Figure 1.4) [8]. Figure 1.8 also showed that if we can keep going at our current pace by 2030 the projection shows that the Solar PV can be cheapest compared to any other sources of energy.
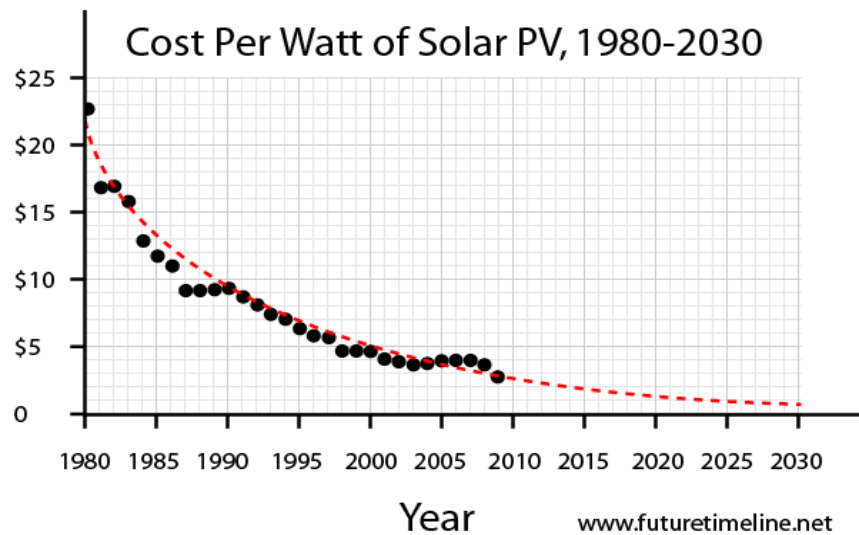
Figure 1.4: Exponential decrease in cost of solar power ($/Watt) over the years [8]

1.4 Photovoltaics

The process of converting solar energy to electricity is called photovoltaics. This process can be done using solar cells [9]. It is becoming a very important renewable source of energy. Although people have started using it to in 19th century to solar energy, the first real photovoltaic device was demonstrated in the 1950s by Bell lab. It has seen a real boost in

research and development of photovoltaics specially in satellite applications. But these solar cells were very expensive. In 1980s the research in silicon solar cells showed a lot of promise by achieving efficiency more than 20%. Then slowly lot of thin film and multi-junction solar cells have got interest from various research groups. And now this industry is looking very promising for long term energy solution [9].

1.5 Outline of This Thesis

The chapter 2 describes the device physics and equivalent circuit model of solar cells. Different characterization techniques, which can be used to understand the operational principle and troubleshoot the problems, has been described in chapter 3. In chapter 4 we have described material properties of perovskite and challenges that we face with perovskite solar cells. Then in chapter 5 we have presented different fabrication techniques available for perovskite. In this chapter, we have also demonstrated a method to optimize the power conversion efficiency of a p-i-n structured perovskite solar cell. We have developed a model on photon-induced degradation of perovskite solar cells based on generation and migration of ions and proposed a modified equivalent circuit model to describe this phenomenon in chapter 6. Then in chapter 7 we have studied how different factors can affect the photon-induced degradation. We have studied the influence of the transport layers, stoichiometry of perovskite (PbI_2 to MAI molar ratio), the biasing conditions at which the device is kept during photo-degradation, fabrication techniques of perovskite (Solution or Vapor) and perovskite grain size on photon-induced degradation and dark-recovery. Finally, in chapter 8 we have presented the future work regarding how photon-induced can be minimized with optimization of several factors.

REFERENCES

1   US News, "The 2015 U.S. and World Populations"

2   BP: Statistical Review of World Energy, Workbook (xlsx), London, 2016

3   Ellabban, Omar; Abu-Rub, Haitham; Blaabjerg, Frede (2014). "Renewable energy resources: Current status, future prospects and their enabling technology". Renewable and Sustainable Energy Reviews. 39: 748–764 [749]. doi:10.1016/j.rser.2014.07.113

4   National Geography, "non-renewable energy",
        Link: https://www.nationalgeographic.org/encyclopedia/non-renewable-energy/

5   "REN21, Renewables Global Status Report 2012" (PDF). Ren21.net. Archived from the original (PDF) on 11 August 2014. Retrieved 11 August 2014.

6   Ipsos 2011, p. 3

7   Perez R., and M. Perez, A fundamental look at energy reserves for the planet
        Link: http://www.asrc.albany.edu/people/faculty/perez/Kit/pdf/a-fundamental-look-at%20the-planetary-energy-reserves.pdf

8   US Energy Information Administration (EIA) in June, 2015
        Link: http://www.jc-solarhomes.com/PV/low_cost_pv.htm

9   PV Education
        Link: http://www.pveducation.org

CHAPTER 2. DEVICE PHYSICS OF SOLAR CELLS

2.1 Introduction

Solar cell is a kind of electronic device which absorbs sunlight and converts solar energy directly to electricity. Both current and voltage can be generated upon incident of sunlight on solar cell. Thus, it can generate electric power from solar energy. This process requires a material which can absorb the sunlight create electron-hole pairs. These electron-hole pairs can diffuse and drift before getting collected by the contact layers. These higher energy electron and holes can flow through an external circuit from a solar cell and generate photo-current. Finally, these higher energy electrons and holes dissipate energy into an external load, return to the solar cell and recombine. Although there are lot of different materials that are suitable for photovoltaic energy conversion, but mostly in practice we use PN junction to convert solar energy to electricity.
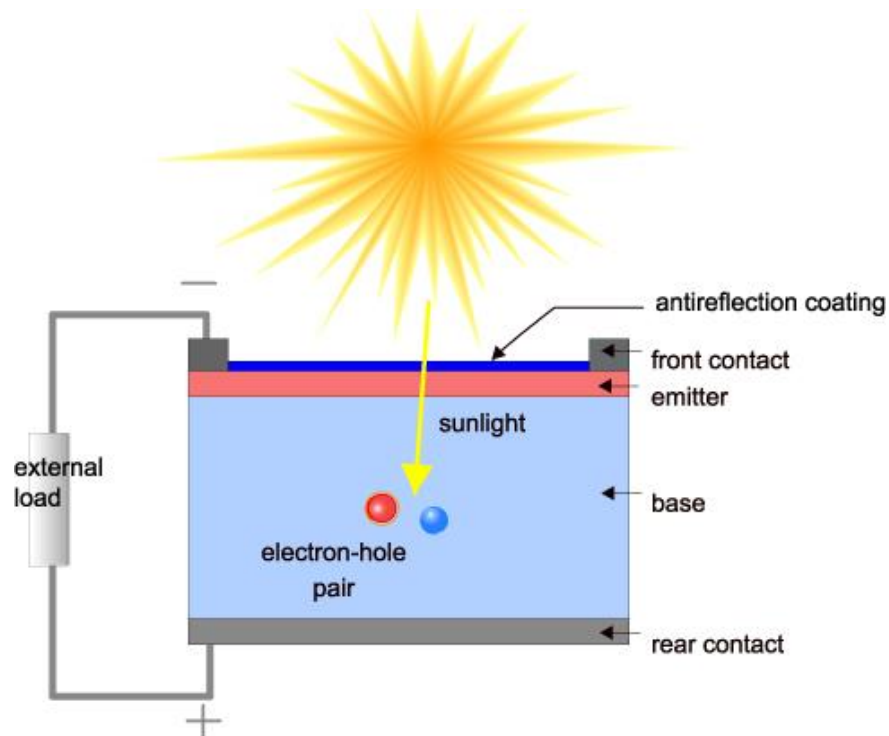
Figure 2.1: Cross section of a solar cell [1]

So, the basic steps in operation of a solar cell involves the following four processes [1]:

- ❖ The generation of photo-generated electron-hole pairs
- ❖ The collection of these photo-generated carriers to generate electrical current
- ❖ The generation of large voltage across the solar cell
- ❖ The dissipation of power into the external load and parasitic resistances

There are four basic processes which play role in photovoltaic energy conversion. They are:

- (i)   Absorption of incident photons
- (ii)   Generation of free electron-hole pairs
- (iii)   Transport of photo-generated carriers
- (iv)   Collection of photo-generated carriers

In the following sections of this chapters, these processes will be discussed in detail with the help of semiconductor device physics. The mechanism of losing these photo-generated carriers also known as recombination will also be discussed.

2.2 Absorption of Incident Photons

The first step of conversion of solar energy to electricity involves the absorption of incident photons. The absorption of these photons depends on the quantum energy of each photons and the energy levels of the absorber layer. When a photon in incident on a material and have been absorbed, it can excite an electron to from the lower energy state to a higher energy state. We know that the energy levels inside a material is quantized. So, the incident photon must be high enough energy to transfer an excited electron to an allowed higher energy

state. If the energy of the incident photon is not high enough, the photon will not be absorbed rather will be transmitted through the material. So, to absorb the energy of a photon at least two-level energy system is required. And to utilize this energy the lifetime of the carrier at the excited state must be greater than the time required for a carrier to transfer from a lower energy state to a higher energy state. There is a forbidden gap between the lower and higher energy levels. The lower energy level is called valance-band and higher energy level is commonly known as conduction band. And the difference between these energy levels is called bandgap of the material. For a two level-system in a material a negatively charged electron can absorb a photon equal or greater than the bandgap of the material and have transition to higher energy conduction band. In a semiconductor material, this transition can happen in two different ways:

(i)   Band-to-band transition (figure 2.2)

(ii)   Transition assisted by defect states (figure 2.3)
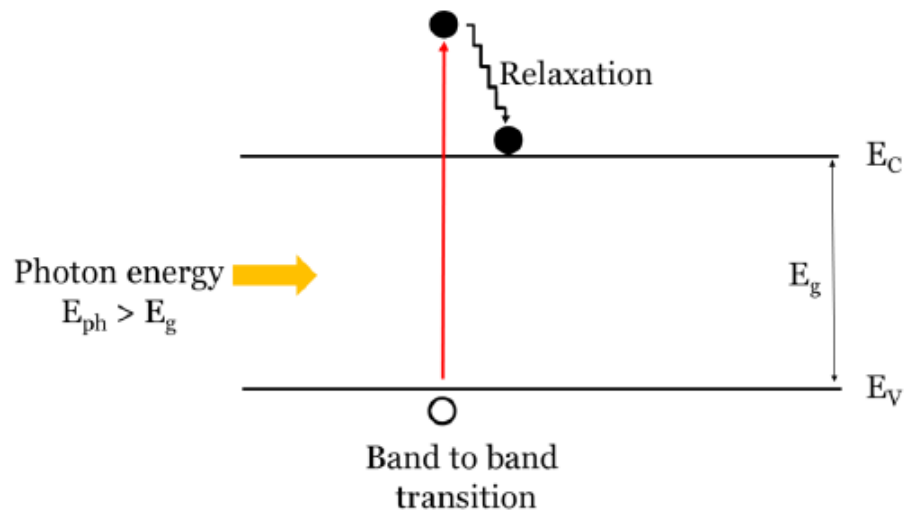
Figure 2.2: Absorption through band-to-band transition when incident photon has higher energy than the bandgap [3]
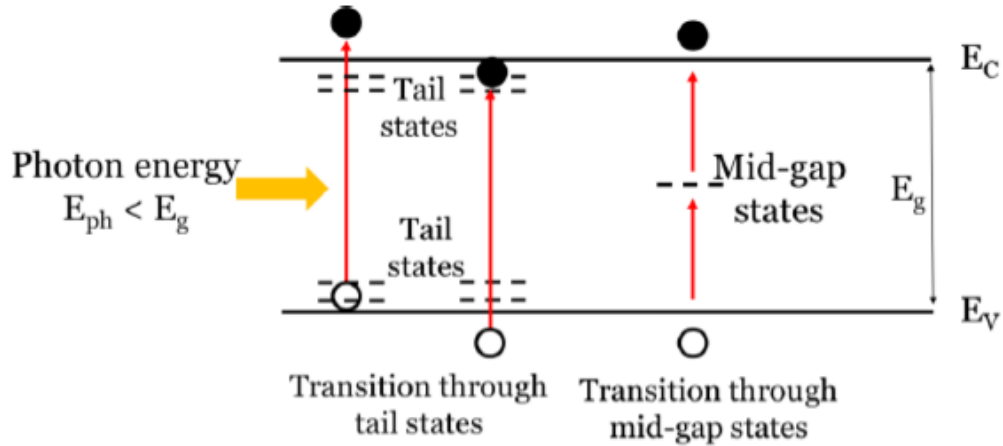
Figure 2.3: Absorption assisted by defect states when incident photon has lower energy than the bandgap [3]

Figure 2.2 graphically demonstrates the absorption through band-to-band transition when the incident photon has lower energy than the bandgap. If the photon energy is higher than the bandgap the electron can move to an energy state even higher than the conduction band before going through a relaxation process and dissipates the excess energy ($hv - E_g$) as thermal energy.

Figure 2.3 graphically demonstrates the absorption assisted by transition through the defect states within the bandgap. This phenomenon can happen if the incident photon has energy lower than the bandgap. This transition can be assisted by either tail states, midgap states or both. If the energy of incident photon is such that it doesn't support either band-to-band or trap assisted transition, then it just transmits through and material and contributes to the loss mechanism of a solar cell.

The band-to-band transition can also be classified into two categories: direct transition and indirect transition.
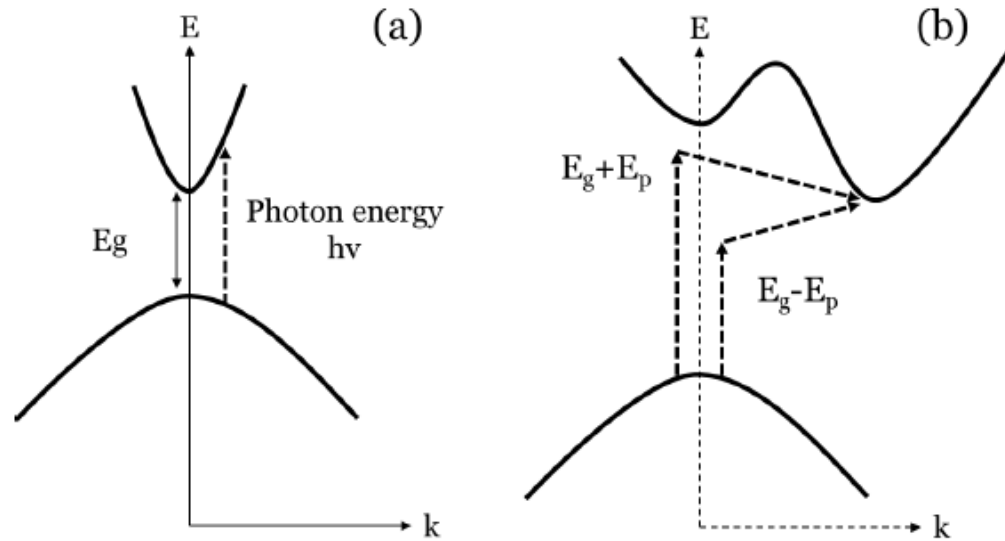
Figure 2.4: Absorption through band-to-band transition (a) direct transition (b) indirect transition [3]

For direct transition, the transition of electron from lower energy state to higher energy state involves only change in energy as the momentum of electrons and holes is the same in both conduction and valance band. In case of indirect transition, the transition of electron involves change in both energy and momentum. Based on either direct or indirect transition is allowed semiconductor materials can be classified into two categories: direct bandgap and indirect bandgap material. If a material allows direct transition of electron from valance to conduction band it is called direct bandgap material. On the other hand, if transition of electron needs change in both energy and momentum the material can be classified as indirect bandgap semiconductor. Both direct and indirect bandgap semiconductor can serve as absorber layer for photovoltaics applications.

How good a material is an absorber layer can be defined by absorption coefficient which is a function of wavelength of incident photon. The absorption coefficient of a direct bandgap semiconductor can be given by [5],

$$\alpha = A(h\upsilon - E_g)^{\frac{1}{2}} \tag{2.1}$$

Where, A is the proportional constant which is a function of effective electron and hole masses.

For indirect bandgap semiconductor, the absorption coefficient when an absorption of photon involves is given by [5],

$$\alpha = \frac{A(h\upsilon - E_g + E_p)^2}{e^{\frac{E_p}{kT}} - 1} \tag{2.2}$$

Again, A is the proportional constant which is a function of effective electron and hole masses and E_p is the energy of photon that is being absorbed.

As the tail and midgap state usually has very low density the absorption coefficient associated with this kind of transition is also very small. But it gives information about the distribution of sub-gap states. The expression for this kind of transition is given by [6],

$$\alpha = Ae^{\frac{h\upsilon}{E_u}} \tag{2.3}$$

Here, E_u is called Urbach energy which is a function of tail and mid-gap defect states' distribution.

As light travels through the material the intensity goes down exponentially with distance and it can be expressed as,

$$I = I_0 e^{-\alpha x} \tag{2.4}$$

Where, I is the intensity at distance x, I_0 is the intensity of light before any absorption and α is the absorption coefficient. This equation can be used to determine how much light has been absorbed for a given thickness of the semiconductor.

For semiconductor materials in photovoltaics application absorption coefficient is a very important parameter as it determines how much light the material is going to absorb within a given thickness. The higher the absorption coefficient the more light can be absorbed within a given thickness. In other words, for a semiconductor material with higher absorption coefficient needs thinner layer to absorb the photons effectively. Figure 2.5 shows absorption coefficient for different semiconductor materials used as absorber layers in photovoltaic applications. We can see that perovskite has higher absorption coefficient that c-Si which means very thin film (~500-600nm) of perovskite can be used to absorb most of the photons effectively.
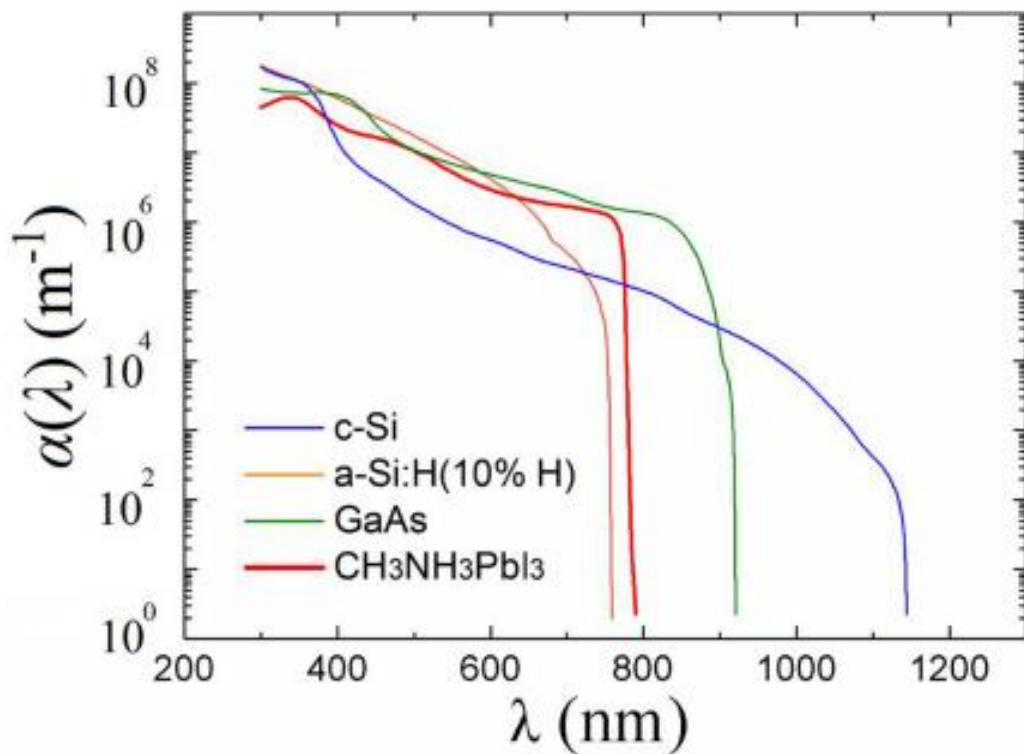
Figure 2.5: Absorption coefficient for different semiconductor materials used as absorber layers in photovoltaic applications [7]

2.3 Generation of Free Electron-hole Pairs

Absorption of photon gives rise to an excited electron into the conduction band as well as a vacancy of electron, which is also known as a hole in the valance band. The electron-hole pair generated from the same absorption event are bound together with an attractive coulomb force. This bound electron-hole pair gains stability to an energy state which is slightly below the energy of an unbound electron and hole satisfying minimization of energy in nature. This quasi-neutral charge particle is called an exciton. So, absorption of photon generates exciton which needs some extra energy to create free electron and hole.

Whether a photon-absorption event in a material will result in generation of exciton or free electron or hole depends on the exciton binding energy for that material. For photovoltaic application, we prefer the exciton binding energy to be lower than thermal energy which is given by $1/kT$; where k in Boltzmann constant and T is the temperature. At room temperature, this thermal energy is about 26 meV. So, if the binding energy of exciton is less than 26 meV expect to have free electron hole pair upon photon absorption (example: crystalline silicon, perovskite etc.). On the other hand, if the exciton binding energy is higher than thermal energy, then photon absorption generates exciton and it requires external energy to create free electrons and holes. For example, organic semiconductors have exciton binding energy higher than thermal energy and it needs type II heterojunction structure to make it work.

The exciton binding energy in a semiconductor is a function of dielectric constant of the material. The higher the dielectric constant the lower the coulomb attraction force between the generated electron-hole pair and so, has lower exciton binding energy. The exciton binding energy in a material can be calculated using equation (2.5),

$$E_b = \frac{\mu e^4}{2\hbar^2 \mathcal{E}^2} \tag{2.5}$$

Where, E_b is the exciton binding energy, μ is the effective mass of electron, $\mathcal{E}$ is the dielectric constant of the semiconductor material.

For example, crystalline silicon has a dielectric constant of 11.9 which means it has exciton binding energy of 15 meV [8]. Perovskite has dielectric constant of about 60 which means it has exciton binding energy of about 0.59 meV (This will be discussed later in this thesis). Both perovskite and crystalline silicon has exciton binding energy lower than the thermal energy which means these materials have free electrons and holes with absorption of photon. On the other hand, the organic semiconductors have very low dielectric constant which is in the range of 2-5. As a result, they have exciton binding energy in the range of 0.2-1 eV which is much higher than thermal energy of 26 meV [9]. Thus, organic semiconductors have exciton generated with absorption of photons. For photovoltaic applications, it is expected to have exciton binding energy lower than thermal energy to achieve high power conversion efficiency.

2.4 Transport of Photo-generated Carriers

The next step for generation of electricity in photovoltaics is separation and collection of photo-generated free charge carriers. This process can be contributed by two transport mechanisms: diffusion-based transport and drift-based transport [10,11]. If the transport of charge carriers is driven by gradient in concentration in the semiconductor material, then this process is known as diffusion-based transport. On the other hand, if the transport of these carriers is driven by electric field inside the semiconductor material, then this process is known as drift-based transport. As a solar cell generally works at a maximum power point condition where we achieve a near flat band condition, the electric field inside the device is significantly

small in normal operating condition. In this condition, the diffusion-based transport dominates over drift-based transport. Thus, the collection efficiency of the photo-generated carriers is dependent on diffusion length of electron and holes. If we consider both diffusion and drift based transport, which is also known as ambipolar transport, then transport equation is given by [10,11],

$$\frac{\partial \Delta n}{\partial t} = D' \frac{\partial^2 \Delta n}{\partial x^2} + \mu' \mathcal{E} \frac{\partial \Delta n}{\partial x} + G - R \qquad (2.6)$$

Where, Δn is the excess of electron concentration, μ' is ambipolar mobility, $\mathcal{E}$ is the net electric field, D' is ambipolar diffusion coefficient, G is generation rate and R is recombination rate.

The ambipolar mobility can be given by [10,11],

$$\mu' = \frac{\mu_n \mu_p (p - n)}{n \mu_n + p \mu_p} \qquad (2.7)$$

The ambipolar diffusion coefficient can be given by [10,11],

$$D' = \frac{n \mu_n D_p + p \mu_p D_n}{n \mu_n + p \mu_p} \qquad (2.8)$$

Where, μ_n and μ_p are electron and hole mobilities respectively, D_p and D_n are electron and hole diffusion coefficients respectively, n and p are electron and hole concentration respectively.

In a n-type semiconductor for low level injection equation (2.6) becomes,

$$\frac{\partial \Delta p}{\partial t} = D_p \frac{\partial^2 \Delta p}{\partial x^2} + \mu_p \mathcal{E} \frac{\partial \Delta p}{\partial x} + G - \frac{\Delta p}{\tau_p} \qquad (2.9)$$

Where, τ_p is lifetime of hole.

In a p-type semiconductor for low level injection equation (2.6) becomes,

$$\frac{\partial \Delta n}{\partial t} = D_n \frac{\partial^2 \Delta n}{\partial x^2} + \mu_n \mathcal{E} \frac{\partial \Delta n}{\partial x} + G - \frac{\Delta n}{\tau_n} \tag{2.10}$$

Where, τ_n is lifetime of electron.

The transport of carriers in photovoltaic process is dominated by minority carriers. In the next part both the diffusion and drift controlled transport processes have been explained.

2.4.1 Diffusion-based transport of carriers:

If the transport of charge carriers is driven by gradient in concentration in the semiconductor material, then this process is known as diffusion-based transport. If we consider an n-type material where minority charge carriers are holes and there is no generation of excess charge with internal electric field inside the material is zero, then the transport of minority charges is dominated by diffusion of these charge carriers. Then the continuity equation in equation (2.9) becomes,

$$\frac{\partial \Delta p}{\partial t} = D_p \frac{\partial^2 \Delta p}{\partial x^2} - \frac{\Delta p}{\tau_p} = 0 \tag{2.11}$$

The solution of this second order differential equation is,

$$\Delta p = \Delta p(x = 0)e^{-\frac{x}{L_p}} \tag{2.12}$$

Here, L_p is hole diffusion length and is given by,

$$L_p = \sqrt{D_p \tau_p} \tag{2.13}$$

If we consider a p-type material where minority charge carriers are electrons and there is no generation of excess charge with internal electric field inside the material is zero, then the continuity equation in equation (2.10) becomes,

$$\frac{\partial \Delta n}{\partial t} = D_n \frac{\partial^2 \Delta n}{\partial x^2} - \frac{\Delta n}{\tau_n} = 0 \qquad (2.14)$$

The solution of this second order differential equation is,

$$\Delta n = \Delta n(x = 0)e^{-\frac{x}{L_n}} \qquad (2.15)$$

Here, L_n is electron diffusion length and is given by,

$$L_n = \sqrt{D_n \tau_n} \qquad (2.16)$$

Both equation (2.12) and (2.15) suggests that the minority carrier concentration will decay exponentially during transport by diffusion. Higher the diffusion length greater the probability for the charge carriers being collected. If the thickness of the absorber layer in a solar cell is t and diffusion dominates the transport then it is expected that $L_n, L_p \gg t$. Satisfying this condition will enhance the collection efficiency significantly.

2.4.2 Drift-based transport of carriers:

If the transport of these carriers is driven by electric field inside the semiconductor material, then this process is known as drift-based transport. If the diffusion length within a material is low then we need electric field to assist the charge transport. In other words, we need drift based transport (for example, amorphous silicon and organic solar cells).

If we consider an n-type material where minority charge carriers are holes and there is no generation of excess charge with significant electric field inside the material, then the

transport of minority charges is dominated by drift of these charge carriers. Then the continuity equation in equation (2.9) becomes,

$$\frac{\partial \Delta p}{\partial t} = \mu_p \mathcal{E} \frac{\partial \Delta p}{\partial x} - \frac{\Delta p}{\tau_p} = 0 \qquad (2.17)$$

The solution of this second order differential equation is,

$$\Delta p = \Delta p(x = 0)e^{-\frac{x}{R_p}} \qquad (2.18)$$

Here, R_p is called drift range of holes and is given by,

$$R_p = \mu_p \tau_p \mathcal{E} \qquad (2.19)$$

If both drift and diffusion based transport contributes in transport of charge carriers, then a critical electric field can be defined which determines whether the transport is dominated by diffusion or drift. This critical electric field is given by [10,12],

$$\mathcal{E}_c = \frac{kT}{qL_p} \qquad (2.20)$$

If the net internal electric field, $\mathcal{E} > \mathcal{E}_c$ then the transport of carriers is dominated by drift. On the other hand, If the net internal electric field, $\mathcal{E} < \mathcal{E}_c$ then the transport of carriers is dominated by diffusion.

Now, if we consider a p-type material where minority charge carriers are electrons and there is no generation of excess charge with significant electric field inside the material, then the transport of minority charges is dominated by drift of these charge carriers. Then the continuity equation in equation (2.10) becomes,

$$\frac{\partial \Delta n}{\partial t} = \mu_n \mathcal{E} \frac{\partial \Delta n}{\partial x} - \frac{\Delta n}{\tau_n} = 0 \qquad (2.21)$$

The solution of this second order differential equation is,

$$\Delta n = \Delta n(x = 0)e^{-\frac{x}{R_n}} \qquad (2.22)$$

Here, R_n is called drift range of electrons and is given by,

$$R_n = \mu_n \tau_n \mathcal{E} \qquad (2.23)$$

The critical electric field is given by [10,12],

$$\mathcal{E}_c = \frac{kT}{qL_n} \qquad (2.24)$$

If the net internal electric field, $\mathcal{E} > \mathcal{E}_c$ then the transport of carriers is dominated by drift. On the other hand, If the net internal electric field, $\mathcal{E} < \mathcal{E}_c$ then the transport of carriers is dominated by diffusion.

If the diffusion length of minority charge carrier is significantly lower within a material, then a p-i-n sandwich kind of structure can be used to improve charge transport. This kind of sandwich structure involves an intrinsic absorber layer is sandwiched within a doped p-type and n-type semiconductor. The direction of the electric field will be from the n-type semiconductor to the p-type semiconductor. The p-type and n-type semiconductors are often termed as hole transport layer (HTL) and electron transport layer (ETL) respectively. After the free electrons and holes are generated these carriers will drift in opposite directions assisted by the internal electric field. As the transport will be drift dominated the low diffusion length will not affect the collection efficiency. The p and n-type layers are usually significantly thinner compared with thinner compared to the intrinsic layers to reduce the loss due to low diffusion lengths.

2.5 Collection of Photo-generated Carriers

The final step for photovoltaic process is to collect the photo-generated carriers. After the carriers are transported to the electrodes, they need to be collected by an ohmic contact between semiconductor and electrode. To collect electron the semiconductor work function of semiconductor must be higher than work function of electrode so that the junction doesn't form a schottky barrier. On the other hand, to collect holes work function of electrode must be higher than work function of semiconductor. Thus, a proper choice of electrodes is required along with the transport layers to achieve high power conversion efficiency of solar cells.

2.6 Recombination

Recombination is one of the loss mechanisms for solar cells which leads to loss in photo-generated carriers. It will reduce the collection efficiency of photo-generated carriers. The excited electron from the conduction band can release energy and recombine with a hole in valance band to return to ground state. This kind of recombination can be either radiative or non-radiative. If this recombination process releases excess of energy in form of photon then this recombination process is called radiative recombination. If this recombination process releases energy in form of phonons then this recombination is known as non-radiative recombination. There are three major recombination mechanisms: band-to-band recombination, trap assisted recombination (SRH recombination) and Auger recombination as illustrated in figure 2.7.
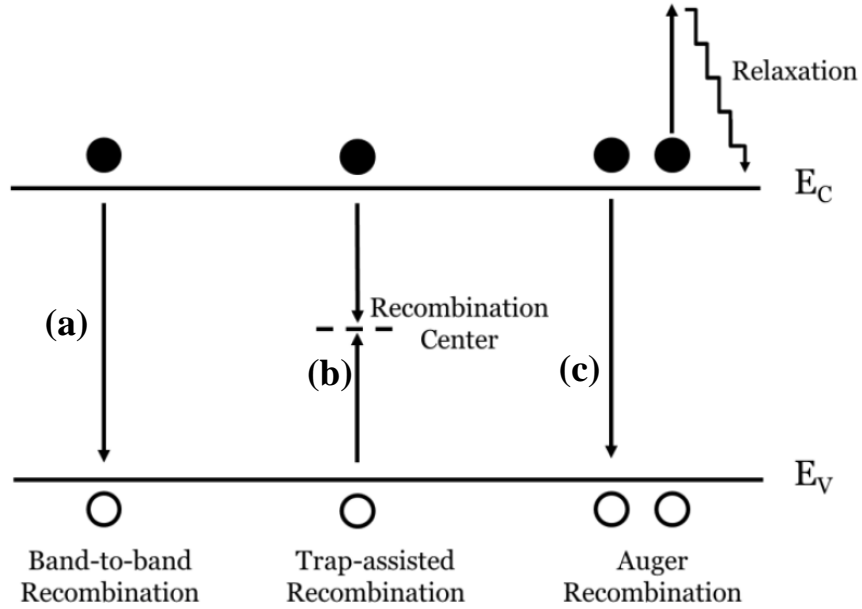
Figure 2.6: Different recombination mechanisms: (a) Band-to-band, (b) Trap-assisted and (c) Auger recombination [10]

2.6.1 Band-to-band recombination [10,11]

For band-to-band recombination the excited electron from conduction band recombines with a hole in valance band and releases excess of energy in the form of a photon. The released photon has energy almost equal to the bandgap of the material. Thus, this kind of recombination is a radiative recombination. The rate of band-to-band recombination is given by,

$$R = C_B(np - n_i^2) \tag{2.25}$$

Where, C_B is the recombination coefficient, n and p are electron and hole carrier concentrations respectively, n_i is intrinsic carrier concentration. We can consider two levels of injection: low level or small signal and high level or large signal injection.

(i)   Low-level injection:

For small signal condition during low level injection ($\Delta n, \Delta p \ll n$) on a n-type semiconductor ($n \gg p$ and $n \gg n_i$), we can simplify equation (2.25) as,

$$R = C_B n \Delta p = \frac{\Delta p}{1/C_B n} \qquad (2.26 \text{ a})$$

If the minority carrier lifetime, $\tau_B = \frac{1}{C_B n}$ then equation (2.26) becomes,

$$R = \frac{\Delta p}{\tau_B} \qquad (2.26 \text{ b})$$

For a p-type semiconductor ($p \gg n$ and $p \gg n_i$) with low level injection ($\Delta n, \Delta p \ll p$) we can simplify equation (2.25) as,

$$R = C_B p \Delta n = \frac{\Delta n}{1/C_B p} \qquad (2.27)$$

If the minority carrier lifetime, $\tau_B = \frac{1}{C_B p}$ then equation (2.26) becomes,

$$R = \frac{\Delta n}{\tau_B} \qquad (2.28)$$

The lifetime of minority carriers is a function of majority carrier concentration for band-to-band recombination for low-level injection.

(ii)   High-level injection:

For large signal condition during high level injection ($\Delta n, \Delta p \gg n_0, p_0$) then equation (2.25) can be simplified as,

$$R = C_B \Delta n \Delta p = C_B np = C_B n^2 = C_B p^2 \qquad (2.29)$$

2.6.2 Trap-assisted recombination or SRH recombination [10,11]

As showed in figure 2.6 (b) a hole from the valance band and an electron from the conduction band can recombine assisted by a trap sate within the bandgap of the material. This kind of recombination is known as trap-assisted recombination. It is also known as Schockley-Read-Hall or SRH recombination. It can take place either inside the bulk of a material or at the interfaces between two materials. The recombination rate for SRH recombination can be expressed as,

$$R = \frac{np - n_i^2}{\tau_p(n + n_1) + \tau_n(p + p_1)} \tag{2.30}$$

Where, n_1 and n_2 are constants and follows the following equations,

$$n_1 = n_i e^{\frac{(E_{T'} - E_i)}{kT}} \tag{2.31}$$

$$p_1 = n_i e^{\frac{(E_i - E_{T'})}{kT}} \tag{2.32}$$

$$n_1 p_1 = n_i^2 \tag{2.33}$$

The carrier lifetimes for electron and hole is given by,

$$\tau_p = \frac{1}{C_p N_T} \tag{2.34}$$

$$\tau_n = \frac{1}{C_n N_T} \tag{2.35}$$

Here, C_p and C_n are SRH recombination coefficients for hole and electron respectively and N_T is the trap density of states. The minority carrier lifetime is a function of density of traps.

Again, we can consider both low-level and high-level injection.

(i)   Low-level injection:

For small signal condition during low level injection ($\Delta n, \Delta p \ll n$) on a n-type semiconductor ($n \gg p$ and $n \gg n_i$), we can simplify equation (2.30) as,

$$R = \frac{\Delta p}{\tau_p} = C_p \Delta p N_T \qquad (2.36)$$

For a p-type semiconductor ($p \gg n$ and $p \gg n_i$) with low level injection ($\Delta n, \Delta p \ll p$) we can simplify equation (2.30) as,

$$R = \frac{\Delta n}{\tau_n} = C_n \Delta n N_T \qquad (2.37)$$

For trap-assisted recombination with low level injection the minority carrier lifetime is inversely proportional to the density of traps.

(ii)   High-level injection:

For large signal condition during high level injection ($\Delta n, \Delta p \gg n_0, p_0$) then equation (2.30) can be simplified as,

$$R = \frac{\Delta n}{\tau_n + \tau_p} = \frac{\Delta p}{\tau_n + \tau_p} \qquad (2.38)$$

Here, the effective carrier lifetime, $\tau = \tau_n + \tau_p$ is larger than carrier lifetime in low level injection. So, the minority carrier lifetime at large signal condition is lower than at small signal condition if the recombination is dominated by SRH recombination.

2.6.3 Auger recombination [10,11]

The mechanism of Auger recombination has been illustrated in figure 2.6(c). During this process energy released from a band-to-band or trap-assisted recombination will give rise to an excited electron into the conduction band, before this excited electron goes through thermal relaxation and settles at the bottom of conduction band. The Auger recombination dominates if the material is very heavily doped.

Auger recombination rate for a n-type semiconductor can be expressed by the following equation,

$$R = C_A n(np - n_i^2) \tag{2.39}$$

For a p-type semiconductor,

$$R = C_A p(np - n_i^2) \tag{2.40}$$

Where, C_A is Auger recombination coefficient, n and p are electron and hole concentrations respectively, n_i is the intrinsic carrier concentration.

For n-type semiconductor with low level injection the rate of recombination in equation (2.39) can be simplified to,

$$R = C_A n_0^2 \Delta p = \frac{\Delta p}{\tau_p} \tag{2.41}$$

Where, the minority carrier lifetime for hole is given by,

$$\tau_p = \frac{1}{C_A n_0^2} \tag{2.42}$$

For p-type semiconductor with low level injection the rate of recombination in equation (2.40) can be simplified to,

$$R = C_A p_0^2 \Delta n = \frac{\Delta n}{\tau_n} \qquad (2.43)$$

Where, the minority carrier lifetime for electron is given by,

$$\tau_n = \frac{1}{C_A p_0^2} \qquad (2.44)$$

The lifetime of minority carriers for Auger recombination is inversely proportional to the square of dopant density.

2.6.4 Combined minority carrier lifetime [10,11]

If all three recombination processes are playing a role, the effective minority carrier lifetime can be obtained from the following equation,

$$\frac{1}{\tau} = \frac{1}{\tau_B} + \frac{1}{\tau_T} + \frac{1}{\tau_A} \qquad (2.45)$$

Where, τ_B, τ_T, τ_A are minority carrier lifetime for band-to-band, trap-assisted and Auger recombination respectively.

2.7 Working Principle of p-i-n Structured Solar Cells

The sandwich type device structure can help to carrier collection efficiency significantly. This kind of structure can be classified as two types: p-i-n and n-i-p (figure 2.7). If the light first enters the device through n^+ layer (electron transport layer or cathode) before getting absorbed in the absorber i-layer followed by p^+ layer (hole transport layer or anode), then this structure is known as n-i-p structure [figure 2.7 (a)]. And if the light is first incident on the p^+ layer (hole transport layer or anode) followed by absorber i-layer and n^+ layer

(electron transport layer or cathode), then this device structure is known as p-i-n structure [figure 2.7 (b)]. There are several choices for each of these layers as showed in figure 2.7.
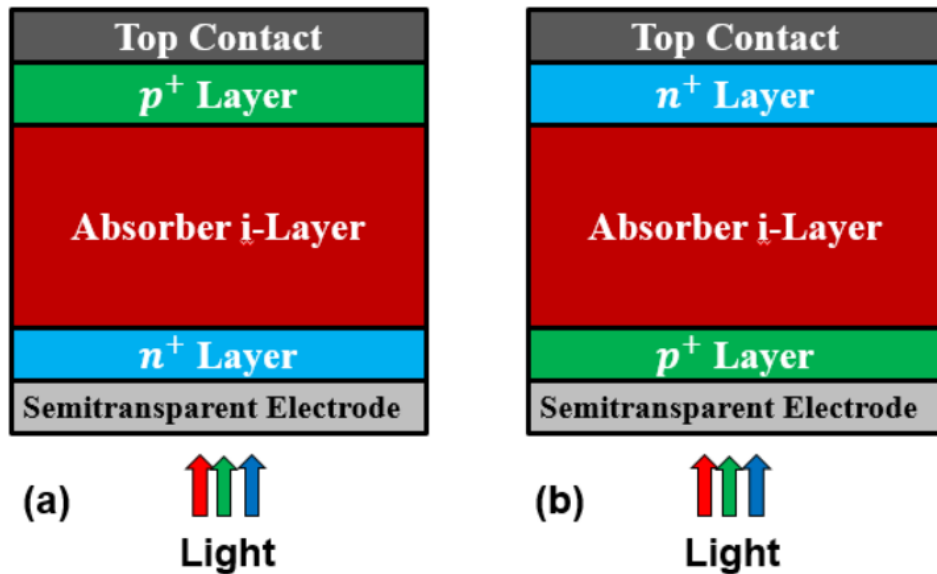
Figure 2.7: Structure of single junction solar cells (a) n-i-p (b) p-i-n (The figure is not drawn to scale)

The working principle of this sandwich kind of single junction solar cell can be explained in figure 2.8 using p-i-n structure as an example. First, the incident photon is absorbed within Absorber i-Layer and generates free electrons and holes [Figure 2.8 (a)]. Then these photo-generated carriers will go through ambipolar transport towards absorber-transport layers' interfaces. The transport layers must be chosen very carefully so that the band edges satisfy the required conditions to separate the photo-generate electron and holes. The n+ electron transport layer must have its conduction band matched with the absorber i-layer which allows this layer to collect electron [Figure 2.8 (b)]. At the same time, this n+ semiconductor must have a very high bandgap compared to the absorber i-layer which allows this layer to create a barrier for holes [Figure 2.8 (c)]. Thus, it collects only the electrons. On the other side, the p+ hole transport layer must have a valance band matched with the valance band of absorber

i-layer which allows it to collect holes without any significant barrier [Figure 2.8 (d)]. This layer must have a high bandgap so that it can block the electrons from being collected at this end [Figure 2.8 (e)]. The high bandgap of p+ hole transport layer also ensures that it is transparent for most of the photons and allows them to be absorbed in the absorber layer.
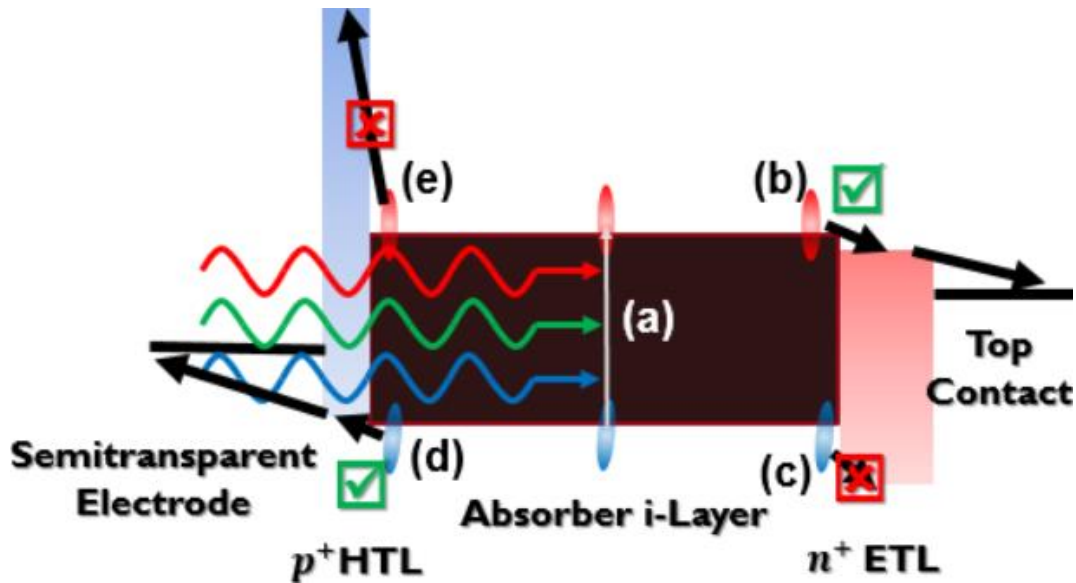
Figure 2.8: Simplified band diagram to explain the working principle of a p-i-n structured single-junction solar cell (a) Absorption of incident photon and generation of free electrons and holes (b) Collection of electrons through cathode (c) Blocking holes in absorber-cathode interface (d) Collection of holes through anode (c) Blocking electrons in absorber-anode interface

2.8 Shockley-Queisser (SQ) Limit

Using the generation, recombination and transport equations developed in the previous sections can be used to calculate the theoretical efficiency of a solar cell. These calculations were done by Shockley and Queisser in 1961 [13]. While doing the calculations in their work they only considered absorption loss, black-body radiation loss and radiative recombination loss to determine maximum achievable photo conversion efficiency of solar cells. The result from their work of maximum achievable efficiency as a function of active layer bandgap has been reported in figure (2.9).
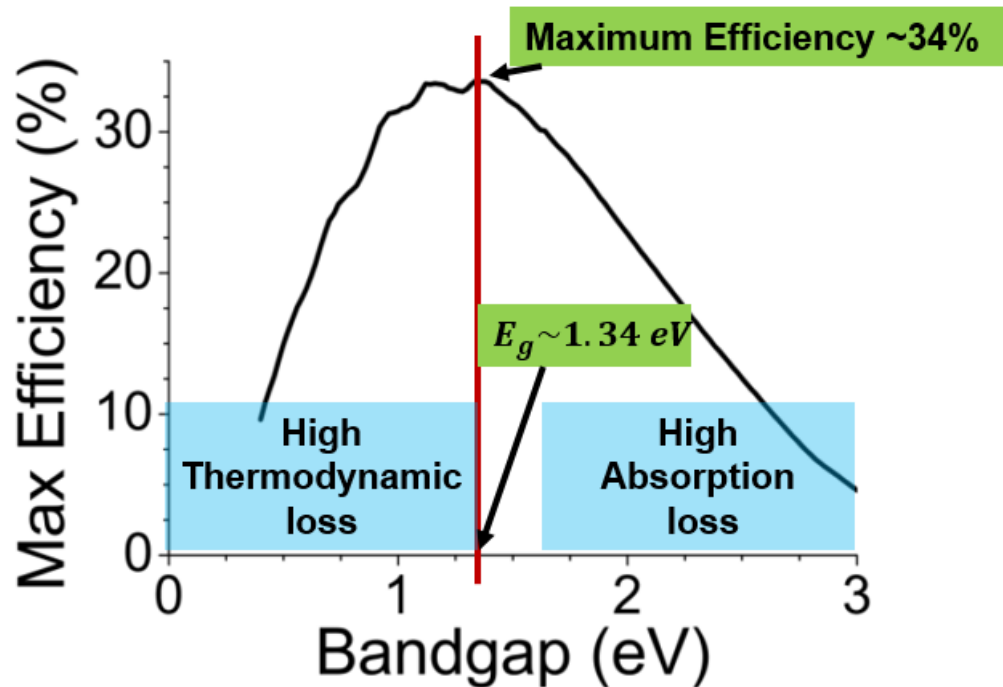
Figure 2.9: Schockley-Queisser limit of maximum power conversion efficiency for a single junction solar cell as function of absorber layer bandgap [13]

Initially with increasing bandgap of the absorber semiconductor the power conversion efficiency increases because of decrease in thermodynamic loss. When the bandgap of the material is about 1.34 eV the power conversion efficiency reaches at maximum of about 34%. If we keep increasing the bandgap of the material beyond 1.34 eV there is significant loss in absorption. Thus, the power conversion efficiency decreases with increasing bandgap.

There are several recombination losses and parasitic losses present inside a solar cell which results in the photo conversion lower than Schockley-Queisser limit. Considering other loss mechanisms, the NREL chart shows that the maximum achievable efficiency that can be achieved from a single junction solar cell is about 30%. Figure 2.10 different energy loss proportions as a function of bandgap of the material and figure 2.11 shows the actual photo conversion that has been achieved from different technologies.
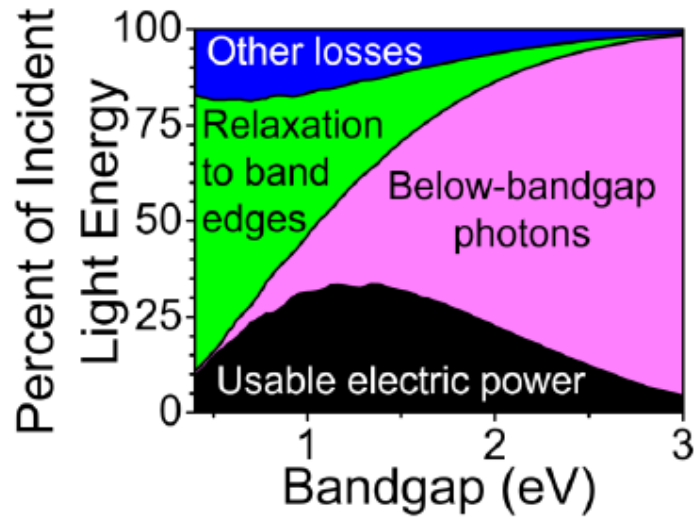
Figure 2.10: Proportion of different energy loss mechanisms as a function of bandgap [15]
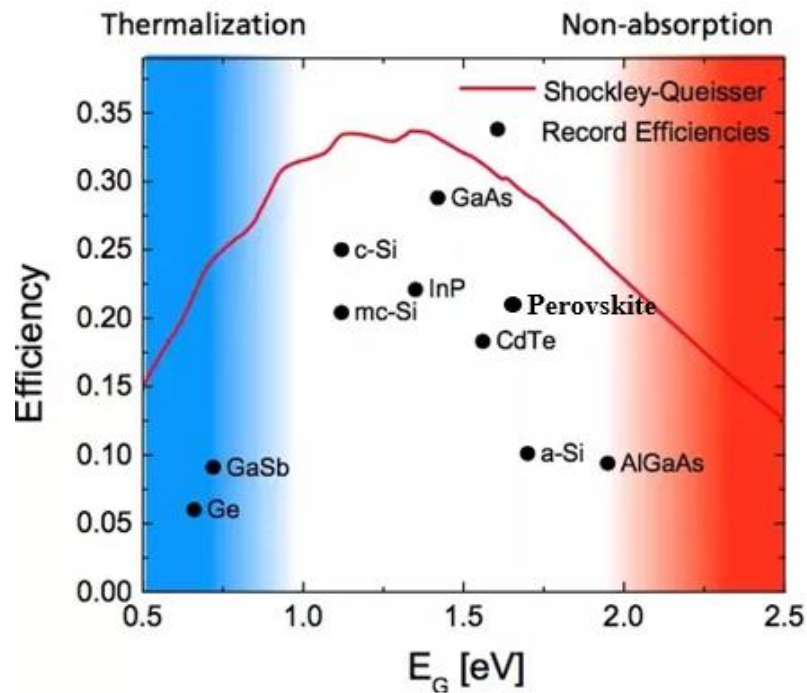
Figure 2.11: The maximum photo conversion efficiencies achieved from different technologies along with the Schockley-Queisser limit [14]

There are several ways to increase the photo conversion efficiency beyond Schockley-Queisser limit such as photon up-conversion, concentrated photovoltaics etc. Multi junction or tandem solar cells can also be helpful to improve the photo conversion efficiency.

2.9 Equivalent Circuit of a Solar Cell

The equivalent circuit of a solar cell can be represented by a single diode, a current source, which represents the photo-generated current, in parallel with the diode along with series and shunt resistance. The equivalent circuit of a solar cell using single diode has been showed in figure 2.12.
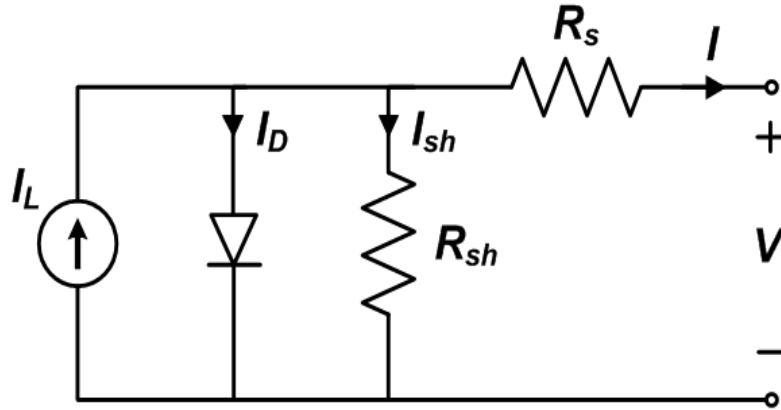
Figure 2.12: The equivalent circuit of a solar cell using a single diode model [15]

The current extracted from the solar cell through an external load can be given by the following equation,

$$I = I_L - I_0\left[\exp\left(\frac{qV}{nkT}\right) - 1\right] - \frac{V + IR_s}{R_{sh}} \tag{2.46}$$

Where, I_L is the photo-generated current, I_0 is the reverse saturation current of the diode, n is the ideality factor of the diode, R_s and R_{sh} are series and shunt resistance respectively, V is the applied voltage across the solar cell.

To represent the solar cell more precisely along with different kinds of recombination in the in the bulk of it, it is necessary to use a two-diode model as showed in figure 2.13.
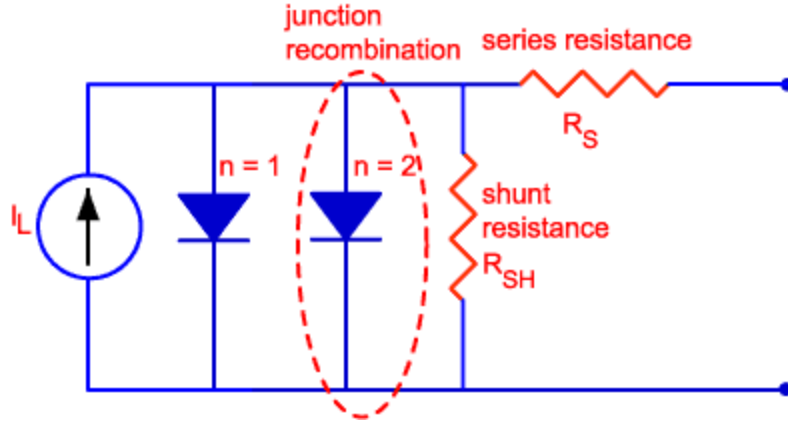
Figure 2.13: The equivalent circuit of a solar cell using a two-diode model [1]

Under illumination the current from the solar cell is given by,

$$I = I_L - I_{01}\left\{exp\left[\frac{q(V + IR_s)}{kT}\right] - 1\right\} - I_{02}\left\{exp\left[\frac{q(V + IR_s)}{2kT}\right] - 1\right\} - \frac{V + IR_s}{R_{sh}} \qquad (2.47)$$

Two diodes represent two possible recombination inside the bulk of solar cell: band-to-band and trap-assisted recombination. At low bias across the device at low level injection when the device is still depleted the diode current is proportional to $e^{\frac{qV}{2kT}}$ where the ideality factor of the diode is 2. At higher bias across the device with high injection level transport through quasi-neutral region dominates and the diode current is proportional to $e^{\frac{qV}{kT}}$ where the ideality factor of the diode is 1.

Under illumination the photo generated current is negative until we increase the bias high enough to have positive current through the device. Thus, during illumination single-diode model can be used to represent the solar cell.

REFERENCES

1   PV Education
        Link: http://www.pveducation.org

2   Pranav Joshi, Ph.D. dissertation, "Understanding the photostability of perovskite solar cell", Iowa State University (2016)

3   Liang Zhang, Ph.D. dissertation, "Device physics of perovskite solar cells", Iowa State University (2016)

4   Mehran Samiee, Ph.D. dissertation, "Device physics of organic and perovskite solar cells", Iowa State University (2015)

5   J. I. Pankove, "Optical processes in semiconductors", Dover Pub., New York, 1971

6   F. Urbach, "The long-wavelength edge of photographic sensitivity and of the electronic absorption of solids", Phys. Rev., 92, 1324 (1953). doi:10.1103/PhysRev.92.1324

7   Xie, Z., et al., Refractive index and extinction coefficient of CH3NH3PbI3 studied by spectroscopic ellipsometry. Optical Materials Express, 2015. 5(1): p. 29-43

8   Green, M.A., Improved value for the silicon free exciton binding energy. Aip Advances, 2013. 3(11)

9   Knupfer, M., Exciton binding energies in organic semiconductors. Applied Physics a-Materials Science & Processing, 2003. 77(5): p. 623-626

10   R. F. Pierret, Advanced semiconductor fundamentals. (Addison-Wesley Publishing Company, Reading, 1987)

11   B. G. Streetman and S. K. Banerjee, Solid state electronic devices. (Pearson Education, New Jersey, 2006), 6th edition

12   R. A. Smith, Semiconductors. (Cambridge Univeristy Press, London and New York, 1968)

13   W. Shockley and H. J. Queisser, " Detailed balance limit of efficiency of p-n junction solar cells", J. Appl. Phys., 32, 510 (1961). doi:10.1063/1.1736034

14   Quora, "Physical limitation in solar PV efficiency"
        Link: https://www.quora.com/What-are-the-physical-limitations-were-hitting-in-solar-PV-efficiency-and-where-might-we-see-breakthroughs

15   Wikipedia, "Shockley–Queisser limit",
        Link: https://en.wikipedia.org/wiki/Shockley%E2%80%93Queisser_limit

CHAPTER 3.   CHARACTERIZATION TECHNIQUES OF SOLAR CELLS

3.1 Introduction

To understand the operational principle of the device as well as to troubleshoot the problems, we need to do different electrical and optical characterizations. The basic concepts for different characterization techniques have been discussed in this chapter:

3.2 Current-Voltage (IV) Measurement

This is the most basic measurement to characterize solar cells where we apply voltage across a solar cell and measure the current through it. This measurement can be done either under illumination (Light IV) or in dark (Dark IV). We can interpret a lot of important parameters of a solar cell using these measurement techniques.

3.2.1 Light IV measurement [1,3]

The power conversion efficiency of a solar cell can be determined from light IV measurement. During this measurement, we apply voltage across the solar cell under illumination and measure the current through it. The evolution of a light IV curve with the help of equivalent circuit has been showed in figure 3.1. This IV curve of a solar cell is the superposition of the IV curve of the diode in the dark with photo-generated current.

In dark, the IV response of a solar cell is like the IV response of a diode [figure 3.1(a)]. The equation of the of this IV response is given by,

$$I = I_0[\exp\left(\frac{qV}{nkT}\right) - 1] \qquad (3.1)$$

Where, I_0 is the reverse saturation current of the diode, V is the applied voltage, n is ideality factor of the diode.
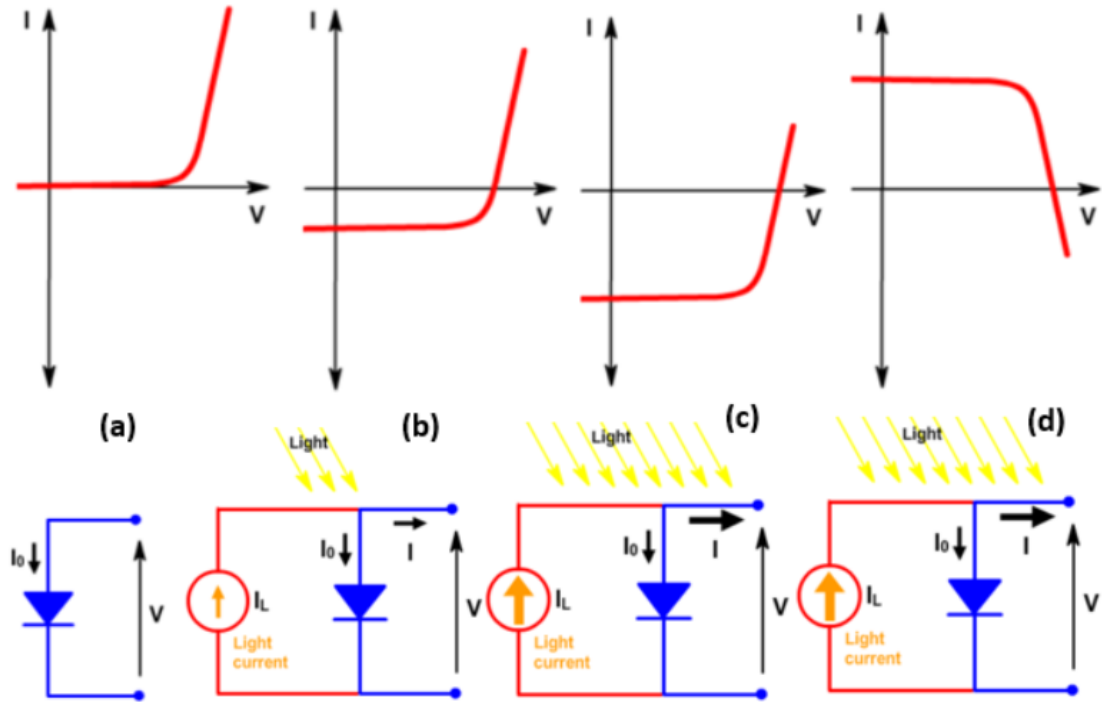
Figure 3.1: Effect of light on Current-Voltage (IV) Characteristics of a solar cell along with approximated equivalent circuit (a) In dark I-V response is like a diode (b) Under illumination the I-V characteristics shifts as it generates power (c) The greater the illuminated light intensity, the greater the shift (d) The convention is to invert the current axis as the cell generates power [1]

Under illumination, the IV response of a solar cell shifts into the fourth quadrant as power is generated from the cell [figure 3.1(b)] which is represented by a current source in parallel with the diode in the equivalent circuit. The equation of the of this IV response is given by,

$$I = I_0 \left[\exp\left(\frac{qV}{nkT}\right) - 1 \right] - I_L \tag{3.2}$$

where, I_L is photo-generated current

The greater the illuminated light intensity, the greater the shift of light IV curve in the fourth quadrant [figure 3.1(c)].
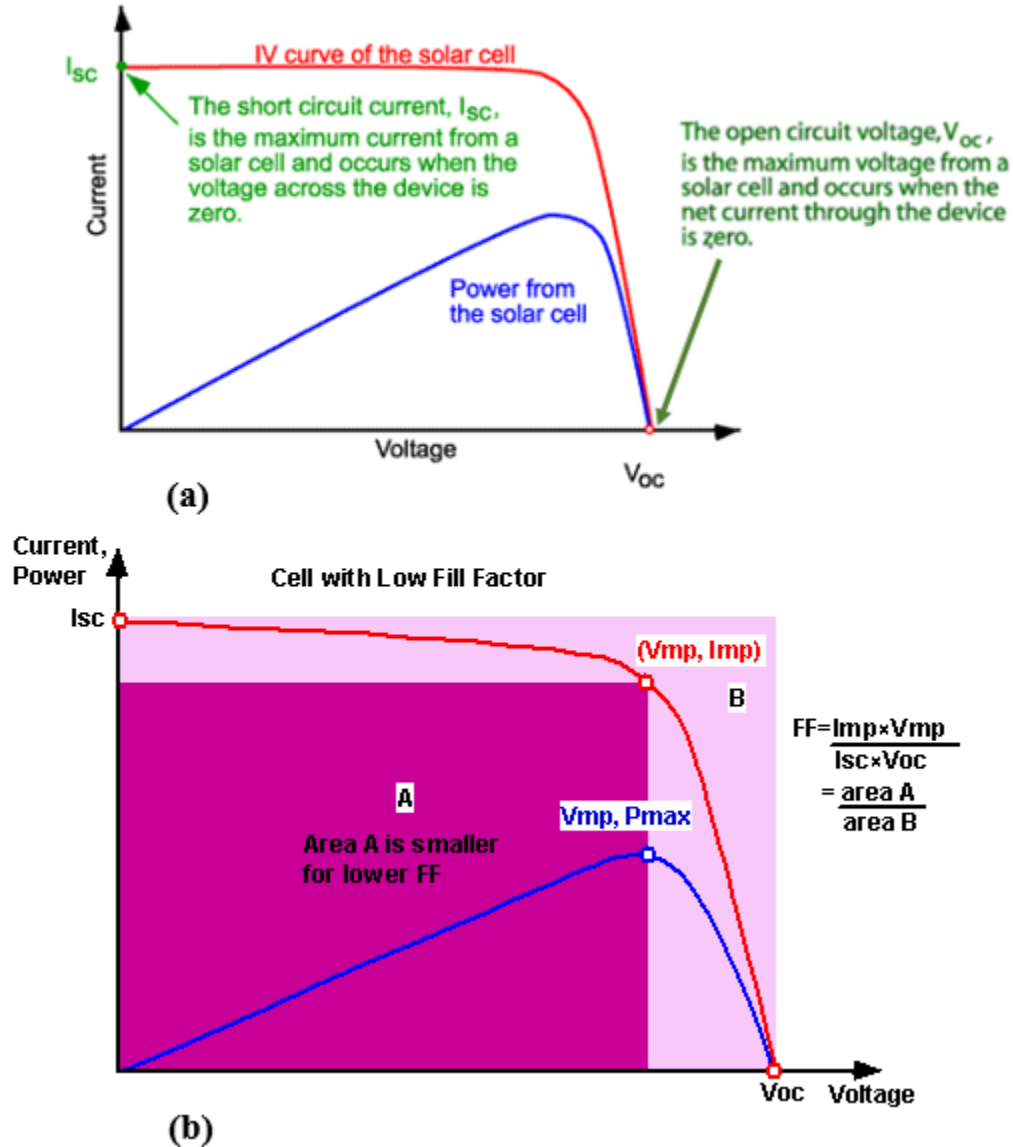
Figure 3.2: Some key parameters from the light IV response of a solar cell (a) Short-circuit current and open-circuit voltage (b) output power as a function of applied voltage and defining fill factor of a solar cell [1]

In convention, the current axis is inverted and represented the light IV curve in the first quadrant and the equation of this IV response can be given by,

$$I = I_L - I_0 \left[\exp\left(\frac{qV}{nkT}\right) - 1\right] \tag{3.3}$$

The basic parameters those can be extracted from the light IV curve has been showed in figure 3.2.

(i)   Short-Circuit Current [1]:

The short-circuit current is defined as the maximum current that can be extracted from a solar cell when voltage across the device is zero. The short-circuit current depends on the generation and collection of photo-generated carriers. Thus, it depends on the several optical and electrical factors such as the incident light spectrum, absorption coefficient and thickness of the active layer, area of the solar cell and the collection efficiency which is dependent on minority carrier lifetime. The short-circuit current density is given by,

$$I_{sc} = qAG(L_n + L_p) \tag{3.4}$$

Where, G is the generation rate, L_n and L_p are electron and hole diffusion lengths respectively, A is area of the solar cell. For an ideal solar cell ignoring the resistive loss mechanisms, the short-circuit current is identical to the photo-generated current [1].

(ii)   Open-Circuit Voltage [1]:

The open-circuit voltage of a solar cell is the maximum voltage that we can achieve across it when the current through it is zero. The open-circuit voltage can be express by the following equation,

$$V_{oc} = \frac{nkT}{q} \ln\left(\frac{I_L}{I_0} + 1\right) \tag{3.5}$$

where, I_L is photo-generated current, I_0 and n are reverse saturation current and ideality factor of the diode respectively, $\frac{kT}{q}$ is the thermal voltage.

The reverse saturation current depends on recombination inside the bulk active layer. V_{oc} is also a function of the carrier concentration and is given by the following equation [1,4],

$$V_{oc} = \frac{kT}{q} \ln \left\{ \frac{(N_A + \Delta n)\Delta n}{n_i^2} \right\} \tag{3.6}$$

Where, N_A is the doping concentration, n_i is the intrinsic carrier concentration and Δn is excess carrier concentration.

(iii)   **Fill Factor [1]:**

Both at open-circuit and short-circuit conditions the power extracted from the solar cell is zero. Figure 3.2(b) shows the electric power, $P = VI$ as a function of applied voltage and it suggests that if we extract power at a certain voltage and current, we can extract the maximum power from the solar cell. The fill factor can be defined as the ratio between the maximum power from the solar cell to the product of open-circuit voltage and short-circuit current. The fill factor (FF) of a solar cell has been illustrated in figure 3.2(b) and is given by,

$$FF = \frac{V_m I_m}{V_{oc} I_{sc}} \tag{3.7}$$

Where, V_m and I_m are voltage and current at maximum power point respectively

The maximum fill factor of a solar cell can be given by the following equation [1,5],

$$FF = \frac{v_{oc} - \ln(v_{oc} + 0.72)}{v_{oc} + 1} \tag{3.8}$$

Where, v_{oc} is the normalized V_{oc} and is given by,

$$v_{oc} = \frac{V_{oc}}{nkT/q} \tag{3.9}$$

(iv) <u>**Power Conversion Efficiency [1]:**</u>

The power conversion efficiency is the most common parameter that can be used to compare one solar to the other and can be calculated as the ratio between the maximum power that can be extracted from a solar cell to the input power. The power conversion efficiency,

$$\eta = \frac{P_{max}}{P_{in}} \tag{3.10}$$

$$\eta = \frac{V_{oc}I_{sc}FF}{P_{in}} \tag{3.11}$$

The input power for the standard AM1.5 spectrum is $100 \; mW/cm^2$.
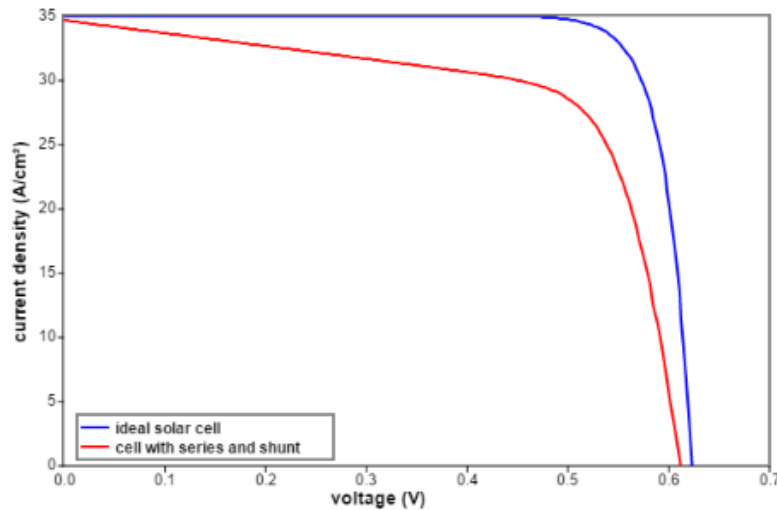
Figure 3.3: Light IV curve of an ideal solar cell (Blue curve) and light IV response for a practical solar cell with parasitic resistance [1,2]

The light IV measurement can also be used to determine the parasitic resistances of a solar cell. The fill factor of the solar cell decreases with increasing series resistance and decreasing shunt resistance. Ideally, we want the series resistance to be zero and shunt resistance to be infinite. Figure 3.3 shows the comparison of two light IV curves: one in ideal condition and the other with non-zero series and non-infinite shunt resistance. The series

resistance of a solar cell can be determined from the slope of the light IV curve when the current through the device is zero (open-circuit condition),

$$R_S = \frac{1}{\partial I/\partial V}\bigg|_{V=V_{oc}} \qquad (3.12)$$

The shunt resistance of a solar cell can be determined from the slope of the light IV curve when the voltage across the device is zero (short-circuit condition),

$$R_{SH} = \frac{1}{\partial I/\partial V}\bigg|_{V=0} \qquad (3.13)$$

3.2.2 Dark IV measurement [1,3]

Dark IV can be used to understand the recombination mechanism in a solar cell. During this measurement, the current through the device is measured by applying voltage across the solar cell in dark. The dark IV can be understood by a two-diode model with equivalent circuit in figure 3.4.
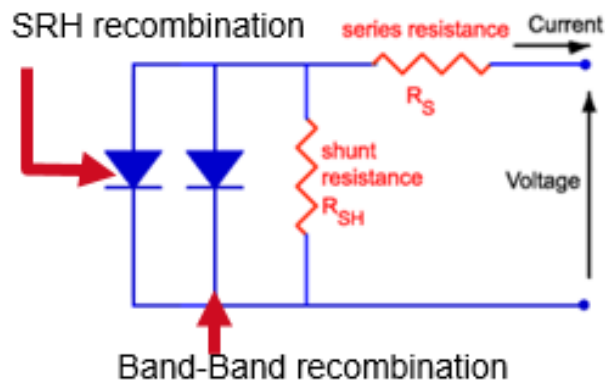
Figure 3.4: Equivalent circuit to understand the dark IV

The dark current is given by the following equation when the photo-generated current is zero,

$$I = I_{01}\left\{exp\left[\frac{q(V + IR_s)}{2kT}\right] - 1\right\} - I_{02}\left\{exp\left[\frac{q(V + IR_s)}{kT}\right] - 1\right\} - \frac{V + IR_s}{R_{sh}} \text{ (3.14)}$$

The dark IV curve is plotted in a semilog curve as showed in figure 3.5.
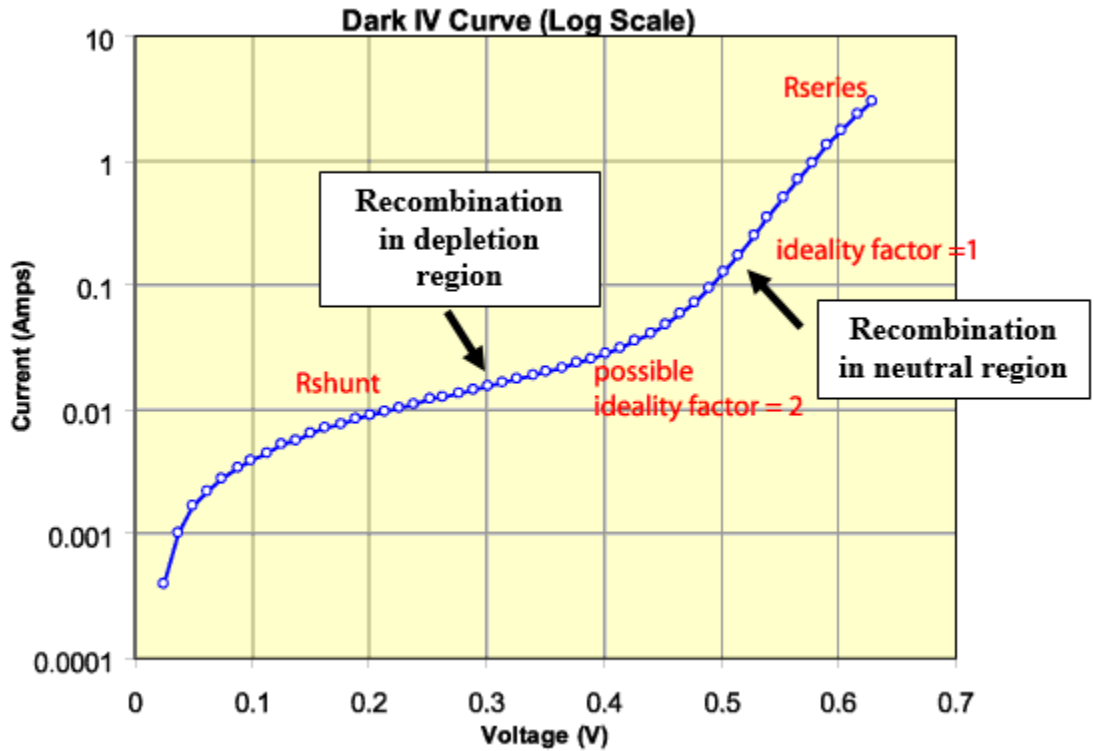
Figure 3.5: Semilog plot of a dark IV curve of a solar cell where different regions indicate different loss mechanisms from the p-n junction [1]

When a lower bias (0-0.1V) is applied across the solar cell the dark IV curve is dominated by the shunt current. Unwanted shunt path (for example, pinhole in the active layer) contributes to the shunt current. For a solar cell, it is excepted to have shunt resistance as high as possible to have shunt current as low as possible. If we keep increasing the voltage across the diode, the current increases exponentially as a function of applied voltage. This exponential curve can be fitted with two linear regions in the semilog plot. The slope of these two exponential regimes are called ideality factors which defines recombination mechanisms in these two regimes. In the lower voltage regime (0.1-0.45V) the ideality factor in 2 which

indicates the recombination in depletion region. The factor I_{01} is a function of minority carrier lifetime in the depletion region which is given by,

$$I_{01} = \frac{qAn_iw'}{2\tau_d} \tag{3.15}$$

Where, A is the area of the solar cell, n_i is the intrinsic carrier concentration, w' is effective depletion width, τ_d is carrier lifetime in depletion region.

At higher voltage regime (0.45-0.6V) the second exponential term dominates with an ideality factor of 1. This term is dominated by recombination in neutral region. The factor I_{02} is dependent on electron and hole diffusion lengths and is given by,

$$I_{02} = qA\left[\frac{D_n n_{p0}}{L_n} + \frac{D_p p_{n0}}{L_p}\right] \tag{3.16}$$

Where, A is the area of the solar cell, D_n and D_p are diffusion coefficients of electrons and holes respectively, L_n and L_p are minority carrier diffusion lengths of electrons and holes respectively, n_{p0} and p_{n0} are minority carrier concentrations of electrons and holes respectively in the neutral region.

At higher voltage regime, the dark current is dominated by the series resistance as the voltage drop across the series resistance becomes significant. In this regime, the dark IV response is no-longer exponential. So, besides the recombination mechanisms we can also extract the series and shunt resistance of the solar cell.

The ideality factors can be deviated from their ideal values if other recombination mechanisms are also contributing. For example, the Auger recombination has a characteristic ideality factor of $\frac{2}{3}$ and high carrier injection results in a characteristic ideality factor of 2 [1].

3.3 Quantum Efficiency [1,6]

External Quantum efficiency is defined as the ratio between the number of carriers collected to the number of photons at given wavelength of incident photon. Thus, quantum efficiency is expressed as a function of wavelength and is given by,

$$External\ Quantum\ Efficiency\ (\lambda) = \frac{Number\ of\ carriers\ collected\ (\lambda)}{Number\ of\ photons\ incident\ (\lambda)} \quad (3.17)$$

In other words, the external quantum efficiency is the measure of how efficiently a solar cell and absorb incident photon as well as collect the generated carriers. If all the incident photons are absorbed and all the photo-generated carriers are collected the quantum efficiency at that wavelength is 100%. The quantum efficiency as a function of incident photon wavelength for an ideal and a practical solar cell has been showed in figure 3.6. The "external quantum efficiency" of a solar cell includes reflection and transmission as optical losses. If we the quantum efficiency is calculated with photons which are not either transmitted or reflected, it is called "internal quantum efficiency".

The external quantum efficiency of a practical solar cell showed in figure 3.6 can be divided into three regimes based on the incident wavelength:

(i)   At very low wavelength ($< 300nm$) when the incident photon has very high energy the number of photons in AM1.5 spectrum is very low. Also, these high energy photons will also get absorbed in the substrate and transport layer (for instance, for organic and perovskite solar cells on glass substrate the incident photons with wavelength less than 300nm will get absorbed by glass as well as transport layer). As a result, the quantum efficiency is almost zero in low wavelength regime.

(ii)   For higher wavelength (> 1100 nm for crystalline-silicon) when the incident photon

energy is higher the bandgap of the absorber layer, no light will be absorbed. As a

result, the quantum efficiency in this regime is zero.
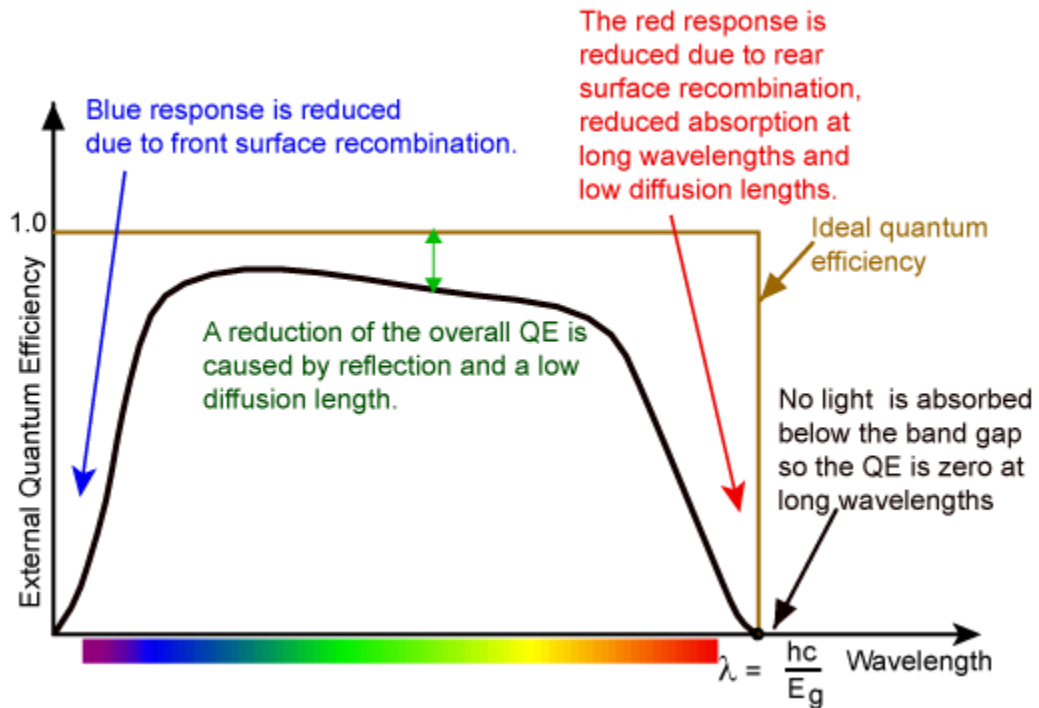
*Figure 3.6: The quantum efficiency of a silicon solar cell (black curve) and an ideal
solar cell (brown curve) simulated with solar spectrum AM1.5 [1]*

(iii)   In between these two regimes the external quantum efficiency is affected by surface

and bulk recombination. As these recombination mechanisms affect the collection

probability of photo-generated carriers, the quantum efficiency also decreases from

the ideal value of 1. For instance, blue photons have higher energy and the absorption

coefficient is also higher. Thus, most of the blue photons get absorbed very close to

the front surface. The higher the surface defect density near the front surface, the more

the quantum efficiency will suffer for incident of blue photons. By doing passivation

at front surface this problem can be mitigated. Again, the green photons have moderate

energy and they mostly will get absorbed in the bulk of the solar cell. Thus, the

collection efficiency in this regime will be affected by low diffusion lengths of photo-generated electrons and holes. The lower the carrier diffusion lengths, the lower the quantum efficiency will be in this regime. Similarly, for incident of red photons which have lower energy will get absorbed close to the rear surface. Thus, the higher the surface defect density at rear surface, the lower the quantum efficiency at this regime. The quantum efficiency in this regime can be improved by rear surface passivation.

The internal quantum (IQE) efficiency for a finite solar cell is given by,

$$IQE = \frac{\alpha^2 L^2}{\alpha^2 L^2 - 1}\left[1 - \frac{1}{\alpha L}\left\{\frac{\frac{SL}{D}\left\{\cosh\left(\frac{t}{L}\right) - e^{-\alpha t}\right\} + \sinh\left(\frac{t}{L}\right) + \alpha L e^{-\alpha t}}{\frac{SL}{D}\sinh\left(\frac{t}{L}\right) + \cosh\left(\frac{t}{L}\right)}\right\}\right] \quad (3.18)$$

Where, α is the absorption coefficient, S is the surface recombination velocity, L is minority carrier diffusion length, D is diffusion coefficient, t is thickness of active layer.

Usually, at high enough energy the absorption coefficient is high and $t \gg L$, $\alpha L \gg 1$ the equation 3.18 can be reduced to,

$$IQE = \frac{\alpha L}{1 + \alpha L} \quad (3.19)$$

$$\frac{1}{IQE} = 1 + \frac{1}{\alpha L} \quad (3.20)$$

So, from the slope of $1/IQE$ vs $1/\alpha$ plot the minority carrier diffusion length can be determined.

The short-circuit current can be calculated by integrating the product of the internal quantum efficiency and photon flux,

$$J_{sc} = q \int_{0}^{\infty} IQE(\lambda)\Gamma(\lambda)d\lambda \tag{3.21}$$

Where, $\Gamma(\lambda)$ is the photon at a wavelength of λ.
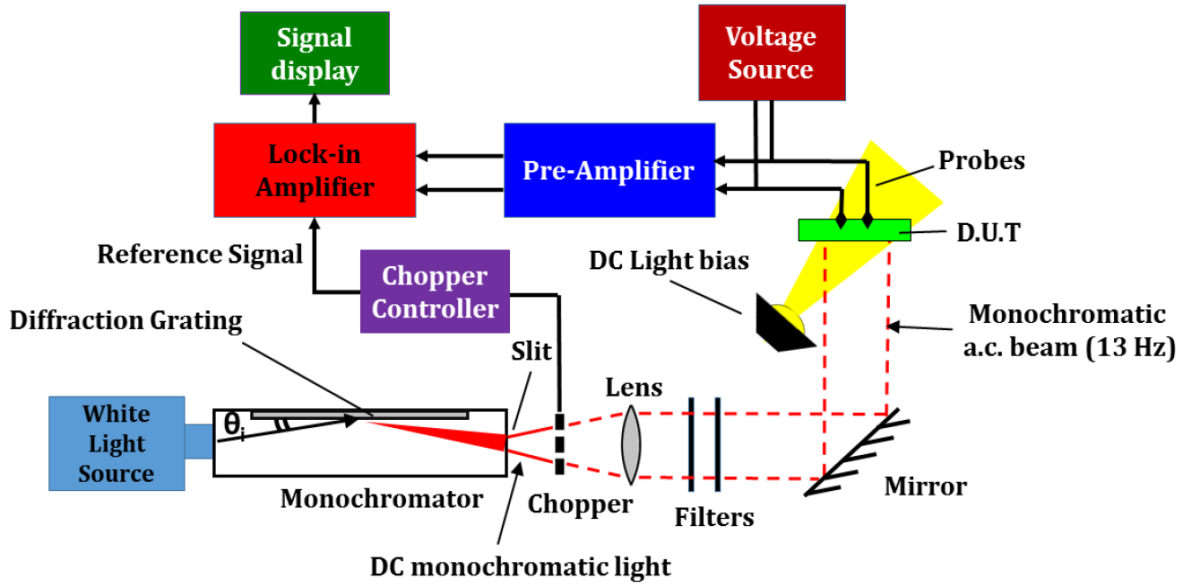
Figure 3.7: Quantum efficiency measurement setup. D.U.T is the sample or reference solar cell [6]

The quantum efficiency measurement setup has been showed in figure 3.7. White light from halogen bulk passes through a monochromator. Using diffraction grating inside the monochromator the light of desired wavelength can be achieved as it depends on the incident angle of white light. The rest of the light is filtered from the desired wavelength using a slit at the end of the monochromator. Then this D.C. light is converted into a A.C. light source using an optical chopper with frequency of 13 Hz. Then the lens collimates the incident light which then passes through optical filters to remove harmonics other than the desired wavelength. Using a mirror at 45° angle this monochromatic beam is incident on the sample and the sample is connected to probes for collecting signal. This signal is then fed into a preamplifier. Then a

lock-in amplifier has been used to filter the unwanted signal of frequencies other than chopper frequency, as this lock-in amplifier is synchronized with the chopper frequency. Then the response from the sample is read using the lock-in amplifier. A D.C. voltage source allows to measure the quantum efficiency at different bias voltage. Whereas a D.C. light source allows us to measure with light bias [6].

During this measurement, the photon flux of the beam is measured using a reference cell. The quantum efficiency at different wavelength is known for this reference solar cell. Signal for both reference and the sample is measured and the quantum efficiency of the sample can be determined from the following equation [6],

$$QE \ of \ sample(\lambda) = \frac{Signal \ from \ Sample \ (\lambda)}{Signal \ from \ reference \ (\lambda)} x \frac{Area \ of \ reference \ cell}{Area \ of \ sample} xQE \ of \ reference(\lambda)$$

3.4 Sub-gap Quantum Efficiency

Because of midgap and tail defect states the quantum efficiency doesn't decrease to zero instantaneously for energy of photons below the bandgap because there will be absorption through the defect states [Figure 3.8]. Using quantum efficiency precisely in this regime we can measure the distribution midgap density of states in a semiconductor. This method is known as "Sub-gap Quantum Efficiency". Figure 3.8 show the midgap and tail density of states where tail states are exponentially distributed and midgap states have Gaussian distribution. Knowing the density of states helps us to understand the recombination mechanisms inside the active layer. That is why sub-gap quantum efficiency is a very powerful tool for diagnosis of solar cells. The measurement setup is similar to quantum efficiency measurement as shown in figure 3.7.
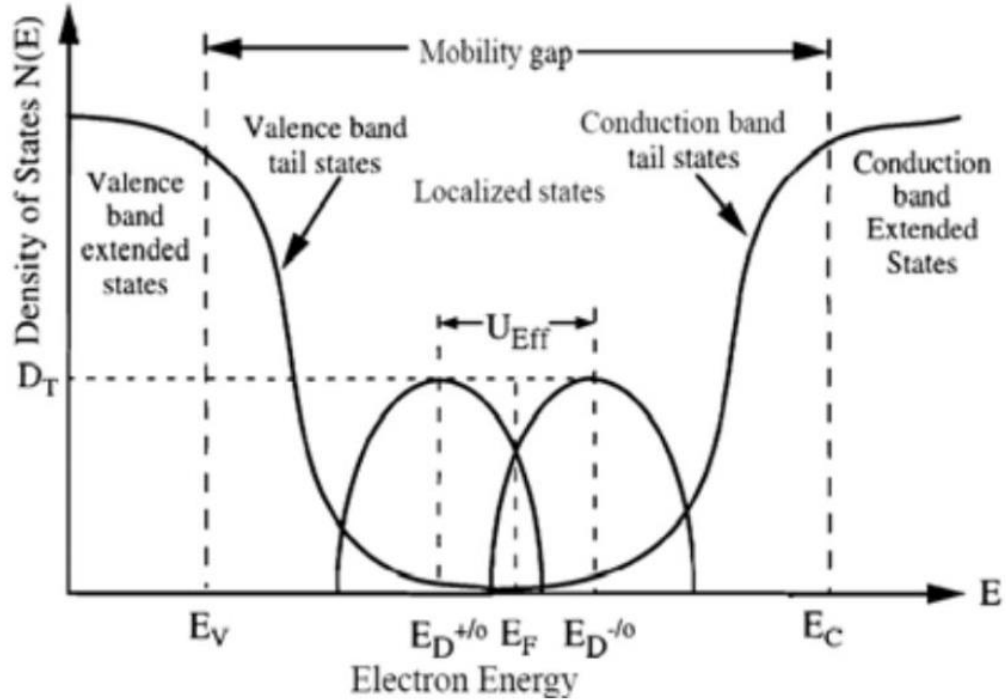
Figure 3.8: Density of states in a semiconductor. Tail states are exponentially distributed and midgap states have Gaussian distribution [7]
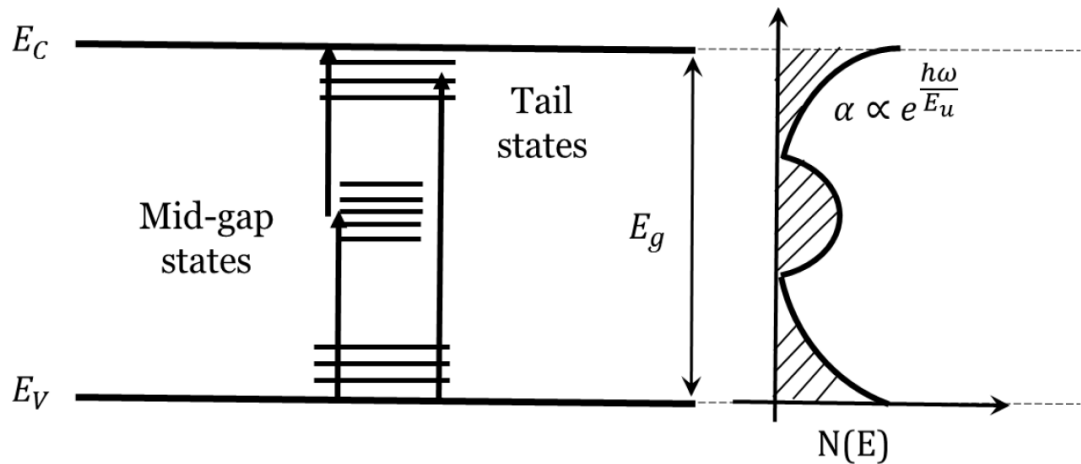
Figure 3.9: Transitions through midgap and tail defect states [2]

In the region where the absorption coefficient decreases exponentially due to exponentially distributed tail states, the absorption coefficient is given by [6,8,9],

$$\alpha = \alpha_0 * exp\left[-\frac{E_g - h\upsilon}{E_u}\right] \qquad (3.22)$$

Where, α_0 is the absorption coefficient in the band-edge, E_g is bandgap of the material, $h\upsilon$ is photon energy, E_u is Urbach energy. The Urbach energy is the measure of how broadly the tail states are distributed inside the bandgap of the material.
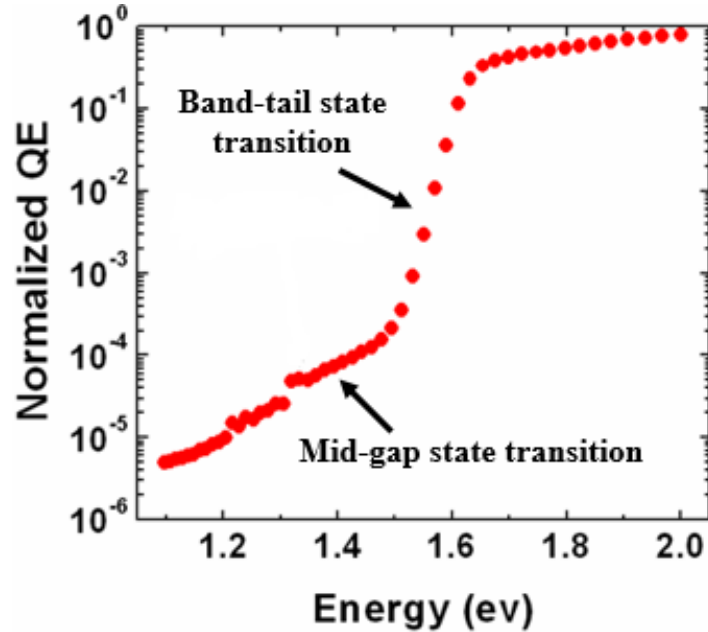
Figure 3.10: Sub-gap QE of perovskite solar cell [2]

Sub-gap quantum efficiency of a perovskite solar cell has been showed in figure 3.10. When the incident photon energy drops below the bandgap of perovskite (~1.6 eV), there is an exponential decrease in normalized QE. This regime corresponds to the absorption through tail states. We can calculate the Urbach energy from the slope of this curve in this regime. The Urbach energy of perovskite is about 16 meV which is lower than Urbach energy in organic solar cells (~50 meV). That means the spreading of tail states is lower in perovskite compared to organic solar cells which is a result from the perovskite being more crystalline. When the incident photon energy decreases even further the absorption is dominated by midgap state transitions [2].

3.5 Capacitance Vs Voltage (CV)

Capacitance-Voltage measurement is a very powerful tool to measure the dopant density of a pn junction solar cell. Band diagram of a Schottky diode has been showed in figure 3.11. In that figure, E_C and E_V are energy levels of conduction band and valance band respectively, E_F is the Fermi energy level, W_d is the depletion width of the pn junction and V_{bi} is the built-in potential.

Band diagram of a schottky junction
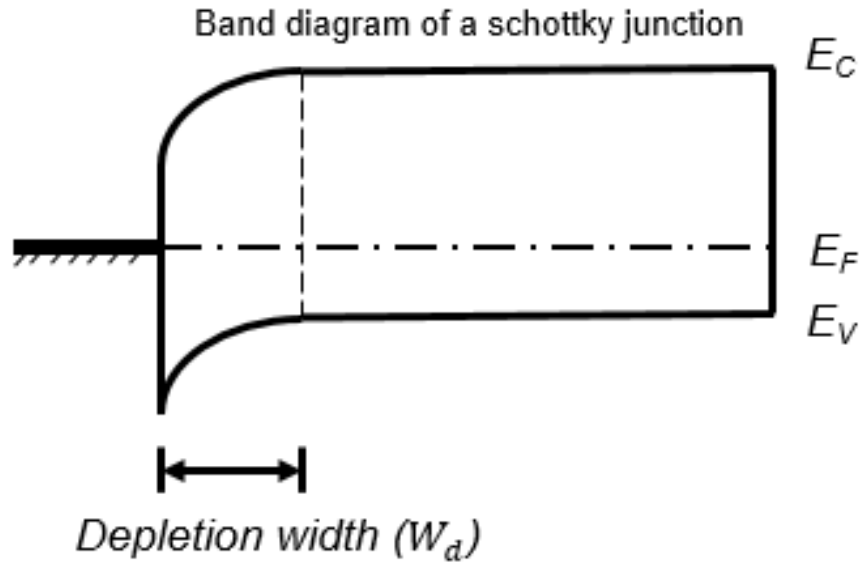
Figure 3.11: Band diagram of a Schottky PN junction [2]

The depletion width of the one-sided $(p - n^+)$ junction in figure 3.11 is given by,

$$W_d = \sqrt{\frac{2\epsilon(V_{bi} - V)}{qN_A}} \tag{3.23}$$

The junction capacitance is given by,

$$C = \frac{\epsilon A}{W_d} = A\sqrt{\frac{q\epsilon N_A}{2(V_{bi} - V)}} \tag{3.24}$$

$$\Rightarrow \frac{1}{C^2} = \frac{2(V_{bi} - V)}{q \epsilon N_A A^2} \tag{3.25}$$

Here, ϵ is dielectric constant of the semiconductor, A is the area of the cell and V is applied voltage across the junction. From equation 3.25 if we plot $1/_{C^2}$ as a function of applied voltage V, it can be fitted with a straight line where slope is inversely proportional to the dopant density, N_A and the intercept is proportional to be built-in potential, V_{bi} of the pn junction. The plot of $1/_{C^2}$ vs V for an ideal pn junction is showed in figure 3.12.
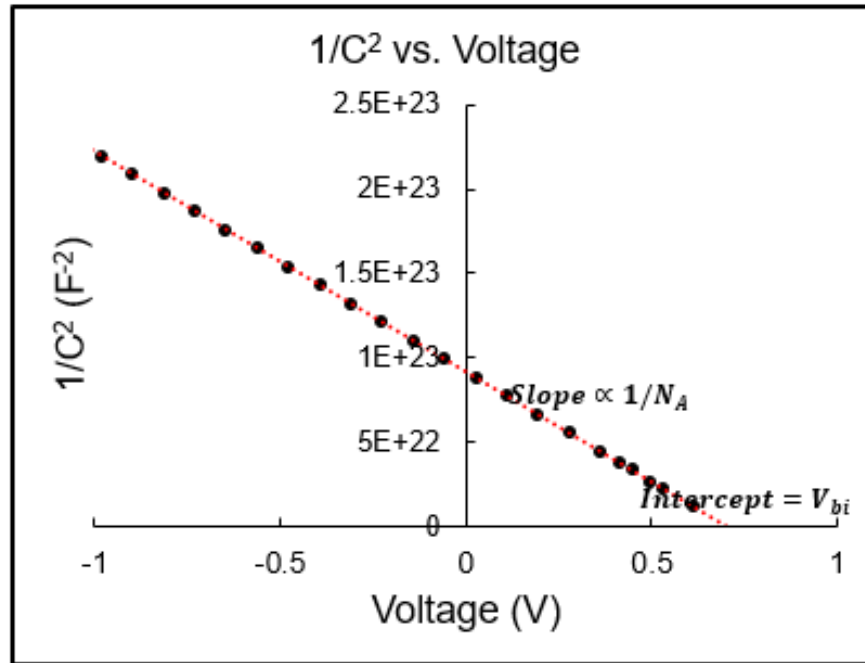
Figure 3.12: Ideal Capacitance-Voltage profile for an ideal one-sided $p - n^+$ junction with acceptor dopant density N_A and built-in potential V_{bi} [2]

3.6 Capacitance Vs Frequency (CF)

By varying the frequency of the AC signal while measuring capacitance we can measure the density of states at different energy levels within the bandgap of a semiconductor.

The density of states will help us to understand the recombination mechanism of a solar cell and the loss of photo-generated carriers.

If there is a defect state at energy level E_T within the bandgap, then the emission rate from these trap states to the conduction band can be expressed as [2,12,13],

$$e_n = v_0 \, exp\left[-\frac{E_C - E_T}{kT}\right] \qquad (3.26)$$

Where, v_0 is the attempt-to-escape frequency (ATEF), E_C and E_T are the energy levels for conduction band and trap states respectively.

If an AC bias is applied across a solar cell, whether the trapped electrons in the defect states can respond to the applied signal depends or not depends on the energy level of the trapped states and the AC signal frequency. Equation 3.26 shows that as the trap state goes deeper within the bandgap, the electron emission rate of the trap state decreases exponentially.
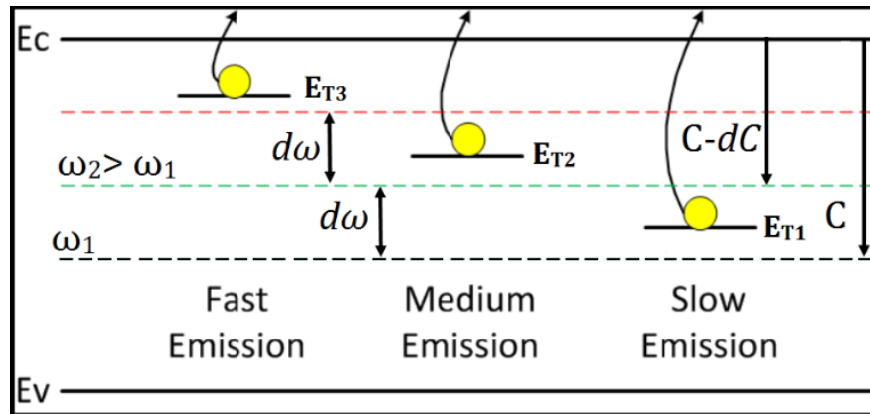
Figure 3.13: Higher emission rate of shallow trap allows them to contribute to the capacitance at both high and low frequencies. As deeper traps have low emission rates, they only respond to lower frequencies [6]

Figure 3.13 shows how traps at different energy levels contribute to the measured capacitance as function of applied AC signal frequency. If the emission rate of electrons for a trap state is higher than the applied signal frequency, those traps can respond to the applied external AC signal and leads to increase in measured capacitance of the device. If the emission

rate is lower than the applied signal frequency, those traps will not respond to the applied signal and will not contribute to the measured capacitance. In other words, from equation 3.26 as the shallow traps have higher emission rate, they can respond to both high and low frequencies of the applied external signal. Thus, the shallow traps contribute to the capacitance measured with either low or high frequencies. But the deeper the traps are inside the bandgap, the lower the emission rate they have. These deeper traps cannot charge or discharge following the external AC signal if the frequency of this signal is higher than the emission rate of these traps. Thus, the deeper traps will respond to only the lower frequencies and will contribute to the measured capacitance. The density of the traps can be determined from this capacitance vs frequency measurement, as the density of traps will be proportional to the differential of capacitance with frequency.

The density of states can be calculated using the following equation [2,6],

$$N_T(E_\omega) = -\frac{V_{bi}}{qW_d}\frac{dC}{d\omega}\frac{\omega}{kT} \tag{3.27}$$

Where, V_{bi} is the built-in potential, W_d is the depletion width, C is the measured device capacitance, $\omega = 2\pi f$ is the angular frequency of applied signal, E_ω is the "probing depth" which can be determined from the demarcation energy given by,

$$E_\omega = \frac{kT}{q}ln\left(\frac{\omega_0}{\omega}\right) \tag{3.28}$$

Where, $\omega_0 = 2\pi v_0$ is angular attempt-to-escape frequency (ATEF). The traps with energy lower than this demarcation energy will respond and contribute to the capacitance measured. By reducing the applied signal frequency, the demarcation energy can be increased which will allow deeper traps to respond and will increase the measured capacitance.

The attempt-to-escape frequency can be expressed as,

$$v_0 = N_C v_{th} \sigma_n \tag{3.29}$$

Where, N_C is the effective density of states in the conduction band, v_{th} is the thermal velocity and σ_n is the electron capture cross-section of the trap.

A typical capacitance vs frequency response and measured trap density of traps from this response has been showed in figure 3.14.
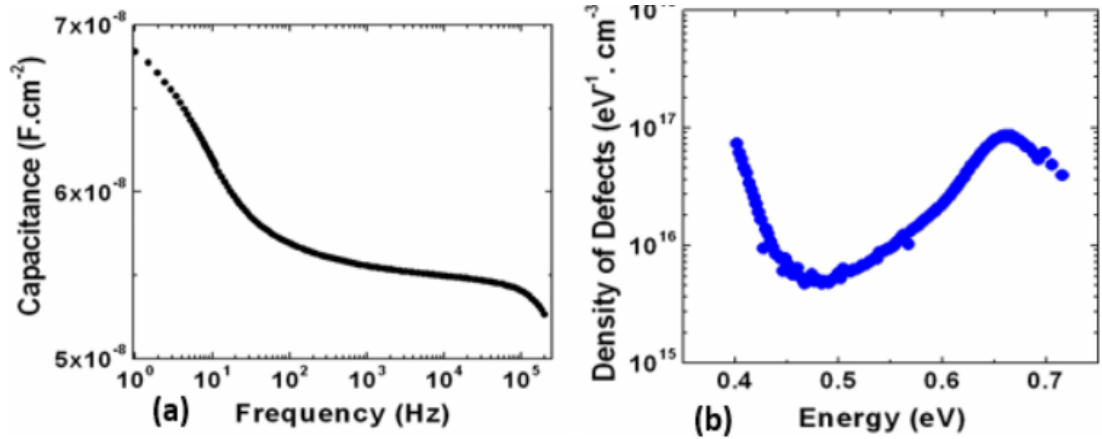
Figure 3.14: (a) Capacitance vs Frequency response of a perovskite solar cell (b) Trap density of states calculated from the CF response. Perovskite has a peak density of states at about 0.66 eV below the conduction band [2]

Both the effective density of states (N_C) and thermal velocity (v_{th}) are dependent on temperature as,

$$N_c \propto T^{3/2}, v_{th} \, \alpha \, T^{1/2} \tag{3.30}$$

Which gives the attempt-to-escape frequency is proportional to the square of temperature,

$$v_0 \propto T^2 \tag{3.31}$$

Thus, equation 3.26 can be expressed as a function of temperature [2,6],

$$ln\left(\frac{e_n}{T^2}\right) = \ln(\xi) - \frac{E_A}{kT} \tag{3.32}$$

Where, $E_A = E_C - E_T$ is the activation energy of the trap states and ξ is the proportional constant in equation 3.31.

From the Arrhenius plot $ln\left(\frac{e_n}{T^2}\right)$ vs $\frac{1}{kT}$ the intercept gives the attempt-to-escape frequency and the slope gives the activation energy. So, by measuring capacitance vs frequency at different temperatures we can measure the attempt-to-escape frequency and activation energy of trap states of a material. This characterization technique is known as Capacitance-Frequency-Temperature (CFT) measurement.
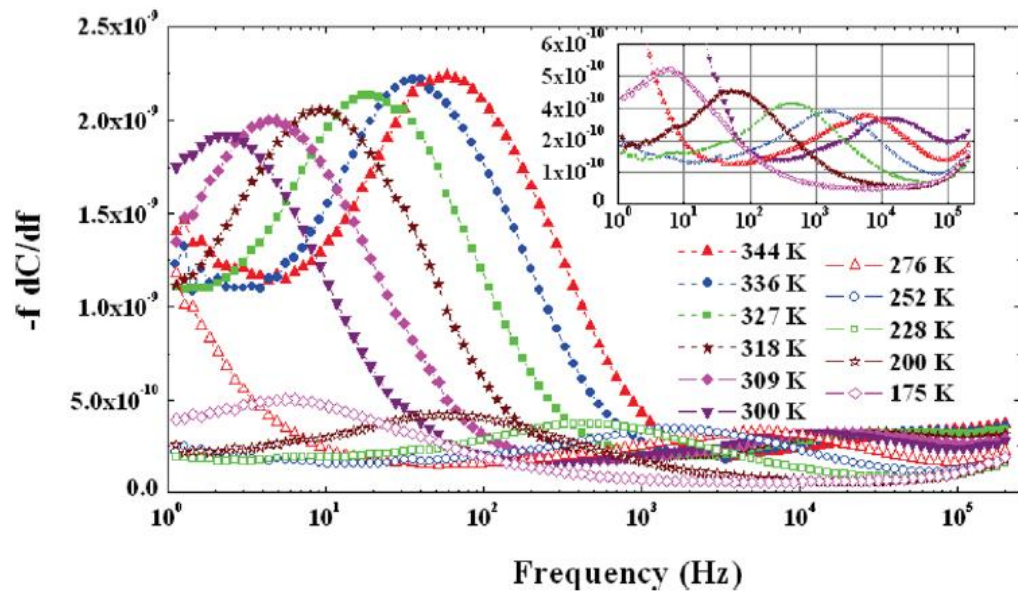
Figure 3.15: Capacitance vs Frequency plotted as $f\frac{dC}{df}$ as a function of frequency measured at different temperature [14]

Figure 3.15 shows the capacitance vs frequency measurement of a perovskite solar cell at different temperature and plotted as $f\frac{dC}{df}$ vs f. The capacitance increases with increase in temperature as the emission rate of the trap increases at higher temperature. The peaks are

related to the emission rates at different temperature. The Arrhenius plot of $\ln(\frac{f_{peak}}{T^2})$ vs $1/kT$ has been showed in figure 3.16. The slopes in figure 3.16 indicate that perovskite has trap energies of 0.66 eV and 0.24 eV below the conduction band. The attempt-to-escape frequency that has been calculated from the peaks for the dominant trap is $2 \ x \ 10^{11} s^{-1}$.
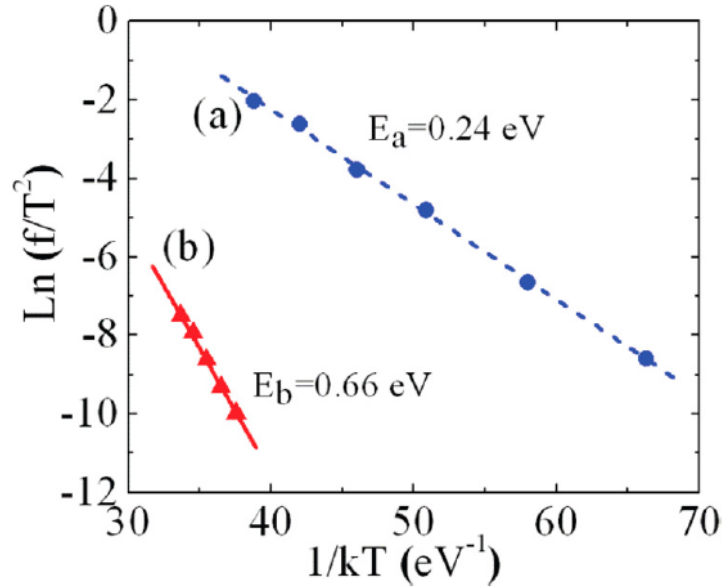
Figure 3.16: Arrhenius plot of peak frequencies in figure 3.15 as a function of 1/kT.
The attempt-to-escape frequency is about $2 \ x \ 10^{11} s^{-1}$ and activation energies of traps are
0.24 eV and 0.66 eV below the conduction band [14]

3.7 Photon-induced Degradation

Photon-induced degradation can be used to measure the change in basic photovoltaic characteristics (short-circuit current, open-circuit voltage, Fill factor and power conversion efficiency) as discussed in section 3.2 while the solar cell is under continuous illumination for several hours or days. This characterization technique helps us to understand the degradation mechanism of a solar cell influenced by incident photons. This is a very important characterization technique for perovskite and organic solar cells as these devices show significant degradation in performance under continuous illumination. During this

measurement, we measure the photovoltaic parameters in a periodic interval usually under illumination at one-sun intensity and calculate the normalized degradation of these photovoltaic parameters. Figure 3.17 shows a typical photon-induced degradation of a perovskite solar cell illuminated under one-sun intensity for 100 hours.
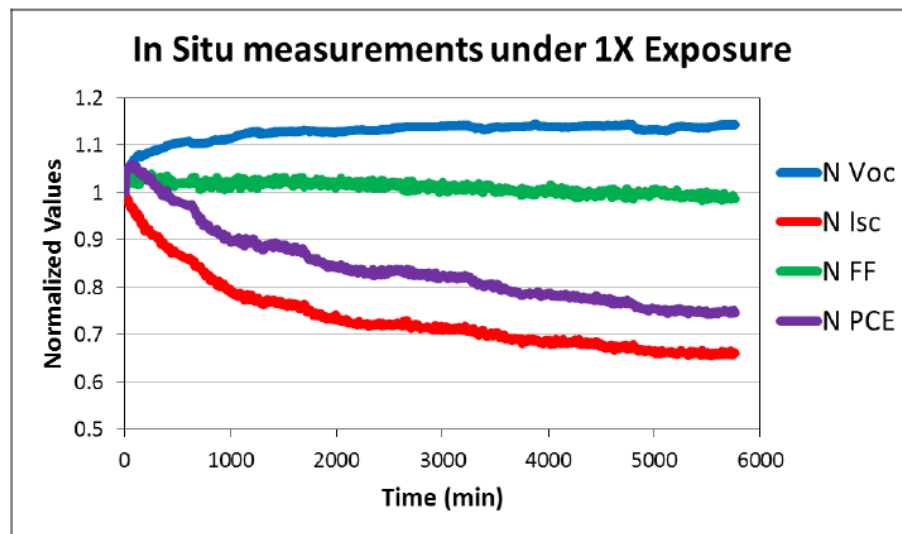
Figure 3.17: Photon-induced degradation of a perovskite solar cell under one-sun intensity (AM1.5). The photovoltaic parameters were measured for 100 hours at 10 minutes interval [15]

The perovskite and organic solar cells are also known to degrade in presence of oxygen and moisture. Encapsulating the device will help to eliminate the effect of moisture and oxygen, this encapsulation layer will trap heat during illumination which may also accelerate the degradation of these devices. So, to study the effect of photon only in degradation we need to get rid of moisture and oxygen from the degradation chamber rather than encapsulating the device. We have two degradation setups in our laboratory which help us to get inert environment during photon-induced degradation study (Figure 3.18): Environmental chamber and Glovebox.

Figure 3.18 (a) shows the schematic diagram and figure 3.18 (b) shows the setup of the environmental degradation chamber. In this setup, we need to expose the chamber in

atmosphere while load the sample. Then to remove the moisture and oxygen from the chamber we evacuate it to a very low pressure ($\sim 10^{-6} T$). For this purpose, the chamber is connected to a roughing pump and a turbo pump which is supported by a backing pump. The chamber is sealed with a vacuum-sealed lid. After evacuating the chamber, we can fill it with pure nitrogen. To make sure the temperature remains constant we have a fan connected inside the chamber. The chamber is sealed so that there is no air leakage from the atmosphere.
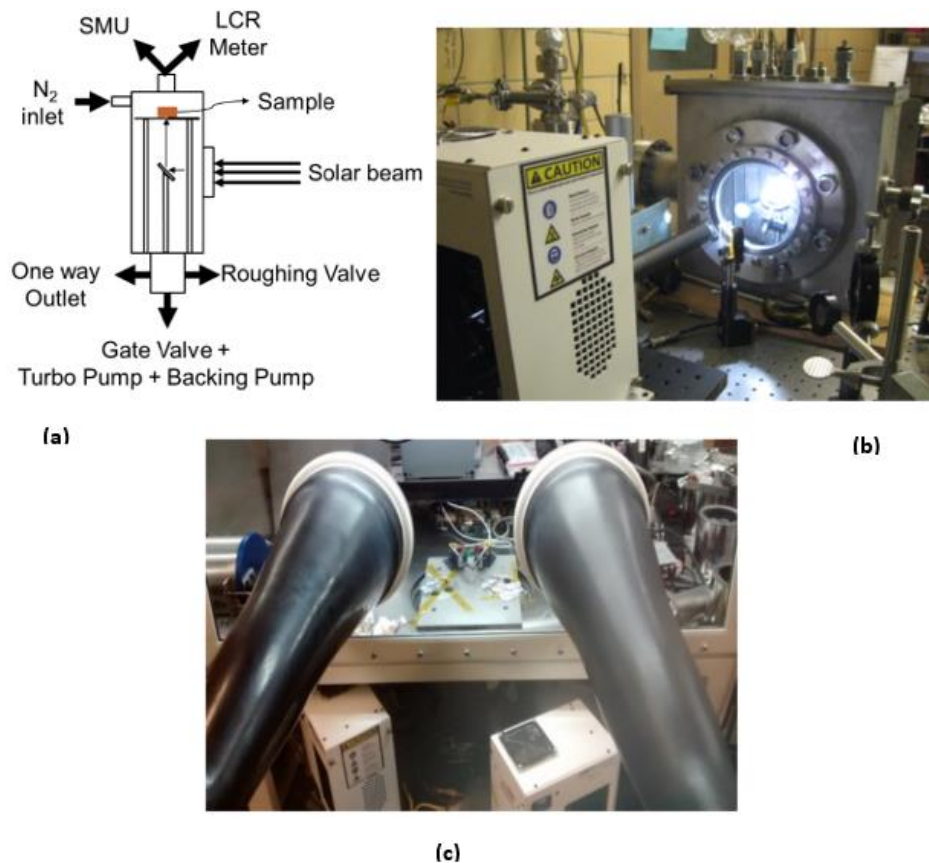
Figure 3.18: Photon-induced degradation setup (a) Schematic-diagram of environmental chamber setup (b) Environmental chamber (c) Degradation chamber inside glove-box [15]

Figure 3.18 (c) shows the setup inside glovebox to measure the photon-induced degradation. An inert nitrogen environment is always maintained inside a glovebox with both

moisture and oxygen less than 0.1 ppm. The samples are transferred trough a transfer chamber which can be purged with pure nitrogen before transferring inside the glovebox.

Both the systems can be maintained in a complete inert environment during the photo-degradation study and a transparent quartz window has been used for illumination from a solar simulator on the sample. Quartz window has been used to ensure minimum absorption of the incident light. Both systems have SMU and LCR meter connected from outside the chamber. The SMU is used to measure the basic photovoltaic parameters (short-circuit current, open-circuit voltage, fill factor and power conversion efficiency) and LCR meter is used to measure the capacitance vs voltage and capacitance vs frequency profile of the solar cell.
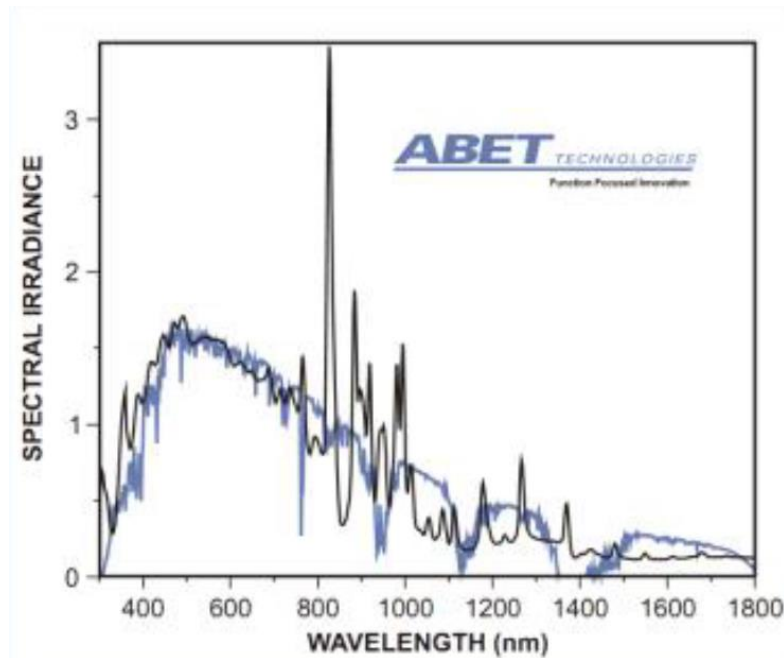
Figure 3.19: Spectrum of the ABET 105000 (Black curve) compared with standard AM1.5 spectrum (Blue curve) [15]

For the light source, we have used a ABET 105000 solar simulator to obtain the full solar spectrum of AM1.5. The spectral irradiance from the ABET 105000 solar simulator compared with the standard AM1.5 solar irradiance has been showed in figure 3.19. A standard silicon solar cell has been used to ensure the intensity of the solar simulator.

REFERENCES

1   PV Education
         Link: http://www.pveducation.org

2   Liang Zhang, Ph.D. dissertation, "Device physics of perovskite solar cells", Iowa State University (2016)

3   F. A. Lindholm, Fossum, J. G., and Burgess, E. L., "Application of the superposition principle to solar-cell analysis", IEEE Transactions on Electron Devices, vol. 26, pp. 165–171, 1979

4   R. A. Sinton and Cuevas, A., "Contactless determination of current–voltage characteristics and minority-carrier lifetimes in semiconductors from quasi-steady-state photoconductance data", Applied Physics Letters, vol. 69, pp. 2510-2512, 1996

5   M. A. Green, "Solar cell fill factors: General graph and empirical expressions", Solid-State Electronics, vol. 24, pp. 788 - 789, 1981

6   Mehran Samiee, Ph.D. dissertation, "Device physics of organic and perovskite solar cells", Iowa State University (2015)

7   E. A. Davis and N. F. Mott, "Conduction in non-crystalline systems v. Conductivity, optical absorption and photoconductivity in amorphous semiconductors", Phil. Mag., 22, 903 (1970)

8   S. John et. al., "Theory of electron band tails and the Urbach optical absorption edge", Vol.57, No. 14, 1986, pp. 1777-1780.

9   F. Urbach, "The long wavelength-edge of photo-graphic sensitivity and of the electronic absorption of solids", Physical Review, 92, 1324, December 1953.

10   L. C. Kimerling, "Influence of deep traps on the measurement of free-carrier distributions in semiconductors by junction capacitance techniques", J. Appl. Phys., 45, 1839 (1974). doi:10.1063/1.1663500

11   T. Walter, R. Herberholz, C. Müller, and H. W. Schock, "Determination of defect distributions from admittance measurements and application to cu(in,ga)se2 based heterojunctions", J. Appl. Phys., 80, 4411 (1996). doi:10.1063/1.363401

12   D. K. Schroder, Semiconductor material and device characterization. (Wiley-IEEE Press, New York, 2015), 3rd edition

13   R. F. Pierret, Advanced semiconductor fundamentals. (Addison-Wesley Publishing Company, Reading, 1987).

14   Mehran Samiee, Siva Konduri, Balaji Ganapathy, Ranjith Kottokkaran, Hisham A. Abbas, Andrew Kitahara, Pranav Joshi, Liang Zhang, Max Noack, and Vikram Dala, "Defect density and dielectric constant in perovskite solar cells", APPLIED PHYSICS LETTERS 105, 153502 (2014)

15   Pranav Joshi, Ph.D. dissertation, "Understanding the photostability of perovskite solar cell", Iowa State University (2016)

CHAPTER 4.   PEROVSKITE SOLAR CELLS

4.1 Introduction

As discussed in chapter 1, to make solar energy a prime source of energy the cost must be reduced significantly. Silicon is still the most popular material for photovoltaics. Although the cost of silicon solar panels has reduced significantly over the last few decades, we need to find some new photovoltaic materials which would lower the cost of solar panels as well as increase the power conversion efficiency.

Perovskite solar cells can meet both these criteria. Low material cost, ease of fabrication and easy roll-to-roll processing makes perovskite solar cells very exciting choice. Also, various research groups have already reported to have power conversion efficiencies more than 20% [1]. Figure 4.1 shows the power conversion efficiency evolution of perovskite solar cells compared with other solar technologies.
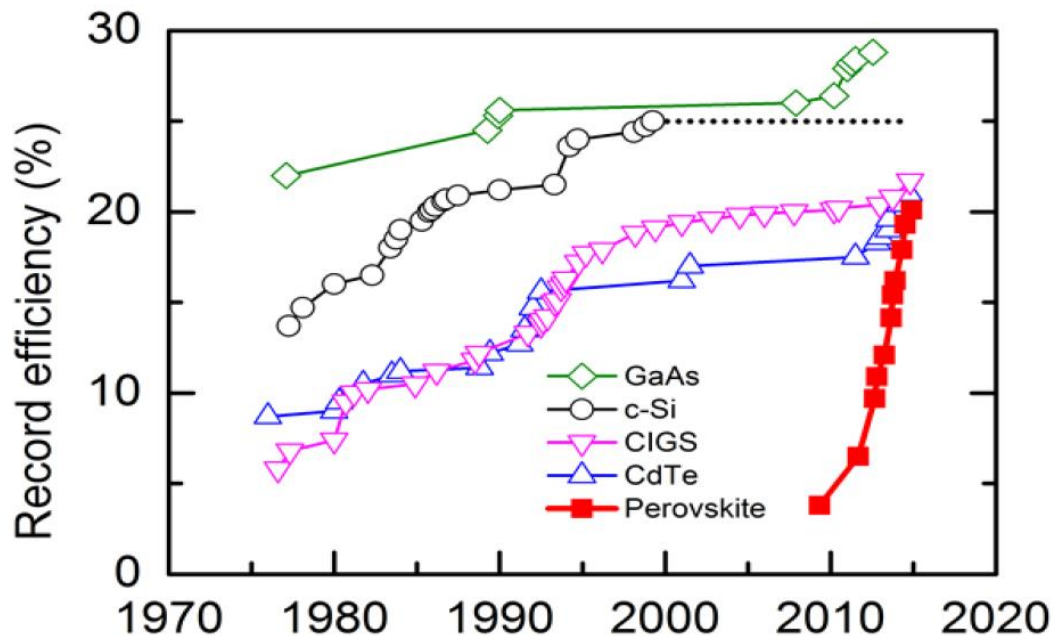
Figure 4.1: Evolution of power conversion efficiency of perovskite solar cells compared with other solar technologies [3,4]

Perovskite also has a bandgap pf 1.6 eV which makes it a very exciting choice as a high

bandgap cell. Figure 4.2 shows the contour plot of Shockley–Queisser limit for a tandem solar
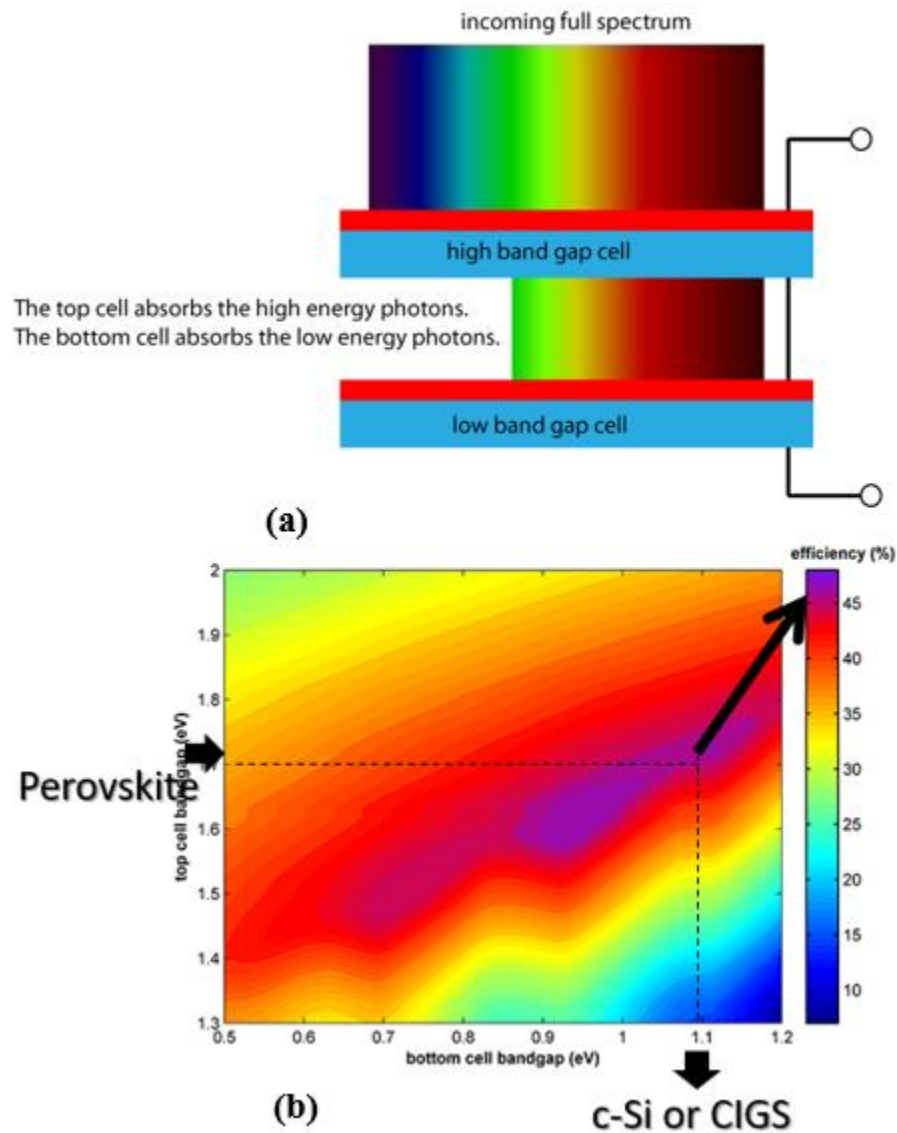
cell,

Figure 4.2: (a) Series-connected tandem solar cell (b) Maximum efficiency of a two-junction tandem solar cell [2]

The maximum efficiency that can be obtained from two-junction series connected solar

cell is 47%. At this peak efficiency, the top cell has a bandgap of 1.63 eV and the bottom cell

has a bandgap of 0.96 eV [2]. Perovskite can be used as a top cell where we don't have a

material at 0.96 eV. But, crystalline silicon or CIGS (bandgap of about 1.1 eV) is closer to 0.96 eV. With perovskite as top cell and c-Si or CIGS as bottom cell can give a maximum theoretical efficiency of about 44%. Thus, perovskite as a photovoltaic material has huge potential not only as a low-cost material but also to obtain a high power-conversion efficiency.

4.2 Perovskite

Perovskite is a crystal structure with a general crystal structure ABX_3, where A is a cation with +1 vacancy of electron, B is a also a cation but with +2 vacancies and X is an anion (either halogen or oxygen). Figure 4.3 shows a generalized lattice structure of perovskite.
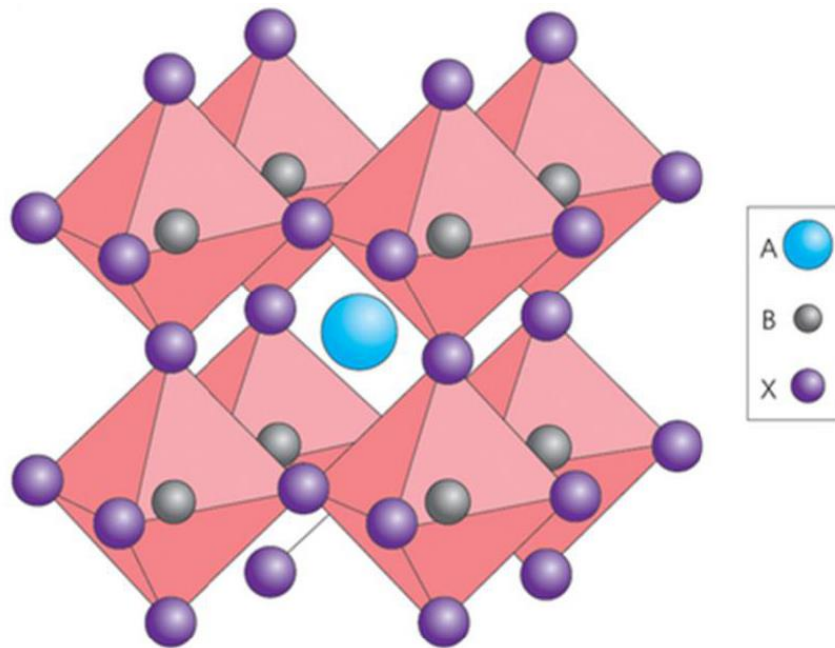
Figure 4.3: Lattice structure of Perovskite (ABX_3) [5]

To form perovskite, the ionic radii of A, B and X must satisfy the following tolerance and octahedral factors [6],

$$\text{Tolerance factor, } t = \frac{R_A + R_X}{\sqrt{2(R_B + R_X)}} \text{ and } 0.81 < t < 1.11 \qquad (4.1)$$

$$\text{Octahedral factor, } \mu = \frac{R_B}{R_X} \text{ and } 0.44 < \mu < 0.9 \qquad (4.2)$$

Where, R_A, R_B and R_X are ionic radii of A, B and X respectively.
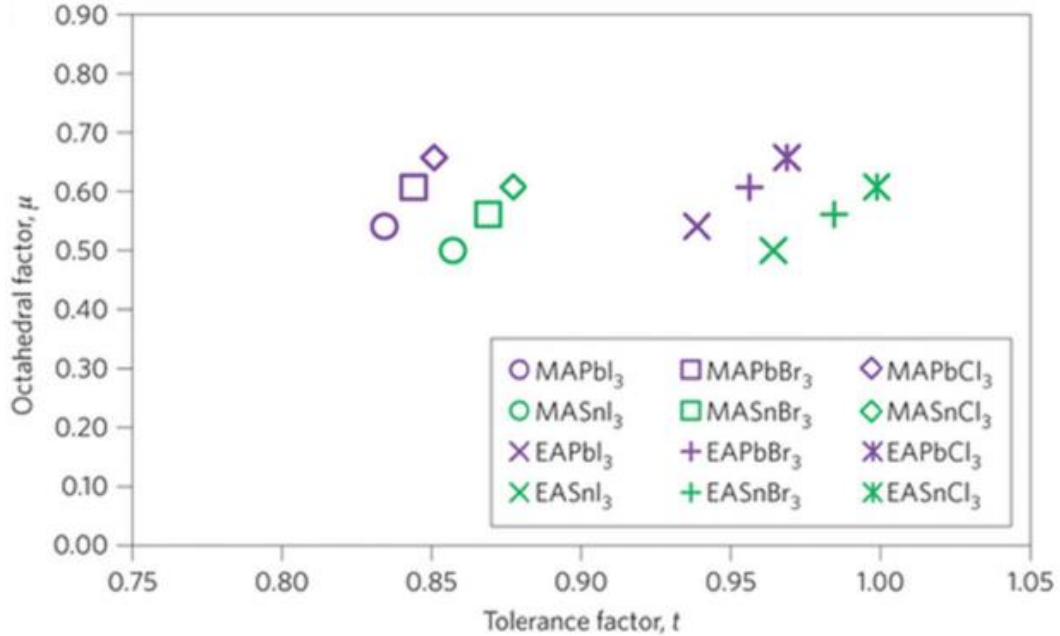
Figure 4.4: Material combinations for lead-halide perovskite which satisfy the tolerance and octahedral factor limits as described in equation 4.1 and 4.2 [5]

Figure 4.4 shows combination of different materials which satisfy the necessary tolerance and octahedral conditions to form perovskite. In this figure, A as +1 cation can be: MA is methylammonium ($CH_3NH_3^+$), EA is ethylammonium ($CH_3CH_2NH_3^+$), FA is formamidinium ($NH_2CH = NH_3^+$) or Cesium (Cs). B as +2 cation can be: Lead (Pb) or Tin (Sn). X is a halide anion: Iodine (I), Chlorine (Cl) or Bromine (Br).

Although the use of perovskite as LEDs and thin-film transistor was discovered several decades ago [7,8,11], it was Miyasak's group who first demonstrated the use of perovskite for photovoltaic application in 2006 with a power conversion efficiency of 2.2%. They have used perovskite with $CH_3NH_3PbBr_3$ as absorbing material [9]. The same group in 2009 showed an increase in power conversion efficiency to 3.8% by replacing Bromine with Iodine as $CH_3NH_3PbI_3$ [10]. Then different research groups started optimizing perovskite solar cells by

using different transport layers. In 2011, it was Prak's group who optimized it using TiO_2 as electron transport layer and achieved a power-conversion efficiency of 6.5% [12]. Park's and Grätzel's group in 2012 used spio-MeOTAD as hole-transport layer and achieved a power-conversion efficiency of about 9.7% [13]. In 2013, Seok's group achieved a power-conversion efficiency of about 12.3% using mix-halide perovskite [14]. Again in 2013, Grätzel's group reported to achieve power-conversion efficiency more than 15% [15]. In the same year, Snaith's group first was the first to deposit perovskite using vapor deposition [16]. Soon after that several groups have reported to achieve power-conversion efficiency more than 20% [1,17,18].

4.3 Properties of Perovskite

To understand the carrier transport and device degradation mechanism as well as optimize the cell efficiency we need to know the electronic and optical properties of the film.

4.3.1 Absorption coefficient, α

The absorption coefficient is a very important characteristic for an absorber layer. The higher the absorption coefficient the thinner the absorber layer we need to absorb incident light effectively. Figure 4.5 shows the comparison of absorption coefficient at different wavelengths among different photovoltaic materials. This figure suggests that perovskite has absorption coefficient ($\sim 10^5 - 10^6 \ cm^{-1}$) significantly higher than crystalline silicon. That means only about 100 nm – 1 µm of perovskite film is enough to absorb most of the incident photons efficiently.
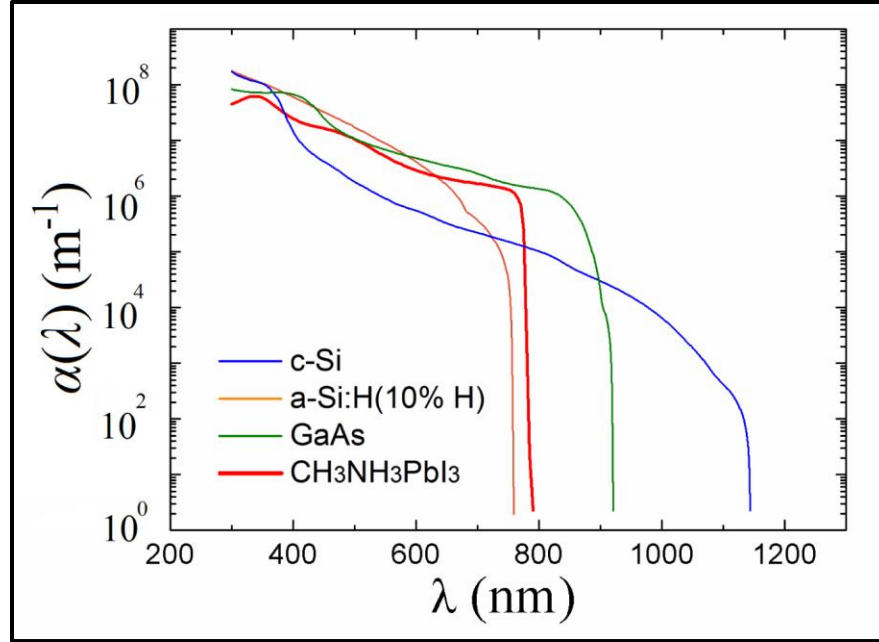
Figure 4.5: Comparison of absorption coefficient at different wavelengths among different photovoltaic materials [19]

4.3.2 Bandgap, E_g

Bandgap is a very important parameter for a photovoltaic material, because according to Shockley–Queisser limit the maximum theoretical efficiency that can be achieved is dependents on bandgap of the material. Perovskite is a direct bandgap material. The bandgap can be found from the "Tauc plot" of α^2 vs $h\upsilon$. We can measure quantum efficiency and use it instead of the absorption coefficient, because for energy closer to the bandgap the quantum efficiency can be expressed as [2],

$$QE\ (\lambda) = c\alpha(\lambda)t \qquad (4.3)$$

Where, t is the thickness of the absorbing layer, α is the absorption coefficient at incident wavelength of λ and c is a constant.
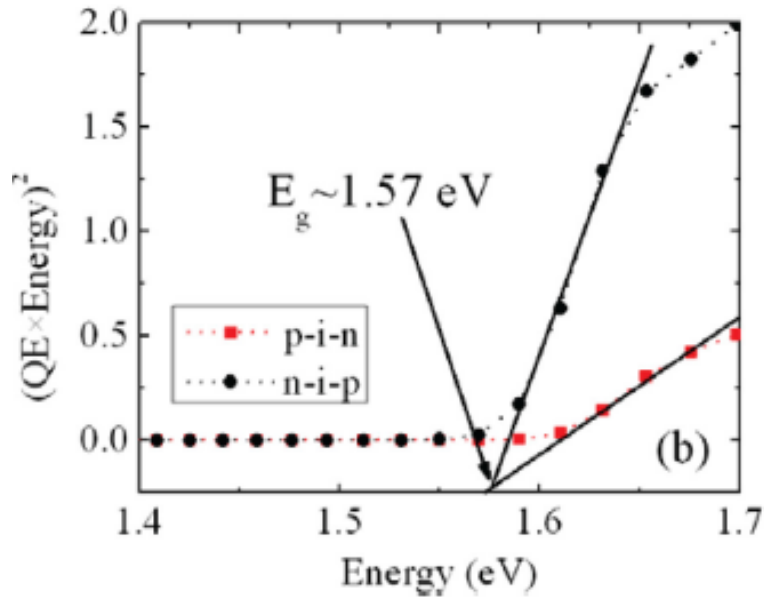
Figure 4.6: $(Quantum\ Efficiency\ x\ Energy)^2\ vs\ Energy$ plot to calculate the bandgap of perovskite. It indicates a bandgap of about 1.58 eV [20]

Figure 4.6 shows $(Quantum\ Efficiency\ x\ Energy)^2\ vs\ Energy$ plot to calculate the bandgap of perovskite. This figure shows that the bandgap of perovskite is about 1.58 eV. According to the Shockley–Queisser limit the maximum efficiency that can be obtained from a single junction perovskite solar cell is 31%. The maximum efficiency that can be obtained from a double-junction tandem solar cell as perovskite as high bandgap cell and either c-Si or CIGS as low bandgap cell is about 44 %. So, perovskite can give a huge boost in power conversion efficiency.

Hoke et al. showed an interesting aspect of perovskite in 2015 [21]. They showed that for a mixed halide perovskite the bandgap can be varied by changing the relative composition of Iodine and Bromine. The general formula of this mixed halide perovskite can be expressed as $CH_3NH_3PbI_{3-x}Br_x$. By varying the relative composition between Iodine and Bromine the bandgap of perovskite can be varied from about 1.55 eV to about 2.20 eV (as showed in Figure 4.7).
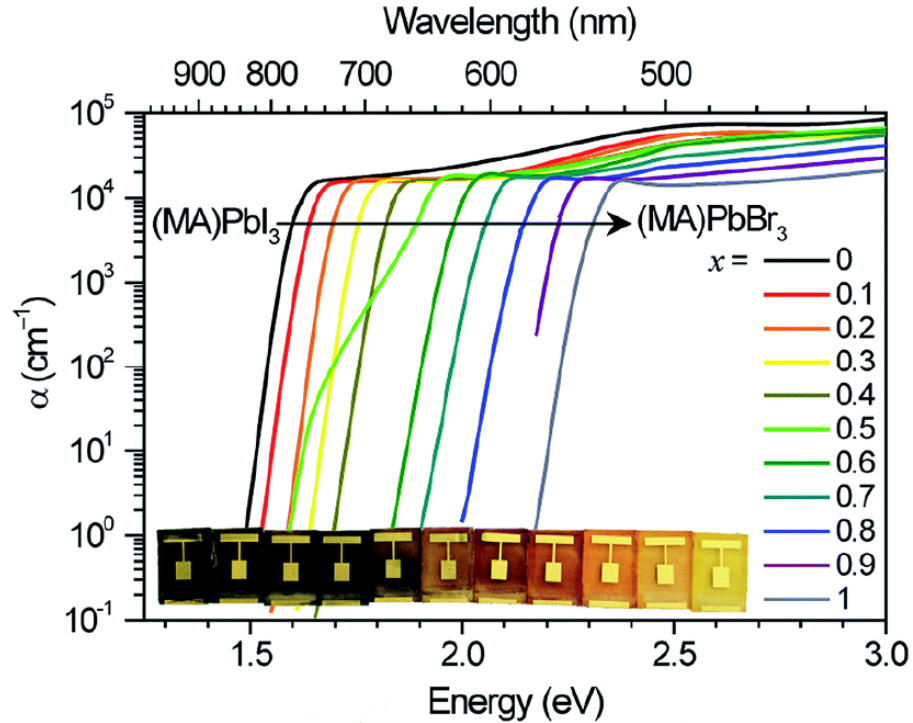
Figure 4.7: Absorption coefficient of mixed-halide perovskite with different relative composition of Iodine and Bromine [21]

4.3.3 Diffusion length

Perovskite is known to have very high carrier diffusion lengths. Several groups have reported that the diffusion length is the order of micro-meters [22,23,24]. 24. La-o-vorakiat et al. have measured the diffusion length of carriers at different temperatures by using of time-resolved terahertz spectroscopy (Figure 4.8). They revealed that the diffusion length can exceed 1 µm. The diffusion length at room temperature can vary from the one measured at low temperature, which suggests the change is recombination mechanism with change in temperature [24]. Several research groups [22,23,25] have reported that perovskite has very high carrier mobility and carrier lifetime, which results in longer diffusion length and higher collection efficiency.
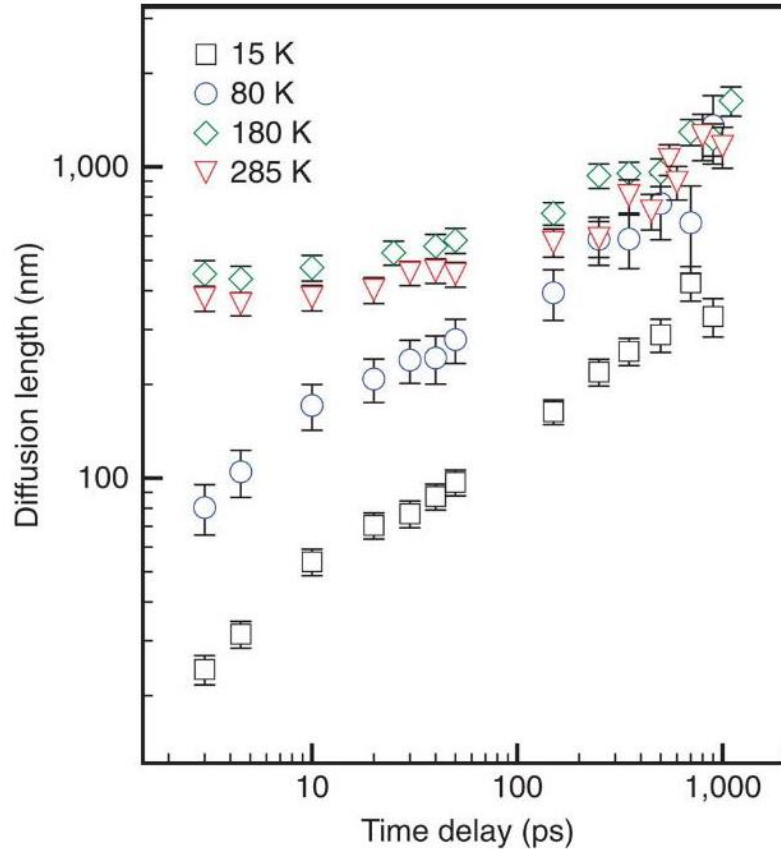
Figure 4.8: Carrier diffusion length in perovskite at different temperatures [24]

4.3.4 Defect density

The density of defects inside the bandgap of a photovoltaic material is a very important factor, as the recombination mechanism depends on the trap density of states. Figure 4.9 shows the sub-gap quantum efficiency measurement of a perovskite solar cell and the calculated Urbach energy is about 15 meV which is lowes than a-Si and organic materials (~50 meV). This means perovskite has better crystallinity.
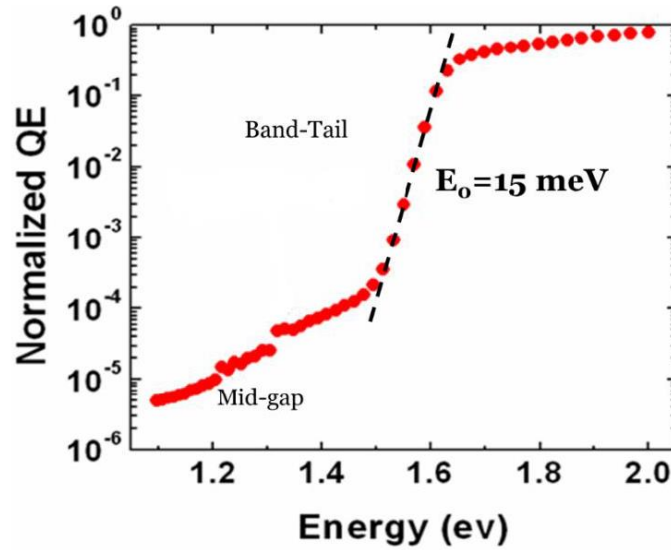
Figure 4.9: Sub-gap quantum efficiency of perovskite solar cell. The calculated Urbach energy is about 15 meV [26]
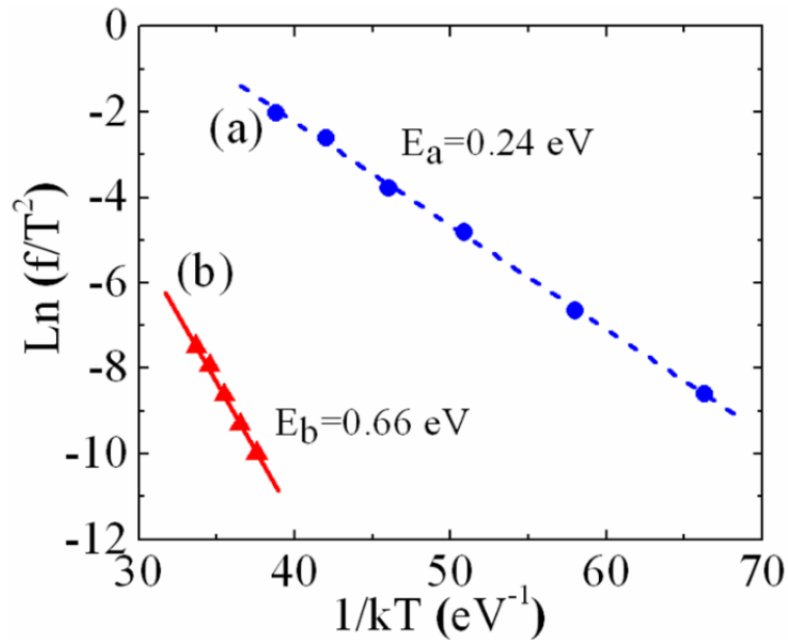
Figure 4.10: Arrhenius plot using Capacitance-Frequency-Temperature (CFT) measurement shows two defect levels: (i) shallower traps have activation energy of about 0.24 eV and (ii) deeper traps have activation energy of about 0.66 eV [20]

Mehran et al. by using Capacitance-Frequency-Temperature (CFT) measurement techniques showed that there are two levels of defect within the bandgap of perovskite as

showed in the Arrhenius plot in figure 4.10 [20]. The shallower trap level has an activation energy of about 0.24 eV and the deeper trap level has activation energy of about 0.66 eV. And the attempt-to-escape frequency (ATEF) measured from this measurement is $2x10^{11}$ Hz at room temperature. They have also measured the trap density of states (t-DOS) profile using the Capacitance vs Frequency measurement (Figure 4.11). The t-DOS in figure 4.11 (a) shows that the midgap states have a peak at 0.66 eV below the conduction band which is also consistent with the Arrhenius plot at figure 4.10. The t-DOS of the midgap state can be fitted with a Gaussian distribution as showed in figure 4.11 (b).
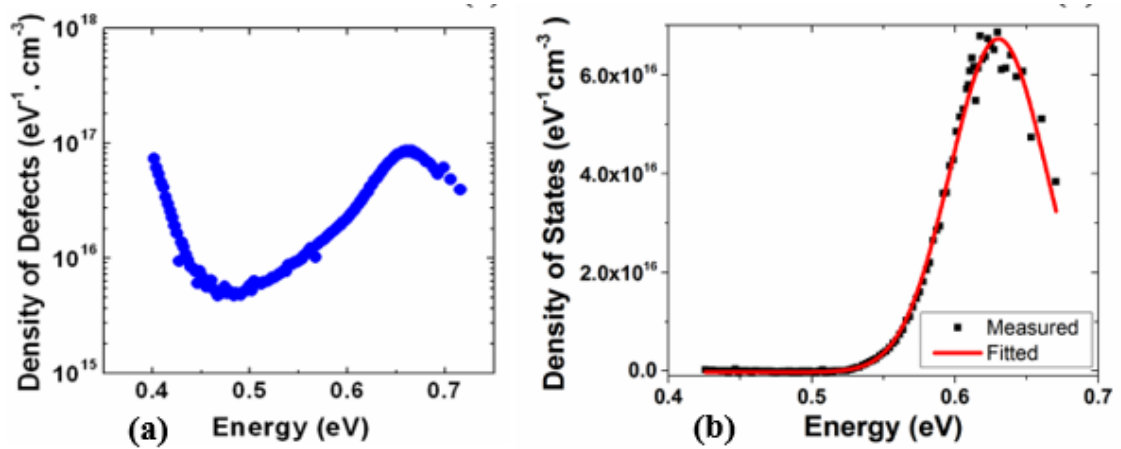
Figure 4.11: Capacitance vs Frequency profile of perovskite solar cell (a) Density of states (t-DOS) distribution within the bandgap of perovskite (b) t-DOS of the midgap state fitted by Gaussian distribution [20]

4.3.5 Dielectric constant

As discussed in chapter 2, whether a photon-absorption event in a material will result in generation of exciton or free electron or hole depends on the exciton binding energy for that material. For photovoltaic application, we prefer the exciton binding energy to be lower than thermal energy which is given by $1/kT$; where k in Boltzmann constant and T is the temperature. At room temperature, this thermal energy is about 26 meV.

The exciton binding energy in a semiconductor is a function of dielectric constant of the material. The higher the dielectric constant the lower the coulomb attraction force between the generated electron-hole pair and so, has lower exciton binding energy.

The dielectric constant can be calculated from capacitance of a solar cell when it is fully depleted at reverse bias and measured at high frequency (200kHz). Although the perovskite layer is significantly thicker, but it has a very high dielectric constant. The capacitance of a perovskite layer is comparable with the capacitance of the transport layer as well. As a result, the device capacitance (apparent capacitance) that we measure is combination from the capacitance of perovskite as well as the transport layers. A schematic of this case has been showed in figure 4.12.
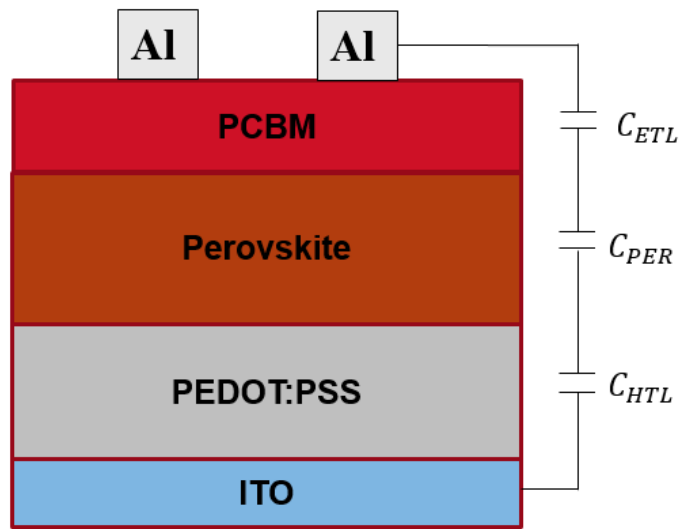
Figure 4.12: Series connected capacitor assumption of a solar cell

Considering the series capacitance model, the apparent capacitance measured from the device is given by,

$$\frac{1}{C_{apparant}} = \frac{1}{C_{ETL}} + \frac{1}{C_{PER}} + \frac{1}{C_{HTL}} \tag{4.4}$$

Where, C_{ETL}, C_{PER} and C_{HTL} are capacitance contribution from electron transport layer, perovskite and hole transport layer respectively. Then equation 4.4 can be expressed as,

$$\frac{1}{\epsilon_{apparant}} = \frac{1}{C_{transport}} * \frac{1}{t} + \frac{1}{\epsilon_{PER}} \tag{4.5}$$

Where, t is the thickness of perovskite layer, $C_{transpor}$ is the capacitance contribution from the transport layers, $\epsilon_{apparent}$ is the dielectric constant measured device capacitance, ϵ_{PER} is the dielectric constant of perovskite. Equation 4.5 suggests that due to the contribution from transport layer capacitance the $\epsilon_{apparent}$ is always lower than ϵ_{PER}. During this experiment, we have fabricated devices with structure showed in figure 4.12 with different perovskite layer thickness. Then we have calculated the apparent dielectric constant of the device from the measured apparent capacitance of the device ($C_{apparent}$). Then we have plotted the apparent dielectric constant as a function of perovskite layer thickness for several values of possible ϵ_{PER}. Finally, by measuring the actual apparent dielectric constant as a function of perovskite layer thickness and plotting it the same curve, we can deduce the actual dielectric constant of perovskite (as showed in figure 4.13).

From figure 4.13, it shows that perovskite has dielectric constant of about 60 which means it has exciton binding energy of about 0.59 meV which is lower than the thermal energy of about 26 meV. Thus, a photon-absorption event in perovskite will result in generation of free electrons and holes.
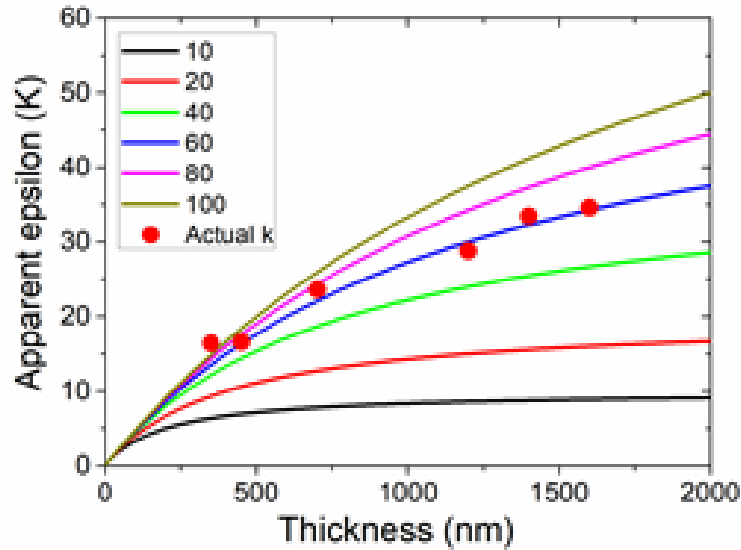
Figure 4.13: Fit of apparent dielectric constant of the perovskite (determined from capacitance and thickness) vs. thickness for of the perovskite layer for various values of true dielectric constant. The best fit is for ε(real) of ~60. The accuracy of the fit improves as the thickness increases, i.e. when the capacitance of the perovskite becomes small

4.4 Challenges with Perovskite

There are some inherent challenges working with perovskite. First, there are some serious environmental challenges like Contains Lead (Pb), which is an environmentally hazardous material and device performance degrades in presence of moisture. It is also not thermally stable because it starts to degrade (decompose) at temperature above 100C. One of the most serious problems is that it is not photo-stable, which means the device performance changes under different illumination and biasing conditions. Hysteresis in Light IV measurement is another inherent problem which means the Light IV measurement depends on scan speed and direction as well as pre-biasing conditions. In this section I will discuss about these inherent challenges.

4.4.1 Environmental stability

Environmental instability is a challenge to work with perovskite. It decomposes in presence of moisture. Zhao et al. in 2016 explained the perovskite degradation in presence of moisture and showed that redox reactions are fundamental to explain this degradation. They also suggested that metal contacts such as Ag, Al, Yb or Cr as metal contacts act as catalyst to enhance this degradation process [27]. The mechanism of this degradation through a redox reaction has been showed in figure 4.14.

$$2Al + 4(MA)PbI_3 + 2H_2O \rightarrow (MA)_4PbI_6 \cdot 2H_2O + 3Pb + 2Al^{3+} + 6I^-$$
$$2Al + 3(MA)_4PbI_6 \cdot 2H_2O \rightarrow 12MAI + 3Pb + 2Al^{3+} + 6I^-$$
$$MAI \leftrightharpoons MA + HI$$
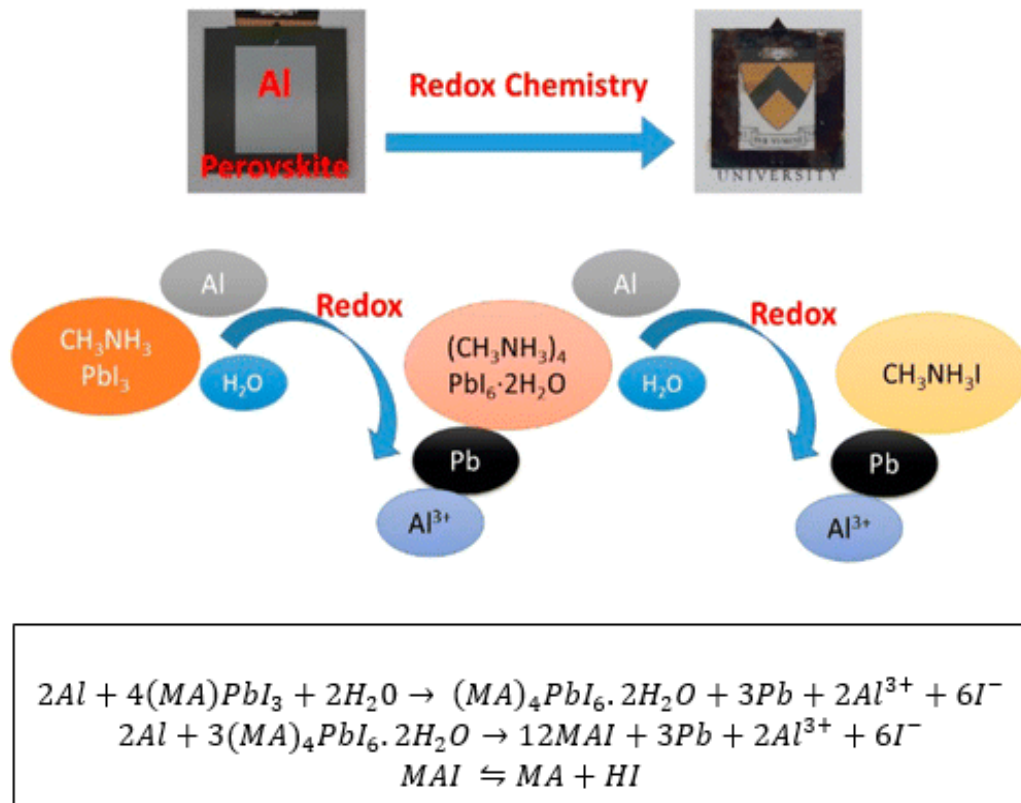
Figure 4.14: Perovskite decomposition in presence of moisture through a redox reaction and assisted by Aluminum [27]

In presence of moisture Al^0 helps Pb^{2+} to Pb^0 through a redox reaction converting $(MA)PbI_3$ to $(MA)_4PbI_6 \cdot 2H_2O$. Then through another redox reaction $(MA)_4PbI_6 \cdot 2H_2O$ decomposes to MAI and PbI2. Then MAI reacts with H_2O and produces MAI & HI, which

accelerates the process and repeats this cycle. Figure 4.15 shows the In situ XRD diffraction analysis of perovskite during various exposure time in moisture and it shows an increase in XRD peak counts within Lead (Pb) diffraction window with increasing exposure duration.
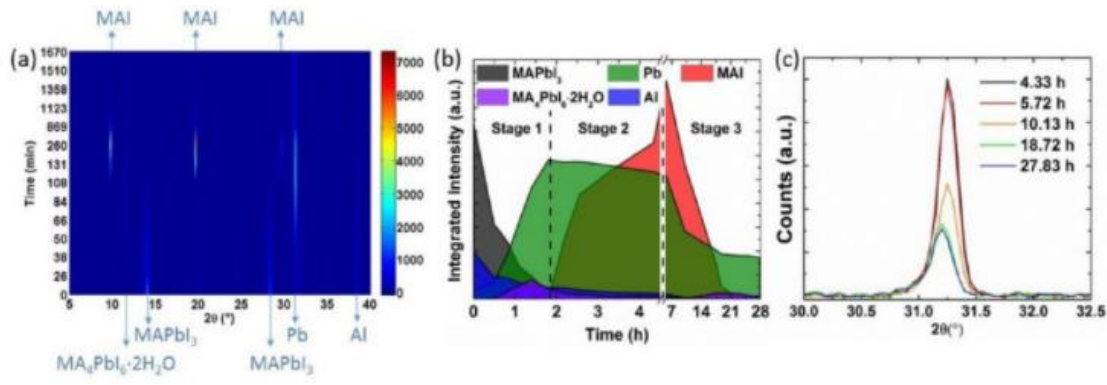
Figure 4.15: XRD analysis during degradation in presence of moisture with Aluminum as catalyst (a) XRD spectra as a function of time (b) Integrated XRD peak for key materials with time (c) XRD in the Lead (Pb) diffraction window during various exposure time [27]

4.4.2 Self-degradation in dark

Perovskite solar cells not only degrades in presence of moisture, they also show self-degradation in an inert nitrogen environment. The mechanism behind this has been explained by Back et al. by corrosion of the metal electrodes (Al or Ag) by inherent ionic defects in bulk perovskite. This phenomenon leads to the intrinsic inherent degradation even in inert nitrogen environment [28]. The mechanism behind this intrinsic self-degradation has been showed in figure 4.16.

Solution-processed perovskite crystal films inevitably contain numerous ionic defects (e.g., halide or MA ions), particularly at the crystal boundaries. Because of extremely small migration activation energy (about 0.1eV) the halide ionic defects easily migrate to other layers (upper or lower layers) through the crystal boundaries in the devices even without decomposition of perovskite layer. The released corrosive halide ions contaminate the

conductive metal (Al or Ag) electrodes and form a thin insulating layer that causes performance

degradation in perovskite solar cells [28].
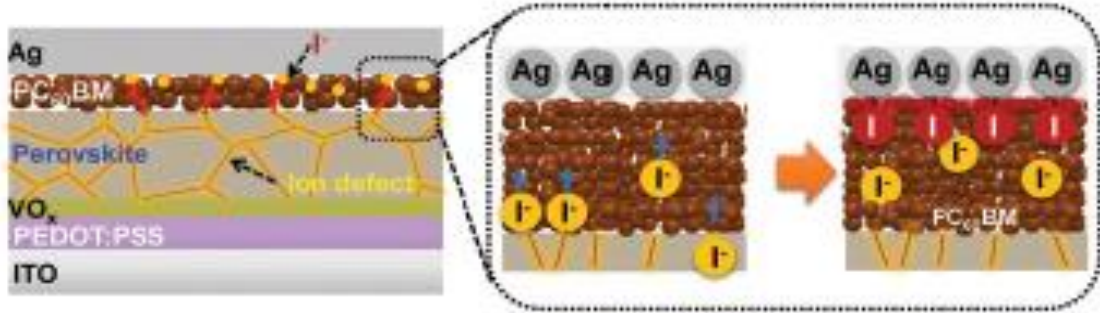
Figure 4.16: Self-degradation of perovskite solar cell in dark assisted by Iodine ions which migrates through ETL (PC60BM) and reacts with silver [28]

4.4.3 Light IV hysteresis
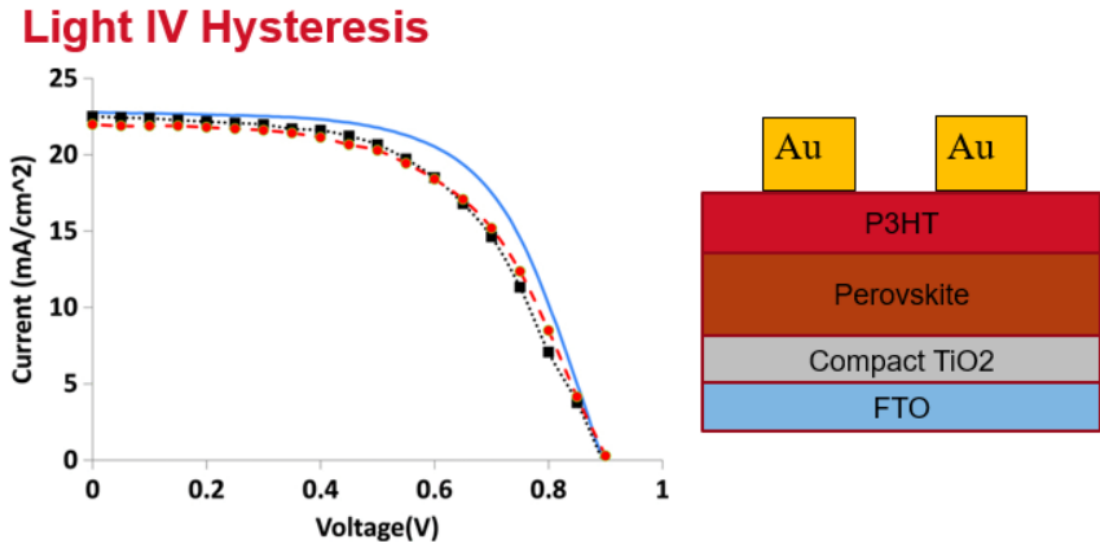
Figure 4.17: Hysteresis curve for a vapor deposited cell (NIP). The blue curve is the original, going from high-bias to low-bias. The red dotted curve is going from low-bias to high-bias (with 2 min wait between points), and the black square curve is the next scan going from high-bias to low-bias. There is very little change in short circuit current [29]

Hysteresis in Light IV curve can be defined as if the voltage across a solar cell is swept

from low-bias to high-bias and then immediately swept from high-bias to low-bias the two

Light-IV curves don't super impose on each other. In other words, the device performance is different depending on scan direction and scan speed.

The figure 4.17 shows an example of light IV hysteresis taken on a NIP device fabricated on TiO_2. But the PIN devices on either NiO or PTAA doesn't show any hysteresis in light IV which will be discussed in the later part of this report.
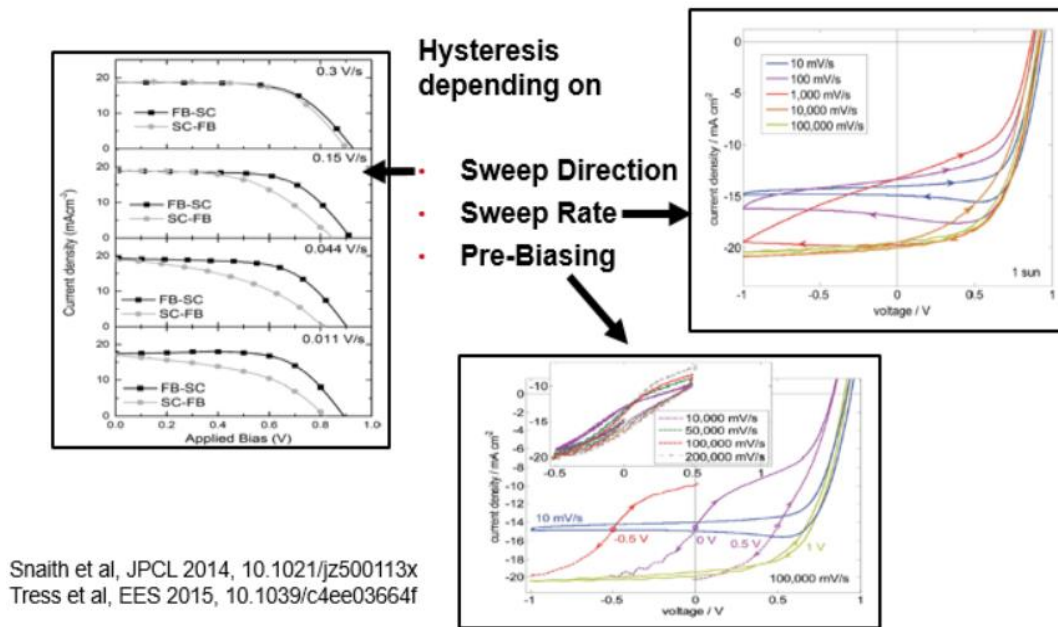
Figure 4.18: Light IV hysteresis dependence (a) Sweep Direction (b) Sweep Rate (c) Pre-Biasing condition [30,31]

The Light IV hysteresis depends on several factors such as scan speed, scan direction and pre-biasing condition. The figure 4.18 shows examples of how light IV hysteresis depends on different factors. Different experiments show that the hysteresis becomes worse as the scan speed increases. Slower scan speed usually doesn't show any significant hysteresis. This behavior can be explained by the Mcghee et al.'s group (figure 4.19). They showed that the light IV characteristics show transient behavior with a time constant less than 15s as we scan

from either direction. When we are scanning too fast we are only measuring the peaks of the transients. Thus, the Light IV measurement is dependent on scan speed.

Transient Behavior in Light IV Measurement
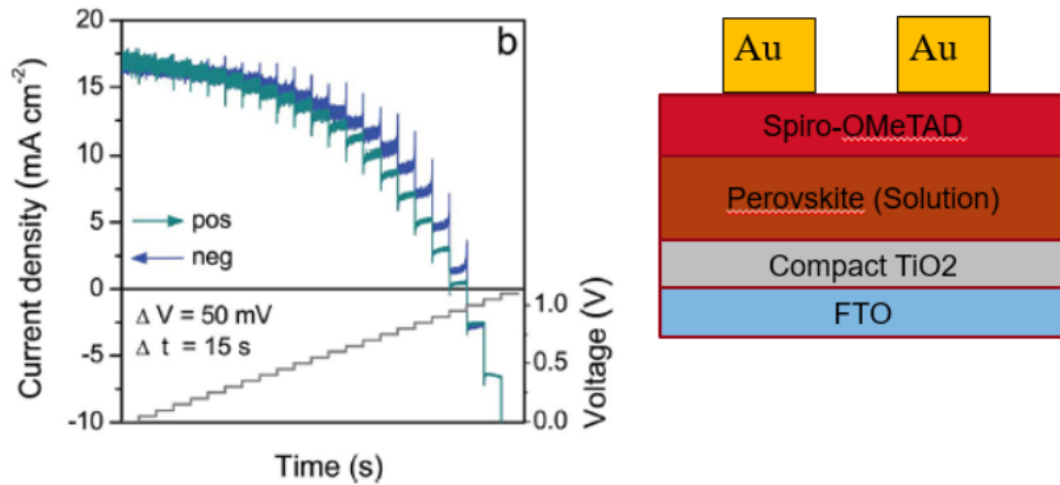
Figure 4.19: Transient behavior in Light IV response on NIP structure solar cell on compact TiO_2 [32]

4.4.4 Open-circuit voltage evolution

This phenomenon can be defined as the open circuit voltage evolves during illumination at open circuit condition. Similar phenomena can be observed even when the device is kept in dark with bias across it. Depending on whether we apply positive or negative bias, the open circuit voltage can either increase or decrease respectively. The rate of voltage evolution is also a function of the magnitude of applied voltage.

The open-circuit voltage evolution during illumination in open-circuit condition as well as evolution during different biasing conditions has been showed in figure 4.20. This measurement was done on an NIP device with structure as showed in figure 4.17. The detailed physics behind this open-circuit evolution will be discussed in the later part of this report.
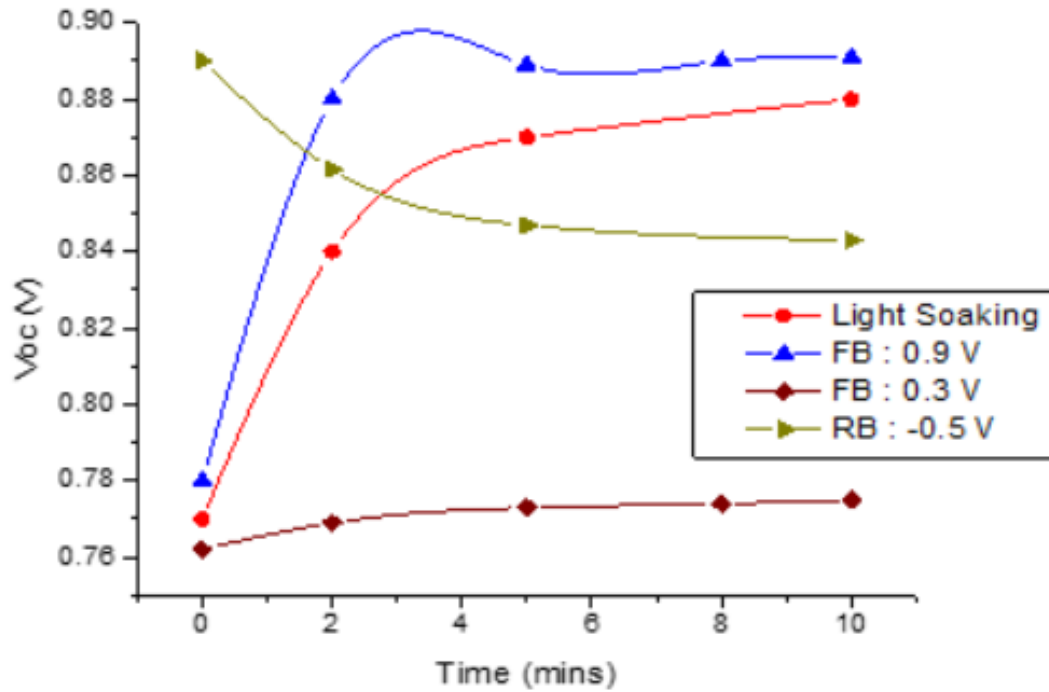
Figure 4.20: Shows the comparison of open circuit voltage evolution of 400 nm perovskite solar cell at different biasing conditions prior to measurement. Here in case of all the biasing conditions the device was kept in dark. We can clearly observe that at forward bias of 0.9 V in dark the open circuit voltage increases very rapidly as the rate of ion migration is very high at this bias. But in case of forward bias of 0.3 V in dark the open circuit voltage evolution is insignificant as we don't have any significant ion migration at this biasing voltage. There is very slight increase in open circuit voltage because of the exposure during measurement but that is not significant. At reverse bias in dark the open circuit voltage decreases with time as expected.

4.4.5 Ion migration in bulk perovskite

The origin of hysteresis can be explained by different theories such as Ion migration, Ferro-electricity, charge trapping and capacitive effects, among which Ion migration is widely accepted.
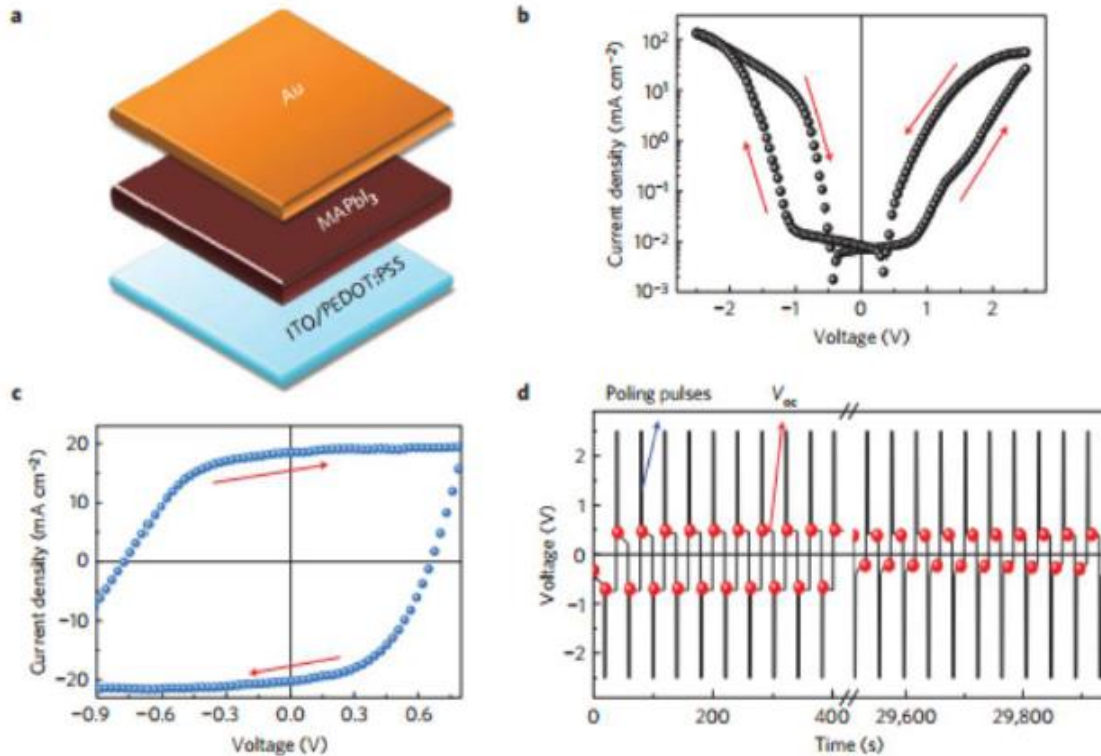
Figure 4.21: Ion migration in bulk perovskite (a) Device structure of a symmetric perovskite device (b) Device under continuous sweep ranging from -2.5V to +2.5V (c) Photo-current hysteresis of the symmetric device (d) Open-circuit voltage of the device after repeated poling by +2.5V and -2.5V bias for more than 750 cycles [33]

Perovskite is well known to be an ionic conductor. Perovskite ($CH_3NH_3PbI_3$) can easily decompose and generate ions. These generated ions can move in presence of E-field and can easily alter the internal electric field. Z. Xiao and J. Huang et al. showed some interesting results which can be explained by migration of ions in bulk perovskite [figure 4.21]. They used a sandwich like structure where perovskite was sandwiched between two p-type materials. So, during light exposure there should be no photo-voltage developed and the IV response under illumination should not depend on sweep direction. But experimentally, the polarity of the device changes with bias. Figure 4.21 (b) & (c) shows IV curve in dark and light exposure respectively. Figure 4.21 (c) shows switchable photo-voltaic characteristics where by polling

with pre-bias the sandwich like structure can generate photo-voltage and act as a photo-voltaic device. This phenomenon can be explained by migration of ions inside bulk perovskite. Perovskite has both positively and negatively charged ions inside bulk material. When bias is applied across the device depending on the biasing direction ions can either accumulate towards the interfaces or migrate back towards the bulk. Thus, the internal electric field inside the material also changes. This change in internal electric is responsible for switchable photo-voltaic behavior.
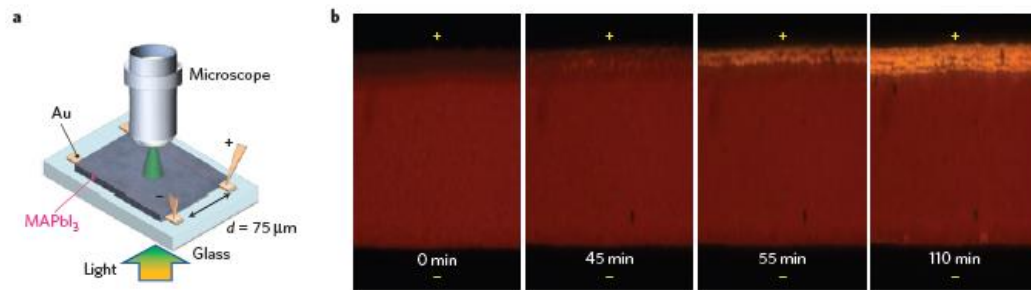
Figure 4.22: Polling in bulk perovskite (a) Instrumentation and device structure used in in-situ monitoring of polling process (b) Microscope photos of perovskite layer during polling process. The electrical field applied on the perovskite film was $1.2\,V\mu m^{-1}$ [33]
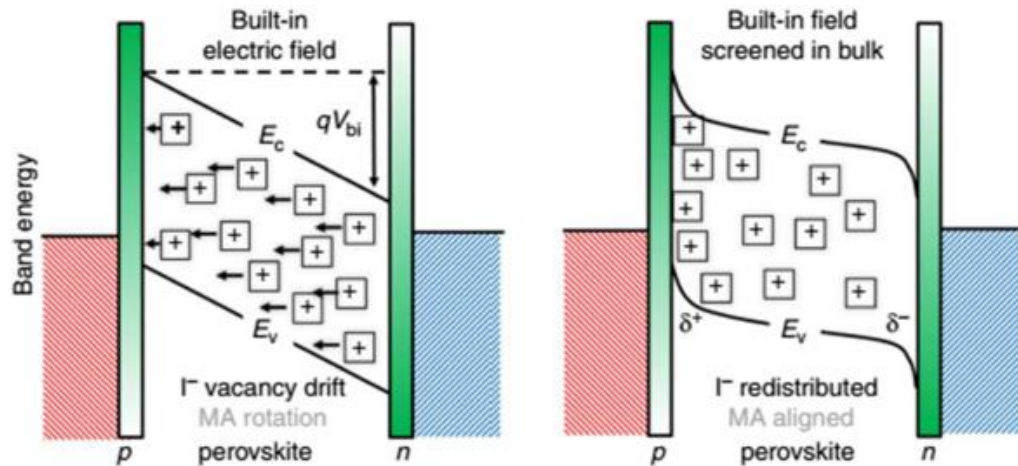
Figure 4.23: Band diagram of perovskite solar cell (a) Before ion migration (b) After ion migration [34]

Z. Xiao and and J. Huang et al. also showed another conclusive evidence of ion migration by observation of composition and morphology changes during poling of lateral device. That dynamic process was recorded and several snapshots are presented in figure 4.22. It shows that the anode of the device becomes transparent after 2 hours bias pooling with electric field $> 1\ V\mu m^{-1}$.

Before the ion migration process positive charged cations and negative charged anions are anions are uniformly distributed inside bulk perovskite. With influence of the internal electric field, the cations drift towards the interface between perovskite-hole transport (p-type) layer and anions drift towards perovskite-electron transport (n-type) layer. These ions change the internal electric field profile inside bulk perovskite and changes the IV characteristics of the solar cell. Change in band-diagram due to ion migration is well emphasized by Eames et al. (Figure 4.23).

Walsh et al. calculated the formation energy of different possible anions and cations and concluded that Mythael-Amine (MA) and Iondine (I) vacancies have lowest formation energy. That means most of the ions generated in bulk perovskite are positive charged MA cations and negative charged I anions. The detailed formation energy for different possible decomposition calculated by Walsh et al. is given in Table 4.1.

Table 4.1: Formation energy of ions in perovskite [34,35]

Reaction	ΔH_S [eV per defect]	K_c	n [cm^{-3}]
$nil \rightarrow V'_{MA} + V''_{Pb} + 3V_I^\bullet + MAPbI_3$	0.14	0.41	2×10^{19}
$nil \rightarrow V'_{MA} + V_I^\bullet + MAI$	0.08	3.82	2×10^{20}
$nil \rightarrow V''_{Pb} + 2V_I^\bullet + PbI2$	0.22	0.02	8×10^{17}

Also, we know that rate of migration is inversely proportional to the exponential of activation energy,

$$r_m = \exp(-\frac{E_A}{k_B T}) \qquad (4.6)$$

Where, E_A is the activation energy for ion migration, k_B is Boltzmann constant and T is the temperature.

In other words, the lower the activation energy, the easier and more probable for that ion to migrate. Eames et al. has calculated the activation energy for ion migration which is presented in table 4.2.

MA cations and Iodine anions have lowest activation energy for migration and thus, it is easier for these two ions to move compared to other ions. From formation energy and activation energy calculations, it can be interpreted that MA cations and I anions are most dominant species in ion migration process inside bulk perovskite.

Table 4.2: Calculation of Activation energy for ionic migration in perovskite [34,35]

Table 1 | Calculated activation energies for ionic migration in CH$_3$NH$_3$PbI$_3$.

Migrating vacancy	Defect notation	E_A (eV)
I$^-$	$V_I^{\bullet}$	0.58
Pb^{2+}	V_{Pb}''	2.31
CH$_3$NH$_3^+$ (MA$^+$)	V_{MA}'	0.84

The migration of ion species is mediated by vacancy defects.
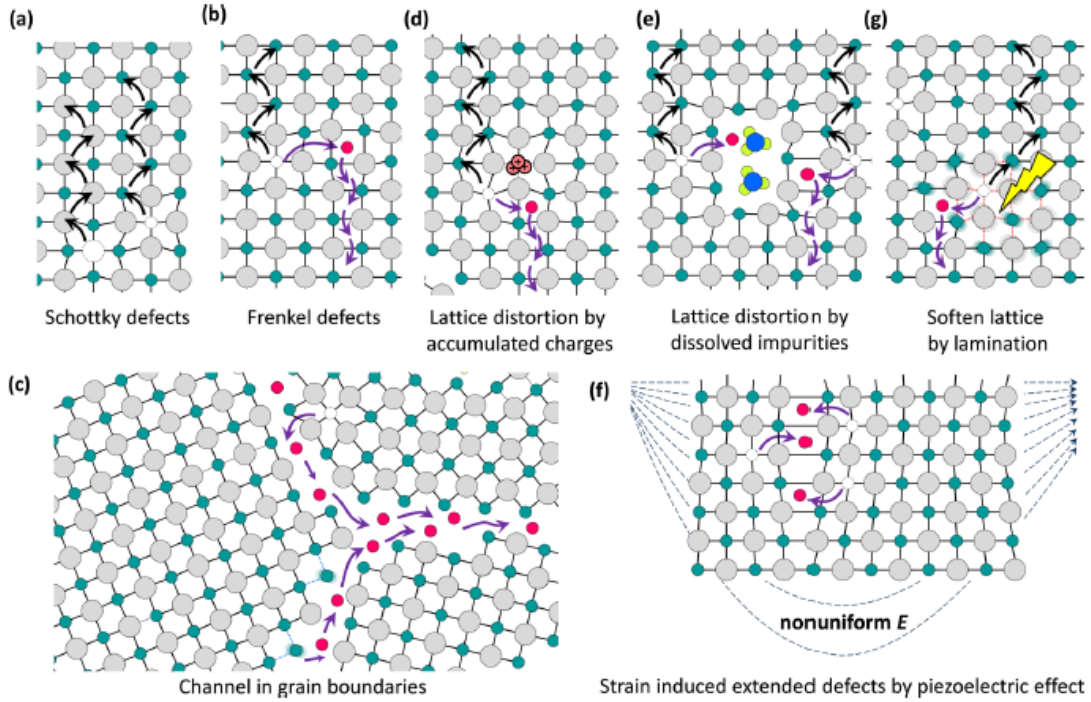
Figure 4.24: Different probable ion migration site in perovskite [36]
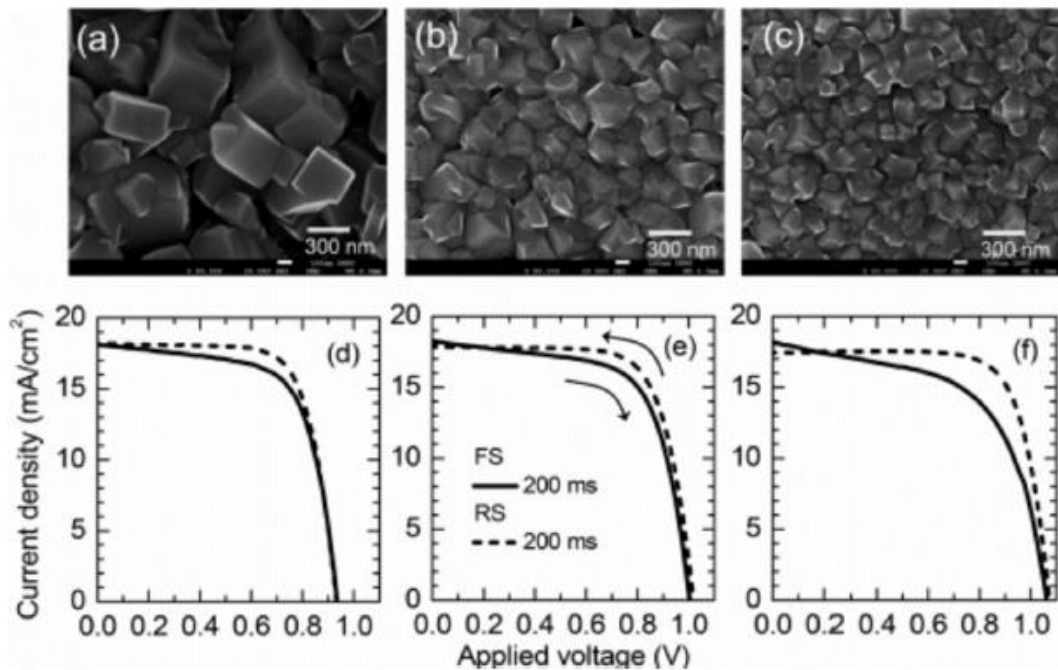
Figure 4.25: Increase in perovskite grain size reduces hysteresis in Light IV response [37]

Yuan et al. showed that among several possible ion migration sites (figure 4.24), migration through channel in grain boundaries is the most dominant one. They also showed that the activation energy for ion migration is about half when we consider migration through crystal grain boundaries. And because of soft chemical bonding in the grain boundary sites the formation energy of ions is also lower for smaller grain size polycrystalline film. Thus, smaller grain size is not only favorable for migration of ions but also assists the generation of ions.

H.S. Kim and N.G. Park et al. showed that light IV hysteresis is also dependent on grain size of perovskite [figure 4.25]. Larger grain size device shows lower hysteresis and smaller grain size devices show more hysteresis in Light IV response.

Later in this report, I will also show that increasing grain size of perovskite polycrystalline film helps to reduce photon-induced degradation.

4.5 Optimum E-field for Ion-migration in Perovskite

In these section, I have discussed the mechanism of ion migration and determined the optimum electric field required to initiate the ion migration. I have also explained the reason behind significant evolution of open circuit voltage and efficiency during light soaking in open circuit condition. Finally, I will relate this optimum electric field with light IV measurements.

The device structure and the light IV characteristic that we have used during this experiment is shown in figure 4.26. This was a n-i-p structure device with compact TiO_2 as an electron transport layer (ETL) and P_3HT as a hole transport layer (HTL). The efficiency of the device was 9% after 20 mins of light soaking in open circuit condition and the hysteresis is also showed in figure 4.26. We have used three different thicknesses of the perovskite layer of around 400, 500 and 600 nm.
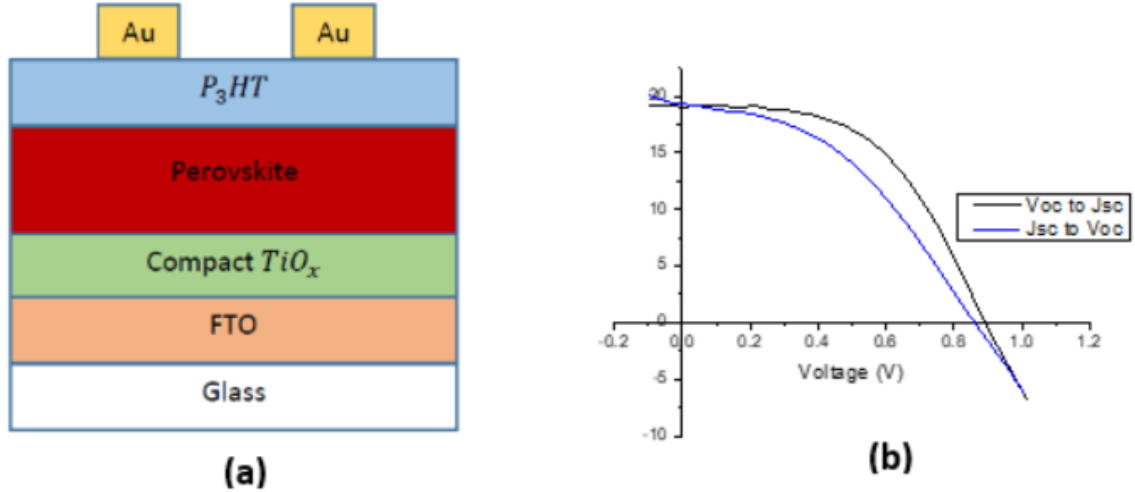
Figure 4.26: (a) Schematic diagram of the n-i-p perovskite device which is used for our measurements (b) The light IV characteristics (400 nm perovskite thickness) of that device after 20 minutes of light soaking in open circuit condition. The black line was scanned from high-bias to low-bias and the blue line was scanned from low-bias to high-bias.

In figure 4.27 the process of ion migration has been described. First in short circuit condition due to the built-in potential the positive ions move towards the hole transport layer (HTL) and forms a space charge region near the perovskite-HTL interface and that makes perovskite n-type doped near the HTL interface. Similarly, the negative ions move towards the electron transport layer (ETL) and forms a space charge region near the perovskite-ETL interface and that makes the perovskite p-type doped ETL interface. Then these two space charge regions create an electric field opposing the built-in electric field.

So now we have an effective built-in potential which is lower than original built-in electric field and given by,

$$V'_{bi} = V_{bi} - V_{ion} \qquad (4.7)$$

This process continues until the effective built-in field is large enough to move these ions and form space charge. So finally, it reaches a steady-state condition and there is a net electric field due to the effective built-in potential. Now if we apply forward bias these ions

migrate in the opposite direction and finally reaches a steady state condition again. In this case

to have significant ion migration we must apply forward bias more than a threshold voltage.

We call this threshold voltage as onset of ion migration voltage (V_{onset}).

Figure 4.27: The process of ion migration (a) Due to the built-in potential the positive ions move towards the HTL and negative ions move towards ETL (b) The ions move towards the contact layers and form space charge regions which develops an electric field opposing the built-in electric field. The effective built-in potential is reduced to $V'_{bi} = V_{bi} - V_{ion}$ (c) If we apply bias in forward direction above a threshold voltage the ions start to migrate in a direction indicated in the figure. We have an effective net voltage, $V_{net} = V_{bi} - V_{ion} - V_{app}$

The reason we must apply a minimum voltage to initiate this ion migration is that we must overcome the barrier due to the effective built-in potential and there might be some interface charge traps as well. Below this threshold voltage we might have some ion migration due to diffusion as the barrier lowers because of applying a small forward bias but above this threshold voltage ion migration due to drift dominates and we have observed a significant increase in migration of ions. In this section, I have showed a method to calculate this onset of ion migration voltage from capacitance vs time plot at different bias. The measured net capacitance can be expressed as,

$$C_{net} = \frac{dQ}{dV} \tag{4.8}$$

The capacitance that we measure at a given bias voltage has three charge components: the depletion charge due to the built in potential, the injection charge due to applied bias and the ion charge due to ion migration. So, total charge that contributes to the net capacitance can be expressed as,

$$Q = Q_{depl} + Q_{inj} + Q_{ion} \tag{4.9}$$

The net voltage (V) is effective on all three types of charges and so we can take derivative with respect to V on both sides of equation 4.9,

$$\frac{dQ}{dV} = \frac{dQ_{depl}}{dV} + \frac{dQ_{inj}}{dV} + \frac{dQ_{ion}}{dV} \tag{4.10}$$

Equation 4.10 can be expressed as three capacitance components,

$$C_{net} = C_{depl} + C_{inj} + C_{ion} \tag{4.11}$$

From equation 4.11, we can see that the measured net capacitance can be expressed as linear combination of depletion, injection and ion capacitance components. Thus, we can express the contribution of capacitance from migration of ions can be expressed as,

$$C_{ion} = C_{net} - \left(C_{depl} + C_{inj} \right) \qquad (4.12)$$

If we can find a way to determine the combination of depletion and injection capacitance ($C_{depl} + C_{inj}$), by subtracting this amount from the measured capacitance we can get the capacitance due to ion migration. From the parallel plate capacitance approximation, we can relate the amount of charges and the capacitance due to ion migration,

$$Q_{ion} = V C_{ion} \qquad (4.13)$$

We can express the rate of ion migration as a function of rate of change in capacitance. Figure 4.28(a) shows the ionic capacitance vs time curve for a n-i-p device with perovskite layer thickness of 400 nm. For this measurement before starting measurement at any bias we have kept the device at short circuit condition in dark to stabilize the capacitance and to ensure that the device is at similar initial condition before measuring at every bias. Then we have instantaneously changed the bias from short circuit condition to a specific biasing voltage. So, at time t=0 assuming there is no ion migration the capacitance we have measured indicates the combination of depletion and injection capacitance components. Then we have measured the capacitance at different time. If we deduct the capacitance at time t=0 from measured capacitance at time $t = t_1$, we can get the ionic capacitance due to ion migration. Then we have plotted this ionic capacitance as a function of time [figure 4.28(a)]. From this figure, we can see that initially the capacitance increases very quickly and finally reaches a linear or steady state condition. Another important thing to observe from this plot is that the slope of these curves at linear region increases with increasing bias voltage as the rate of ion migration

is higher at higher bias voltage. Thus, the slope of this linear region is a function of rate of ion migration. Then we have plotted the slope of steady state response as a function of bias voltage [figure 4.28(b)] which can be fitted as a straight line. The line has an intercept at x-axis of 0.45 V. This intercept shows that below 0.45 V the rate of ion migration is negligible and above 0.45 V we have significant ion migration. We call this threshold voltage as onset of ion migration voltage. We have also repeated the same procedure below 0.45 V (at 0.3 V and 0.35 V) to observe if there is any significant ion migration or not and we have observed that the change in ionic capacitance is not significant below this threshold voltage [figure 4.28(a)]. The onset of ion migration voltage will vary with change in perovskite layer thickness. So, we have calculated the optimum electric field (E_{opt}) that is required for ion migration which is independent of thickness and we have got a value of 1.13 $V\ \mu m^{-1}$ for this 400nm device which is consistent with the result reported by Xiao et al. [33] and Deng et al. [38] where they have reported that to switch the photo-current direction from polling effect they had to apply an electric field of around 1$V\ \mu m^{-1}$. We have also repeated the same experiment for 500 nm and 600 nm thick perovskite layer devices and we have obtained this optimum electric field of 1.18 $V\ \mu m^{-1}$ and 1.05 $V\ \mu m^{-1}$ respectively.

Table 4.3: Optimum electric field required for ion migration at different perovskite layer thickness

Thickness (Perovskite)	$V_{onset}(V)$	$E_{opt}\ (V\ \mu m^{-1})$
400 nm	0.45	1.13
500 nm	0.59	1.18
600 nm	0.63	1.05
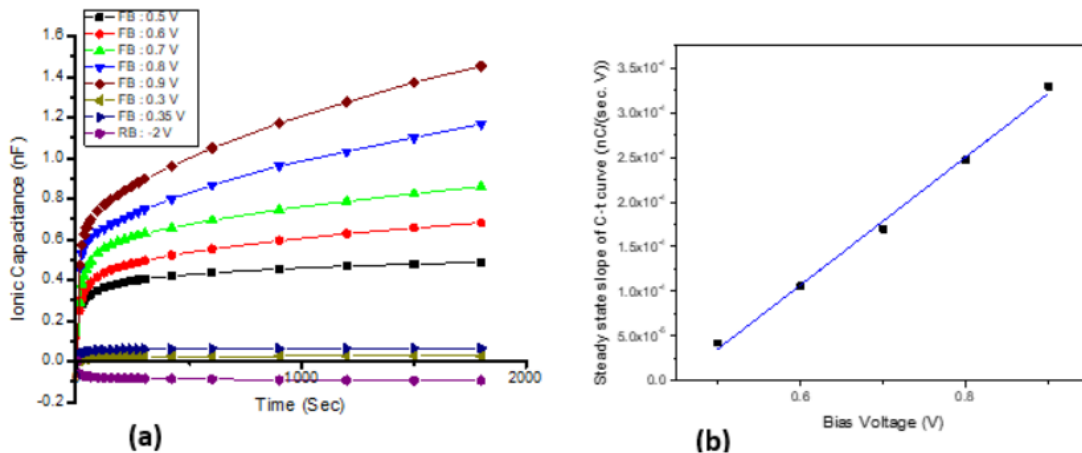
Figure 4.28: Calculation of onset of ion migration voltage and optimum electric field required for ion migration in a 400nm perovskite layer n-i-p device (a) Plot shows ionic capacitance as a function of time at different forward biasing conditions. The graph clearly shows the slope at linear region increases with increasing forward bias voltage. That signifies the rate of ion migration is higher at higher bias voltage. (b) Plot shows the slope of linear region at different bias voltage as a function of bias voltage. We can fit the data points by a straight line and the x-intercept gives the onset of ion migration voltage. From this voltage, we can calculate the optimum E-field required for ion migration.

Now there are several research groups who have reported the significant increase in open circuit voltage and efficiency during light soaking [33,38,39]. This behavior can be explained from ion migration. As we have showed in short circuit condition the ions move near the contact layers to form space charge regions and that reduces the effective built-in potential. As a result, the starting open circuit voltage is lower. When the device is illuminated the photo-voltage acts as forward bias and initiates ion migration which increases the effective built-in potential and so the open circuit voltage increases. The increased open circuit voltage further increases the ion migration and as a result increases the effective built-in potential as well as the open circuit voltage. This process continues until the open circuit voltage saturates as the drift and reverse diffusion of ions are balanced [38].

Figure 4.29: These plots show the comparison of light IV curves of 400 nm perovskite (n-i-p) solar cell at different biasing conditions before measurements (a) Shows the evolution of light IV curves during light soaking in open circuit condition for 20 minutes. We can clearly observe the evolution of open circuit voltage with time. The arrow shows the direction of evolution with increasing time. The efficiency showed on the graph is after 20 mins of light soaking. (b) Shows the evolution of light IV curves when it was kept in dark at forward bias with biasing voltage of 0.9 V which is greater than the onset of ion migration voltage of 0.45 V. We can clearly observe the evolution of open circuit voltage with time. Again, the arrow shows the direction of evolution with increasing time. The efficiency on the graph is after 10 mins of forward bias at 0.9 V in dark. (c) Shows the light IV curves when he device was kept in dark for 20 minutes in forward bias at biasing voltage of 0.3 V which in smaller than the onset of ion migration voltage of 0.45 V. As we have predicted that we don't have significant ion migration at this voltage, we don't have signification voltage evolution. (d) Shows the light IV curves when the device was kept in dark at reverse bias condition with biasing voltage of -0.5 V after the open-circuit voltage saturates at the maximum value. As we have expected the open circuit voltage decreases with increasing time. The arrow shows the direction of light IV characteristic change with time.

If our model is accurate, we should also observe the open circuit voltage evolution even when we apply a bias in forward direction in dark. And as we have discussed for the 400nm device if we apply forward bias more than 0.45 V we should observe voltage evolution as the ion migration is significant in this range. Similarly, if we apply a forward bias less than 0.45 V we should not observe any significant voltage evolution as we can neglect ion migration in this range. Also in reverse bias, the open circuit voltage should decrease as the ions move in opposite direction. From figure 4.29 we can see that the open circuit voltage saturates very quickly if we keep it in dark at forward bias voltage of 0.9 V [figure 4.29(b)] compared to light soaking [figure 4.29(a)]. At a forward bias voltage of 0.3 V the open circuit voltage should not increase significantly [figure 4.29(c)] although we have seen very slight increase as the device was under illumination during the measurements. So, the results from light IV also matches with the result that we have got from the ionic capacitance vs time curves.

REFERENCES

1   Nam-Gyu Park, "Organometal Perovskite Light Absorbers Toward a 20% Efficiency Low-Cost Solid-State Mesoscopic Solar Cell" J. Physical chemistry letters, 4, pp. 2423–2429 (2013)

2   PV Education
         Link: http://www.pveducation.org

3   Pranav Joshi, Ph.D. dissertation, "Understanding the photostability of perovskite solar cell", Iowa State University (2016)

4   RLE perovskite seminar series, MIT

5   Green, M.A., A. Ho-Baillie, and H.J. Snaith, "The emergence of perovskite solar cells", Nature Photonics, 2014. 8(7): p. 506-514. doi:10.1038/nphoton.2014.134

6   C. Li, X. Lu, W. Ding, L. Feng, Y. Gao, and Z. Guo, "Formability of abx3 (x = f, cl, br, i) halide perovskites", Acta Crystallogr B, 64, 702 (2008). doi:10.1107/S0108768108032734

7   D. B. Mitzi, S. Wang, C. A. Feild, C. A. Chess, and A. M. Guloy, "Conducting layered organic–inorganic halides containing <110>-oriented perovskite sheets", Science, 267, 1473 (1995). 35

8   D. B.Mitzi, K. Chondroudis, and C. R. Kagan, "Organic-inorganic electronics", IBM J. Res. Dev., 45, 29 (2001). 36

9   A. Kojima, K. Teshima, T. Miyasaka, and Y. Shirai, "Novel photoelectrochemical cell with mesoscopic electrodes sensitized by lead-halide compounds (2)", in Proc. 210th ECS Meeting (ECS, 2006)

10   A. Kojima, K. Teshima, Y. Shirai, and T. Miyasaka, "Organometal halide perovskites as visible-light sensitizers for photovoltaic cells", J. Am. Chem. Soc., 131, 6050 (2009). doi:10.1021/ja809598r

11   H. Topsöe, "Krystallographisch-chemische untersuchungen homologer verbindungen", Zeitschrif für Kristallographie, 8, 246 (1884)

12   J. H. Im, C. R. Lee, J. W. Lee, S. W. Park, and N. G. Park, "6.5% efficient perovskite quantum-dot-sensitized solar cell", Nanoscale, 3, 4088 (2011). doi:10.1039/c1nr10867k

13   H. S. Kim, C. R. Lee, J. H. Im, K. B. Lee, T. Moehl, A. Marchioro, S. J. Moon, R. Humphry-Baker, J. H. Yum, J. E. Moser, M. Gratzel, and N. G. Park, "Lead iodide perovskite sensitized all-solid-state submicron thin film mesoscopic solar cell with efficiency exceeding 9%", Sci. Rep., 2, 591 (2012). doi:10.1038/srep00591

14   J. H. Noh, S. H. Im, J. H. Heo, T. N. Mandal, and S. I. Seok, "Chemical management for colorful, efficient, and stable inorganic-organic hybrid nanostructured solar cells.", Nano Lett., 13, 1764 (2013).

15   J. Burschka, N. Pellet, S. J. Moon, R. Humphry-Baker, P. Gao, M. K. Nazeeruddin, and M. Gratzel, "Sequential deposition as a route to high-performance perovskite-sensitized solar cells", Nature, 499, 316 (2013). doi:10.1038/nature12340

16   M. Liu, M. B. Johnston, and H. J. Snaith, "Efficient planar heterojunction perovskite solar cells by vapour deposition", Nature, 501, 395 (2013). doi:10.1038/nature12509

17   W. S. Yang, J. H. Noh, N. J. Jeon, Y. C. Kim, S. Ryu, J. Seo, and S. I. Seok, "High-performance photovoltaic perovskite layers fabricated through intramolecular exchange", Science, 348, 1234 (2015). doi:10.1126/science.aaa9272

18   M. Saliba, T. Matsui, J.-Y. Seo, K. Domanski, J.-P. Correa-Baena, M. K. Nazeeruddin, S. M. Zakeeruddin, W. Tress, A. Abate, A. Hagfeldt, and M. Gratzel, "Cesium-containing triple cation perovskite solar cells: Improved stability, reproducibility and high efficiency", Energy Environ. Sci., 9, 1989 (2016). doi:10.1039/C5EE03874J

19   Ziang et al, Optical Materials Express (2015), DOI:10.1364/OME.5.000029

20   Mehran Samiee, Siva Konduri, Balaji Ganapathy,2 Ranjith Kottokkaran, Hisham A. Abbas, Andrew Kitahara, Pranav Joshi, Liang Zhang, Max Noack, and Vikram Dala, "Defect density and dielectric constant in perovskite solar cells", APPLIED PHYSICS LETTERS 105, 153502 (2014)

21   Hoke, E.T., et al., Reversible photo-induced trap formation in mixed-halide hybrid perovskites for photovoltaics. Chemical Science, 2015. 6(1): p. 613-617

22   Zhao, Y., A.M. Nardes, and K. Zhu, Solid-State Mesostructured Perovskite CH3NH3PbI3 Solar Cells: Charge Transport, Recombination, and Diffusion Length. Journal of Physical Chemistry Letters, 2014. 5(3): p. 490-494

23   Stranks, S.D., et al., Electron-Hole Diffusion Lengths Exceeding 1 Micrometer in an Organometal Trihalide Perovskite Absorber. Science, 2013. 342(6156): p. 341-344

24   La-o-vorakiat et al., Elucidating the role of disorder and free-carrier recombination kinetics in CH3NH3PbI3 perovskite films. Nat Commun, 2015. 6

25   Stoumpos, C.C., C.D. Malliakas, and M.G. Kanatzidis, Semiconducting Tin and Lead Iodide Perovskites with Organic Cations: Phase Transitions, High Mobilities, and Near-Infrared Photoluminescent Properties. Inorganic Chemistry, 2013. 52(15): p. 9019-9038

26   Liang Zhang, Ph.D. dissertation, "Device physics of perovskite solar cells", Iowa State

University (2016)

27   Lianfeng Zhao, Ross A. Kerner, Zhengguo Xiao, YunHui L. Lin, Kyung Min Lee, Jeffrey Schwartz, and Barry P. Rand, "Redox Chemistry Dominates the Degradation and Decomposition of Metal Halide Perovskite Optoelectronic Devices", ACS Energy Lett. 2016, 1, 595−602, DOI: 10.1021/acsenergylett.6b00320

28   Hyungcheol Back, Geunjin Kim, Junghwan Kim, Jaemin Kong, Tae Kyun Kim, Hongkyu Kang, Heejoo Kim, Jinho Lee, Seongyu Leeb and Kwanghee Lee, "Achieving long-term stable perovskite solar cells via ion neutralization", Energy Environ. Sci., 2016,9, 1258-1263, DOI: 10.1039/C6EE00612D

29   Hisham A. Abbas, Ranjith Kottokkaran, Balaji Ganapathy, Mehran Samiee, Liang Zhang, Andrew Kitahara, Max Noack, and   Vikram L. Dalal, "High efficiency sequentially vapor grown n-i-p CH3NH3PbI3 perovskite solar cells with undoped P3HT as p-type heterojunction layer", APL Materials 3, 016105 (2015); DOI: https://doi.org/10.1063/1.4905932

30   Henry J. Snaith, Antonio Abate, James M. Ball, Giles E. Eperon, Tomas Leijtens, Nakita K. Noel, Samuel D. Stranks, Jacob Tse-Wei Wang, Konrad Wojciechowski, and Wei Zhang, "Anomalous Hysteresis in Perovskite Solar Cells", J. Phys. Chem. Lett., 2014, 5 (9), pp 1511–1515, DOI: 10.1021/jz500113x

31   W. Tress, N. Marinova, T. Moehl, S. M. Zakeeruddin, Mohammad Khaja Nazeeruddina and M. Grätzela, "Understanding the rate-dependent J–V hysteresis, slow time component, and aging in CH3NH3PbI3 perovskite solar cells: the role of a compensated electric field", Energy & Environmental Science, Issue 3, 2015

32   E. L. Unger, E. T. Hoke, C. D. Bailie, W. H. Nguyen, A. R. Bowring, T. Heumüller, M. G. Christoforod and M. D. McGehee, "Hysteresis and transient behavior in current–voltage measurements of hybrid-perovskite absorber solar cells", Energy & Environmental Science, Issue 11, 2014

33   Zhengguo Xiao, Yongbo Yuan, Yuchuan Shao, Qi Wang, Qingfeng Dong, Cheng Bi, Pankaj Sharma, Alexei Gruverman & Jinsong Huang, "Giant switchable photovoltaic effect in organometal trihalide perovskite devices", Nature Materials volume 14, pages 193–198 (2015), doi:10.1038/nmat4150

34   Christopher Eames, Jarvist M. Frost, Piers R. F. Barnes, Brian C. O'Regan, Aron Walsh & M. Saiful Islam, "Ionic transport in hybrid lead iodide perovskite solar cells", Nature Communications 6, 7497 (2015), DOI: 10.1038/ncomm8497

35   Aron Walsh, "Principles of Chemical Bonding and Band Gap Engineering in Hybrid Organic–Inorganic Halide Perovskites", J. Phys. Chem. C, 2015, 119 (11), pp 5755–5760, DOI: 10.1021/jp512420b

36   Yongbo Yuan and Jinsong Huang, "Ion Migration in Organometal Trihalide Perovskite and Its Impact on Photovoltaic Efficiency and Stability", Acc. Chem. Res., 2016, 49 (2), pp 286–293, DOI: 10.1021/acs.accounts.5b00420

37   H.-S. Kim and N.-G. Park, "Parameters affecting i–v hysteresis of ch3nh3pbi3perovskite solar cells: Effects of perovskite crystal size and mesoporous tio2layer", J. Phys. Chem. Lett., 5, 2927 (2014). doi:10.1021/jz501392m

38   Yehao Deng, Zhengguo Xiao & Jinsong Huang, "Light-Induced Self-Poling Effect on Organometal Trihalide Perovskite Solar Cells for Increased Device Efficiency and Stability "", Advanced Energy Materials, DOI 10.1002 (2015)

39   Pablo Docampo, James M. Ball, Mariam Darwich, Giles E. Eperon & Henry J. Snaith, "Efficient organometal trihalide perovskite planar-heterojunction solar cells on flexible polymer substrates" Nature Communications, 4, 2761 (2013)

CHAPTER 5. FABRICATION AND OPTIMIZATION OF PEROVSKITE SOLAR CELLS

5.1 Fabrication Methods

As discussed in Chapter 2, perovskite solar cells can have two different structures: p-i-n and n-i-p as showed in figure 5.1. There are different organic or inorganic materials which can serve as electron and hole transport layers. The p^+ layer or hole-transport layers can be either Poly[bis(4-phenyl) (2,4,6-trimethylphenyl) amine] (PTAA), Nickel (II) Oxide (NiO), Poly(3-hexylthiophene-2,5-diyl) (P_3HT), Poly(4-butylphenyldiphenylamine) (Poly-TPD), poly(3,4-ethylenedioxythiophene) polystyrene sulfonate (PEDOT:PSS) etc. The n^+ layer or electron-transport layers can be either Cadmium Sulfide (CdS), Zinc Oxide (ZnO), [6,6]-Phenyl C61 butyric acid methyl ester (PCBM), Titanium-di-oxide (TiO_2) etc. Often, we need to dope these materials to enhance the conductivity. For instance, we can dope Cadmium Sulfide with Indium and dope Zinc Oxide with Aluminum to make them more conductive.
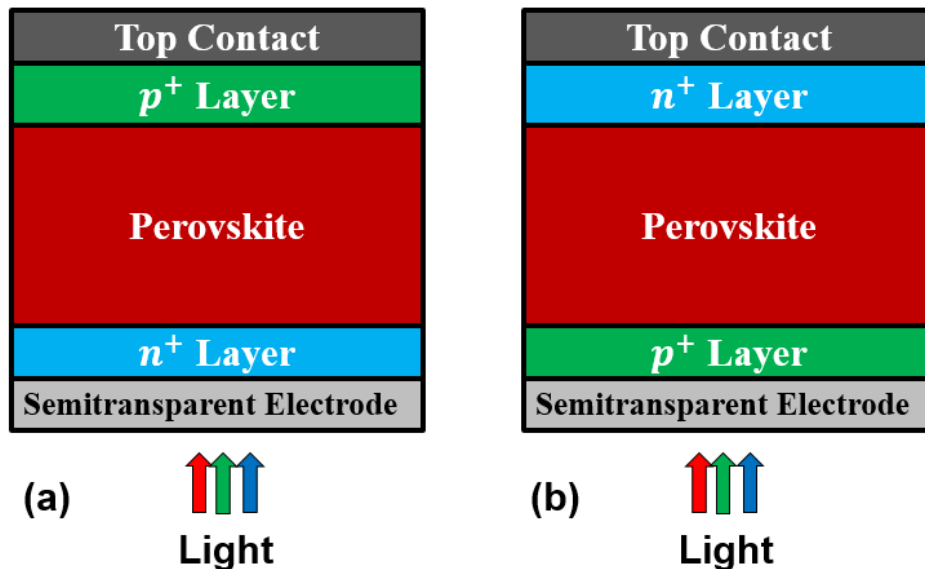
Figure 5.1: Device structure (a) n-i-p structured (b) p-i-n structured perovskite solar cells (The diagram is not drawn to scale)

There are several fabrication techniques available to deposit a layer of perovskite (figure 5.2). The three major categories can be: Solution process, Vapor process or hybrid. In solution process the precursors that are used to form perovskite are dissolved in an organic solvent, commonly in Dimethylformamide (DMF), and spin coated on the substrate to form perovskite. The solution process can be of different types: single solution process, where all the precursors are mixed in a single solution to spin-coat the perovskite layer [1,2,3,4] or sequential process, where the precursors are coated one after the other followed by annealing to form perovskite [5]. Li et al. also developed a method as vacuum flash-assisted solution process with helps to enhance perovskite grain size [6].
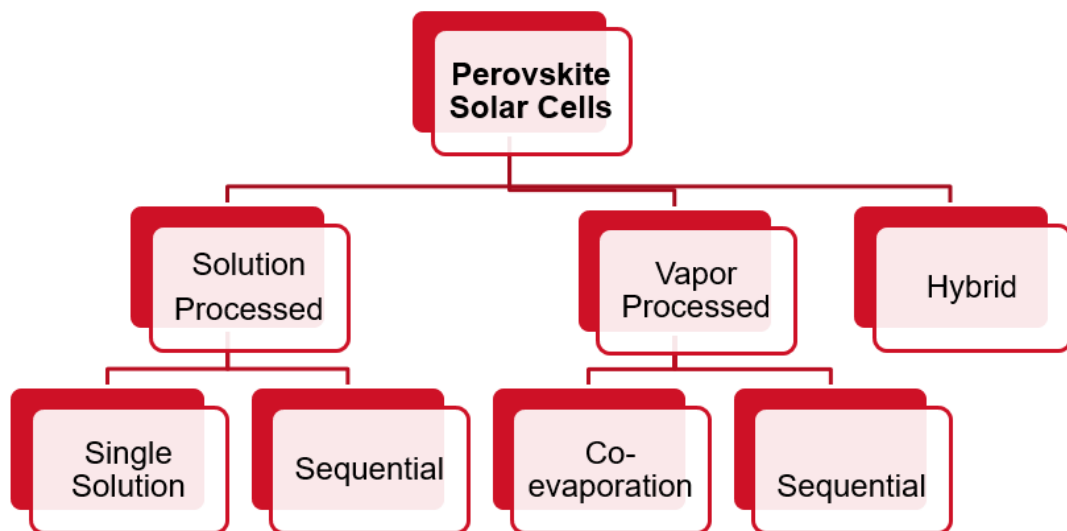
Figure 5.2: Different fabrication techniques for perovskite

In vapor process the precursors are evaporated followed by an annealing process to form perovskite [7,8,9,10,11]. In co-evaporation, all the precursors are evaporated on a substrate together and in sequential process the precursors are evaporated one after the other. Both processes are followed by annealing to from perovskite. Perovskite can also be deposited by hybrid process which is a combination of solution and vapor process, where one of the

precursor is evaporated while the other is spin-coated on the substrate [12]. The most common techniques which are used today is single solution process with anti-solvent method and co-evaporation. Figure 5.3 shows the illustration of solution-processed and vapor-processed fabrication methods of perovskite.
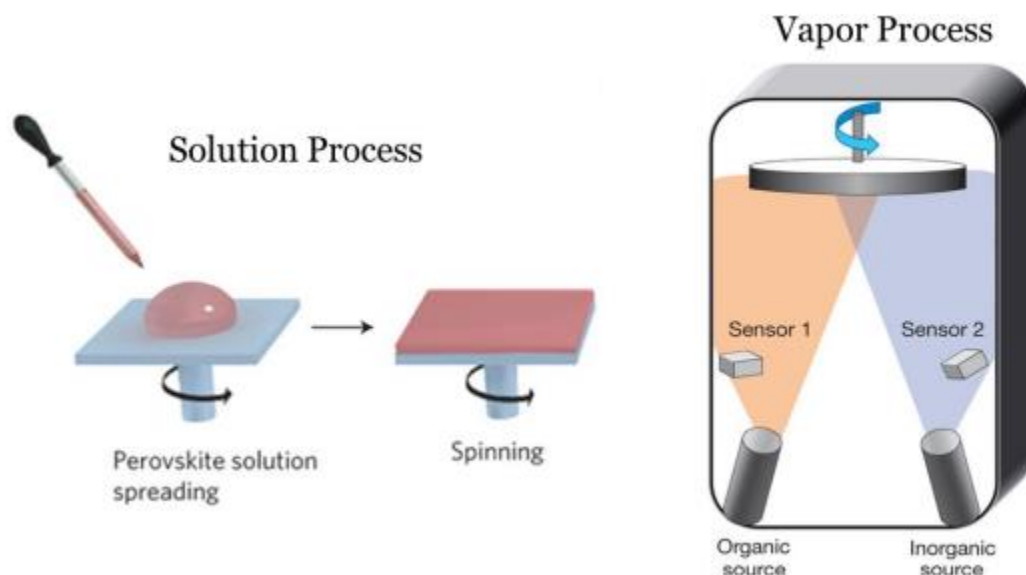
Figure 5.3: Fabrication methods of perovskite: Solution-processed (left) and Vapor-processed (right) [8,13,14]

The most popular form of perovskite is fabricated using an organic precursor methylammonium iodide (MAI) and inorganic perovskite lead iodide (PbI_2). The formation of perovskite follows the following chemical reaction,

$$PbI_2 + CH_3NH_3I \rightarrow CH_3NH_3PbI_3$$
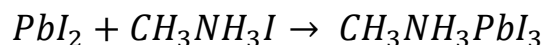
There are several groups who have fabricated mixed halide or non-iodide perovskite also [1,8,15].

In this report, I have used p-i-n structured perovskite solar cells where the hole transport layer is either NiO or PTAA. For fabrication of NiO we have used ebeam evaporation. A 30 nm of NiO was deposited with deposition rate of 0.5Å/s. Then, it was annealed at $200^o C$ for

1 hour in presence of air. For fabrication of PTAA, the ITO substrate was cleaned in air plasma for 10 minutes. Then we have spin coated 2.18 mg/mL PTAA solution in Toluene at 6000 rpm for 40 seconds in a nitrogen filled glovebox followed by an annealing at 150^oC for 10 minutes. This gives about 15-20 nm of PTAA film thickness.

Perovskite was also fabricated in the nitrogen filled glovebox as it degrades in presence of moisture. About 1.6 M perovskite solution, contains CH_3NH_3I, PbI_2, Dimethyl sulfoxide (DMSO) in Dimethylformamide (DMF) with molar ratio of 1:1.05:1, was spin coated at 4000 rpm for 25 seconds with drop cast of chlorobenzene on 10 seconds' delay. This gives about 600 nm of perovskite layer thickness. Then it was annealed at 60°C for 1 minute followed by 100°C for 5 minutes. For the device fabricated on PTAA, the substrate was wetted using DMF before spin-coating of perovskite. The reason behind this will be explained in the later part of this chapter.

Then 20 mg/mL PC60BM in chlorobenzene solution was spin coated at 2000 rpm for 40 seconds. Then the whole structure was annealed at 100°C for 15 minutes. Finally, about 100 nm of Aluminum was deposited using thermal evaporator with a deposition rate of about 2-4 Å/s. A mask was used during Aluminum evaporation to deposit a circular shape contact of area 0.106 cm^2.

5.2 Solvent Annealing of Perovskite

The single solution process using the anti-solvent method [2] gives high quality uniform perovskite film. But the grain size of perovskite is only in the range of 200-300 nm. Later in this report, I will discuss that larger grain size of perovskite will enhance the photo-stability of these solar cells. One way to enhance the perovskite grain size is solvent annealing.

Xiao and Huang et al. first proposed the solvent annealing process [16]. The solvents such as DMF [16] and DMSO [17] which can dissolve the perovskite has been used for the solvent annealing process. The kinetics behind the grain enhancement has been described by Xiao et al. and Liu et al. [16,17] as showed in figure 5.4.
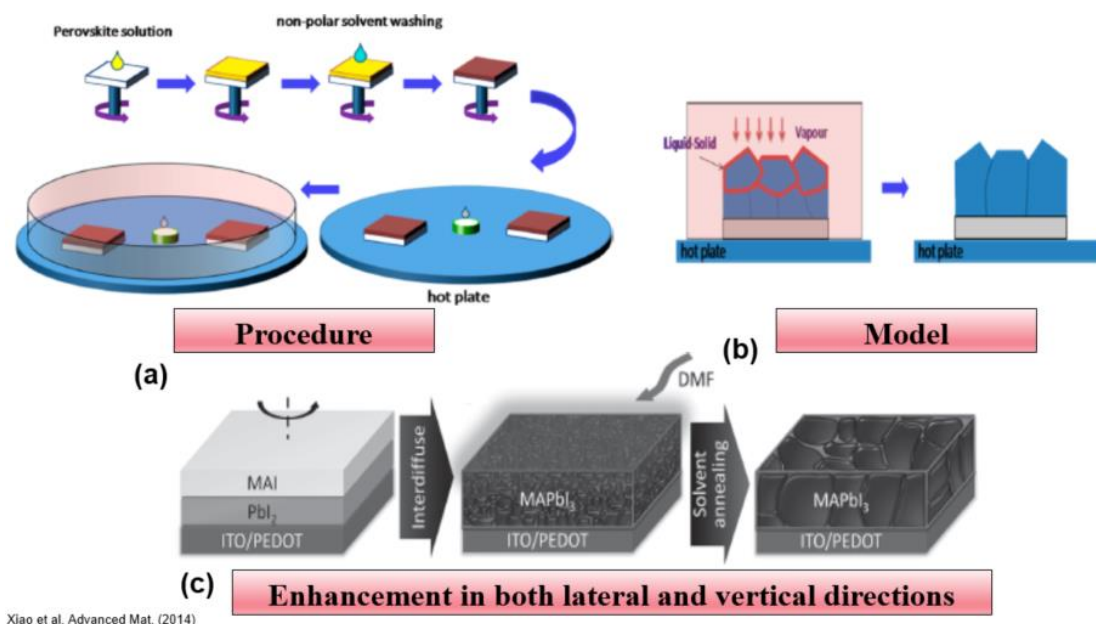
Figure 5.4: Perovskite grain size enhancement using solvent annealing (a) Process of solvent annealing after spin coating perovskite solution (b) Formation of liquid-solid state between grains which leads to formation of larger grains (c) Solvent annealing helps enhancement of perovskite in all three dimensions [16,17]

The figure 5.4 shows a common procedure for grain size enhancement (solvent annealing). For the solvent-annealed device, after spin coating perovskite it was annealed in presence of solvent (10 uL DMF in this case) [Figure 5.4 (a)]. Xio et al. and Liu et al. has explained the mechanism behind grain size enhancement. Per their model when the film is placed in a solvent vapor at an elevated temperature with in a closed space the vapor will condense on the film surface. The solvent vapor can migrate through the grain boundaries and form a liquid-solid phase (or quasi liquid phase). Consequently, this liquid phase can play a role of binder, which helps to eliminate the grain boundaries and enhances the grain size. Liu

et al. has also showed that the grain enhancement is a three-dimensional procedure. During this process, the grain size increases both in lateral and vertical directions [Figure 5.4 (c)]. Figure 5.5 shows the grain size enhancement of perovskite using solvent annealing with DMF demonstrated by Liu et al. [17]. They showed that the film without solvent annealing has grain size in the range 100-200 nm. But the perovskite film with solvent annealing has grain size in the order of 1µm.
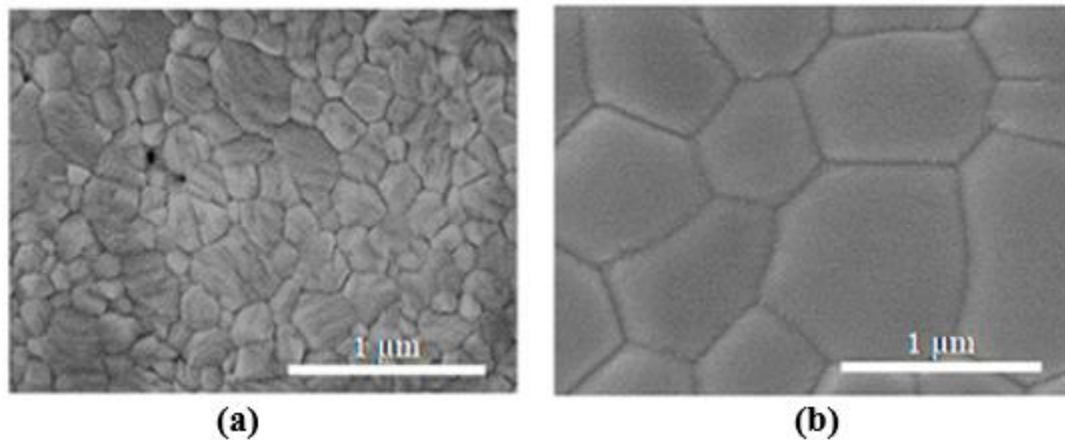
Figure 5.5: Perovskite grain size enhancement by solvent annealing (a) Without solvent annealing (b) With solvent annealing. There is about 10X enhancement in grain size [17]

5.3 Efficiency Optimization on PTAA as HTL

In this section, I will discuss the efficiency optimization process of perovskite solar cell on PTAA as hole transport layer using single solution process. The structure of the device that has been used for this efficiency optimization has been shown in figure 5.7. This figure also shows the band edges of different layers matches very well for the photovoltaic application.

Properties of PTAA
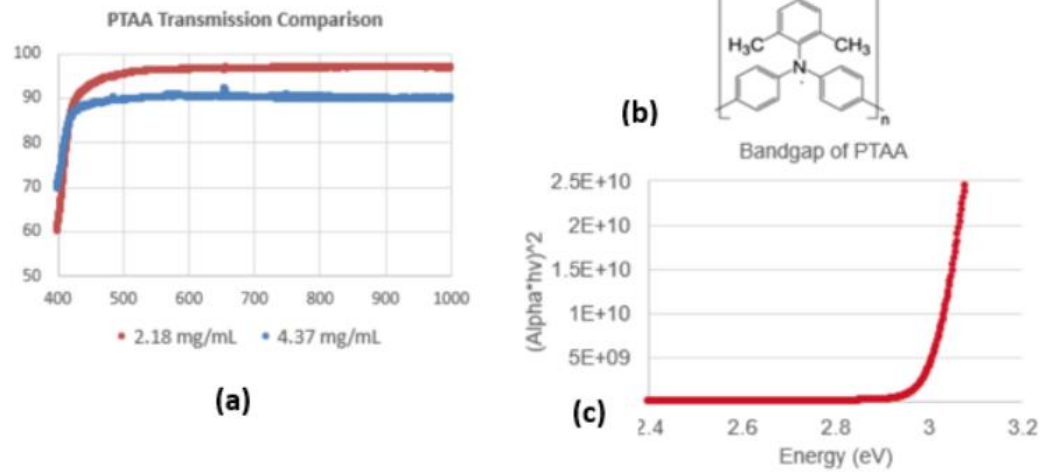
Figure 5.6: Properties of PTAA (a) Transmission for two different thickness PTAA layers (b) Chemical structure of PTAA (c) Tauc curve for band-gap measurement
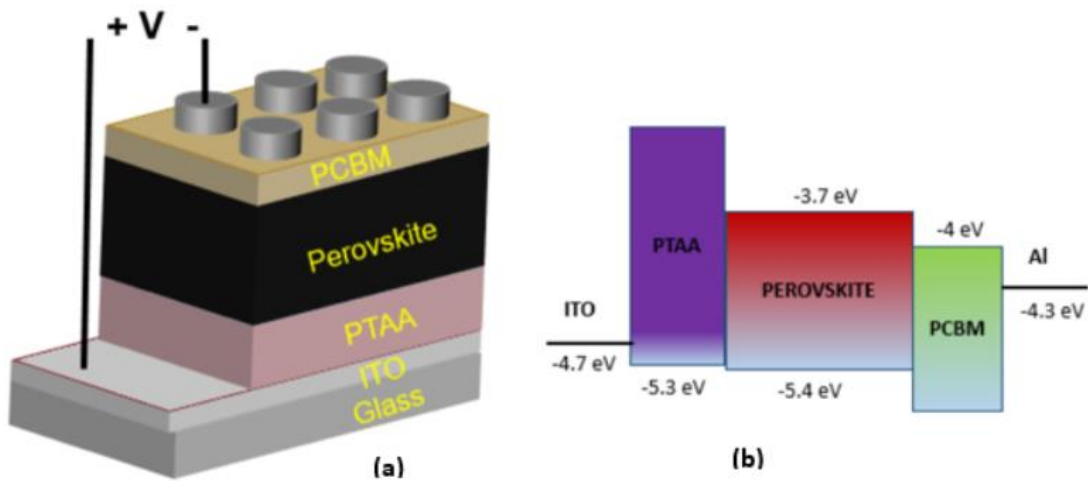
Figure 5.7: Efficiency optimization of perovskite solar fabricated on PTAA as hole transport layer using single solution process (a) Device structure (b) Corresponding band edges

Figure 5.6 physical properties of PTAA. The Tauc plot shows that PTAA is a direct bandgap material with a bandgap of about 3 eV. And the transmission in the visible range significantly increases as we reduce the thickness of PTAA from ~30 nm (4.18 mg/mL solution in toluene as solvent at 6000 rpm for 40 secs) to about 15-20 nm (2.18 mg/mL solution in

toluene as solvent at 6000 rpm for 40 secs). As a result, we expect the short-circuit current to increase with thinner PTAA.

We followed the fabrication procedure as described in section 5.1. Initially, ITO Coated glass substrate was spin coated with 4.36 mg/mL PTAA solution at 6000 rpm for 40 seconds (Thickness of about 30 nm). Then anneal at 150°C for 10 minutes. Then about 1.6M perovskite solution was prepared having PbI_2, CH_3NH_3I and DMSO in DMF with molar ratio 1:1:1. Perovskite was spin coated at 4000rpm for 25 seconds with drop cast chlorobenzene on 10 seconds' delay (Thickness of about 600 nm). Then annealed 60°C for 1 minute and followed by 100°C for 5 minutes. Then 20mg/mL PCBM in chlorobenzene solution was spin coated at 2000 rpm for 40 seconds. Then it was annealed at 100°C for 15 minutes. 100 nm of Aluminum is deposited using thermal evaporator. The area of the contact was $0.106\ cm^2$. The power-conversion efficiency of this solar cell has been showed in figure 5.8.

Voc	Jsc	FF	PCE
1.08	15.3	69	11.2

(a)

(b)
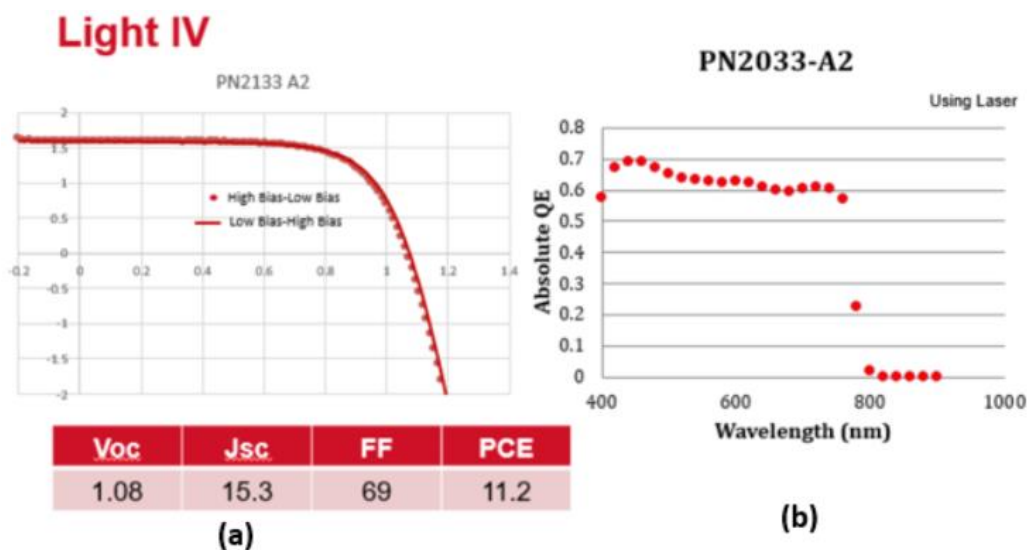
Figure 5.8: One of the first devices made on PTAA before efficiency optimization (a) Light-IV characteristics (b) External Quantum efficiency as function of wavelength

We had a problem with perovskite solution spreading on PTAA. And, the device in figure 5.8 had a huge voltage evolution. The short circuit current was low. The Quantum efficiency suggests that we are losing a lot of photons due loss in transmission.

So, we had some serious challenges to solve before we get good devices on PTAA using single solution process:

1. As the Perovskite-solution doesn't spread on PTAA, the film had a lot of pin-holes. These pin-holes reduce the reproducibility of these devices.

2. They show huge open-circuit voltage evolution. That must because of lot of ions present even when the device is not exposed under light. These ions can alter the electric field inside the absorber perovskite layer. They can redistribute themselves in presence of external electric field which helps the open-circuit voltage evolution.

3. The short circuit current is low because of loss in transmission which can be solved by reducing PTAA thickness.

5.3.1 Solution of spreading problem on PTAA

To solve this problem first, we need to understand the reason behind why to solution doesn't spread. As showed in figure 5.9, if the surface energy between the solution and the surface is too high the molecules tend to gather in small areas rather than spreading on the whole surface. This action helps the contact angle between the solution and the surface to increase. A high contact angle means poor wettability while a low contact angle means high wettability. In general, a 90^0 contact angle is considered as the cut-off between wetting and dewetting. But even with contact angle below 90^0, it can still lead to difficulty in coating. The

thumb rule is that to obtain a good uniform film it is recommended to have contact angle $< 30^0$ [18].
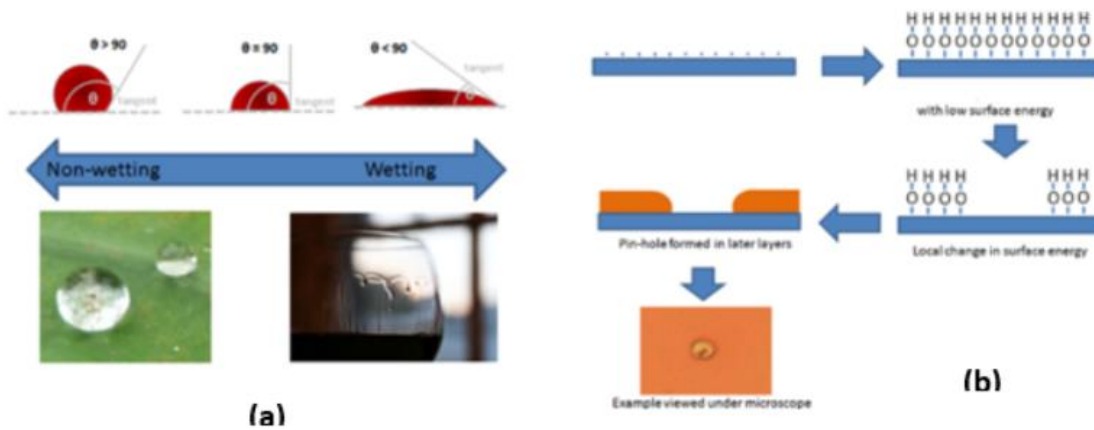
Figure 5.9: Illustration of contact angle related spreading issue (a) Contact angle for Non-wetting and wetting solution (b) High surface energy between solvent and PTAA surface leads to pin-hole [18]

Two possible solutions:

A. Increasing random surface roughness to enhance wettability (Playing with surface geometry)
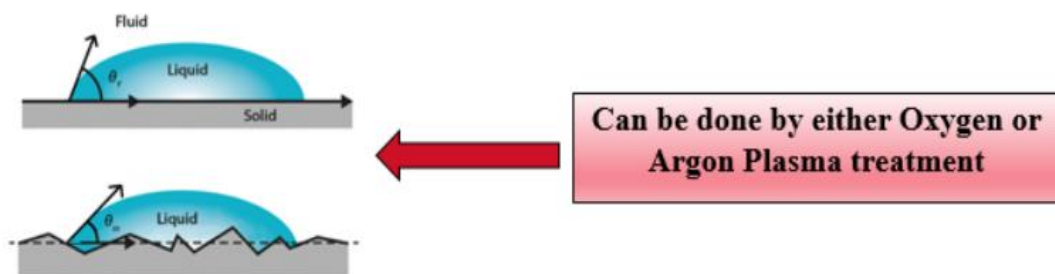
Figure 5.10: Introducing surface roughness can enhance spreading of solution

But this method will only work if the contact angle between a smooth surface and the solution is less than 65^0. If the solution is already wetting, then by introducing random roughness can reduce the contact angle which can overcome the potential barrier due to roughness.

We have tried with Argon and Oxygen plasma treatment on PTAA to increase random roughness.

Argon Plasma Treatment

Voc	Jsc	FF	PCE
0.983	16.32	63	10.1

Voc	Jsc	FF	PCE
0.97	17.1	67	11
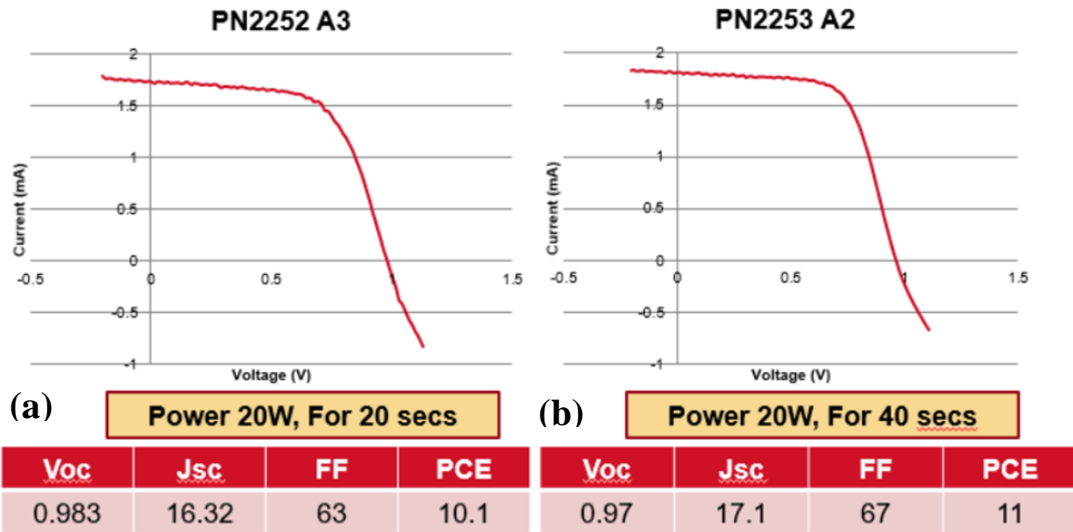
Figure 5.11: Light IV characteristics with Argon plasma treatment of PTAA (a) with 20W power for 20 seconds (b) with 20W power for 40 seconds

Oxygen Plasma Treatment

Voc	Jsc	FF	PCE
0.66	12.3	27	2.1

Voc	Jsc	FF	PCE
0.98	15.1	55	8.1
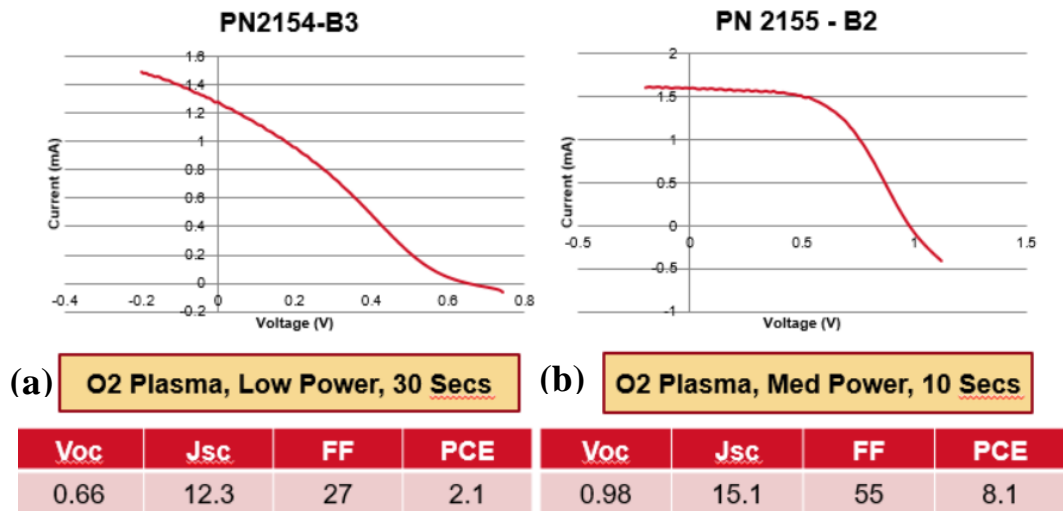
Figure 5.12: Light IV characteristics with Oxygen plasma treatment of PTAA (a) with low power (10W) for 30 seconds (b) with medium power (20W) for 10 seconds

The solar cell efficiencies using Argon plasma treatment with 20W power has been showed in figure 5.11. The argon plasma treatment didn't give us a significant improvement in spreading and no significant improvement in device performance.

Next, we have tried with oxygen plasma treatment at two different power. We have tried at low power (10 W) for 30 seconds and high power (20 W) for 10 seconds. The light IV characteristics and power conversion efficiencies for both the devices have been showed in figure 5.12. Oxygen plasma treatment increases the spread-ability but the device performance goes down. A possible reason may be oxygen reacts with PTAA during treatment. So, increasing the random roughness of the PTAA surface didn't help to enhance the device performance.

B. Changing surface property to enhance wettability (Playing with chemical property)

Figure 5.13: Reducing surface energy can enhance spreading of solution

This is a very well-known procedure for increasing spread-ability of a solution on the surface. By washing with a specific solvent before spin coating can alter the surface chemistry which can help to reduce the surface energy significantly [18]. Thus, the contact angle between the solvent and the surface reduces and it helps the solution to spread on the substrate while spin coating. This process reduces the number of pin-holes and increases reproducibility of the process.

One way we can reduce the surface energy is washing with a solvent (DMF in our case) to change surface chemical property. Pre-wetting the PTAA surface with DMF increases the

spread-ability significantly and there seems to be negligible number of pin-holes. Thus, device performance increases, significantly. But the device still showed huge open-circuit voltage evolution. For example, the Light-IV curve showed in the figure 5.14 was taken after 4 mins of light soaking under open circuit condition. And, the Quantum efficiency shows that there still room for improvement in short-circuit current. Figure 5.14 shows the device performance.
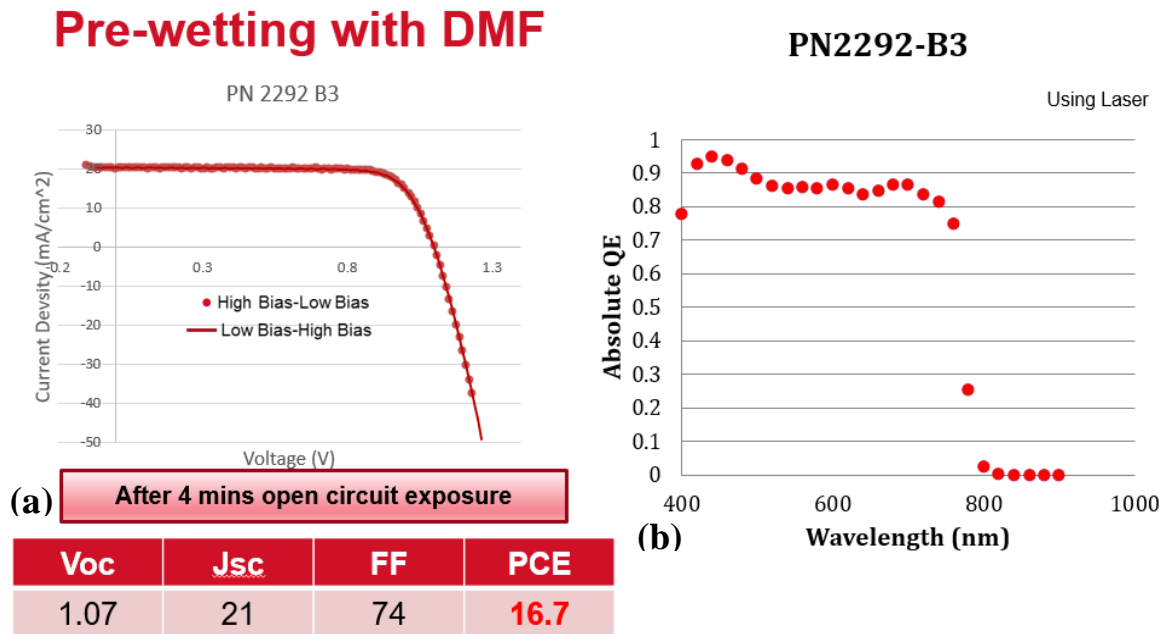
Figure 5.14: Device performance with pre-wash of PTAA with DMF (a) Light IV characteristics (Light IV was taken after open circuit exposure for 4 minutes) (b) External quantum efficiency as a function of wavelength

5.3.2 Solution to open circuit voltage evolution

We can use 1:1.05 Molar Ratio of MAI: PbI_2 (5% Excess PbI2) rather than using 1:1 molar Ratio of MAI: PbI_2. This helps to reduce the open-circuit voltage evolution.

$$MA^+ + I^- + PbI_2 \leftrightarrow MAPbI_3$$
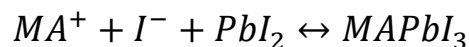
The reason behind open-circuit voltage evolution is that there are ions present inside the bulk perovskite absorber layer. These ions can redistribute themselves in presence of an external electric field. So, the open-circuit voltage increases during light soaking at open-

circuit condition. But when we introduce excess of PbI_2 the equilibrium condition to the above chemical reaction shifts to the right by converting the ions to perovskite. So, the open-circuit voltage evolution decreases as there is less number of ions present in the bulk material. The performance of this device has been shown in figure 5.15. The detailed study of perovskite stoichiometry on device performance will be discussed in chapter 7.
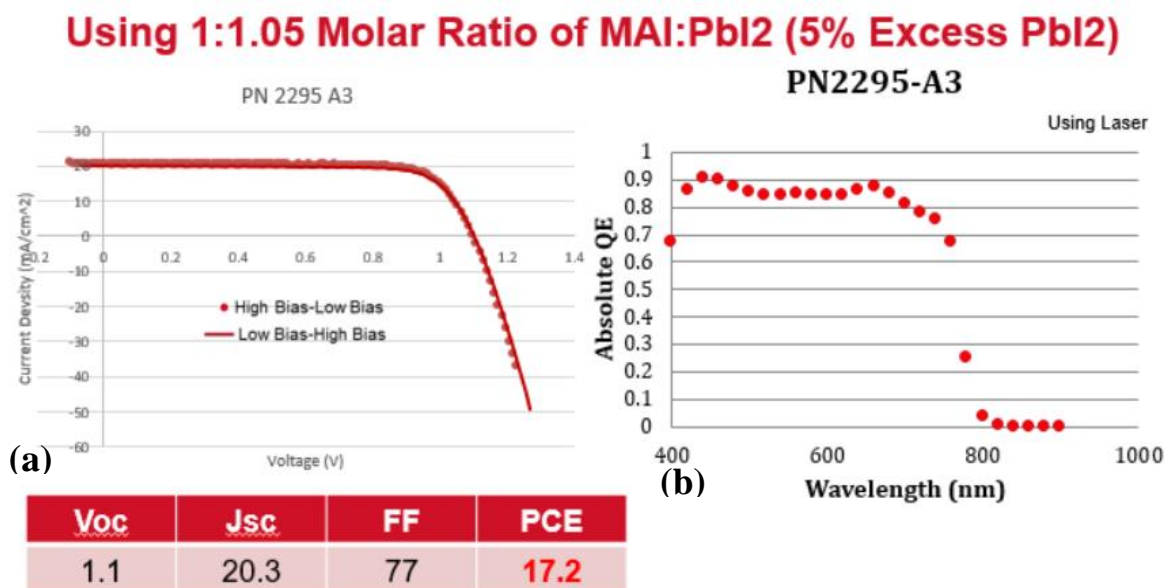
Figure 5.15: Device performance with excess PbI_2 (a) Light IV characteristics (no voltage evolution) (b) External quantum efficiency as a function of wavelength. No light soaking was done before measuring the light IV characteristics

5.3.3 Increase in short-circuit current with thinner PTAA

As the transmission data showed in figure 5.6, there is an increase in transmission with reduced thickness of PTAA, we can also expect the short-circuit current to increase. By reducing the PTAA solution concentration to 2.18 mg/mL, the short-circuit current increases. The difference in transmission is also visible in comparison of Quantum Efficiency data (Figure 5.17). The quantum efficiency is significantly higher for thinner PTAA (~10-15nm)

than thicker PTAA (~30nm). I have got a cell efficiency of 18.5% (Figure 5.16). This is one

of the best cells on PTAA (best using single solution process).

Voc	Jsc	FF	PCE
1.12	21.68	76	18.5
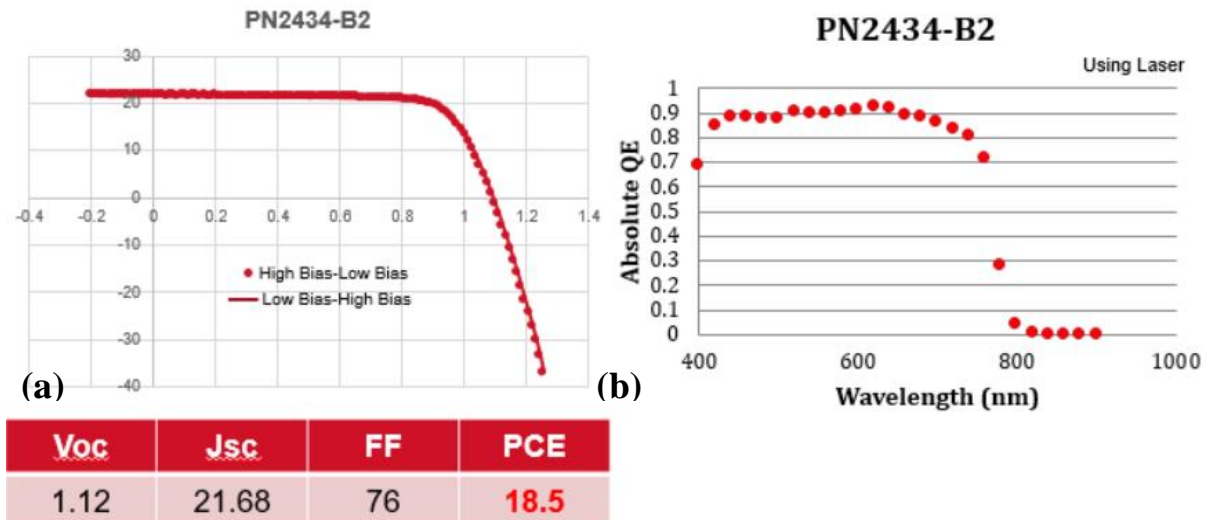
Figure 5.16: Device performance with thinner PTAA layer (a) Light IV characteristics (no voltage evolution) (b) External quantum efficiency as a function of wavelength
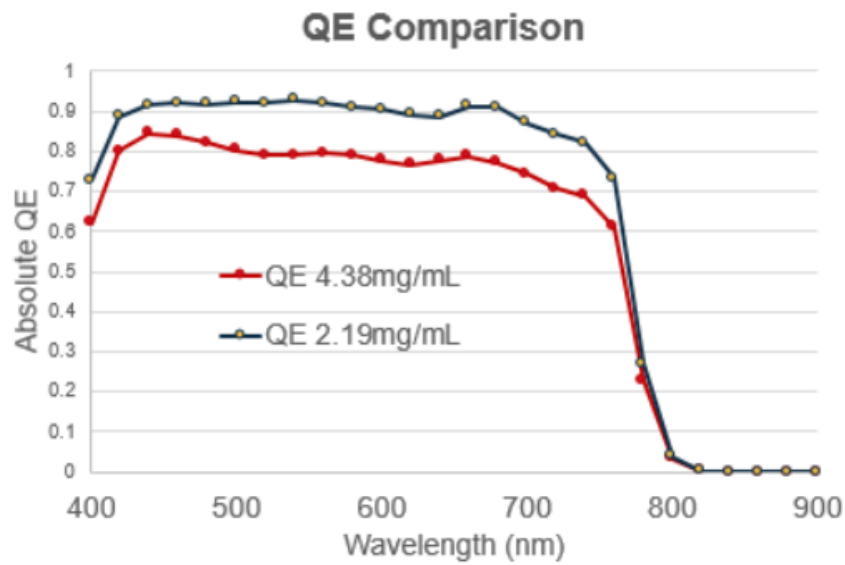
Figure 5.17: External quantum efficiency comparison between two different thickness of PTAA

5.3.4 Statistical analysis
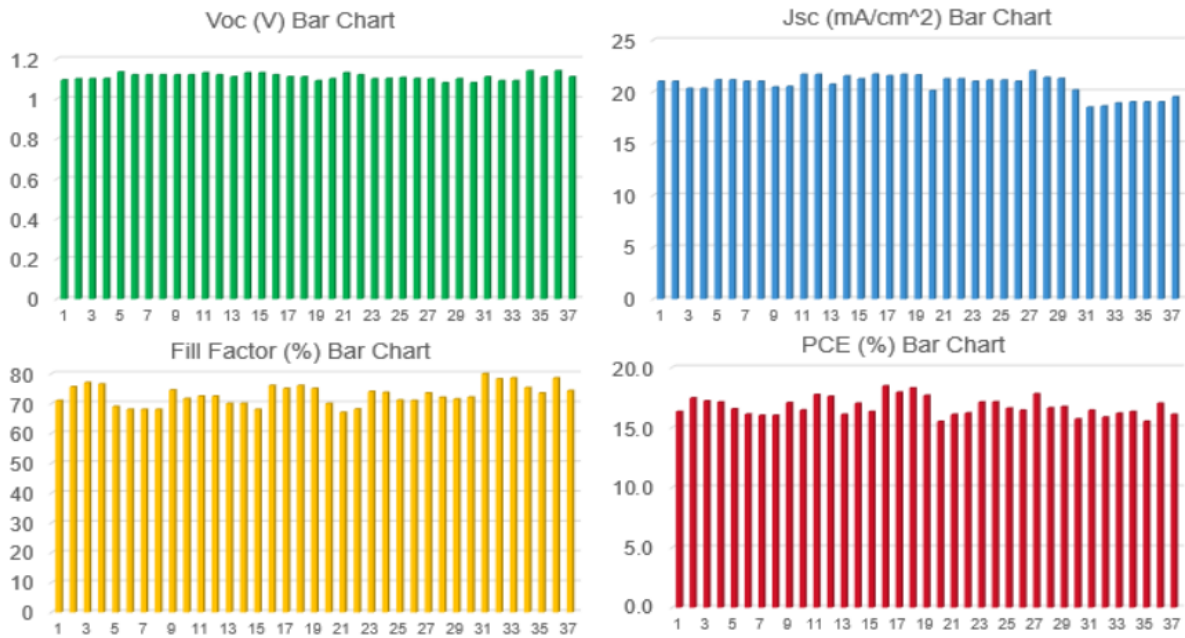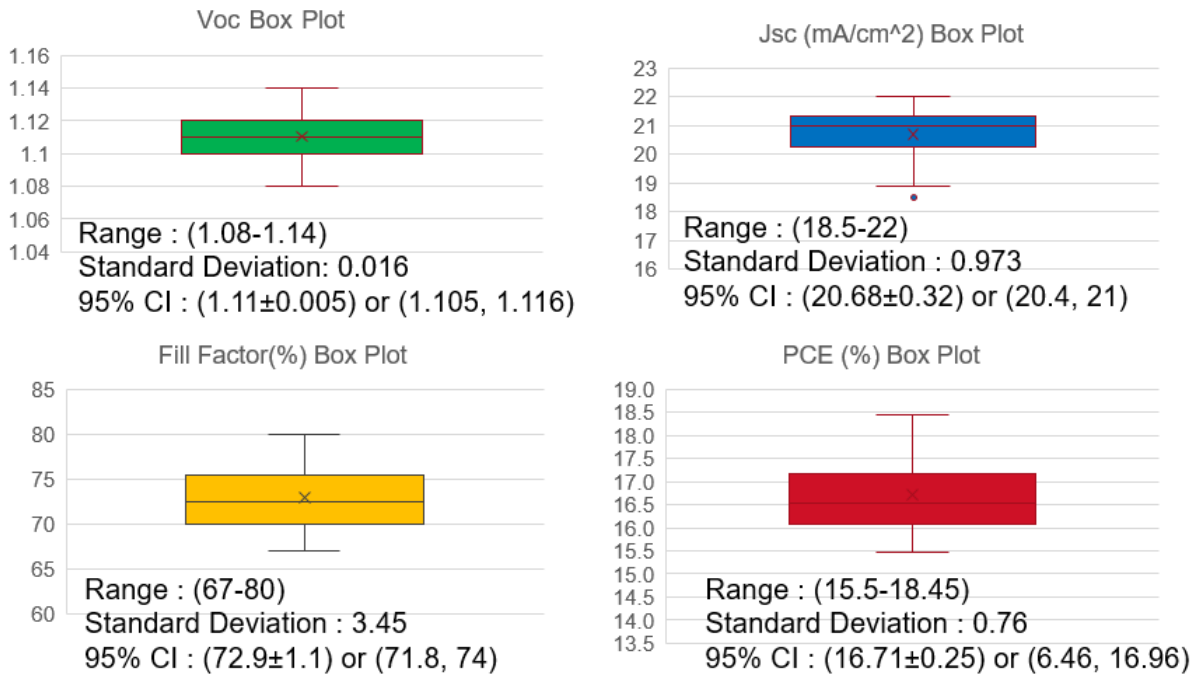
Figure 5.18: Statistical analysis of device performance (a) Bar chart of device attributes (Voc, Jsc, FF, Efficiency) (b) 95% confidence interval of device attributes (Shows the consistency in device performance)

Figure 5.18 shows the statistical analysis of the photovoltaic parameters of the control perovskite solar cell on PTAA (optimized in section 5.3.3). The figure shows statistics for 38 devices. The mean power conversion efficiency is 16.7% with a standard deviation of 0.76, where the maximum efficiency achieved is 18.5%. This analysis shows that the procedure is very reproducible.

5.4 CdS and ZnO as Transparent Electron Transport Layers

CdS and ZnO can serve as transparent top contact of a perovskite solar cell. This transparent contact is important for tandem solar cell as the light will shine from top. Figure 5.19 shows the device structures for both substrate (light is incident from the bottom) and superstrate (light is incident from the top).
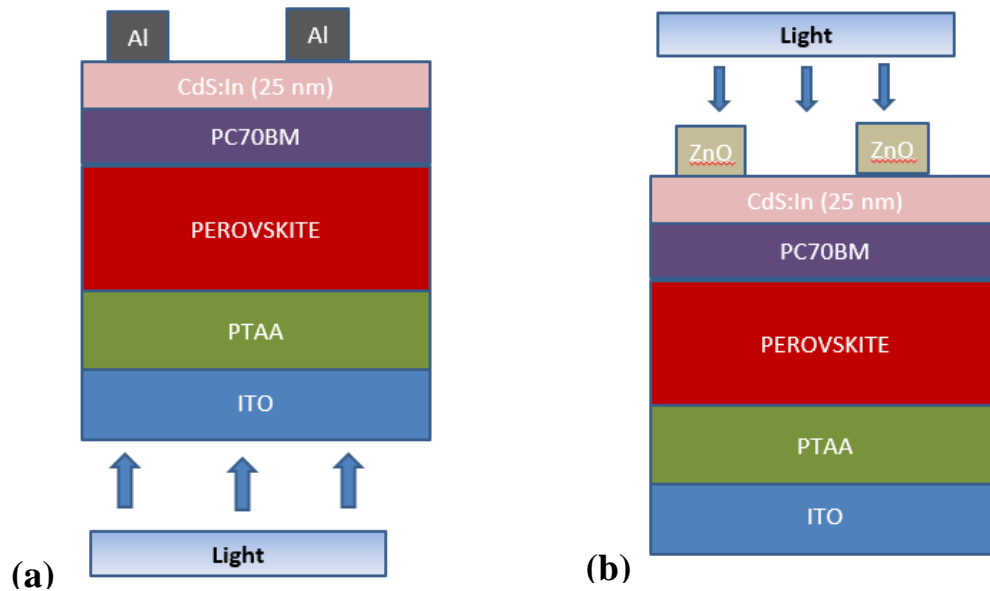
Figure 5.19: Device structure of perovskite solar cell (a) Light shining from bottom (superstrate) (b) Light shining from top (substrate)

On top of PCBM two other Electron transport layers were deposited. Here 25nm of Indium doped CDS was deposited using thermal evaporator (Co-evaporation of CdS and Indium) at a rate of 1-2 Å/s. And 280nm Aluminum doped ZnO was deposited using Argon

plasma sputtering (at room temperature substrate) at 80W power at a rate of 7 Å/s. Here CdS:In layer acts as a buffer layer between ZnO and PCBM because ZnO doesn't make good interfacial contact either with Perovskite or PCBM. The band edges show that both these layers are near-perfect match to have good ohmic contacts without sacrificing any significant open-circuit voltage.

(a)

(b)
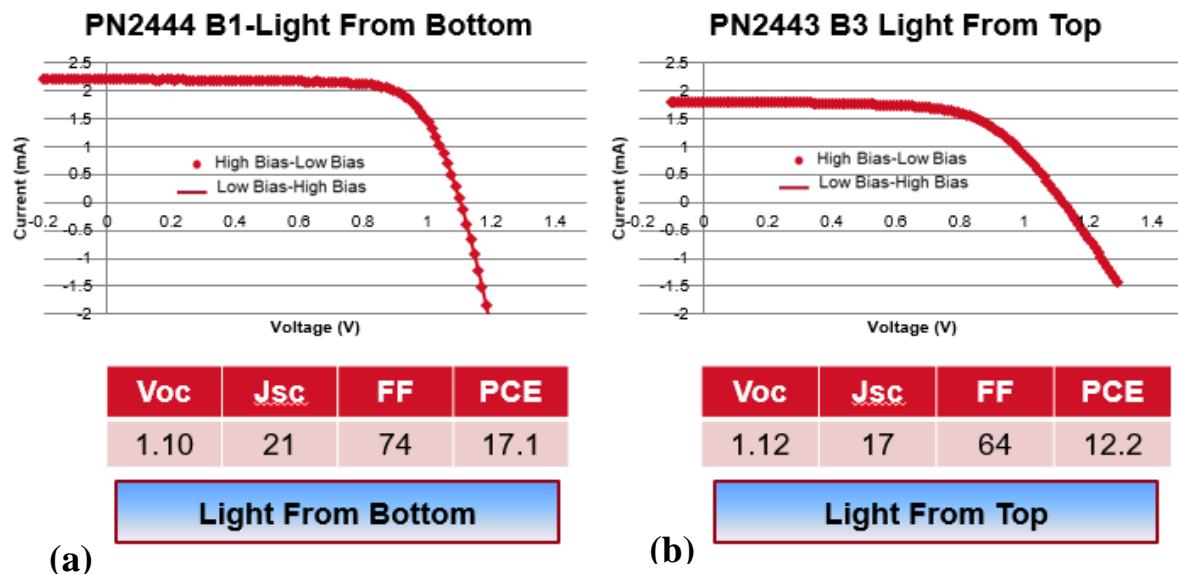
Figure 5.20: Light IV response of perovskite solar cell (a) Light shining from bottom (superstrate) (b) Light shining from top (substrate)

Figure 5.20 shows the power-conversion efficiencies for both superstrate [Figure 5.20 (b)] and substrate [Figure 5.20 (b)] structure. The efficiency for the device with transparent ZnO on top has lower efficiency as the CdS:In layer absorbs photons with energy up to 2.5 eV. This claim can be proved from the quantum efficiency measurement (Figure 5.21). It clearly shows that the quantum efficiency is lower for the device which was measure by light shining through CdS and ZnO layer because of absorption in CdS layer up to 512 nm of wavelength which corresponds to about 2.5 eV of photon energy.
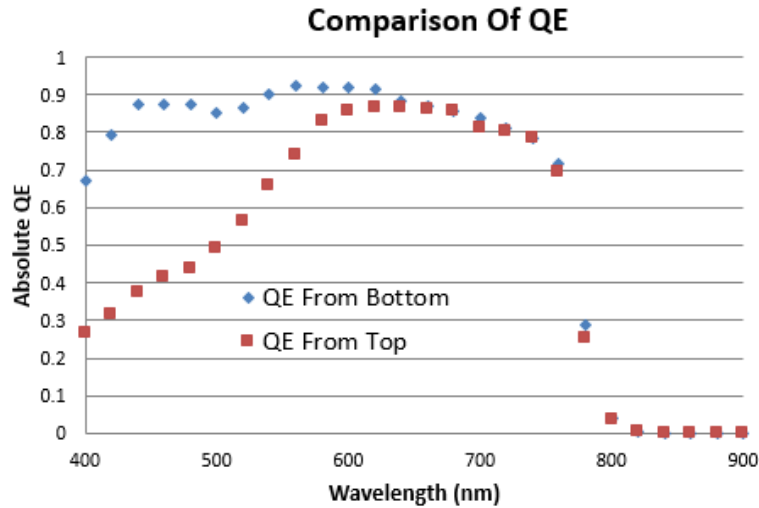
Comparison Of QE

Figure 5.21: External quantum efficiency comparison between substrate and superstrate perovskite solar cells
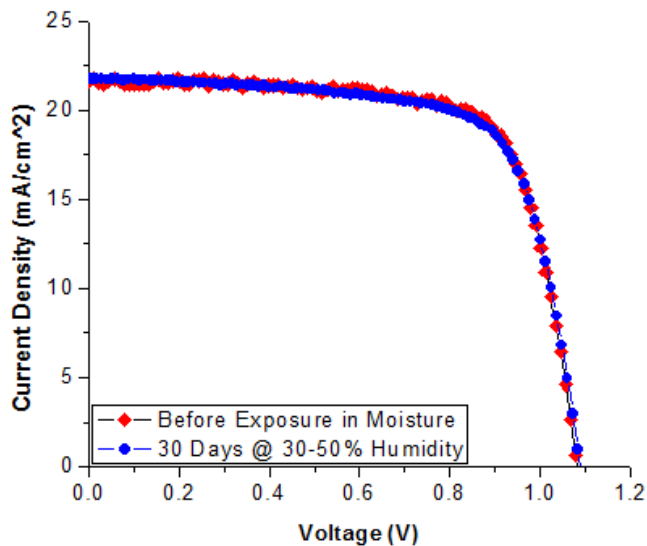
Figure 5.22. Light IV response of perovskite solar cell with CdS/ZnO as buffer layers (i) Just after fabrication (ii) After device was kept in 30-50% humidity for 30 days

CdS and ZnO as buffer layers also help to improve the stability of these devices in presence of moisture. ZnO acts as an encapsulating layer to shield perovskite from moisture and oxygen. Figure 5.22 shows the light IV comparison of perovskite solar cell with CdS/ZnO as buffer layers before exposure in moisture (pristine device), and measured after it was kept at 30-50% humidity outside glovebox for 30 days. Perovskite solar cells with no CdS/ZnO as

buffer layer degrades immediately after exposure to moisture but adding CdS/ZnO as buffer layer improves the device stability in ambient environment for more than 30 days. Table 4 shows the photovoltaic parameters of this device before and after exposure in moisture.

Table 5.1: Photovoltaic parameters for a device with CdS/ZnO as buffer layers before and after exposure in moisture

Condition	$V_{oc}(V)$	$J_{sc}(mA/cm^2)$	$FF(\%)$	$PCE\ (\%)$
Before Exposure in Moisture	1.09	21.6	74	17.4%
After 30 days @30-50% Humidity	1.09	21.5	71	16.7%

CdS and ZnO also acts as a buffer-layer to improve recovery after photon-induced degradation. This phenomenon will be discussed in chapter 7.

5.5 Co-evaporated Perovskite Solar Cell

We use ITO Coated glass substrate and Spin coat 1.43 mg/mL PTAA solution (Thickness of about 10 nm). Then anneal at $150°$ C for 10 minutes. Perovskite was deposited using co-evaporation. For this co-evaporated device, initially 5 nm of PbI_2 was deposited followed by co-evaporation of PbI_2 at 5.85 Å/s and MAI at 3.75-4.2 Å/s. The pressure during deposition was in the range of $9.2 - 10^{-5}\ Torr$. Then it was post annealed at $100°$ C for 1 hour. 20 mg/ml PCBM was spin-coated at 2000 rpm for 40 seconds in a nitrogen-filled glovebox. Then it was annealed at $100°$ C for 15 minutes. Finally, 100 nm of Aluminum was deposited using thermal evaporator at 1-4 Å/s. A mask has been used during Aluminum evaporation which gives a circular contact with an area of $0.106\ cm^2$.
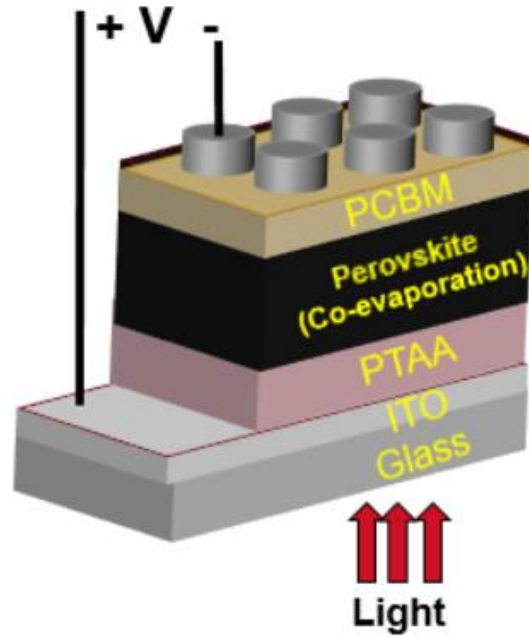
Figure 5.23: Device structures used for photon-induced degradation; Fabricated on PTAA and co-evaporated perovskite

REFERENCES

1   J. B. You, Z. R. Hong, Y. Yang, Q. Chen, M. Cai, T. B. Song, C. C. Chen, S. R. Lu, Y. S. Liu, and H. P. Zhou, "Low-temperature solution-processed perovskite solar cells with high efficiency and flexibility", ACS Nano, 8, 1674 (2014). doi:Doi 10.1021/Nn406020d

2   N. Ahn, D. Y. Son, I. H. Jang, S. M. Kang, M. Choi, and N. G. Park, "Highly reproducible perovskite solar cells with average efficiency of 18.3% and best efficiency of 19.7% fabricated via lewis base adduct of lead(ii) iodide", J. Am. Chem. Soc., 137, 8696 (2015). doi:10.1021/jacs.5b04930

3   Y. Zhou, M. Yang, W. Wu, A. L. Vasiliev, K. Zhu, and N. P. Padture, "Room-temperature crystallization of hybrid-perovskite thin films via solvent–solvent extraction for high-performance solar cells", J. Mater. Chem. A, 3, 8178 (2015). doi:10.1039/c5ta00477b

4   M. Xiao, F. Huang, W. Huang, Y. Dkhissi, Y. Zhu, J. Etheridge, A. Gray-Weale, U. Bach, Y.-B. Cheng, and L. Spiccia, "A fast deposition-crystallization procedure for highly efficient lead iodide perovskite thin-film solar cells ", Angew. Chem., 126, 10056 (2014)

5   Z. Xiao, C. Bi, Y. Shao, Q. Dong, Q. Wang, Y. Yuan, C. Wang, Y. Gao, and J. Huang, "Efficient, high yield perovskite photovoltaic devices grown by interdiffusion of solution-processed precursor stacking layers", Energy Environ. Sci., 7, 2619 (2014). doi:10.1039/c4ee01138d

6   X. Li, D. Bi, C. Yi, J. D. Decoppet, J. Luo, S. M. Zakeeruddin, A. Hagfeldt, and M. Gratzel, "A vacuum flash-assisted solution process for high-efficiency large-area perovskite solar cells", Science, 353, 58 (2016). doi:10.1126/science.aaf8060

7   D. Zhao, W. Ke, C. R. Grice, A. J. Cimaroli, X. Tan, M. Yang, R. W. Collins, H. Zhang, K. Zhu, and Y. Yan, "Annealing-free efficient vacuum-deposited planar perovskite solar cells with evaporated fullerenes as electron-selective layers", Nano Energy, 19, 88 (2016). doi:10.1016/j.nanoen.2015.11.008

8   M. Liu, M. B. Johnston, and H. J. Snaith, "Efficient planar heterojunction perovskite solar cells by vapour deposition", Nature, 501, 395 (2013). doi:10.1038/nature12509

9   Q. Lin, A. Armin, R. C. R. Nagiri, P. L. Burn, and P. Meredith, "Electro-optics of perovskite solar cells", Nat. Photonics, 9, 106 (2014). doi:10.1038/nphoton.2014.284

10   H. A. Abbas, R. Kottokkaran, B. Ganapathy, M. Samiee, L. Zhang, A. Kitahara, M. Noack, and V. L. Dalal, "High efficiency sequentially vapor grown n-i-p ch3nh3pbi3 perovskite solar cells with undoped p3ht as p-type heterojunction layer", APL Materials, 3, 016105 (2015). doi:10.1063/1.4905932

11   O. Malinkiewicz, A. Yella, Y. H. Lee, G. M. Espallargas, M. Graetzel, M. K. Nazeeruddin, and H. J. Bolink, "Perovskite solar cells employing organic charge-transport

layers", Nat. Photonics, 8, 128 (2014). doi:Doi 10.1038/Nphoton.2013.141

12   Q. Chen, H. Zhou, Z. Hong, S. Luo, H. S. Duan, H. H. Wang, Y. Liu, G. Li, and Y. Yang, "Planar heterojunction perovskite solar cells via vapor-assisted solution process", J. Am. Chem. Soc., 136, 622 (2014). doi:10.1021/ja411509g

13   N. J. Jeon, J. H. Noh, Y. C. Kim, W. S. Yang, S. Ryu, and S. I. Seok, "Solvent engineering for high-performance inorganic-organic hybrid perovskite solar cells", Nat. Mater., 13, 897 (2014). doi:10.1038/nmat4014

14   Liang Zhang, Ph.D. dissertation, "Device physics of perovskite solar cells", Iowa State University (2016)

15   G. Balaji, P. H. Joshi, H. A. Abbas, L. Zhang, R. Kottokkaran, M. Samiee, M. Noack, and V. L. Dalal, "Ch3nh3pbi3 from non-iodide lead salts for perovskite solar cells via the formation of pbi2", Physical chemistry chemical physics: PCCP, 17, 10369 (2015). doi:10.1039/c5cp00073d

16   Z. Xiao, Q. Dong, C. Bi, Y. Shao, Y. Yuan, and J. Huang, "Solvent annealing of perovskite-induced crystal growth for photovoltaic-device efficiency enhancement", Adv. Mater., 26, 6503 (2014). doi:10.1002/adma.201401685

17   J. Liu, C. Gao, X. He, Q. Ye, L. Ouyang, D. Zhuang, C. Liao, J. Mei, and W. Lau, "Improved crystallization of perovskite films by optimized solvent annealing for high efficiency solar cell", ACS applied materials & interfaces, 7, 24008 (2015). doi:10.1021/acsami.5b06780

18   Becker, H; Gärtner, Analytical and Bioanalytical Chemistry. Volume 390, Issue 1, pp 89–111 (2008)

CHAPTER 6. PHOTON-INDUCED DEGRADATION OF PEROVSKITE SOLAR CELLS

6.1 Introduction

Environmental instability is problem for perovskite solar cells. This can be solved by encapsulation. But the alarming problem is the instability of these solar cells under illumination and this cannot be avoided as the solar cell must work under light. To mitigate this problem first we have to understand the detailed physics behind this photo-instability. Pranav el al. [1,2] studied the photo-degradation of p-i-n structured perovskite solar cell on NiO as hole-transport layer (ITO/NiO/Perovskite/PCBM/Al) and explained the degradation using migration and generation of ions. The device structure is given in figure 6.1. In this chapter I will explain the physics of photon-induced degradation and develop a complete mathematical model. Finally, I will propose a modified equivalent circuit model to explain this degradation mechanism.

6.2 Photon-induced Degradation

The conditions under which all the photon-induced degradations were performed are:

➢ Perovskite solar cells are kept at constant illumination under simulated solar spectrum of one-sun intensity [AM1.5].

➢ All degradations are done under open-circuit condition (except specified otherwise) as it is close to the maximum power point.

➢ All light IV measurements during exposure is measured from High Bias- Low Bias.

➢ The light IV measurement was started at about 15% higher than Open-circuit voltage

➢ Light IV measurements were done very fast to negate the effect of ionic motion

(About 100 mV/Second)
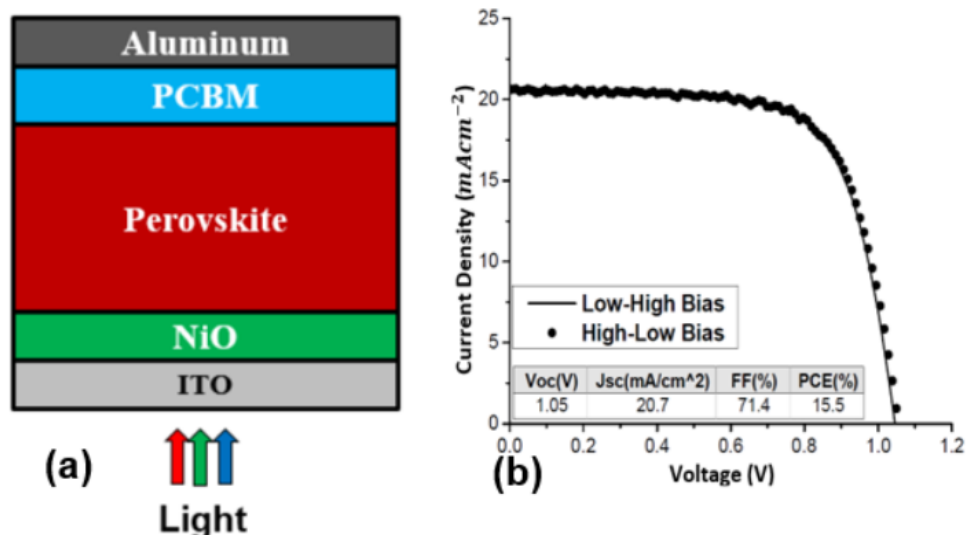
Figure 6.1: (a) Device structure and (b) Light IV characteristics of the solar cell used for photon-induced degradation study. The starting power-conversion efficiency is 15.5%

Figure 6.1 shows the device structure and starting light IV characteristics of the device that has been used in this photon-induced degradation study. The photon-induced degradation result has been reported in figure 6.2. Please note the increase in open circuit voltage and decrease in short-circuit current during this degradation.

6.2.1 Short-circuit current degradation

It is very well known that there are mobile ions present in bulk perovskite which can redistribute themselves in presence of electric field. At thermal equilibrium, the positive ions move towards the HTL and negative ions move towards to ETL due to internal electric field (figure 6.3). Because of high electric field present at the interfaces these ions do not contribute to recombination with photo-generated carriers. But during exposure in open-circuit condition as the internal electric field decreases the mobile ions can migrate towards bulk perovskite.

And in addition to that more ions are generated by high energy photons. The generated electron

hole pairs recombine with the ions to contribute to current loss.
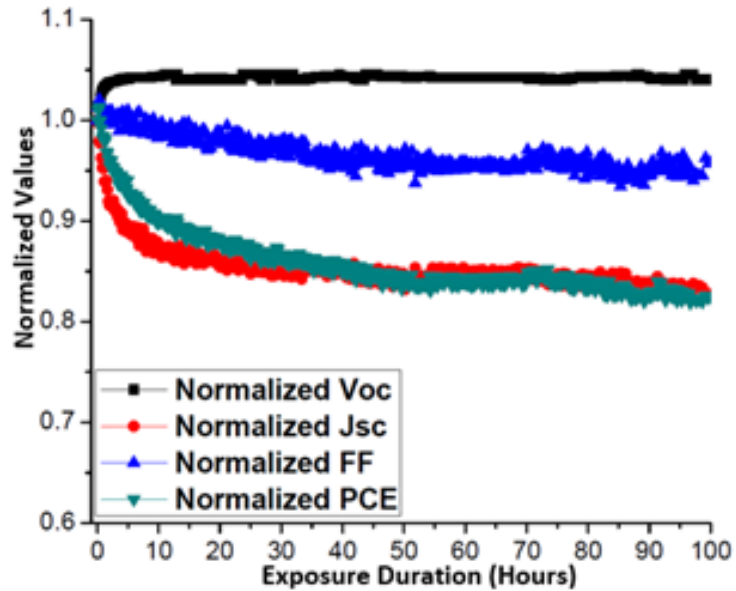
Figure. 6.2: Photon-induced degradation measured at one-sun intensity in open-circuit condition for 100 hours

$$MA^+ + electron \rightarrow MA$$
$$I^- + hole \rightarrow I$$
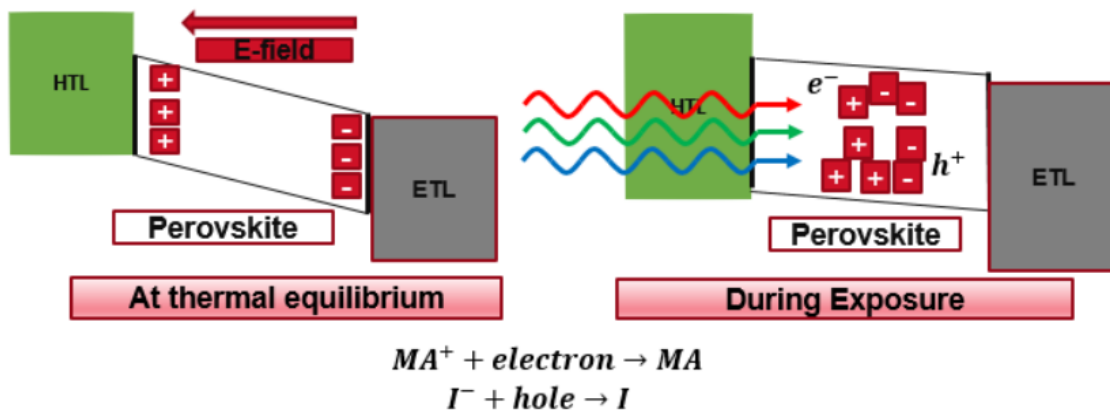
Figure 6.3: Band diagram explaining short-circuit current degradation due to generation and migration of ions in perovskite; At thermal equilibrium (left), during photo exposure in open circuit condition (right)

The degradations in short-circuit current density can be fitted with a double-exponential

equation as,

$$J_{sc}(t) = J_{sc,t=0} - \Delta J_{sc} \qquad (6.1)$$

$$\Delta J_{sc} = J_{sc,t=0} \left[a_m \left(1 - e^{-\frac{t}{t_{cm}}} \right) + a_g \left(1 - e^{-\frac{t}{t_{cg}}} \right) \right] \qquad (6.2)$$

With boundary conditions,

$$(i) \; a_m + a_g = \frac{\Delta J_{sc}}{J_{sc,t=0}} \Big|_{t\to\infty} \qquad (ii) \Delta J_{sc} = 0 \text{ at t=0} \qquad (6.3)$$

It is understandable why we need two exponentials to fit the short-circuit current degradation if we consider both migration and generation of ions contribute in this photon-induced degradation. We can consider the first exponential takes care of the migration of ions with a time constant of t_{cm} and a magnitude of a_m. And the second exponential models the generation of ions with a time constant of t_{cg} and a magnitude of a_g. For NiO the values which can describe the short-circuit current degradation are: $t_{cm} = 2 \; hours$, $a_m = 0.084 \; mAcm^{-2}$, $t_{cg} = 20 \; hours$, $a_g = 0.084 \; mAcm^{-2}$.

6.2.2 Open-circuit voltage evolution

Two understand the open circuit voltage evolution we need to consider two components which play a role in open circuit voltage evolution during light exposure:

➤ Increase in open circuit voltage due to migration of ions from contact layers to the bulk

➤ Decrease in open circuit voltage due to increase in non-radiative recombination

(i)   Increase in open circuit voltage due to migration of ions:
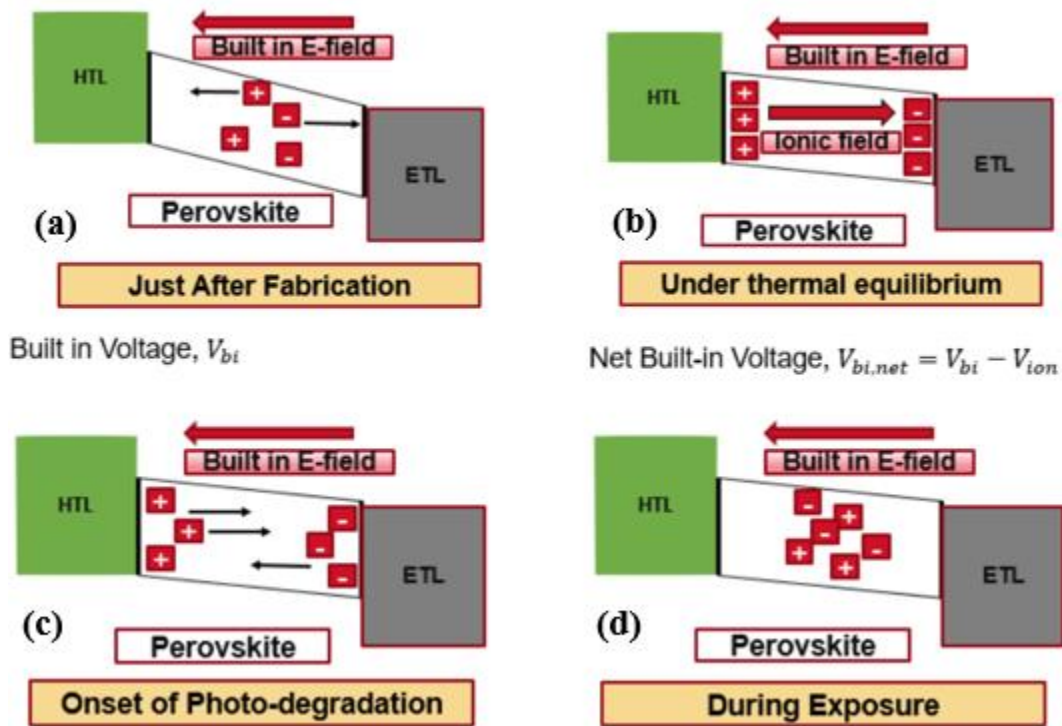
Figure 6.4: Band diagram explaining the first component of open-circuit voltage evolution, increase in Voc due to ion migration (a) Just after fabrication ions are starting to accumulate towards perovskite-contact layers' interfaces (b) band diagram under thermal equilibrium (c) At the onset of photo-degradation ions are starting to accumulate towards bulk perovskite (d) During exposure ions have migrated towards neutral bulk perovskite

At thermal equilibrium, ions near the contact layers create an electric field opposing the built-in electric field. Thus, reduces the net electric filed and reduces the open-circuit voltage [Figure 6.4(b)]. Here, the parameter V_d is defined as the difference in open circuit voltage if there are no ions at thermal equilibrium ($V_{oc,0}$) and the actual open circuit voltage measured at time t=0 ($V_{oc,t=0}$, before exposure). The V_d for NiO is 0.07V. At the onset of photo-degradation these ions start moving from the perovskite-contact layer interfaces towards the neutral bulk region and so, the open circuit voltage starts to increase towards the value if there were no ions present at thermal equilibrium with a time constant $t_{cm} = 2\ Hours$ which

is consistent with the time constant obtained from degradation in current [Figure 6.4 (c), (d)]. This is first component behind the change in open circuit voltage. So, the change in open-circuit voltage due to ion migration is given by,

$$\Delta V_{oc,i}(t) = V_d(1 - e^{-\frac{t}{t_{cm}}}) \tag{6.4}$$

$$V_d = V_{oc,0} - V_{oc,t=0} \tag{6.5}$$

Where, the open-circuit voltage if there is no ion present is given by [3],

$$V_{oc,0} = \frac{nkT}{q}\ln\left(\frac{J_L}{J_0} + 1\right) \tag{6.6}$$

$$J_0 = \frac{15q\sigma}{k\pi^4}T^2\int_{u}^{\infty}\frac{x^2}{e^x - 1}dx \,; u = \frac{E_G}{kT} \tag{6.7}$$

(ii)   Decrease in open circuit voltage due to increase in non-radiative recombination:
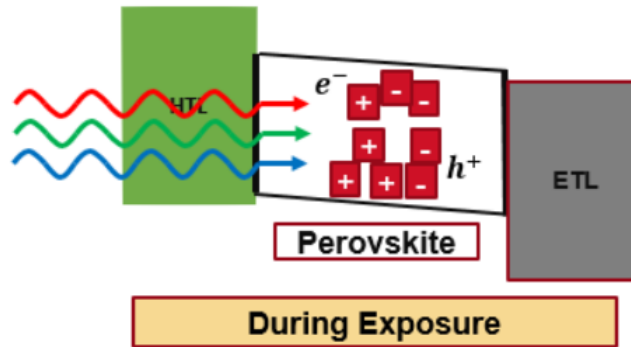
Figure 6.5: Band diagram explaining the second component of open-circuit voltage degradation, decrease in Voc due to increase in non-radiative recombination

As ions are generated during exposure, these ions recombine with the generated electron hole pairs and there is an increase in non-radiative recombination. Due to increase in recombination the lifetime of electrons and holes will decrease. Thus, the open circuit voltage

will decrease (Figure 6.5). The expression of open circuit voltage considering non-radiative recombination but no ion migration is given by [4],

$$V_{oc,r} = \frac{kT}{q}\ln\left(\frac{N_B J_{sc}\tau}{q n_i^2 W}\right)$$
(6.8)

Let's assume

- Lifetime of carriers and short circuit current at t=0 is $\tau_{t=0}$ and $J_{sc,t=0}$

- Lifetime of carriers and short circuit current at t=t is $\tau_{t=t}$ and $J_{sc,t=t}$

Assuming all other parameters are constant,

Open-circuit voltage at time t=0,

$$V_{oc,r,t=0} = \frac{kT}{q}\ln\left(\frac{N_B J_{sc,t=0}\tau_{t=0}}{q n_i^2 W}\right)$$
(6.9)

And open-circuit voltage at time t=t,

$$V_{oc,r,t=t} = \frac{kT}{q}\ln\left(\frac{N_B J_{sc,t=t}\tau_{t=t}}{q n_i^2 W}\right)$$
(6.10)

Decrease in V_{oc} due to non-radiative recombination,

$$\Delta V_{oc,r}(t) = V_{oc,r,t=0} - V_{oc,r,t=t} = \frac{kT}{q}\ln\left(\frac{J_{sc,t=0}\tau_{t=0}}{J_{sc,t=t}\tau_{t=t}}\right)$$
(6.11)

The short circuit current density is given by,

$$J_{sc} = qG(L_n + L_p)$$
(6.12)

Where, L_n and L_p are diffusion lengths of electrons and holes respectively.

Assuming $L_n = L_p = L$, $J_{sc} = 2qGL = 2qG\sqrt{D\tau}$
(6.13)

Here, τ is equivalent carrier lifetime and D is equivalent carrier diffusion coefficient.

The short circuit current density at time t=0,

$$J_{sc,t=0} = 2qG\sqrt{D\tau_{t=0}} \tag{6.14}$$

The short circuit current density at time t=t,

$$J_{sc,t=t} = 2qG\sqrt{D\tau_{t=t}} \tag{6.15}$$

The expression of ration between current densities between time t=0 to t=t becomes,

$$\frac{J_{sc,t=0}}{J_{sc,t=t}} = \sqrt{\frac{\tau_{t=0}}{\tau_{t=t}}} \tag{6.16}$$

$$\frac{\tau_{t=0}}{\tau_{t=t}} = \left(\frac{J_{sc,t=0}}{J_{sc,t=t}}\right)^2 \tag{6.17}$$

Substituting the expression of ratio between lifetimes in the equation of change in open circuit voltage,

$$\Delta V_{oc,r}(t) = V_{oc,r,t=0} - V_{oc,r,t=t} = 3\frac{kT}{q}\ln(\frac{J_{sc,t=0}}{J_{sc,t=t}}) \tag{6.18}$$

Total Change in V_{oc} at time t=t,

$$\Delta V_{oc}(t) = V_{oc,t=t} - V_{oc,t=0} = \Delta V_{oc,i} - \Delta V_{oc,r} \tag{6.19}$$

$$\Delta V_{oc}(t) = V_d(1 - e^{-\frac{t}{t_{cm}}}) - 3\frac{kT}{q}\ln(\frac{J_{sc,t=0}}{J_{sc,t=t}}) \tag{6.20}$$
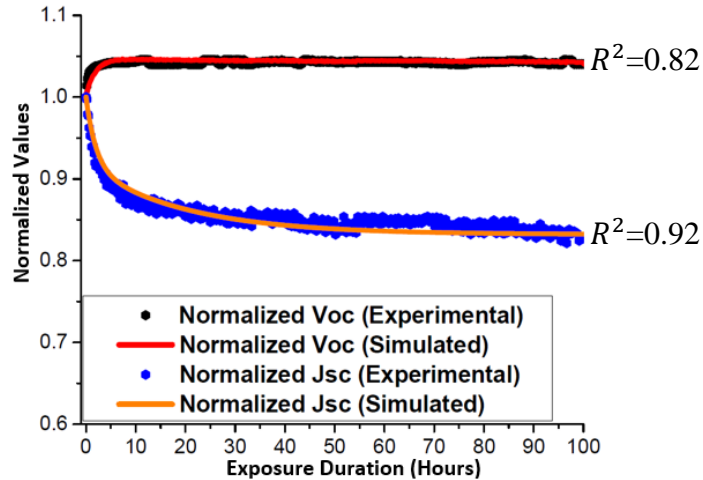
Figure 6.6: Comparison of normalized open-circuit voltage evolution and short-circuit current degradation between experimental and simulated result obtained from our model.

Figure 6.6 shows the comparison between experimental and simulated results over 100 hours of photon-induced degradation for normalized open-circuit voltage and short-circuit current. This result shows that the experimental result matches very well with the simulation result.

6.3 Proposed Circuit Model for Perovskite Solar Cells
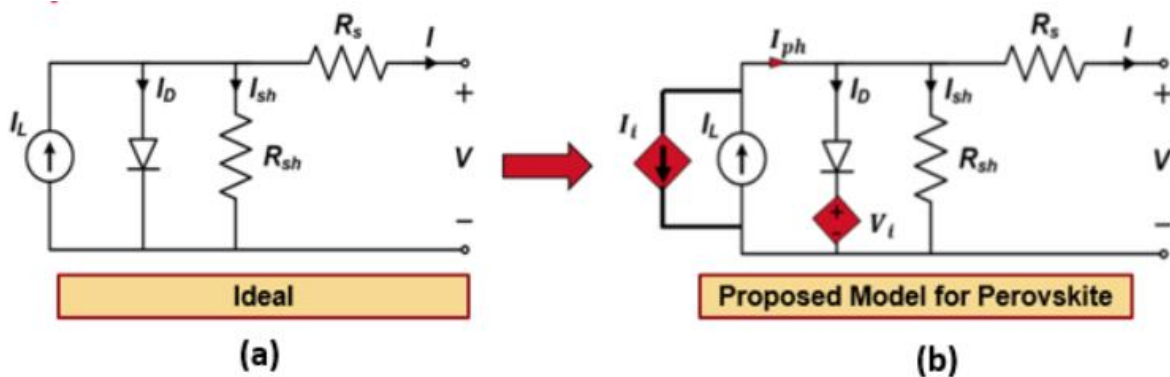
Figure 6.7: Modified equivalent circuit model of a perovskite solar cell (a) Ideal single diode mode (b) Proposed circuit model for perovskite solar cell considering both migration and generation of ions

Figure 6.7 (b) shows our proposed single diode circuit model for perovskite solar cells. Here, the modifications proposed is to add an additional dependent voltage source in series with the diode and dependent current source in parallel to the photo-generated current source from an ideal circuit model [Figure 6.7 (a)]. The magnitude of the dependent voltage source depends on amount of open-circuit voltage increase due to ion migration and amount of decrease in open-circuit voltage due to increase in non-radiative recombination. And the polarity can be either positive or negative depending on which of the two components is dominant. If ion migration dominates $V_i(t) > 0$, on the other hand if non-radiative recombination dominates over ion migration $V_i(t) < 0$. This can be explained by the following mathematical expressions:

$$V_i(t) = V_d \left(1 - e^{-\frac{t}{t_{cm}}}\right) - 3\frac{kT}{q} ln\left(\frac{J_{sc,t=0}}{J_{sc,t=t}}\right) \tag{6.21}$$

As the degradation in current follows the double exponential model as described earlier in this chapter, the dependent current source has the following expression,

$$I_i(t) = I_{sc,t=0} \left[a_m \left(1 - e^{-\frac{t}{t_{cm}}}\right) + a_g \left(1 - e^{-\frac{t}{t_{cg}}}\right)\right] \tag{6.22}$$

The total current extracted from the solar cell is given by,

$$I = I_L - I_i - I_0 \left[exp\left(\frac{q(V - V_i)}{nkT}\right) - 1\right] - \frac{V + IR_s}{R_{sh}} \tag{6.23}$$

Figure 6.8 shows the simulated light IV using the equivalent circuit diagram in Fig. 3 before and after degradation along with the experimental results obtained on the p-i-n solar cell. The mismatch in light IV after degradation between actual and simulated result comes

from the degradation in series and shunt resistance which we ignored in our equivalent circuit model.
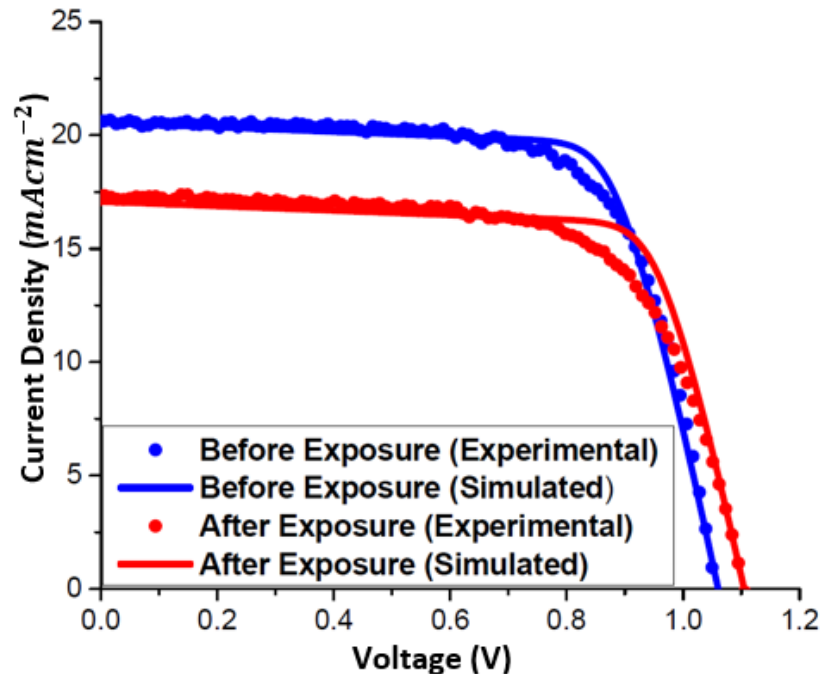
Figure 6.8: Comparison of Light IV curves simulated using the equivalent circuit model [Figure 6.7(b)] before and after degradation for 100 hours at one-sun intensity with the experimental Light IV curves

Finally, both generation and migration of ions contribute to the photon-induced degradation of perovskite solar cells. The degradation in short-circuit current density can be modeled using a double-exponential model which explains both migration and generation of ions. The change in open-circuit voltage can be explained by two opposing components: open-circuit voltage increases due to migration from ions from perovskite-transport layers' interfaces towards bulk perovskite and decreases with increase in non-radiative recombination. These factors can be considered with a dependent current source in parallel with the photo-generated current source and a dependent voltage source in series with the diode to have complete equivalent circuit for perovskite solar cells.

REFERENCES

1   Pranav H. Joshi, Liang Zhang, Istiaque M. Hossain, Hisham A. Abbas, Ranjith Kottokkaran, Satyapal P. Nehra, Mahendra Dhaka, Max Noack, and Vikram L. Dalal, AIP Advances 6, 115114 (2016)

2   Pranav Joshi, Liang Zhang, Ranjith Kottokkaran, Hisham Abbas, Istiaque Hossain, Satyapal Nehra, Mahendra Dhaka, Max Noack, Vikram Dalal, Photovoltaic Specialists Conference (PVSC), 2016 IEEE 43rd, pages 0242-0248

3   PV Education
         Link: http://www.pveducation.org

4   Ronald A. Sinton, " Contactless determination of current–voltage characteristics and minority-carrier lifetimes in semiconductors from quasi-steady-state photoconductance data," in Applied Physics Letters, 69, 2510 (1996)

CHAPTER 7.   FACTORS THAT AFFECT PHOTON-INDUCED DEGRADATION OF PEROVSKITE SOLAR CELLS

7.1 Introduction

There are several factors that affect this photo-instability and recovery

- ➢ The contact layers

- ➢ Stoichiometry (Ratio between $MAI:PbI_2$)

- ➢ The biasing condition at which the device is kept during degradation

- ➢ The fabrication procedure (Solution vs Vapor)

- ➢ Grain size of perovskite (active layer)

7.2 Comparison Between Different Hole Transport Layers (NiO vs PTAA)
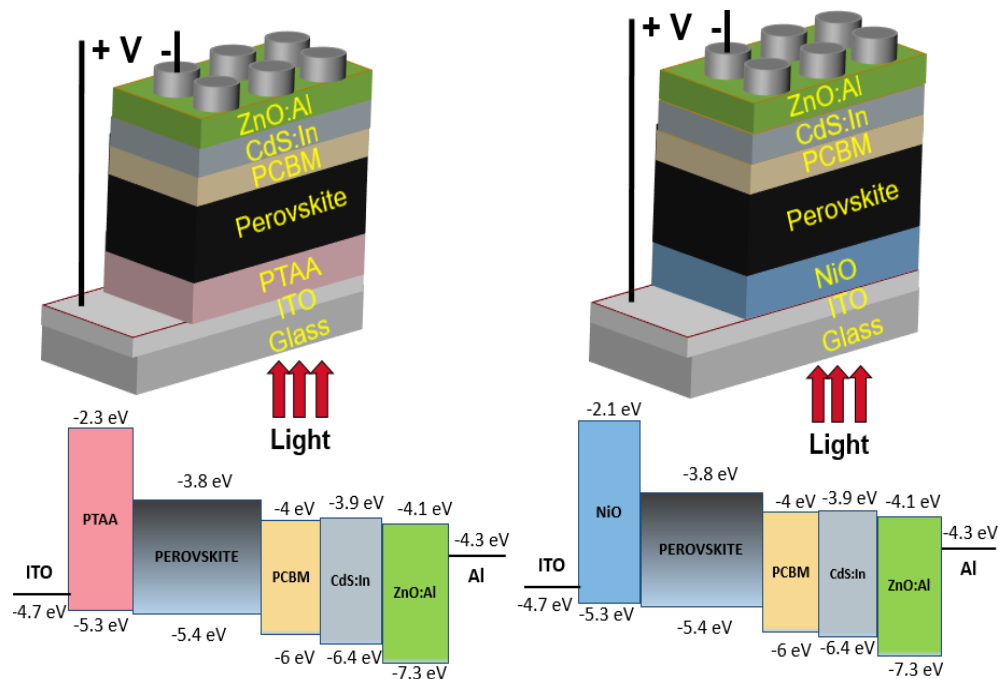
Figure 7.1: Device structure and corresponding band edges; PTAA as hole transport layer (left), NiO as hole transport layer (right)
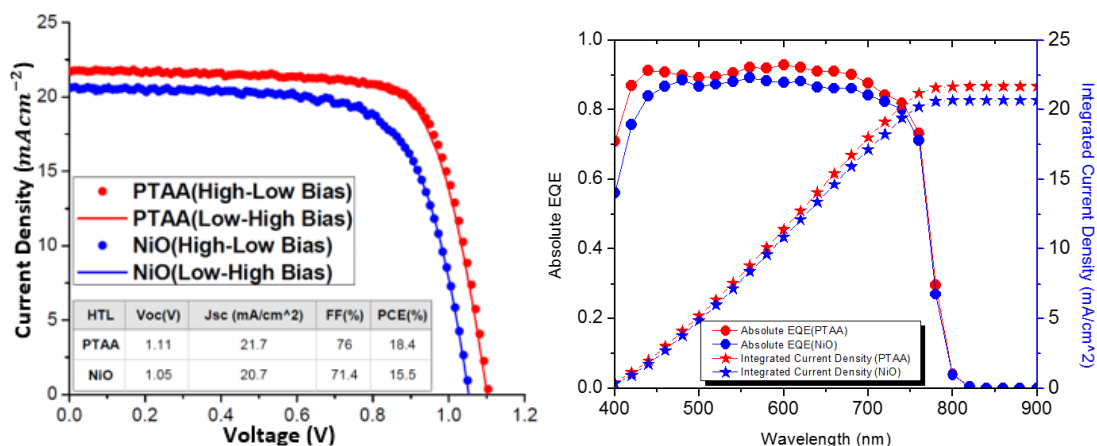
Figure 7.2: Photovoltaic parameters before photon-induced degradation; Light IV characteristics (left), External quantum efficiency and integrated short-circuit current density as a function of incident photon wavelength (right); Red line represents PTAA as HTL and Blue line represents NiO as HTL

Figure 7.1 shows the device structure and corresponding band edges of two devices which have been used for this comparison study. The fabrication method described in chapter 5 has been followed to fabricate these devices. Two additional layers (CdS and ZnO) as electron transport layers have been used as buffer layers. The reason behind using these buffer layers have been discussed in section 7.3.

Table 7.1: Photovoltaic parameters for perovskite solar cells on different HTL

HTL	$V_{oc}(V)$	$J_{sc}(mA/cm^2)$	*FF(%)*	*PCE (%)*
NiO	1.05	20.7	71	15.5
PTAA	1.11	21.7	76	18.4

Figure 7.2 shows the light IV characteristics along with external quantum efficiency and integrated current density of those two devices. The photovoltaic parameters before photon-induced degradation has been given in table 7.1. The photo conversion efficiency of the device fabricated on PTAA as hole transport layer is about 18.4% and on NiO as hole transport layer is about 15.3% before photon induced degradation. None of the devices showed

any hysteresis in light IV measurement. PTAA has higher transmission [Figure 7.3(b)]. Thus, device fabricated on PTAA shows higher short-circuit current density than NiO. The SEM images in figure 7.3(a) which shows the topography of perovskite films fabricated on NiO and PTAA, suggests that there is no significant difference in grain size which can also play a role in photon induced degradation. Both have perovskite grain sizes in the range of about 200-400 nm.
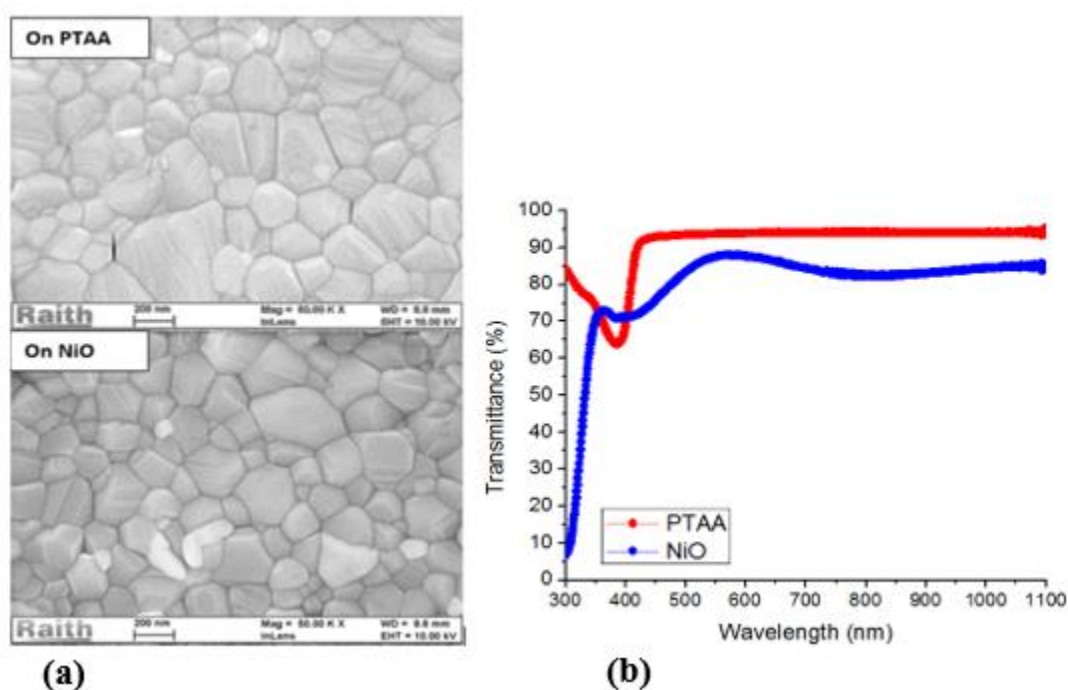
Figure 7.3: (a) SEM images shows the topography of perovskite films deposited on PTAA and NiO (b) Comparison in transmittance at different wavelengths between PTAA and NiO

Then we measured photon-induced degradation on these two types of p-i-n devices in open circuit condition up to 100 hours under one-sun illumination with AM1.5 spectra for comparative study [figure 7.4]. The key features from this photon-induced degradation are:

➢ The open-circuit voltage for the solar cell on PTAA decreases with time under continuous illumination, while the open-circuit voltage increases for the cell fabricated on NiO.

➢ The short-circuit current degrades more for the cell fabricated on PTAA compared to the cell fabricated on NiO.

➢ Thus, the power conversion efficiency degradation for the cell with PTAA as hole transport layer is much higher than power conversion efficiency degradation with NiO.
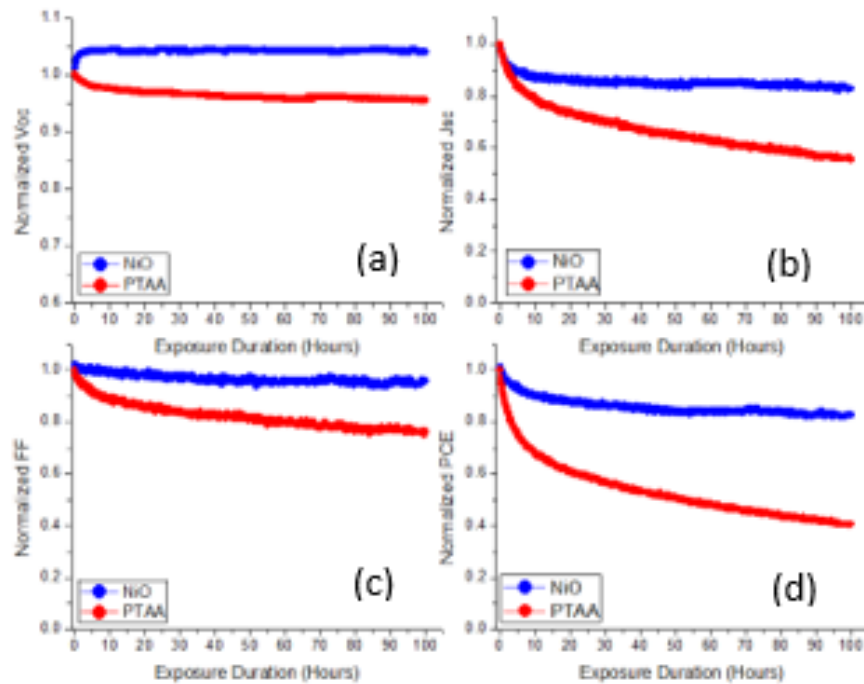
Figure 7.4: Photon-induced degradation comparison of these two p-i-n devices under one-sun intensity (AM1.5) for 100 hours (a) Normalized open-circuit voltage degradation (b) Normalized short-circuit current degradation (c) Fill-factor degradation (d) Degradation in power conversion efficiency

But, encouraging sign is that both devices, either on PTAA or NiO as hole transport layer has recovered in dark. The solar cell fabricated on PTAA has completely recovered in 43 hours at room temperature after light exposure for 100 hours at one sun intensity. And the device fabricated on NiO completely recovered after it was kept in dark for 13 hours at room

temperature. The light IV characteristics of these devices before exposure, after exposure and after recovery has been showed in figure 7.5.
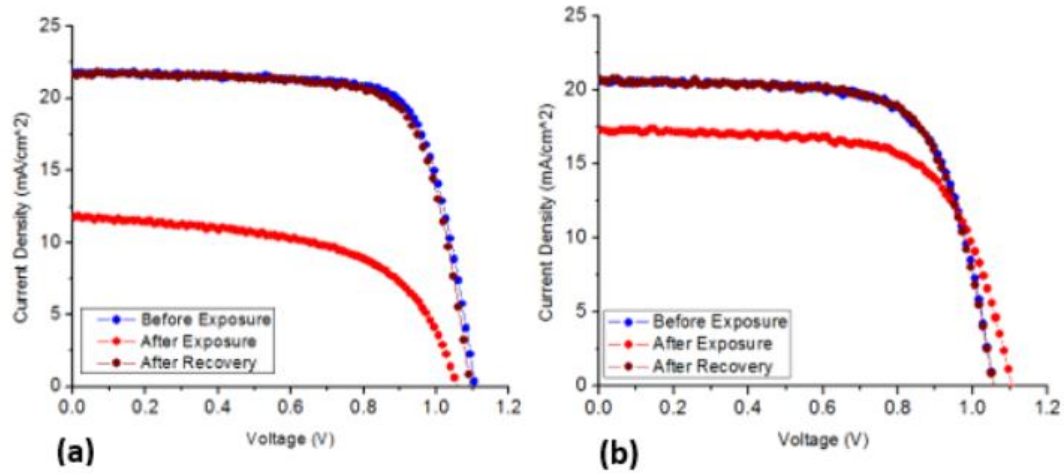
Figure 7.5: Light IV degradation and recovery in dark (a) fabricated on PTAA as HTL (b) fabricated on NiO as HTL

The photo-degradation can be explained by using the ion generation and migration theory during photo-exposure as explained in chapter 6. The change in open-circuit voltage can be explained by two components: increase in open-circuit voltage due to migration of ions from interfaces to bulk perovskite and decrease in open-circuit voltage due to increase in non-radiative recombination. The change in open-circuit is given by,

$$\Delta V_{oc}(t) = V_d(1 - e^{-\frac{t}{t_{cm}}}) - 3\frac{kT}{q}\ln(\frac{J_{sc,t=0}}{J_{sc,t=t}})\qquad(7.1)$$

The V_d for the device fabricated on NiO is 0.07 V and for the device fabricated on PTAA is 0.01 V. The time constant for the migration of ions from interfaces to the bulk perovskite is 2 hours. The open-circuit voltage for the device fabricated on NiO increases over time during photon-induced degradation as migration of ions dominates the generation of ions. But for the device with PTAA as HTL, the open-circuit voltage decreases because the generation of ions dominates the migration of ions during photon-induced degradation.

Also, the short-circuit current degradation follows the double exponential model as showed in chapter 6. The degradation in short-circuit current is given by,

$$\Delta J_{sc} = J_{sc,t=0} \left[a_m \left(1 - e^{-\frac{t}{t_{cm}}} \right) + a_g \left(1 - e^{-\frac{t}{t_{cg}}} \right) \right] \qquad (7.2)$$

For NiO the values which can describe the short-circuit current degradation are: $t_{cm}= 2$ hours, $a_m= 0.084\ mAcm^{-2}$, $t_{cg}=20$ hours, $a_g=0.084\ mAcm^{-2}$. For PTAA the values which can describe the short-circuit current degradation are: $t_{cm}= 2$ hours, $a_m= 0.15\ mAcm^{-2}$, $t_{cg}= 42$ hours, $a_g= 0.3\ mAcm^{-2}$. The change in higher degradation in short-circuit current for the device fabricated on PTAA than fabricated on NiO can be explained by higher transmission of PTAA than NiO, especially in the high energy regime. This allows to generate more ions during photon-induced degradation.
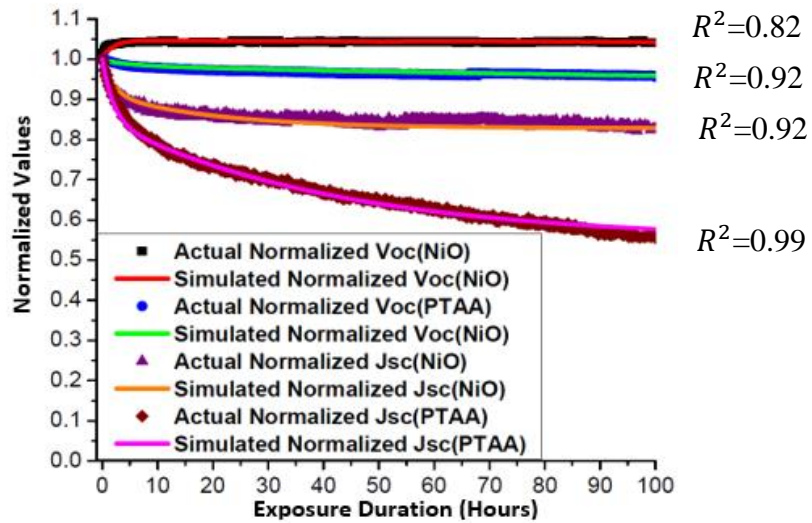
Figure 7.6: Comparison of normalized change in open-circuit voltage and short-circuit current degradation between experimental and simulated result obtained from our model

Figure 7.6 shows the comparison between experimental and simulated results over 100 hours of photon-induced degradation for normalized open-circuit voltage and short-circuit current. Figure 7.7 shows the simulated light IV using the equivalent circuit diagram in Figure

6.7 before and after degradation along with the experimental results obtained on the p-i-n solar cell. The mismatch in light IV after degradation between actual and simulated result comes from the degradation in series and shunt resistance which we ignored in our equivalent circuit model.
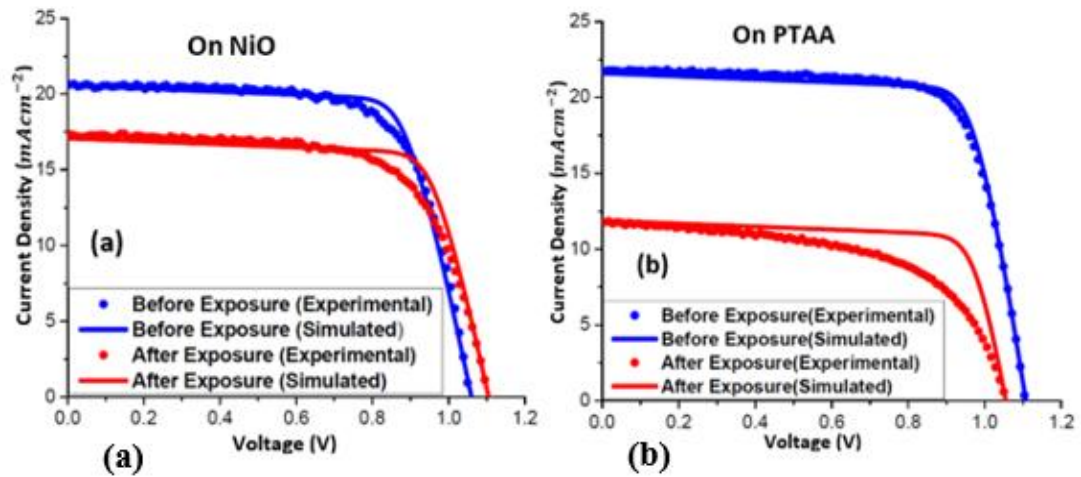
Figure 7.7 Comparison of Light IV curves simulated using the equivalent circuit model (Figure 6.7) before and after degradation for 100 hours at one-sun intensity with the experimental Light IV curves (a) on NiO (b) on PTAA

Some very interesting results can be deduced from the External Quantum Efficiency(EQE) degradation during exposure at 1X intensity and recovery in dark afterwards. The External quantum efficiency comparison for both device structures suggest that there is almost uniform drop down of quantum efficiency compared to the QE before exposure over the visible wavelength range. This result suggests that during degradation the reason behind decrease in short-circuit current is decrease in carrier life-time with increase in Ion density. So, this is an indirect proof that the generated carriers can recombine with generated ions considering there is no significant change in absorption during light exposure.
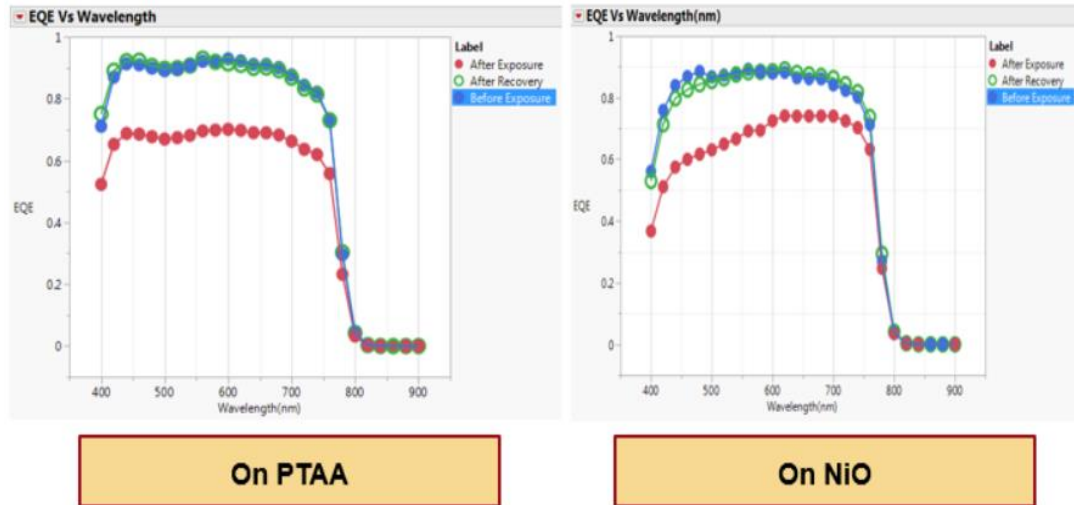
Figure 7.8: External Quantum Efficiency recovery after photon-induced degradation for 100 hours at one-sun (AM1.5) intensity; Fabricated on PTAA (left) and Fabricated on NiO (right)

Now, if we define a parameter QE ratio for a given wavelength and is calculated as,

$$QE\ ratio\ (\lambda) = \frac{EQE\ After\ Exposure\ (\lambda)}{EQE\ Before\ Exposure\ (\lambda)} \tag{7.3}$$
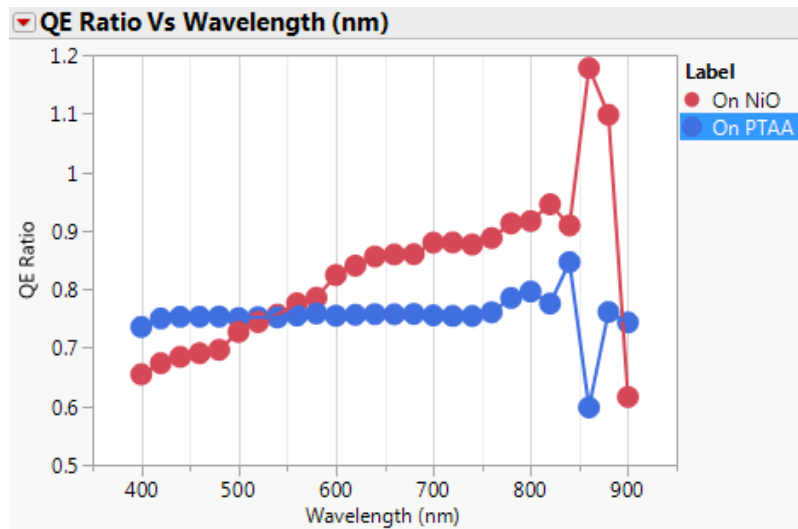
Figure 7.9: QE Ratio as a function of incident photon wavelength (nm)

There is significant difference in evolution of QE ratio with wavelength for devices with PTAA and NiO (Figure 7.9). The results above 800nm is very noisy as it is expected to have a very low absorption. It is expected that most of the higher energy photons are absorbed

very close to the hole transport layer as the absorption coefficient is higher for higher energy photons. The QE ratio is almost flat with wavelength for device fabricated on PTAA which suggests that ion density distribution is almost uniform over the thickness of perovskite. But, there is a gradual increase in QE ratio with wavelength for the device fabricated on NiO. This result suggests that collection efficiency is lower at NiO-Perovskite interface and higher at Perovskite-PCBM interface. This is possible if there is a gradient in ion density with perovskite thickness. In other words, the density of generated ions gradually decreases from NiO to PCBM over perovskite thickness. Thus, there is more recombination of generated carriers near NiO-Perovskite interface than Perovskite-PCBM interface.

Figure 7.10: Capacitance vs Voltage profile recovery after photon-induced degradation for 100 hours at one-sun (AM1.5) intensity; Fabricated on PTAA (left), Fabricated on NiO (right)

There seems to be no significant difference in Capacitance Vs Voltage response on both device structures. The capacitance vs voltage response shifts to the right after light exposure for 100 hours at 1X intensity. The shift to the right indicates the migration of ions from the interfaces towards the bulk perovskite as explained by Pranav et al. [1,2,3]. Then it slowly recovers in dark. And the device fabricated on NiO completely recovered after it was kept in dark for 13 hours at room temperature.

7.3 CdS/ZnO as Buffer Electron Transport Layers
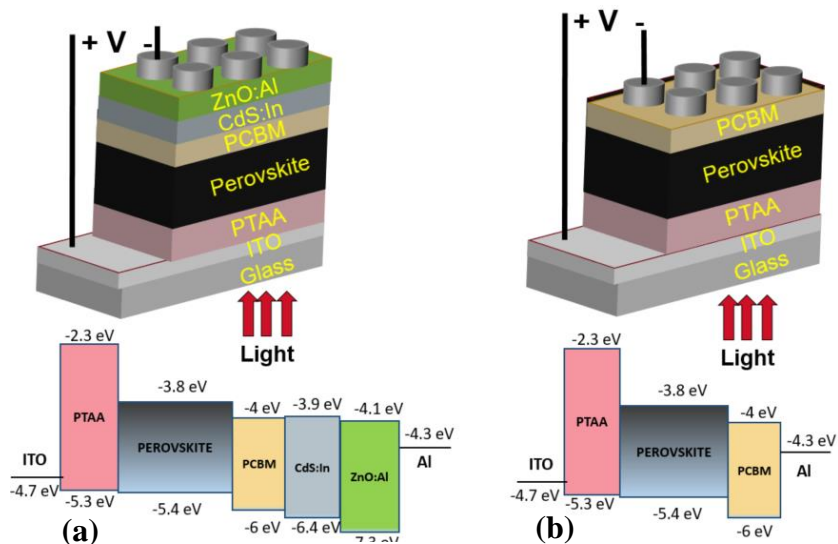
Figure 7.11: Device structures with corresponding band edges used in this experiment (a) With CdS/ZnO as buffer layers (b) With no buffer layers

Figure 7.11 shows the device structure and corresponding band edges which are being compared for this photo-degradation study. One of them [Figure 7.11(a)] has two extra layers Indium doped Cadmium Sulfide and Aluminum doped Zinc Oxide which work as buffer layers. The other device [Figure 7.11(b)] doesn't have these two extra layers. Both the devices showed above have similar efficiencies to start with. The device with CdS/ZnO as buffer layer has a starting power conversion efficiency of 18.4% and the control device had power conversion efficiency of about 17.8%. To make sure that all the changes are due to photon-induced degradation we have a reference contact with similar efficiency which doesn't show any degradation over time in dark. The photovoltaic parameters of these three devices before any degradation has been reported in Table 7.2. None of the devices showed any hysteresis in light IV measurements. Figure 7.12 shows the initial light IV measurement before photon-induced degradation and absolute external quantum efficiency measurements of these devices.
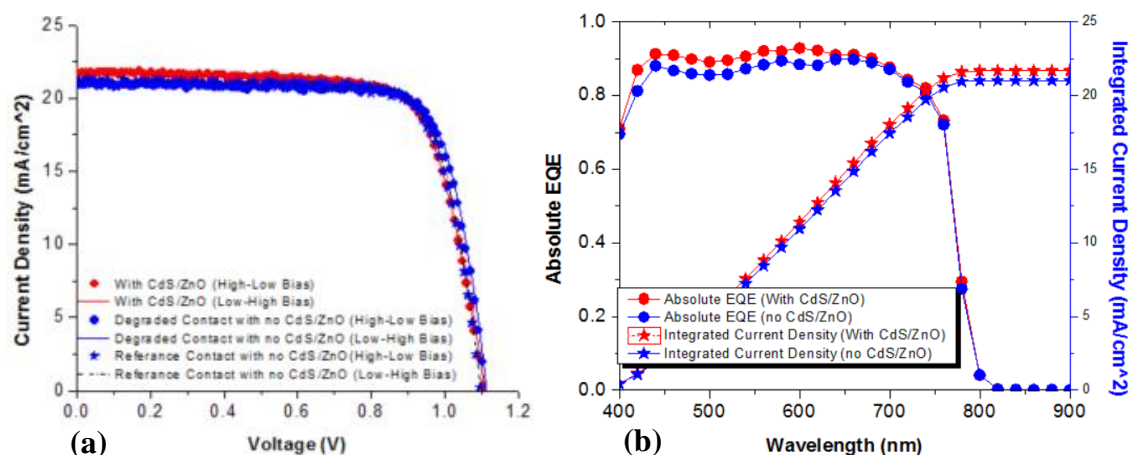
Figure 7.12: (a) Light IV measurements before photon-induced degradation (b) Absolute external quantum efficiency and integrated current density for both devices before photon-induced degradation; Red represents Light IV for device with CdS/ZnO as buffer layers, Blue represents Light IV for device with no buffer layers

Table 7.2: Photovoltaic parameters for perovskite solar cells before photon induced degradation

Device Structure	$V_{oc}(V)$	$J_{sc}(mA/cm^2)$	FF(%)	PCE (%)
With CdS/ZnO as buffer layers	1.11	21.7	76	18.4
No buffer layers-Degraded contact	1.11	21.3	75	17.8
No buffer layers-Reference contact	1.11	21	76	17.7

The photo-degradation comparison for these two devices has been measured at open-circuit condition for 100 hours at one-sun intensity (AM1.5). Figure 7.13 shows that both degraded almost similarly over 100 hours. Table 2 shows that degradation of all the photovoltaic parameters are comparable after 100 hours of photon-induced degradation.
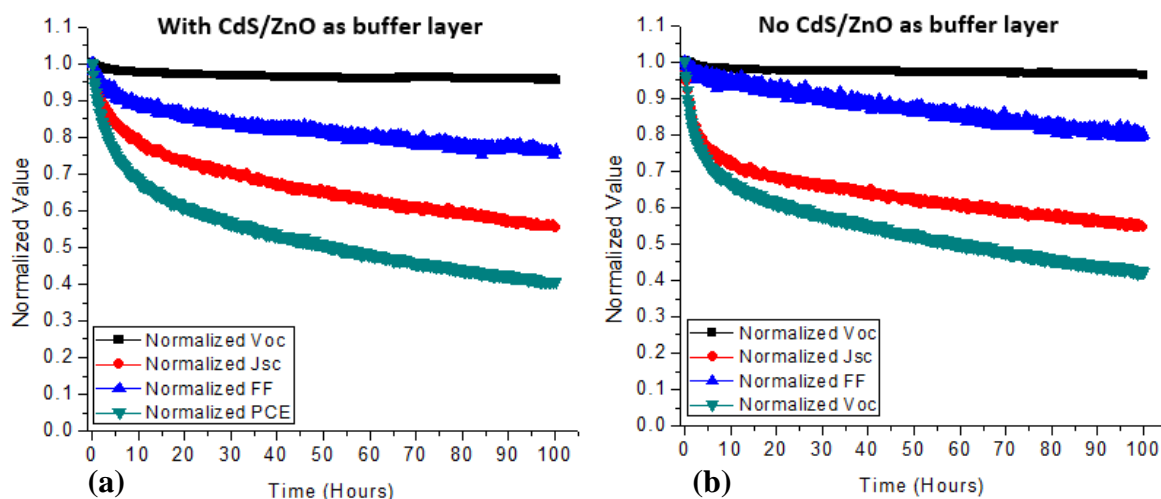
Figure 7.13: Photo-degradation summary for 100 hours at one-sun intensity (AM1.5) (a) Device with CdS/ZnO as buffer layer (b) Device with no buffer layers

Table 7.3: Photon-induced degradation (in percentage) of photovoltaic parameters after exposing for 100 hours at 1 sun intensity in open-circuit condition

Device Structure	$V_{oc}(V)$	$J_{sc}(mA/cm^2)$	FF(%)	PCE (%)
With CdS/ZnO as buffer layers	4%	45%	24%	58%
No buffer layers-Reference contact	4%	45%	20%	57%

*Note: All the parameters decrease with time during photon induced degradation

The interesting factor is that the device which had CdS and ZnO as buffer layers has completely recovered after kept in dark for 43 hours [Figure 7.14(a)]. But the device which didn't have CdS and ZnO as buffer layers didn't recover even after 43 hours in dark [Figure 7.14(b)].
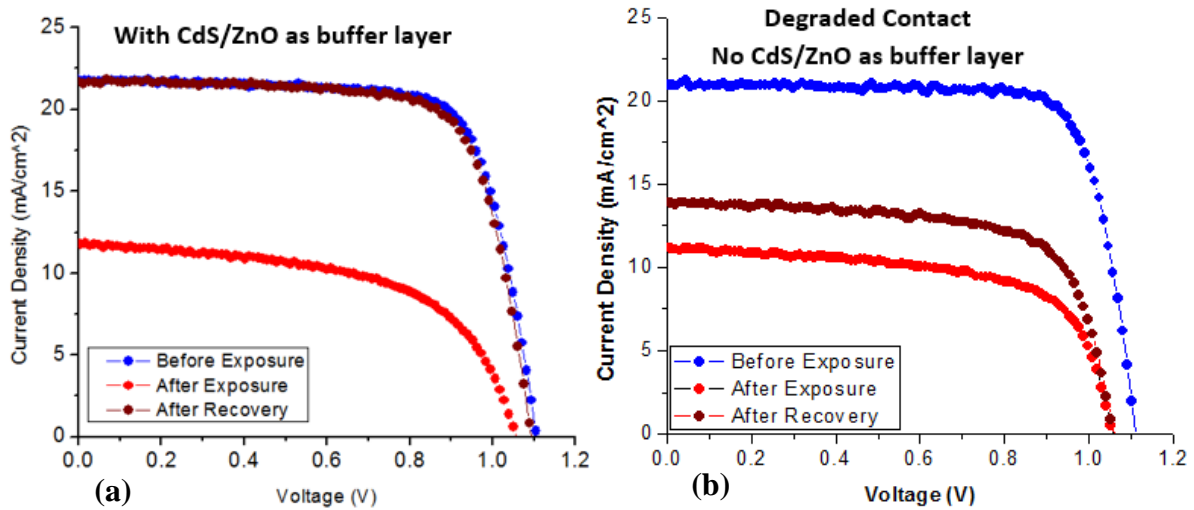
Figure 7.14: Light IV recovery in dark after photon-induced degradation for 100 hours at one-sun intensity (AM1.5) (a) Device with CdS/ZnO as buffer layers (b) Device with no buffer layers

But the reference device in Figure 7.15 shows no change during this period which proves that all these changes are due to photon-induced degradation only. The photovoltaic parameters of these devices before degradation, after degradation and after recovery in dark have been reported in Table 7.4.
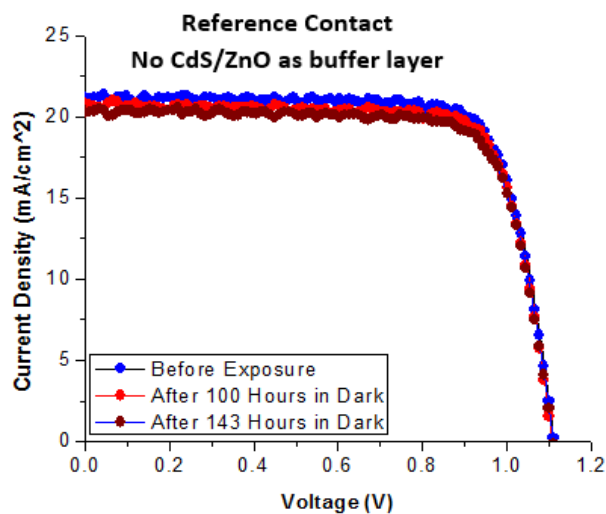
Figure 7.15: Light IV characteristics of the reference device which shows no change during this period

Table 7.4: Photovoltaic parameters comparison for perovskite solar cells before and after degradation along with after recovery

Device Structure		$V_{oc}(V)$	$J_{sc}(mA/cm^2)$	FF(%)	PCE (%)
With CdS/ZnO as buffer layers	Before Degradation	1.11	21.7	76	18.3
	After Degradation	1.06	12.1	59	7.6
	After Recovery	1.10	21.7	75	17.9
No buffer layers- Degraded contact	Before Degradation	1.11	21.3	75	17.8
	After Degradation	1.07	11.7	61	7.6
	After Recovery	1.07	14	69	10.3
No buffer layers- Reference contact	Before Degradation	1.11	21	76	17.7
	After Degradation	1.11	20.8	76	17.6
	After Recovery	1.11	20.5	77	17.5

These photo-degradation and recovery results can be explained by the simplified band-diagrams showed in Figure 7.16 and using the explanation by Lee et al. that iodine ions can contaminate the metal contacts leading to a permanent degradation for these devices [4]. This figure explains the recovery in dark after photo-degradation for devices with and without CdS/ZnO as blocking layers. At thermal equilibrium, due to built-in E-filed positive ions go towards hole transport layer (HTL) and negative ions go towards electron transport layer (ETL) [Figure 7.16 (a) and (d)]. So, we have net electric field inside the active layer. Due to high electric field at the interfaces these ions do not recombine with generated electron-hole pairs. During exposure in open-circuit condition, due to decrease in internal E-field these ions migrate towards the intrinsic active layer. And in addition to that more ions are generated by high energy photons [Figure 7.16 (d) and (e)]. The generated electron hole pairs recombine with the ions to contribute to current loss.
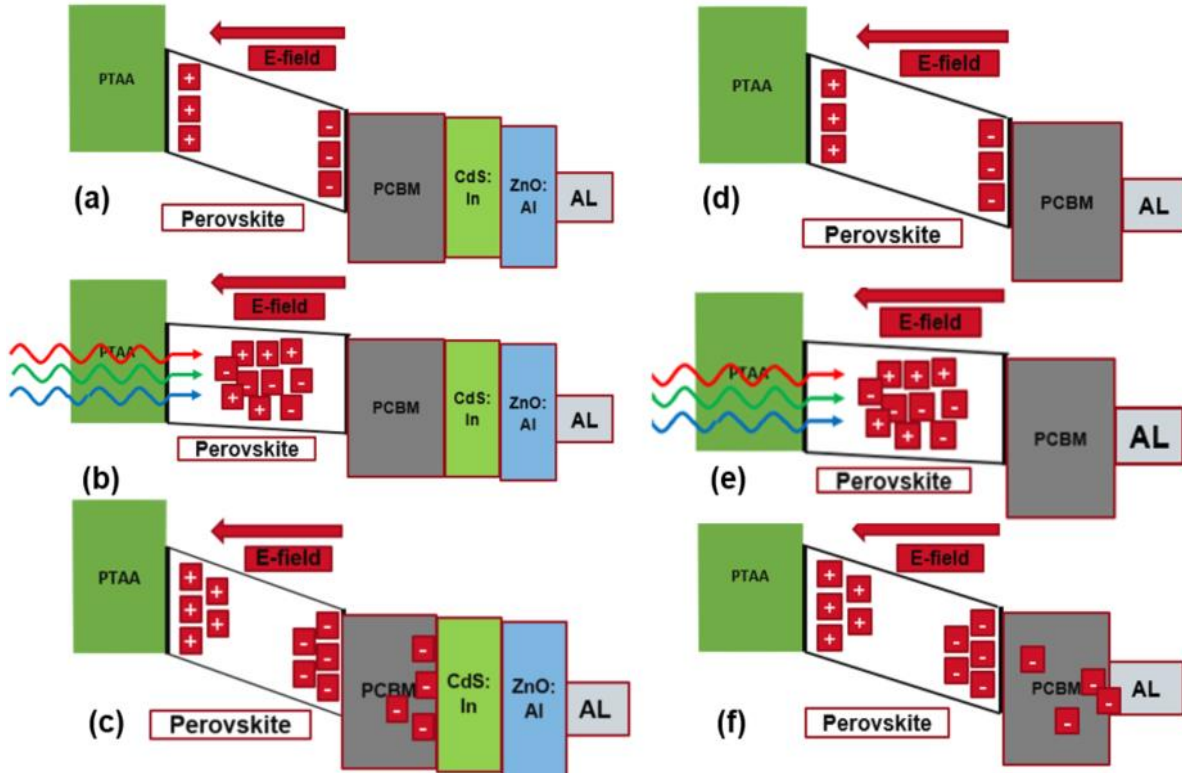
Figure 7.16: Band diagrams to explain recovery in dark after photo-degradation (a),(b),(c) migration and generation of ions during photo-degradation followed by recovery in dark where CdS/ZnO as blocking layer which helps the device to recover completely even after photo-degradation for 100 hours at one-sun intensity (d),(e),(f) migration and generation of ions during photo-degradation followed by recovery in dark where there is no CdS/ZnO buffer layer. During recovery, the Aluminum contact is contaminated by iodine ions as they migrate through PCBM layer. Thus, the device doesn't recover after photo-degradation for 100 hours at one-sun intensity

Just after exposure [Figure 7.16 (c) and (f)] there are more mobile ions present inside bulk perovskite. During recovery, there is sudden increase in electric field from the ETL to HTL inside bulk perovskite. And as the activation energy of migration for iodine ions is lowest [5] and so, they are very easy to migrate. During recovery, suddenly the negative ions' concentration at Perovskite-PCBM interface increases. These ions have high enough energy to punch through PCBM and react with Aluminum [Figure 7.16 (f)]. As these iodine ions contaminate Aluminum contact permanently, the series resistance and short circuit current don't recover. But in case of the device with CdS and ZnO, these iodine ions are blocked by

these buffer layers [Figure 7.16 (c)]. Consequently, this device completely recovers as the Aluminum contact doesn't get contaminated by iodine ions.
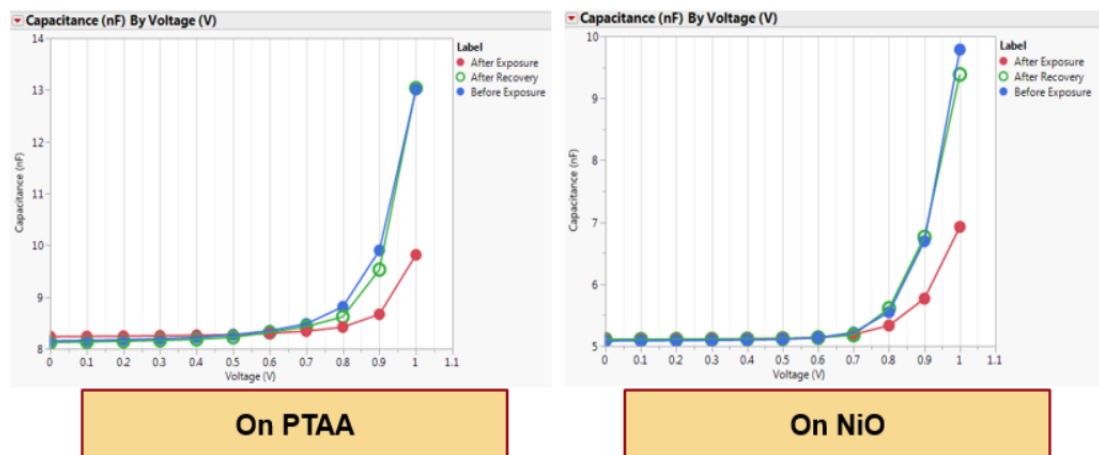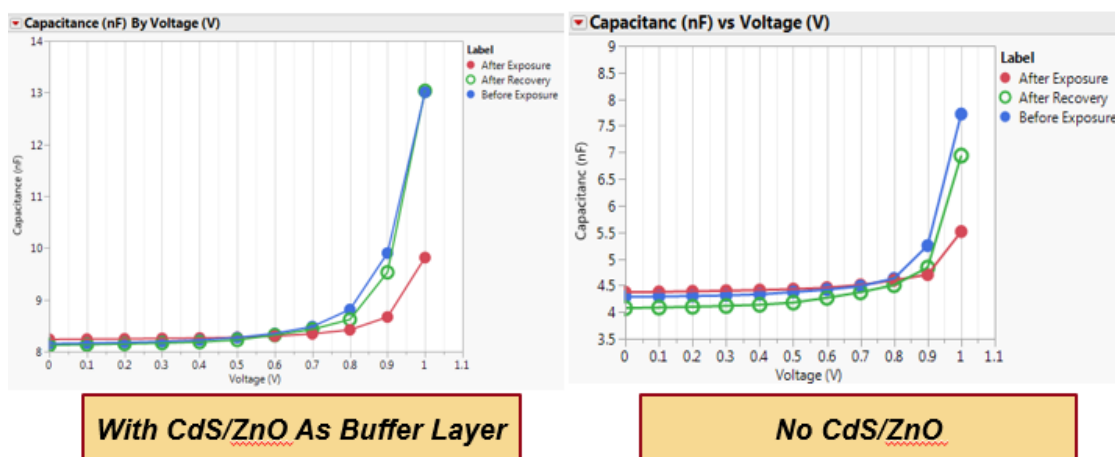

Figure 7.17: Capacitance vs Voltage profile recovery after photon-induced degradation for 100 hours at one-sun (AM1.5) intensity; With CdS/ZnO as blocking layers (left), With no CdS/ZnO (right)

The CV profile looks similar before and after exposure but, it completely recovered for the device with CdS/ZnO as buffer layer and didn't recover for the device with no CdS/ZnO. So, CdS/ZnO act as a buffer layer which helps the perovskite solar cells to recover after photon-induced degradation as these layers block the mobile iodine ions to react with the Aluminum contact.

7.4 Effect of Stoichiometry on Photon-induced Degradation

For this study, solar cells were fabricated with different molar ratio between PbI_2 to CH_3NH_3I in the precursor perovskite solution for photon-induced degradation study. The device structure and power conversion efficiencies of perovskite solar cells with different molar ratio (1, 1.025, 1.05, 1.075 & 1.10) have been reported in figure 7.18 and Table 7.5.
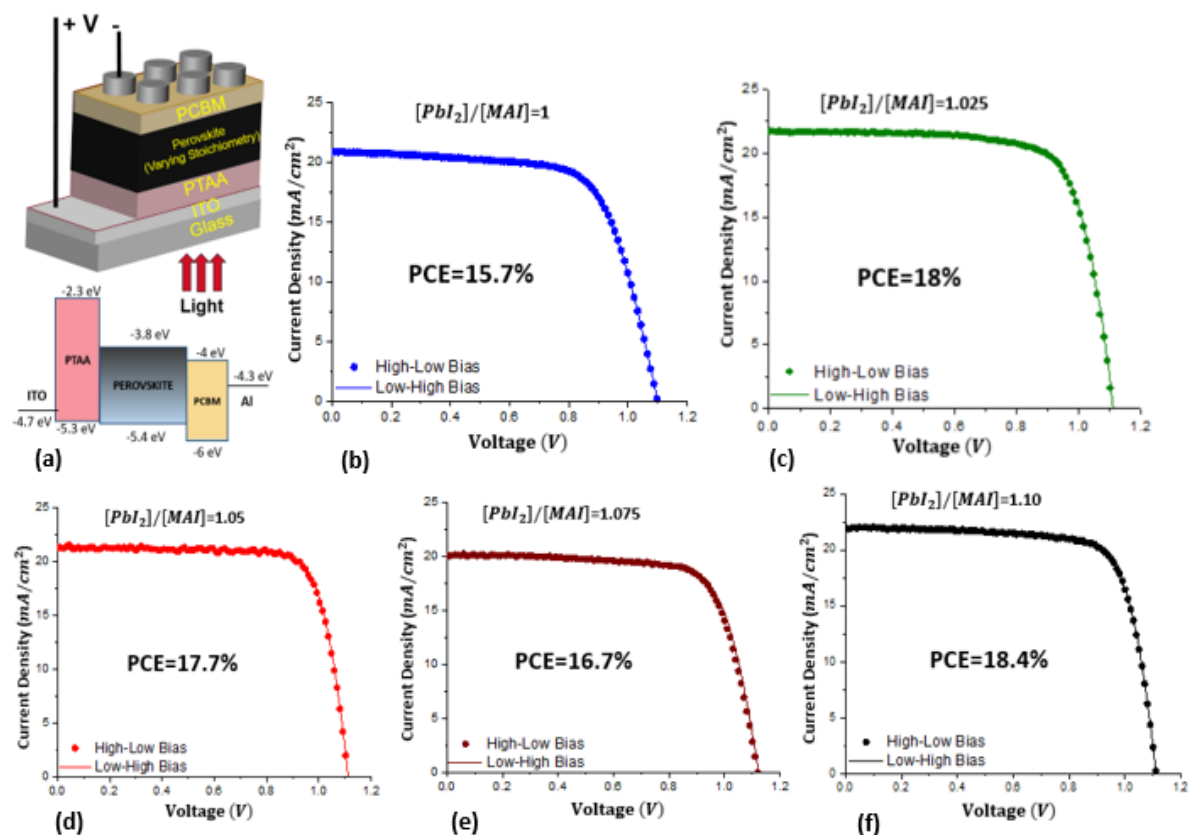
Figure 7.18: (a) Device structure and band edges of perovskite solar cell, light IV along with power conversion efficiencies for devices fabricated with different PbI_2 to CH_3NH_3I molar ratio (b) $[PbI_2]/[MAI]=1$ (c) $[PbI_2]/[MAI]=1.025$ (d) $[PbI_2]/[MAI]=1.05$ (e) $[PbI_2]/[MAI]=1.075$ and (f) $[PbI_2]/[MAI]=1.10$. The solid line represents light IV scanned from low to high bias and dotted line represents light IV scanned from high to low bias. None of the light IV measurements show any hysteresis.

Table 7.5: Photovoltaic parameters for perovskite solar cells fabricated with different stoichiometry

$[PbI_2]/[MAI]$	$V_{oc}(V)$	$J_{sc}(mA/cm^2)$	$FF(\%)$	PCE (%)
*1**	1.07	21.6	68	15.7
*1.025***	1.11	21.8	74	18.0
1.05	1.11	21.3	75	17.7
1.075	1.12	20.1	74	16.7
*1.10***	1.11	22	75	18.4

Note: Measured *4 minutes & **2 minutes after exposing under 1X(AM1.5) intensity

We studied the photon-induced degradation of these devices for 100 hours under 1 sun intensity (AM1.5) in open-circuit condition. The photon-induced degradation and comparison among degradation in short-circuit current density over 100 hours have been reported in figure

7.19. The key take-away from this photon-induced degradation study is that the degradation decreases relative increase in PbI_2 before it reaches a minimum and then again increases with relative increase in PbI_2. The normalized degradation in short-circuit current density after 100 hours as a function of PbI_2 to CH_3NH_3I malor ratio has been reported in figure 7.20. The degradation index has been calculated as,

$$Normalized\ J_{sc}\ degradation\ (t = 100\ Hours) = 1 - \frac{J_{sc,t=100\ hours}}{J_{sc,t=0}}$$

This photon-induced degradation has been repeated several times with different stoichiometry and the cumulative standard error of experiment for this degradation index was calculated as 0.016. This standard error has been used as error bar in figure 7.20. This result can be explained considering both migration and generation of ions during photon induced degradation. The stoichiometry of perovskite precursor solution can affect the initial density of ions at perovskite-transport layer interfaces (figure 7.21). When we have used 1:1 molar ratio between PbI_2 and CH_3NH_3I there some positive MA^+ and negative I^- ions present inside bulk perovskite as according to Walsh et al. this kind of decomposition has lowest formation energy. Thus, the formation of perovskite along with formation of initial ions can be explained by the following chemical reaction:

$$a * MAI + a * PbI_2 \rightarrow y * (MA^+ + I^-) + z * MAPbI_3$$
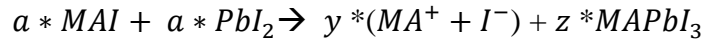
a, y and z are all constants.

In presence of internal electric-field the positive MA^+ ions migrate towards the perovskite-HTL interface and negative I^- ions migrate towards perovskite-ETL interface (Figure 7.21). Because of very high electric field at the interface these ions do not recombine with photo-generated electron-hole pairs. Thus, the initial short-circuit current density before exposure is not affected by this interface trapped ions. But, during the photon-induced

degradation in open-circuit condition these ions can migrate towards the neutral perovskite region. There are more ions generated by high energy photons. These ions in bulk perovskite act as recombination centers for photo-generated electron-hole pairs. Thus, the reduction in collection efficiency leads to the degradation in short-circuit current density.

Now, if we increase the relative concentration of PbI_2 in the perovskite precursor solution, these excess of PbI_2 can shift the chemical reaction to reduce initial ion densities by forming more perovskite atoms. This phenomenon can be explained by the following chemical reaction:

$$y * (MA^+ + I^-) + z * MAPbI_3 + x_1 * PbI_2 \rightarrow y' * (MA^+ + I^-) + z' * MAPbI_3$$

Here, y, z, x_1, y' and z' are all constants. Also, $y' < y$ and $z < z'$. x_1 represents the excess of PbI_2.

Lower initial ion densities at the interfaces leads to lower degradation in short-circuit current density. As we have seen when the $PbI_2\ to\ CH_3NH_3I$ molar ratio changes from 1 to 1.025 the normalized degradation in short-circuit current density decreases. If we keep increasing the relative concentration of PbI_2 at some point we can eliminate the initial densities of ions trapped at the interfaces and the degradation in short-circuit current density reaches minimum (Figure 7.21). That chemical reaction can be illustrated from the following equation:
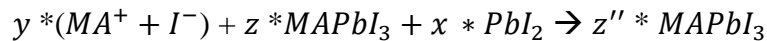
$$y * (MA^+ + I^-) + z * MAPbI_3 + x * PbI_2 \rightarrow z'' * MAPbI_3$$

Here, y, z, x and z'' are all constants. Also, $z < z''$. x represents the excess of PbI_2.

If we keep increasing the relative concentration of PbI_2 then we are adding excess of PbI_2 which can easily decompose and introduce negative I^- ions (Figure 7.21). Thus, the degradation in short-circuit current density will again increase as illustrated in figure 7.20.

In figure 7.22 we can show that the normalized degradations in short-circuit current density for different stoichiometry can be fitted with a double-exponential equation as,

$$J_{sc}(t) = J_{sc,t=0} - \Delta J_{sc} \tag{7.4}$$

$$\Delta J_{sc} = J_{sc,t=0} \left[a_m \left(1 - e^{-\frac{t}{t_{cm}}} \right) + a_g \left(1 - e^{-\frac{t}{t_{cg}}} \right) \right] \tag{7.5}$$

With boundary conditions,

$$(i) \; a_m + a_g = \frac{\Delta J_{sc}}{J_{sc,t=0}} \Big|_{t \to \infty} \qquad (ii) \Delta J_{sc} = 0 \text{ at t=0}$$

Table 7.6 shows the value of coefficients that has been used to fit the normalized degradation in short-circuit current density. It is understandable why we need two exponentials to fit the short-circuit current degradation if we consider both migration and generation of ions contribute in this photon-induced degradation. We can consider the first exponential takes care of the migration of ions with a time constant of t_{cm} and a magnitude of a_m. And the second exponential models the generation of ions with a time constant of t_{cg} and a magnitude of a_g. As a_m is a function of initial ion densities it should have high correlation with degradation in short-circuit current density of devices fabricated with different PbI_2 to CH_3NH_3I molar ratio. FIG. 6(c) shows the correlation between a_m and Normalized short-circuit current degradation after 100 hours. As the figure shows, they can be fitted with a straight line with $R^2 = 0.91$. This indicates that they have a very high correlation.

Figure 7.19: Photon-induced degradation for 100 hours at 1 sun intensity (AM1.5) in open circuit condition for devices fabricated with different PbI_2 to CH_3NH_3I molar ratio. Here all the values are normalized with respect to the values at time, t=0. (a) $[PbI_2]/[MAI]=1$ (b) $[PbI_2]/[MAI]=1.025$ (c) $[PbI_2]/[MAI]=1.05$ (d) $[PbI_2]/[MAI]=1.075$ and (e) $[PbI_2]/[MAI]=1.10$ (f) Comparison in short-circuit current degradation among devices with different PbI_2 to CH_3NH_3I malor ratio
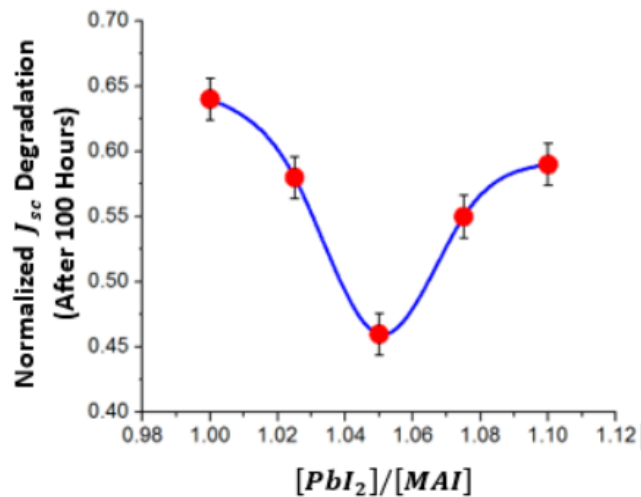
Figure 7.20: Normalized short-circuit current degradation at t=100 hours as function of PbI_2 to CH_3NH_3I malor ratio. The error bar has been calculated from the cumulative standard error
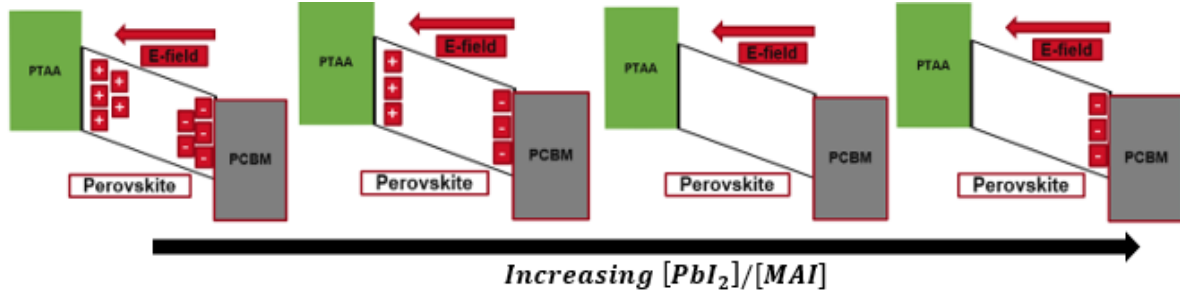
Figure 7.21: Schematic illustration of change in interface charge densities with relative increase in PbI_2 with respect to CH_3NH_3I

Table 7.6: Parameters for fitting J_{sc} degradation with double-exponential model

$[PbI_2]/[MAI]$	a_m	$t_{cm}(minutes)$	a_g	$t_{cg}(minutes)$	R^2
1	0.53	120	0.10	2500	0.90
1.025	0.34	120	0.27	2500	0.97
1.05	0.15	120	0.30	2500	0.99
1.075	0.25	120	0.30	2500	0.99
1.10	0.35	120	0.25	2500	0.99

Figure 7.22: Fitting J_{sc} degradation with double-exponential model (a) $[PbI_2]/[MAI]=1,1.05,1.10$ (b) $[PbI_2]/[MAI]=1.025,1.075$. The solid lines represent fitted line with double exponential and dotted lines represent experimental normalized J_{sc} degradation. (c) The correlation plot between Ion migration coefficient (a_m) and Normalized J_{sc} degradation after 100 hours

In summary, the stoichiometry of perovskite precursor solution can affect the photon-induced degradation as the ion densities at the interfaces is a dependent on PbI_2 to CH_3NH_3I molar ratio. We need to find the optimum value of this molar ratio which will minimize the degradation in short circuit current density.

7.5 Photo-degradation at Different Biasing Conditions (Open vs Short)

The difference in biasing condition during photo-degradation also plays an important role in degradation of device performance because the basing condition affects ion migration. In this experiment, I have used the control device with $[PbI_2]$ to $[MAI]$ ratio of 1.05 (or 5% excess of PbI_2). I have performed photon-induced degradation on two contacts of the same devices kept at two different biasing conditions during illumination (open-circuit and short-circuit). The device structure used for this experiment has been given in figure 7.23.
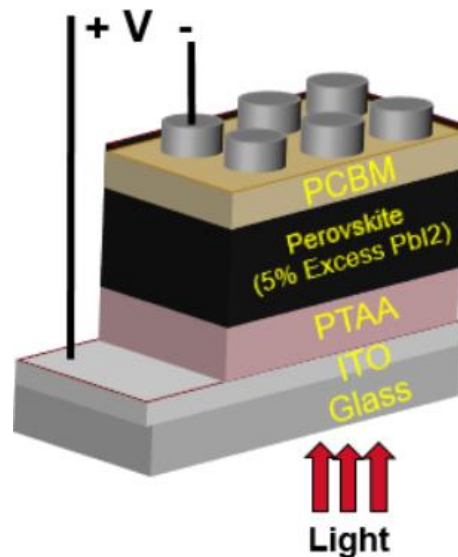
Figure 7.23: Device structure used for the photon-induced degradation at different biasing conditions

Starting Efficiency
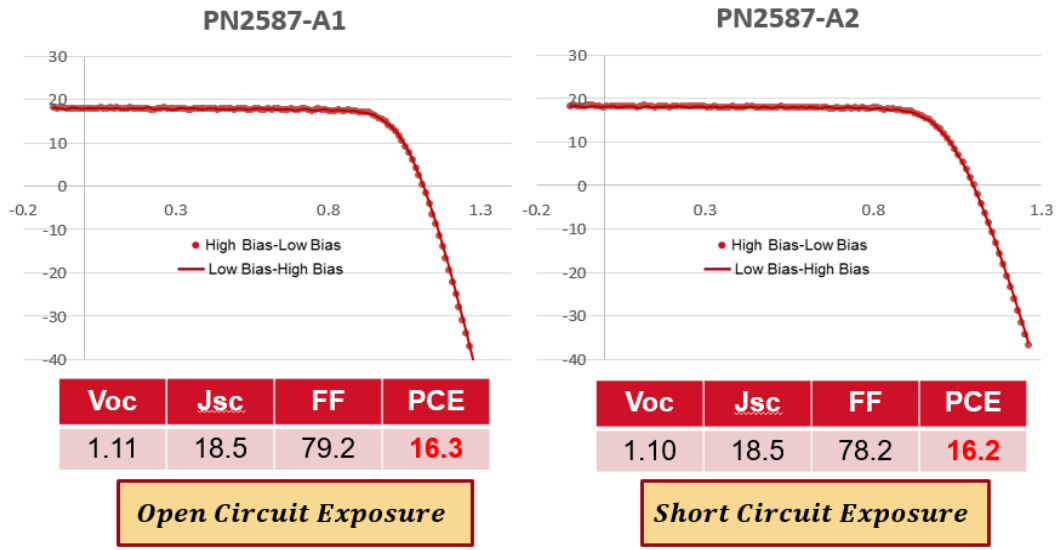
Figure 7.24: Light IV characteristics for the contacts used for photon-induced degradation study at different biasing conditions; open-circuit exposure (left), short circuit exposure (right). Both are identical to start with.

Figure 7.24 shows the light IV characteristics of the contacts used in this experiment before photon-induced degradation. The photovoltaic parameters are identical for both the devices.
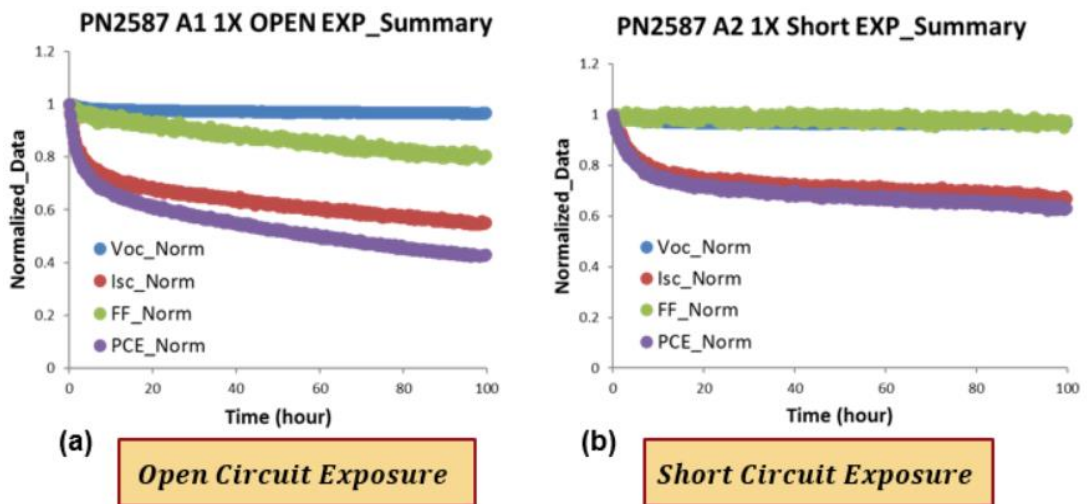
Figure 7.25: Photo-degradation comparison for devices exposure with different biasing conditions (a) Exposure in open-circuit condition (b) Exposure in short-circuit condition

Table 7.7: Photon-induced degradation (in percentage) of photovoltaic parameters after exposing for 100 hours at 1 sun intensity

Exposure Condition	$V_{oc}(V)$	$J_{sc}(mA/cm^2)$	FF(%)	PCE (%)
Open-circuit Exposure	4%	45%	24%	58%
Short-circuit Exposure	4.5%	32.5%	3.6%	37%

*Note: All the parameters decrease with time during photon induced degradation

Figure 7.25 shows the photon-induced degradation in open-circuit condition [Figure 7.25 (a)] and in short-circuit condition [Figure 7.25 (b)]. And the decrease in photovoltaic parameters after 100 hours of degradation has been reported in table 7.7.

Some key take-away points from this photo-degradation are:

➢ The open-circuit voltage degradation is similar for both cases considering photon-induced degradation either in open circuit or short circuit basing condition.

➢ The short-circuit current degrades more in case of open circuit degradation than short circuit degradation condition.

➢ Thus, the power conversion efficiency degradation for the cell exposed in open circuit condition is much higher than power conversion efficiency degradation for the cell exposed in short circuit condition.

Figure 7.26 shows the pairwise comparison of open-circuit voltage and short-circuit current degradation at two biasing conditions.
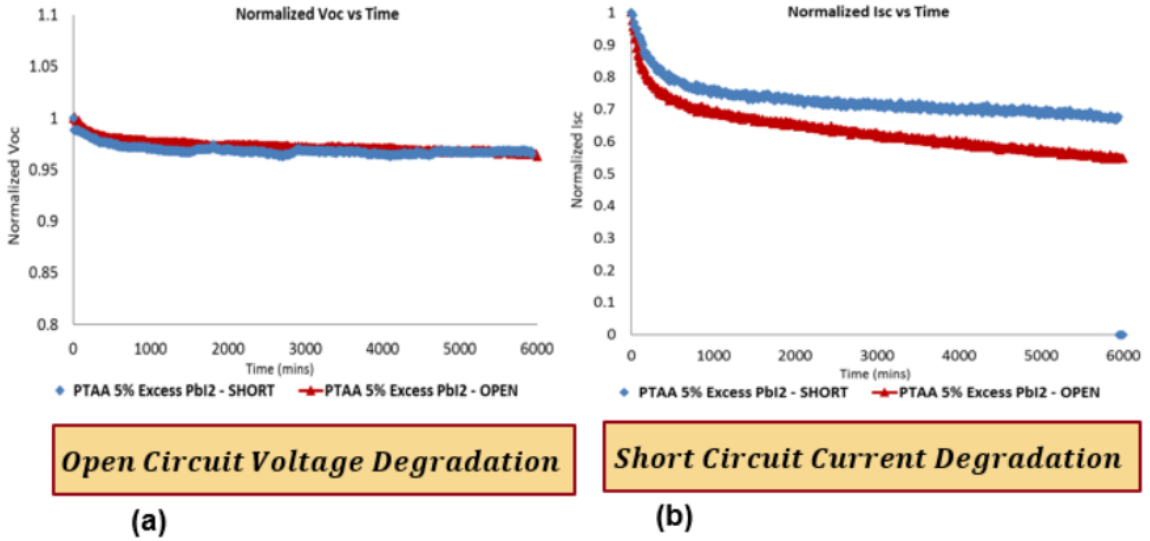
Figure 7.26: Photon induced degradation comparison for 100 hours at one-sun (AM 1.5) intensity (a) Short-circuit current degradation (b) Open-circuit voltage degradation
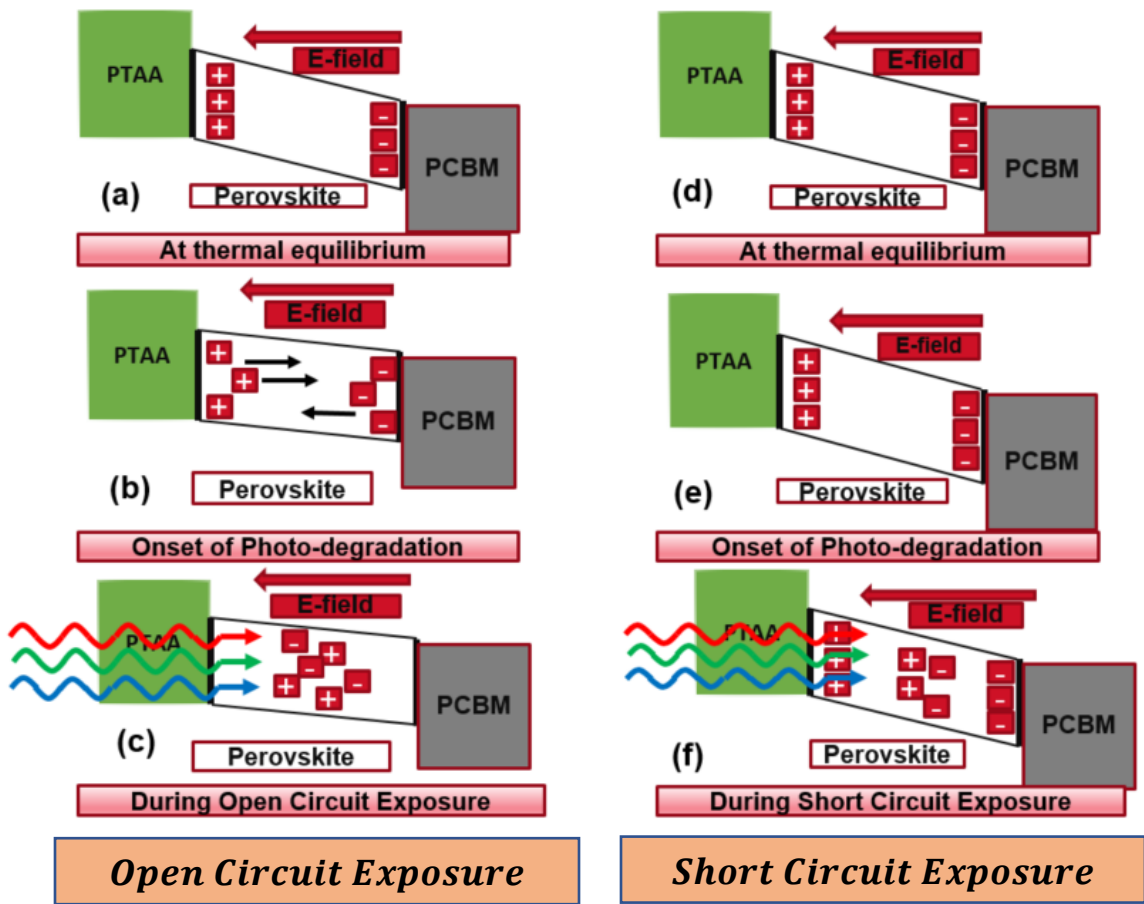
Figure 7.27 Band diagrams to explaining photon-induced degradation in both biasing conditions (a),(b),(c) Degradation in open circuit condition (d),(e),(f) Degradation in short circuit condition

This change in photo-degradation can be explained from the following band-diagram and using our model on photo degradation in figure 7.27.

7.5.1 Explanation for short circuit current degradation

At thermal equilibrium, due to built-in E-filed positive ions go towards hole transport layer (HTL) and negative ions go towards electron transport layer (ETL). So, we have net electric field inside the active layer [Figure 7.27 (a) & (d)]. Due to high electric field at the interfaces these ions do not recombine with generated electron-hole pairs. During exposure in open circuit condition the active layer is almost in flat band condition. Due to decrease in internal E-field these ions migrate towards the intrinsic active layer [Figure 7.27 (b)]. In addition to that, more ions are generated by photons [Figure 7.27 (c)]. These ions recombine with generated electron-hole pairs resulting in short circuit current degradation. But in case of short circuit exposure, there is still high electric field inside the active layer. Because of this high internal electric field ions from contact layers can't migrate towards the intrinsic layer [Figure 7.27 (e)]. Still there is generation of ions by high energy photons during exposure [Figure 7.27 (f)]. The short circuit current degrades because of recombination of generated electron-hole pairs with these generated ions. As the interfacial ions don't contribute to short circuit current degradation, the degradation of short circuit current in case of short circuit exposure is significantly lower than degradation in open circuit condition.

7.5.2 Explanation for open circuit voltage degradation

From the photo-degradation results, the degradation of open circuit voltage is similar for both cases. This result can also be explained from our photo-degradation model. Recalling

our model on open-circuit voltage degradation, there are two components which play a role in open circuit voltage evolution during light exposure:

➢ Increase in open circuit voltage due to migration of ions from contact layers to the bulk

➢ Decrease in open circuit voltage due to increase in non-radiative recombination

In short circuit condition, the ions do not migrate from interfaces to the bulk region. So, the contribution in increase in open circuit voltage due to ion migration is zero (this can be clearly proved from the capacitance-voltage profile presented in figure 7.28). In other words, $V_d = 0$ in our model. But the open-circuit voltage still decreases because of increase in non-radiative recombination inside bulk perovskite. But the effect of this non-radiative recombination component is lower in case of short circuit exposure compared to open circuit exposure as there is less recombination.

In case of open circuit degradation, the ions from interfacial layers migrate towards the bulk perovskite. So, there is a positive contribution of ion migration in increase in open circuit voltage (again this can be proved from the capacitance-voltage profile presented figure 7.28). In other words, $V_d > 0$ in our model. In addition to that open-circuit voltage still decreases because of increase in non-radiative recombination inside bulk perovskite. But the effect of this non-radiative recombination component is higher in case of open circuit exposure compared to short circuit exposure as there is higher degree of recombination.
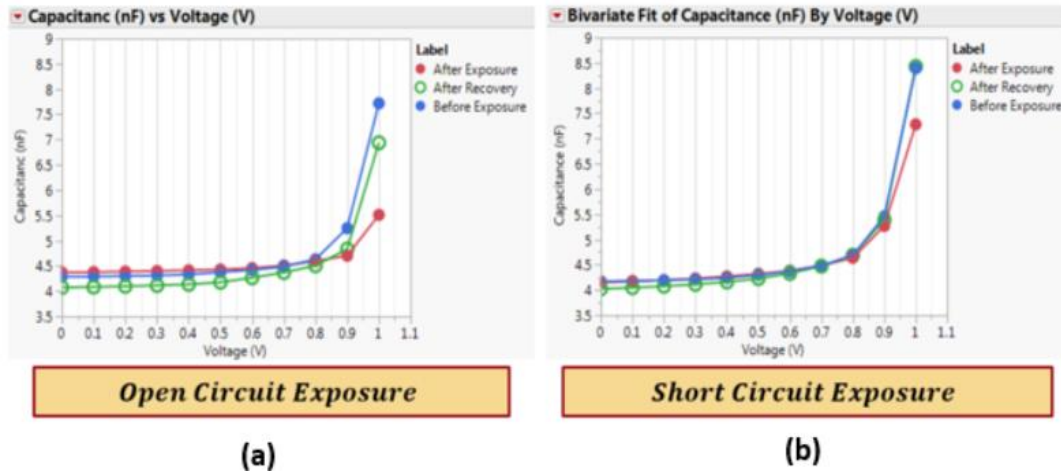
Figure 7.28: Capacitance-Voltage recovery after photon induced degradation for 100 hours at one-sun (AM 1.5) intensity (a) Exposure in open-circuit condition (b) Exposure in short-circuit condition

But result shows that there is no difference in open circuit voltage degradation. This can be explained because in short circuit condition the open-circuit voltage doesn't increase due to ion migration but it also decreases less due to less non-radiative recombination. And in open circuit condition open circuit voltage increases due to ion migration but it also decreases more due to higher decrease in open circuit voltage due to higher non-radiative recombination. These two components add up and results in similar degradation in open circuit voltage. This can also be proved from the simulation result on our model presented later in figure 7.29.

From the Capacitance vs Voltage profile in figure 7.28, during open circuit photo degradation the CV profile shifts to the right (in other words, capacitance decreases at higher bias) which suggests an increase in net built-in potential due to ion migration from contact layers to bulk perovskite. In short circuit photo degradation, there is no significant shift of CV profile (or decrease in capacitance after exposure) which validates our assumption that there is no significant ion migration after exposure in this condition. Recovery condition for the cell

exposed in open circuit condition is 41 hours at room temperature in dark and the cell exposed in short circuit condition in 38 hours at room temperature in dark.
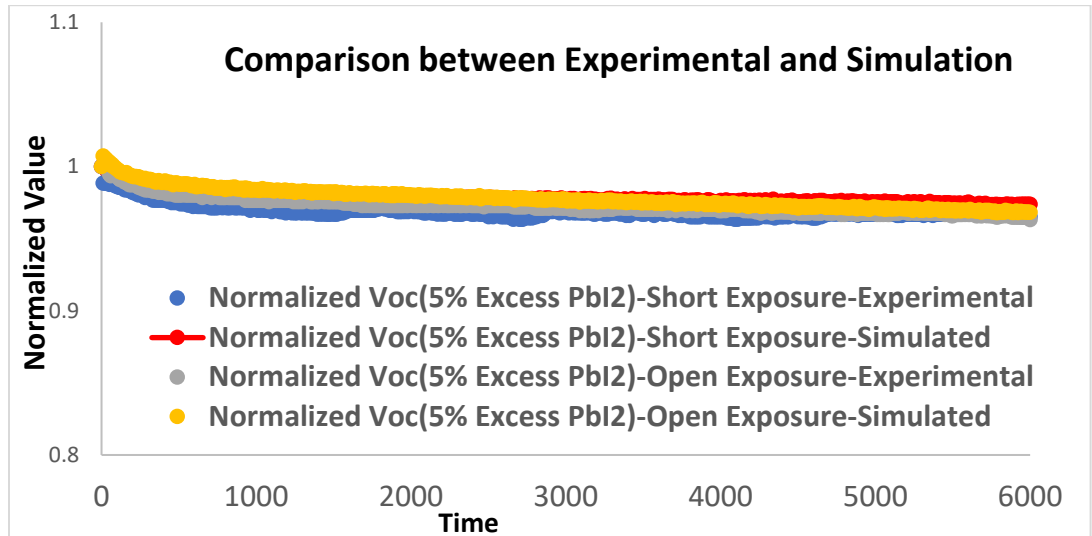
Figure 7.29: Comparison between experimental results to simulated results for open-circuit voltage degradation for 100 hours at one-sun (AM1.5) intensity

Figure 7.29 shows the comparison of open-circuit voltage degradation between the experimental and simulated result from our model. For short-circuit exposure the component of increase in open circuit voltage due to ion migration, V_d is zero. And for open circuit exposure the calculated $V_d = 0.01$V. For both photo-degradation conditions the simulated results match well with experimental results.

7.6 Effect of Fabrication Techniques of Perovskite (Solution vs Vapor)
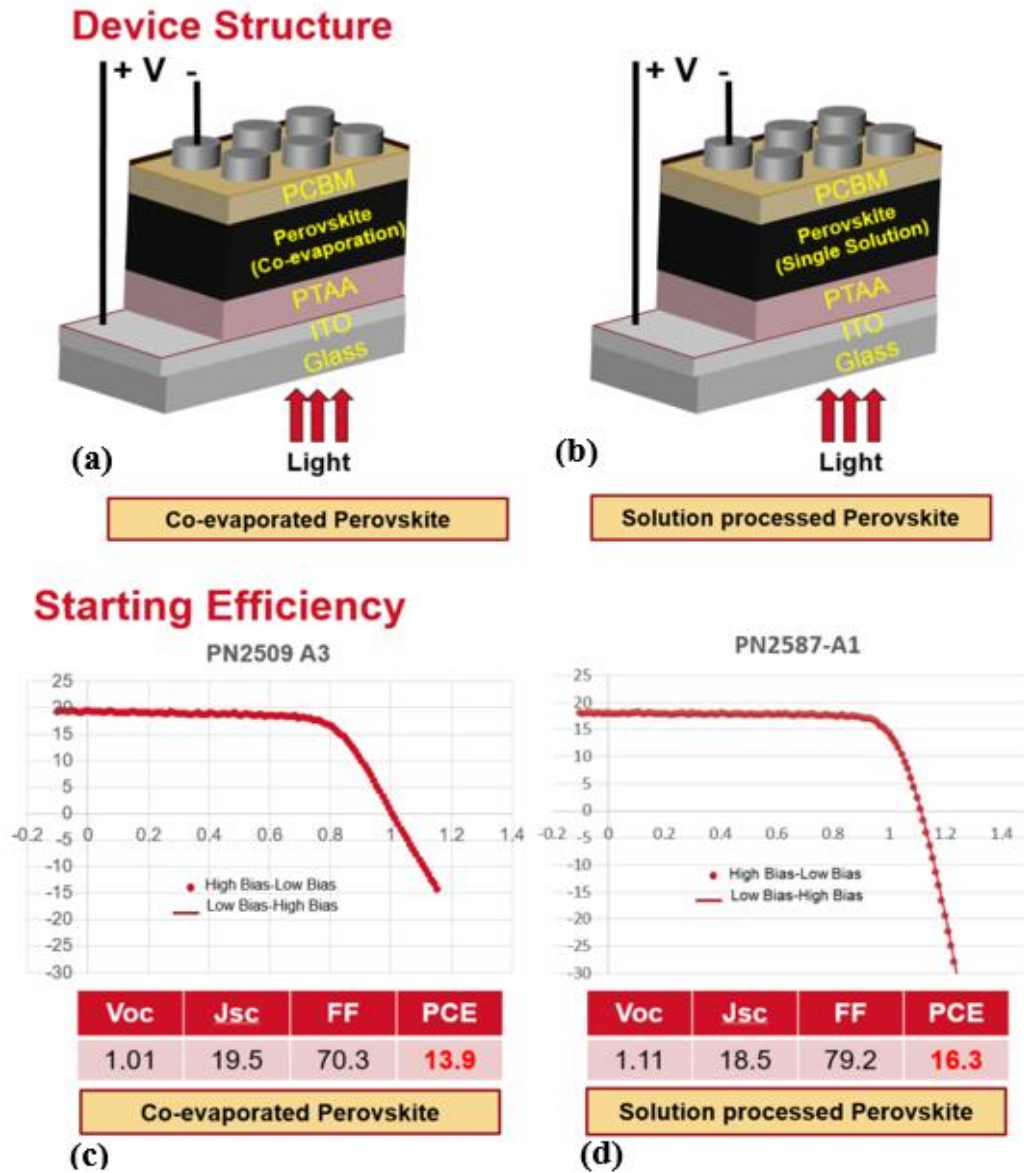
Figure 7.30: Device structure and starting efficiency of devices under consideration for photon-induced degradation comparison (a), (c) Co-evaporated perovskite (b), (d) Solution-processed perovskite (with 5% Excess PbI2)

Both the devices have same structure. The only difference is that for the device left side perovskite is deposited using co-evaporation. The for right one perovskite was deposited using single-solution process. Another major difference is that the co-evaporated perovskite has a thickness of around 350 nm and solution processed perovskite has thickness of about 600 nm.

The starting efficiency for the co-evaporated perovskite device is about 14% and for the solution-processed perovskite is about 16%.

The photo-degradation comparison between these two devices is given below:
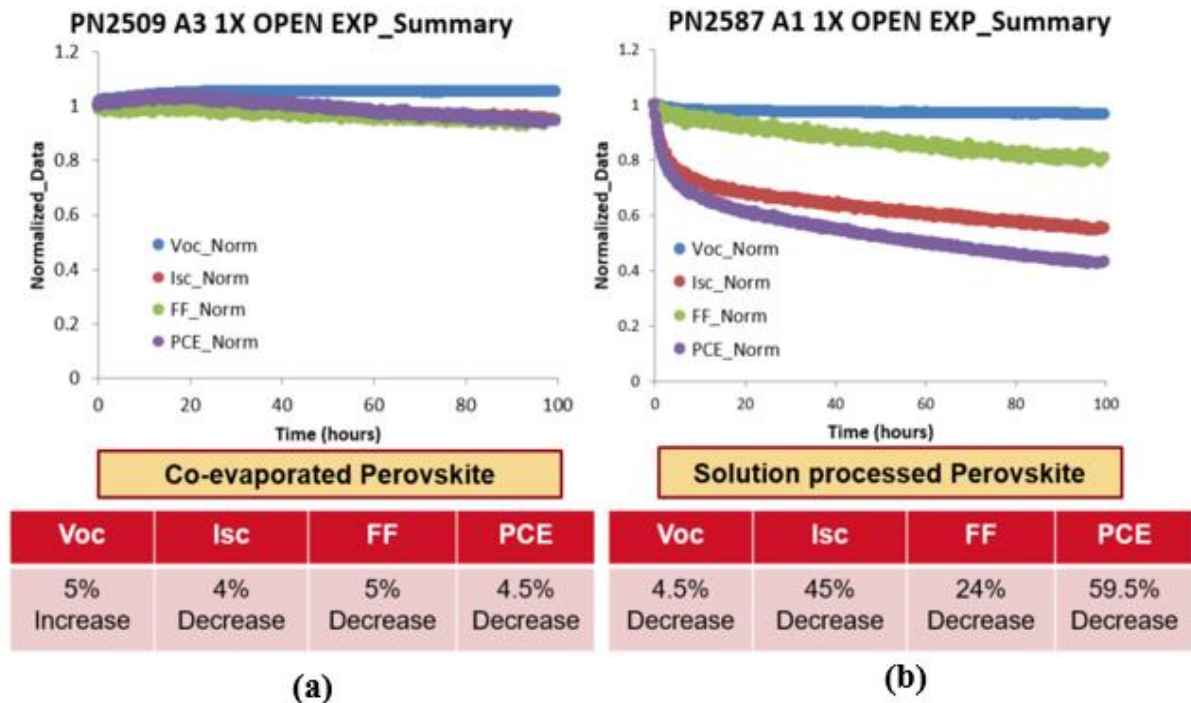
Figure 7.31: Photo-degradation comparison for 100 hours in open-circuit condition at one-sun intensity (AM 1.5) (a) Co-evaporated perovskite (b) Solution processed perovskite with 5% Excess PbI2

Some key take-away points from this photo-degradation are:

➢ The open-circuit voltage increases for the co-evaporated perovskite device and it decreases for solution-processed perovskite solar cell during open circuit exposure for 100 hours at one-sun intensity.

➢ The short-circuit current degrades more for solution processed device compared to vapor processed perovskite solar cells.

➢ Thus, the power conversion efficiency degradation for the cell fabricated with solution-processed perovskite is significantly higher compared to the solar cell fabricated with co-evaporated perovskite.

The co-evaporated perovskite solar cell is one the most photo-stable solar cell ever recorded. Photo conversion efficiency degraded by only 5% over the 100 hours of photon induced degradation at one-sun intensity.
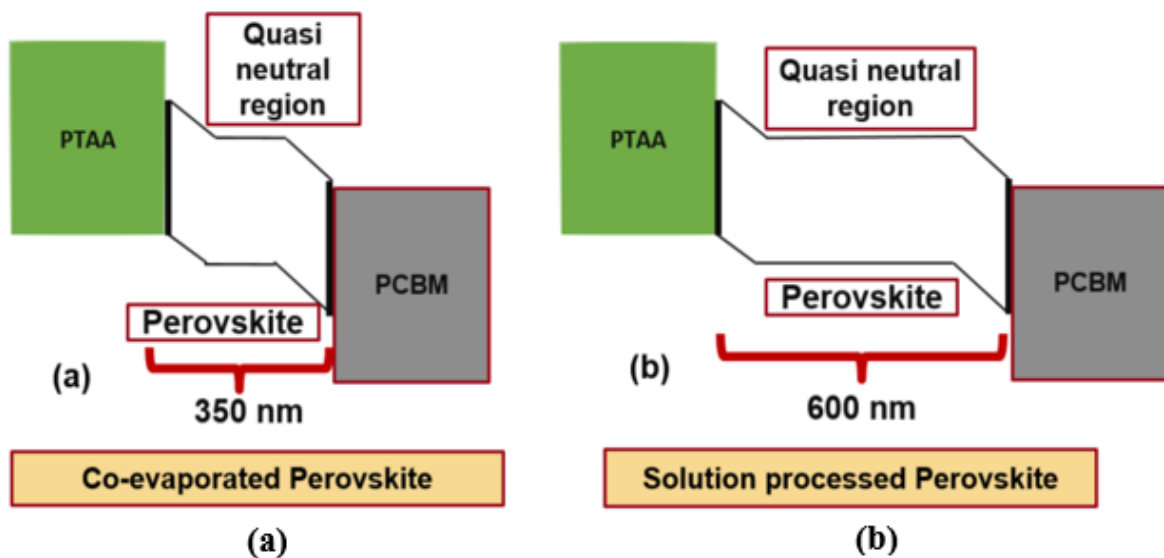
Figure 7.32: Formation of quasi-neutral region in bulk perovskite (a) Co-evaporated perovskite (~350nm) (b) Solution-processed perovskite (~600nm)

The difference in thickness of perovskite may be the reason behind lesser degradation for co-evaporated perovskite solar cell. At thermal equilibrium, due to built-in E-filed positive ions go towards ETL and negative ions go towards HTL. So, we have net electric field inside the active layer. The carrier transport is dominated by drift and so collection efficiency is determined by range, $R = f(E)$. During photo-degradation the ions move to their original position and that forms a quasi-neutral region inside active layer. Now most of the photons are absorbed in the quasi-neutral region. In this region carrier transport is dominated by diffusion. During photo-degradation, a lot of ions are generated by high energy photons. Due to increase

in recombination the carrier life time decreases and the actual diffusion length becomes shorter. In case of solution processed perovskite as the optimum thickness is about 600 nm to achieve maximum power conversion efficiency and the length of quasi neutral region is longer than effective carrier diffusion length [Figure 7.32 (a)]. So, carrier collection efficiency decreases. Thus, short circuit current decreases. For vapor processed device the optimum thickness is about 350 nm to achieve maximum power conversion efficiency. Even if there might be a narrow quasi-neutral region but that might be within carrier diffusion length of perovskite [Figure 7.32 (b)]. Although ions are generated during exposure, because of high electric field the collection efficiency is still very high. Thus, there is no significant degradation in short circuit current and Fill factor in vapor processed device.

7.7   Effect of Grain Size of Perovskite

Grain size of perovskite plays a very significant role in photo-degradation. Higher grain size devices degrade slower. That suggests may be ions migrate through vulnerable grain boundaries and ions can generate easily at brain boundaries as the molecules are loosely bond (chemically). The activation energy for generating ions is lower at grain boundaries. Thus, lower grain size devices degrade more.

A common way to increase the grain size of perovskite film is solvent annealing. The kinetics behind the mechanism of grain size enhancement has been explained Xiao et al. [6] and Liu et al. [7] as discussed in chapter 5.

Figure 7.34 shows the spin-coating and solvent annealing of perovskite on NiO substrate. For the control device, the procedure includes that after spin coating perovskite solution the control device was thermally annealed at 100°C for 10 minutes. But in case of

solvent annealed device after spin coating perovskite it was annealed in presence of solvent

(10 µL DMF in this case) [Figure 7.34].
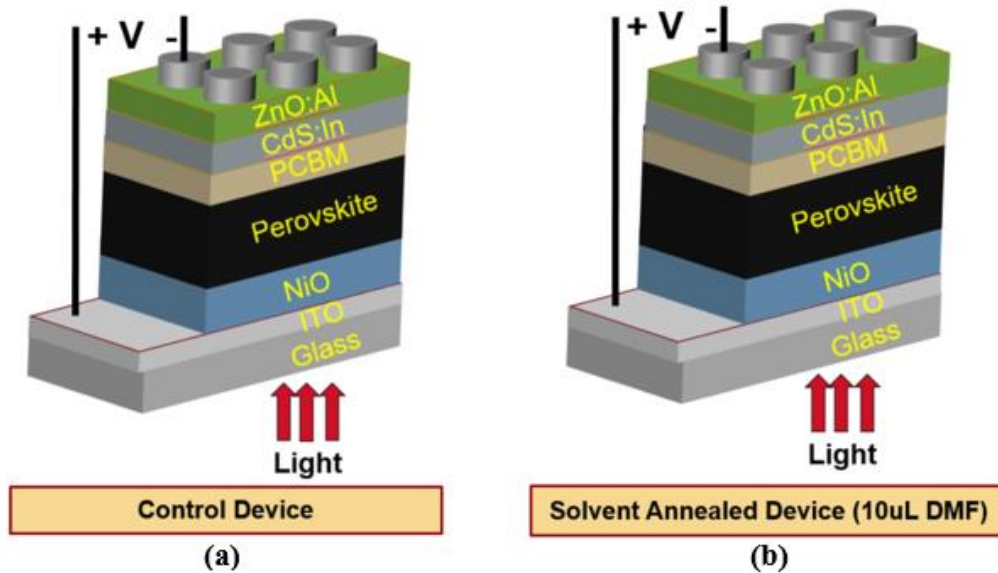
Figure 7.33: Device structure of devices under consideration for photo-degradation comparison (a) Control device with smaller perovskite grain-size (b) Device with solvent annealed perovskite with larger grain size
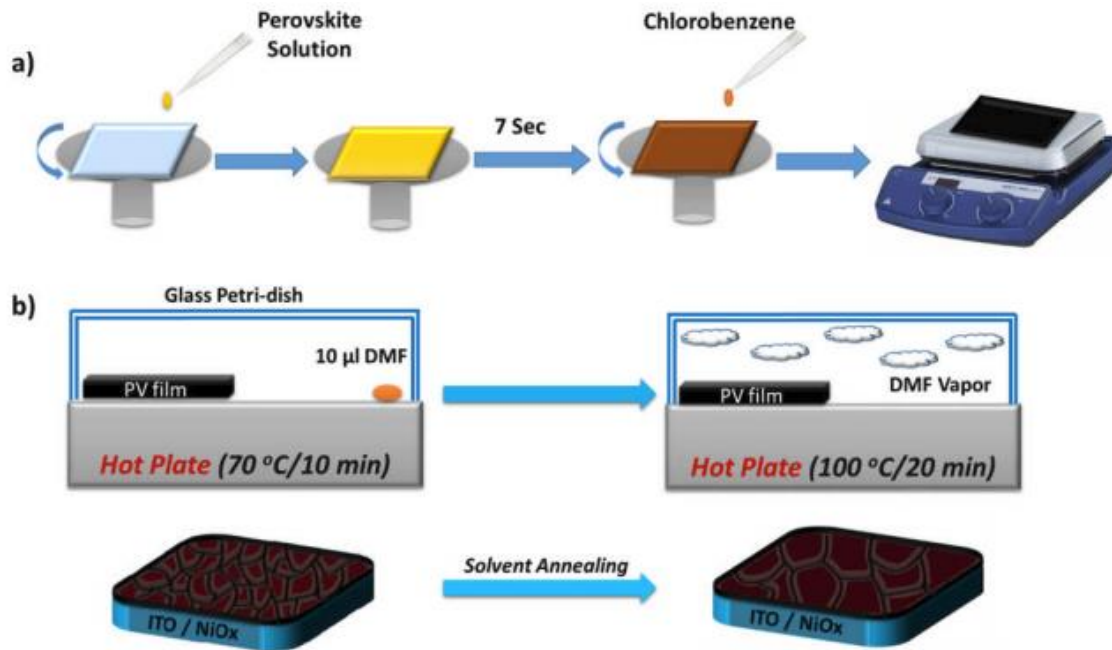
Figure 7.34: Schematic diagram (a) Spin-coating of perovskite on NiO substrate using single solution anti-solvent process (b) Solvent annealing of perovskite
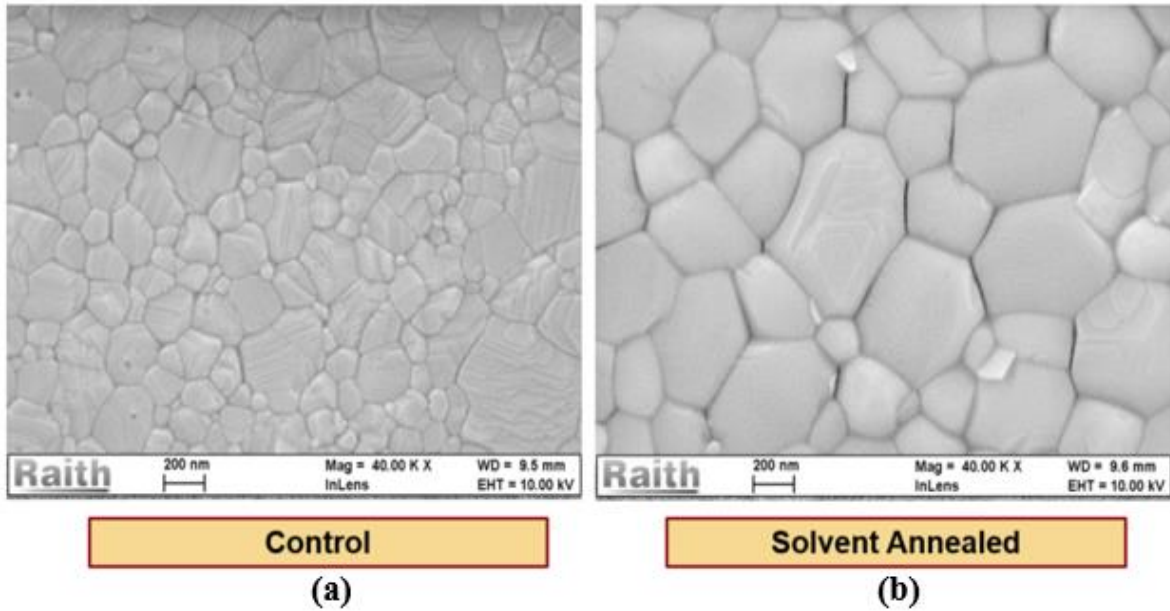
Figure 7.35: SEM images of planner perovskite layer (a) Control perovskite shows grain size of about ~200 nm (b) Solvent annealed perovskite shows grain size of about ~600 nm

The figure 7.35 also shows the SEM images on these two types of perovskite films.

The control device has a grain size of about 200 nm. After solvent annealing process, the grain

size increased by almost 3 times to about 600 nm.
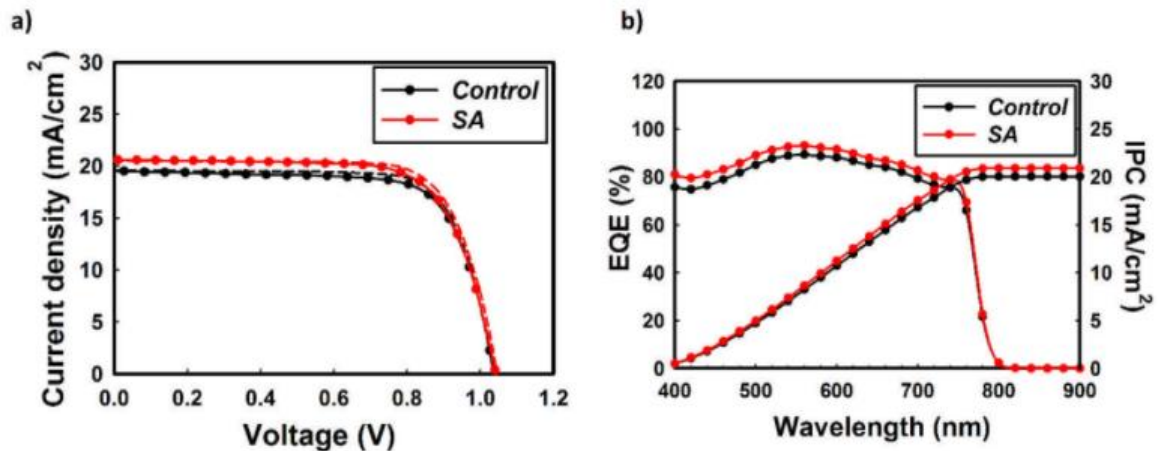
Figure 7.36: Starting efficiencies of devices under consideration for photo-degradation comparison (a) Light IV characteristics; solid-line represents the sweep direction from high-low bias and dotted-line from low-high bias (b) External quantum efficiency. Control device has smaller (~200 nm) perovskite grain-size and device with solvent annealed perovskite has larger (~600 nm) grain size

Table 7.8: Photovoltaic parameters for perovskite solar cells with different grain-size

Condition	$V_{oc}(V)$	$J_{sc}(mA/cm^2)$	FF(%)	PCE (%)
Control	1.03	19.6	75	15.1
Solvent-annealed	1.04	20.5	74	15.7

Figure 7.36 (a) shows the light IV characteristics of these two types of devices. Table 7.8 shows the photo-conversion efficiencies for these devices before photon-induced degradation. Both the devices have similar efficiencies, which suggests that may be the grain boundaries in perovskite are passivated. Thus, the grain size may not influence the starting efficiency but affects the photo-stability significantly.
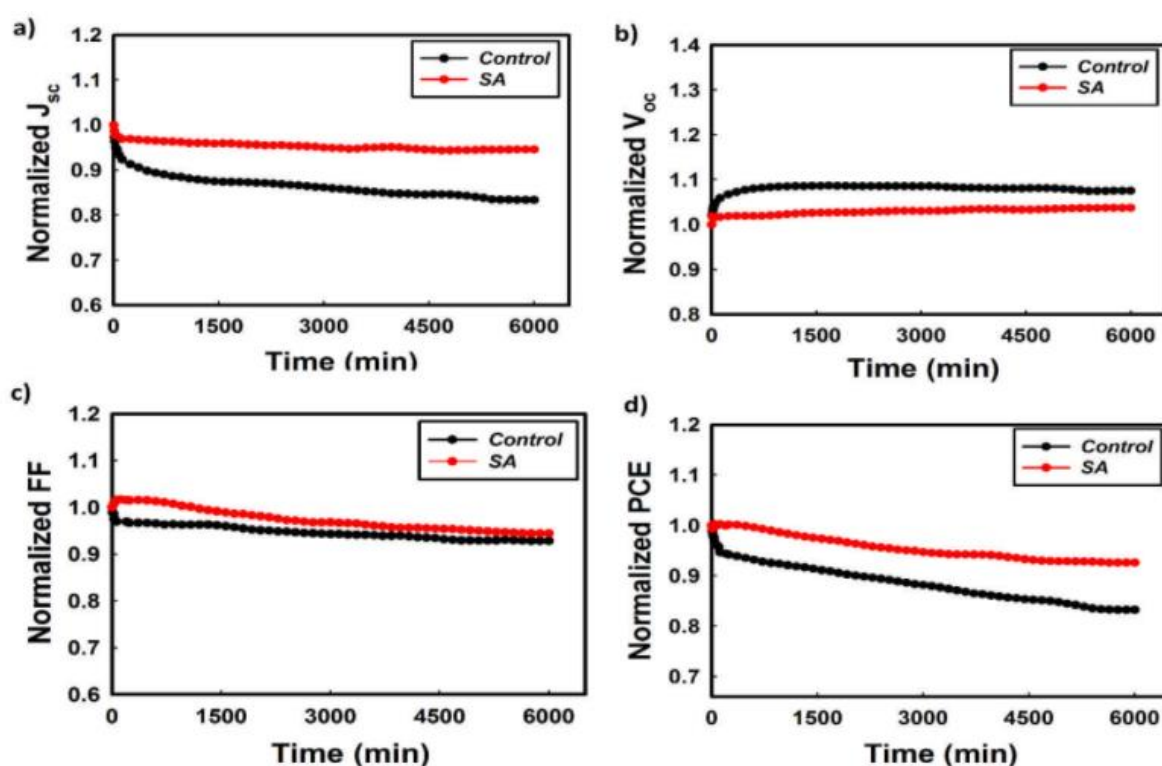
Figure 7.37: Photon-induced degradation comparison for different perovskite grain-size devices (a) Short-circuit current density (b) Open-circuit voltage (c) Fill factor (d) Power-conversion efficiency. This photon-induced degradation was done for 100 hours in open-circuit condition at one-sun intensity (AM1.5)

The photon-induced degradation (Figure 7.37) change in photovoltaic parameters for both the control and solvent annealed devices. The result clearly showed that the control device has degraded more than solvent annealed device.

Some key take-away points from this experiment are:

➢ The open-circuit voltage for the control device increases more than the solvent annealed under continuous illumination at one-sun intensity.

➢ The short-circuit current degrades more for the control device than the solvent annealed perovskite device.

➢ Thus, the power conversion efficiency degradation for the control device is much higher than power conversion efficiency degradation of solvent annealed device.
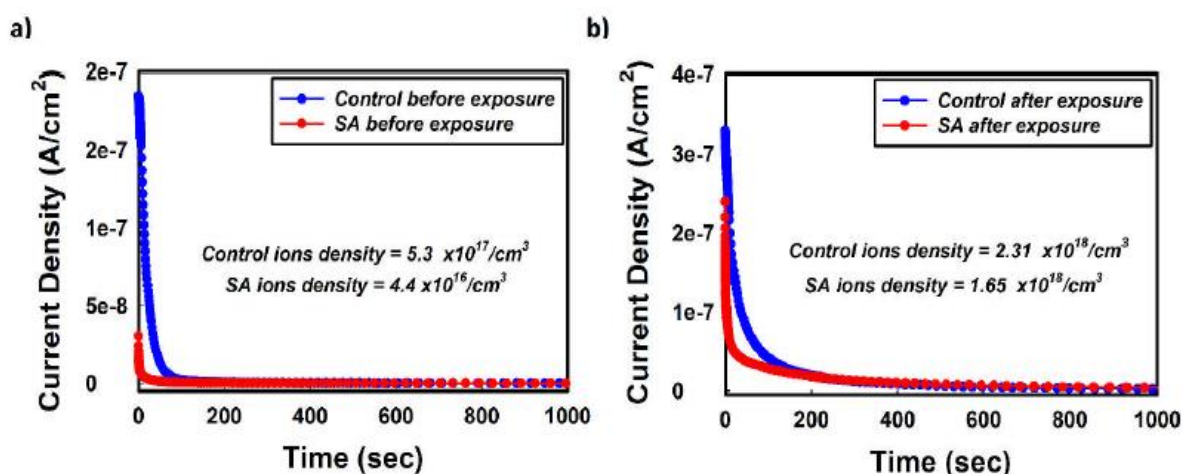
Figure 7.38: Density of ions calculation by transient current method (a) Before exposure (b) After photon-induced degradation

The faster decrease in short circuit current for control device is largely due to smaller grain size of perovskite. Because it several research groups have already showed that the ions are likely to migrate through the grain boundaries. Yuan et al. [10], Walsh et al. [9] and Eames et al. [8] showed that the activation energy for ion migration becomes about half if we consider

migration through crystal grain boundaries along with other migration sites. They also showed that at grain boundaries the formation energy also becomes lower as it is easier for ions to generate because of soft chemical bonding in grain boundary sites for smaller grain size polycrystalline film. Because of lower activation energy for ion migration it is easier for the ions to migrate from the contact layers to the bulk perovskite and in addition to that, because of lower formation energy it is likely that more ions are generated during light exposure for the smaller grain size devices. Thus, more ions are available for recombination with generated carriers. So, the smaller grain size devices show larger short circuit current degradation. Smaller grain-size perovskite has more grain boundaries and these grain boundaries assist the migration of ions. Thus, open-circuit voltage evolves more for the smaller grain-size perovskite device compared to larger grain-size device. The ion density measurement using transient current method [11] shows that solvent annealed device has lower initial ion density than control device [Figure 7.38].
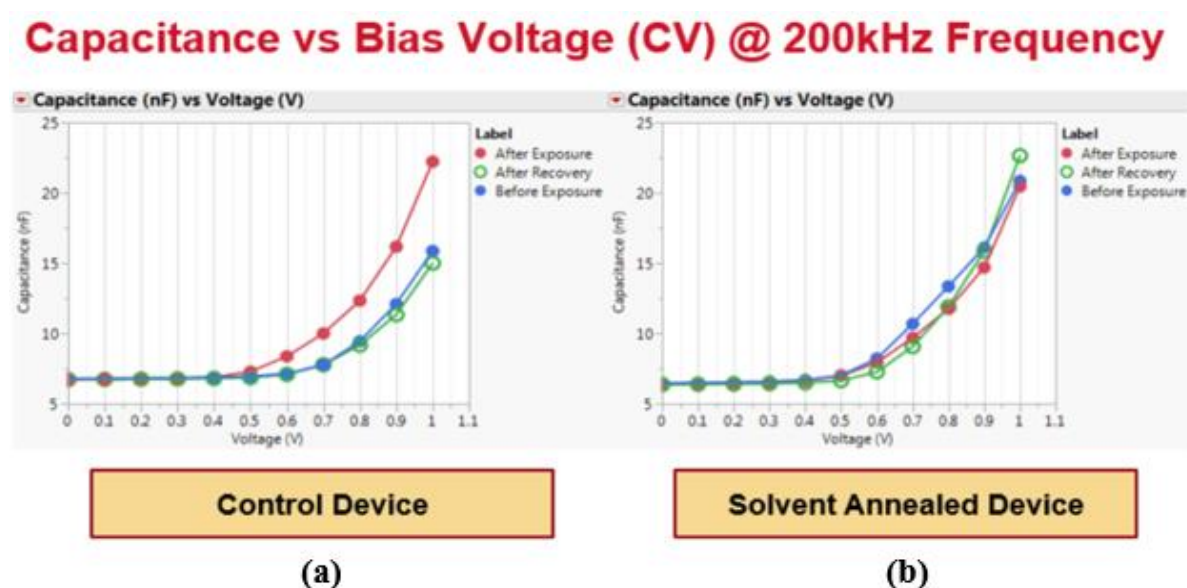
Figure 7.39: Capacitance-Voltage recovery after photon induced degradation for 100 hours at one-sun (AM 1.5) intensity in open-circuit condition (a) Control device with smaller perovskite grain-size (b) Device with solvent annealed perovskite with larger grain size

The CV profile [Figure 7.39] shows that capacitance decreases after exposure for both control and solvent annealed devices indicating an increase in net built-in potential due to ion migration. But for the control case the decrease in capacitance is higher than the solvent annealed device as smaller grain size assists the migration of ions [8,9,10]. The activation energy for ion migration is lower for the control device as it has smaller grain size.

REFERENCES

1   Pranav Joshi, Ph.D. dissertation, "Understanding the photostability of perovskite solar cell", Iowa State University (2016)

2   Pranav H. Joshi, Liang Zhang, Istiaque M. Hossain, Hisham A. Abbas, Ranjith Kottokkaran, Satyapal P. Nehra, Mahendra Dhaka, Max Noack, and Vikram L. Dalal, AIP Advances 6, 115114 (2016)

3   Pranav Joshi, Liang Zhang, Ranjith Kottokkaran, Hisham Abbas, Istiaque Hossain, Satyapal Nehra, Mahendra Dhaka, Max Noack, Vikram Dalal, Photovoltaic Specialists Conference (PVSC), 2016 IEEE 43rd, pages 0242-0248

4   Hyungcheol Back,a Geunjin Kim,a Junghwan Kim,a Jaemin Kong,a Tae Kyun Kim,a Hongkyu Kang,a Heejoo Kim,a Jinho Lee,b Seongyu Leeb and Kwanghee Lee, Energy Environ. Sci., 9, 1258-1263 (2016)

5   Christopher Eames, Jarvist M. Frost, Piers R. F. Barnes, Brian C. O'Regan, Aron Walsh & M. Saiful Islam, Nature Communications 6, Article number: 7497 (2015)

6   Z. Xiao, Q. Dong, C. Bi, Y. Shao, Y. Yuan, and J. Huang, "Solvent annealing of perovskite-induced crystal growth for photovoltaic-device efficiency enhancement", Adv. Mater., 26, 6503 (2014). doi:10.1002/adma.201401685

7   J. Liu, C. Gao, X. He, Q. Ye, L. Ouyang, D. Zhuang, C. Liao, J. Mei, and W. Lau, "Improved crystallization of perovskite films by optimized solvent annealing for high efficiency solar cell", ACS applied materials & interfaces, 7, 24008 (2015). doi:10.1021/acsami.5b06780

8   Christopher Eames, Jarvist M. Frost, Piers R. F. Barnes, Brian C. O'Regan, Aron Walsh & M. Saiful Islam, "Ionic transport in hybrid lead iodide perovskite solar cells", Nature Communications 6, 7497 (2015), DOI: 10.1038/ncomm8497

9   Aron Walsh, "Principles of Chemical Bonding and Band Gap Engineering in Hybrid Organic–Inorganic Halide Perovskites", J. Phys. Chem. C, 2015, 119 (11), pp 5755–5760, DOI: 10.1021/jp512420b

10   Yongbo Yuan and Jinsong Huang, "Ion Migration in Organometal Trihalide Perovskite and Its Impact on Photovoltaic Efficiency and Stability", Acc. Chem. Res., 2016, 49 (2), pp 286–293, DOI: 10.1021/acs.accounts.5b00420

11   Liang Zhang, Ph.D. dissertation, "Device physics of perovskite solar cells", Iowa State University (2016)

CHAPTER 8. CONCLUSION AND FUTURE WORK

In this work, we have optimized device efficiency, studied material properties of perovskite, developed a complete physical model based on generation and migration of ions to understand the photon-induced degradation of perovskite solar cells and studied the influence of different factors which can affect the photon-induced degradation of perovskite solar cells. In this chapter, I will summarize my contribution, conclusion of my work and will propose future work based on this report.

8.1 My Contributions and Conclusion

8.1.1 Efficiency optimization of perovskite solar cell

> ➤ We have optimized the power-conversion efficiency of a p-i-n structured solar cell with PTAA as hole transport layer using single solution method. The maximum efficiency obtained is 18.5% which is highest in the literature using single-solution process on PTAA as HTL.

> ➤ We have performed systematic experiments to solve the spreading issue of Perovskite single-solution on PTAA. We have showed that pre-wetting the PTAA substrate before spin-coating of perovskite helps to minimize surface energy and improves spread-ability. Using this method, we could get pin-hole free uniform perovskite layer which improves reproducibility of these devices.

> ➤ We have showed that by increasing PbI_2 to MAI molar ratio can help to mitigate the open-circuit voltage evolution.

> ➤ We have also developed a solvent annealing process to enhance perovskite grain size.

179

8.1.2 Physical parameters of perovskite

➢ We have calculated the dielectric constant of perovskite by using capacitance spectroscopy and showed that the dielectric constant is about 60.

➢ We have calculated the optimum electric field required to initiate ion migration in a n-i-p structured perovskite solar cell and showed that the optimum E-field is about $1\ V\mu m^{-1}$.

8.1.3 Photon-induced degradation of perovskite solar cells

➢ We have developed a complete physical model based on generation and migration of ions to understand the photon-induced degradation of perovskite solar cells. We have showed that the degradation in short-circuit current can be fitted with a double-exponential model. We have also developed a relationship between the change in open-circuit voltage and short-circuit current during photon-induced degradation.

➢ We have studied the contribution of hole transport layer on photon-induced degradation of perovskite solar cells. We have compared devices fabricated on PTAA and NiO as hole-transport layers for this comparative study. Then, we have showed that the photon-induced degradation on both hole-transport layers can be explained by using our model.

➢ We have showed that Indium doped Cadmium Sulfide and Aluminum doped Zinc Oxide as buffer electron transport layers can help the perovskite solar cells fabricated on PTAA to recover completely after photon-induced degradation. These two buffer layers can also enhance the dark-stability of these solar cells. ZnO:Al enhances the environmental stability of perovskite solar cells in

presence of moisture. ZnO:Al can also act as a transparent top contact for bifacial solar cell which can used as a large bandgap cell for a tandem solar cell with c-Si or CIGS.

➢ We have reported that the stoichiometry of perovskite (PbI_2 to MAI molar ratio) affects the photon-induced degradation of perovskite solar cells. Initially, the degradation decreases with increase in PbI_2 to MAI molar ratio before reaching a minimum. Beyond that point the degradation increases with increase in PbI_2 to MAI molar ratio.

➢ Biasing condition during exposure affects the photon-induced degradation of perovskite solar cells. We have showed that degradation when the device is exposed in open-circuit condition is higher compared to degradation in short-circuit condition. This result can also be explained based on our model.

➢ Fabrication techniques of perovskite (Solution vs Vapor) can also affect the photon-induced degradation. The vapor-processed perovskite solar cell which has thinner optimum thickness to achieve maximum power-conversion efficiency degrades slower compared to solution-processed perovskite solar cells.

➢ Grain size of perovskite can affect the photo-stability. Smaller grain-size perovskite is prone to higher migration and generation of ions which leads to higher photon-induced degradation. The grain size of perovskite can be increased using solvent annealing method followed the spin-coating of perovskite. Larger grain size of perovskite enhances the stability of these solar cells.

➢ We have also developed a modified equivalent circuit model to understand the change in photovoltaic parameters of perovskite solar cells. The degradation in short-circuit current density can be modeled using a double-exponential model which explains both migration and generation of ions. The change in open-circuit voltage can be explained by two opposing components: open-circuit voltage increases due to migration from ions from perovskite-transport layers' interfaces towards bulk perovskite and decreases with increase in non-radiative recombination. These factors can be considered with a dependent current source in parallel with the photo-generated current source and a dependent voltage source in series with the diode to have complete equivalent circuit for perovskite solar cells.

8.2 Future Work

The detailed study of photon-induced degradation of vapor-processed perovskite solar cells is important, as the co-evaporated perovskite solar cells have showed great photo-stability. This degradation can depend on different deposition conditions, process parameters as well as the substrate temperature during co-evaporation.

We also need to find ways to enhance the grain size of perovskite. Several methods such as Vacuum-flashed assisted deposition [3] and solvent annealing [1,2] have been proposed for grain enhancement of perovskite. Our study has showed that larger grain-size perovskite enhances photo-stability. So, it is important to enhance the perovskite grain size even more than micrometers, if possible we need to get single crystal perovskite.

Incorporating Cesium (Cs) during fabrication of perovskite can enhance the stability as it has smaller atomic radius and so, less prone to decomposition after forming perovskite. Gratzel et al. [5] have achieved power-conversion efficiency of perovskite solar cell more than 20%. They have used 5% Cesium during the fabrication process. This work also showed a significant increase in photo-stability with 5% incorporation of Cesium.

Finally, photo-instability is a very challenging problem for perovskite solar cells. This problem can be avoided as solar cells must work under light. The first step to solve the problem is to understand the physics behind it. Several factors can affect the photo-instability of perovskite solar cells. Thus, there might not be a single solution, but a combining optimization of several factors may be needed to solve this problem. The promising fact is that different studies have showed this degradation is to be completely recoverable in dark. This phenomenon suggests that the inherent material property doesn't degrade during photon-induced degradation.

183

REFERENCES

1   Z. Xiao, Q. Dong, C. Bi, Y. Shao, Y. Yuan, and J. Huang, "Solvent annealing of perovskite-induced crystal growth for photovoltaic-device efficiency enhancement", Adv. Mater., 26, 6503 (2014). doi:10.1002/adma.201401685

2   J. Liu, C. Gao, X. He, Q. Ye, L. Ouyang, D. Zhuang, C. Liao, J. Mei, and W. Lau, "Improved crystallization of perovskite films by optimized solvent annealing for high efficiency solar cell", ACS applied materials & interfaces, 7, 24008 (2015). doi:10.1021/acsami.5b06780

3   X. Li, D. Bi, C. Yi, J. D. Decoppet, J. Luo, S. M. Zakeeruddin, A. Hagfeldt, and M. Gratzel, "A vacuum flash-assisted solution process for high-efficiency large-area perovskite solar cells", Science, 353, 58 (2016). doi:10.1126/science.aaf8060

4   M. Saliba, T. Matsui, J.-Y. Seo, K. Domanski, J.-P. Correa-Baena, M. K. Nazeeruddin, S. M. Zakeeruddin, W. Tress, A. Abate, A. Hagfeldt, and M. Gratzel, "Cesium-containing triple cation perovskite solar cells: Improved stability, reproducibility and high efficiency", Energy Environ. Sci., 9, 1989 (2016). doi:10.1039/C5EE03874J

APPENDIX A.   PHOTO-DEGRADATION OF PEROVSKITE SOLAR CELLS: MODELING AND SIMULATION

Istiaque Hossain, Liang Zhang, Mehran Samiee, Pranav Joshi, Ranjith Kottokkaran, Max Noack and Vikram L. Dalal*

Iowa State University, Ames, Iowa, 50010, USA

Abstract

Photon-induced degradation is a well-known challenge for perovskite solar cells. In this report, we have developed a complete physical model on understanding the degradation with the help of a modified equivalent circuit model. We have done photo-degradation on p-i-n structured device in open-circuit condition at one-sun intensity and showed that the experimental result matches well with the simulation result based on our model. We have used the theory based on migration and generation of ions during photo-exposure to explain our results. We also have studied influence of Perovskite-HTL interface on photon-induced degradation of perovskite solar cells.

Introduction

Perovskite solar cells have already showed great potential as thin films solar cell with power conversion efficiency exceeding 20% [5] has already been reported. These solar cells can be deposited with both solution [3] or vapor growth [2] techniques. It has showed some very exciting electronic properties such as high absorption coefficient, long diffusion lengths, low midgap defects, high carrier lifetime etc. which attributes to high power conversion efficiencies. But the challenges with perovskite solar cells include instability in presence of

moisture and degradation during photo-exposure. But the detailed device physics of this photon-induced degradation has not been studied yet. In this report, we propose a modified equivalent circuit model to understand the photon-induced degradation for perovskite solar cells.

Device Fabrication

In this experiment, we have used p-i-n structed (light entering from the p-type transport layer) solar cell with structure Glass/ITO/HTL/Perovskite/PC60BM/Al where HTL can be either PTAA or NiO. We have used ITO Coated glass substrate and evaporated 30nm of NiO using Ebeam evaporation followed by annealing at 200°C for 60 minutes in ambient environment. For PTAA 2.18 mg/mL PTAA in toluene was spin-coated at 6000 rpm for 40 seconds followed by annealing at 150°C for 10 minutes. Then, about 1.6 M perovskite solution, contains MAI (methylammonium iodide), PbI_2, DMSO (Dimethyl sulfoxide) in DMF (Dimethylformamide) with molar ratio of 1:1.05:1, was spin coated at 4000 rpm for 25 seconds with drop cast chlorobenzene on 10 seconds' delay using Park's recipe [3]. This gives about 600nm of perovskite layer thickness. Then it was annealed at 60°C for 1 minute followed by 100°C for 5 minutes. Then 20 mg/mL PC60BM in chlorobenzene solution was spin coated at 2000 rpm for 40 seconds. Finally, 100 nm of Aluminum was deposited using thermal evaporation. The light IV curve of this device has been reported in Fig. 1 before photon-induced degradation with power conversion efficiency of 15.5% on NiO and 18.4% on PTAA.
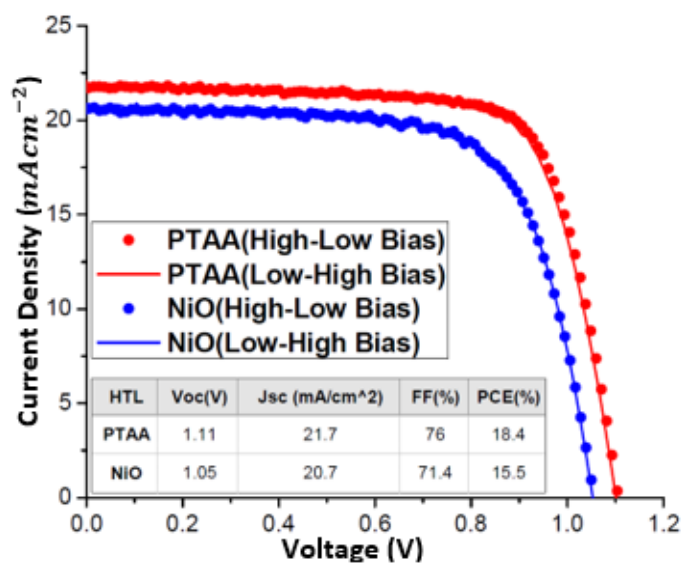
Fig. 1. Light IV curve of p-i-n perovskite solar cell before photon-induced degradation, measured at 1 sun intensity (AM1.5). This device doesn't show any hysteresis in light IV characteristics.

Photon-induced Degradation

Photon-induced degradation of this device was measured at one-sun intensity (AM1.5) with a solar simulator in open-circuit condition for 100 hours. The photovoltaic parameters such as open-circuit voltage, short-circuit current, fill factor and power conversion efficiencies were measured at every 10 minutes in a nitrogen filled glovebox with both oxygen and moisture less than 0.1 ppm.

The photon-induced degradation result has been reported in Fig. 2. Please note decrease in short-circuit current during this degradation for both devices, but open circuit voltage increases on NiO and decreases on PTAA. These results have been explained physically by Pranav et al. by migration and generation of ions theory [1,6]. We will develop a complete model using a modified equivalent circuit in later part of this appendix.

Simulation Results and Discussions

A. Short-circuit current degradation:

It is very well known that there are mobile ions present in bulk perovskite which can redistribute themselves in presence of electric field. At thermal equilibrium, the positive ions move towards the HTL and negative ions move towards to ETL due to internal electric field. Because of high electric field present at the interfaces these ions do not contribute to recombination with photo-generated carriers. But during exposure in open-circuit condition as the internal electric field decreases the mobile ions can migrate towards bulk perovskite. And in addition to that more ions are generated by high energy photons. The generated electron hole pairs recombine with the ions to contribute to current loss. The degradations in short-circuit current density can be fitted with a double-exponential equation as,
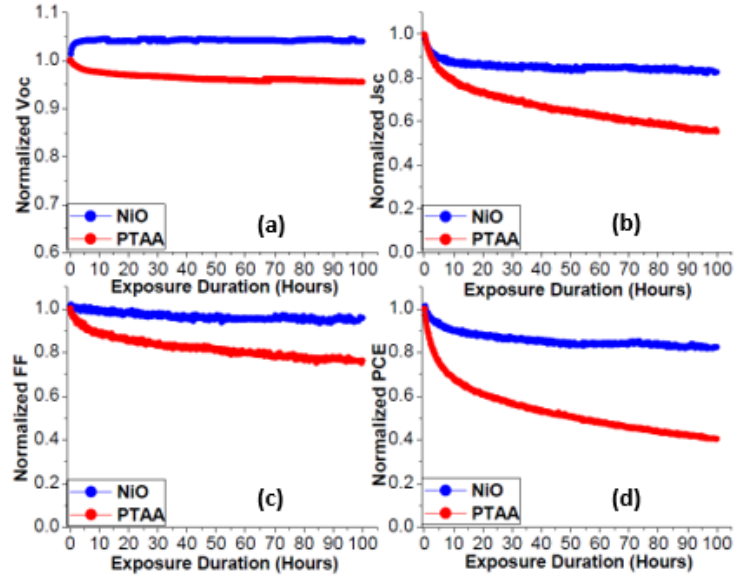
Fig. 2. Photon-induced degradation comparison of these two p-i-n devices under one-sun intensity (AM1.5) for 100 hours (a) Normalized open-circuit voltage degradation (b) Normalized short-circuit current degradation (c) Fill-factor degradation (d) Degradation in power conversion efficiency.

$$J_{sc}(t) = J_{sc,t=0} - \Delta J_{sc} \tag{1}$$

$$\Delta J_{sc} = J_{sc,t=0} \left[a_m \left(1 - e^{-\frac{t}{t_{cm}}} \right) + a_g \left(1 - e^{-\frac{t}{t_{cg}}} \right) \right] \tag{2}$$

With boundary conditions,

$$(i) \; a_m + a_g = \frac{\Delta J_{sc}}{J_{sc,t=0}} \Big|_{t \to \infty} \qquad (ii) \Delta J_{sc} = 0 \text{ at } t=0 \qquad (3)$$

It is understandable why we need two exponentials to fit the short-circuit current degradation if we consider both migration and generation of ions contribute in this photon-induced degradation. We can consider the first exponential takes care of the migration of ions with a time constant of t_{cm} and a magnitude of a_m . And the second exponential models the generation of ions with a time constant of t_{cg} and a magnitude of a_g. For NiO the values which can describe the short-circuit current degradation are: t_{cm}=2 hours, a_m=0.084 mA/cm^2, t_{cg}=20 hours, a_g= 0.084 mA/cm^2. For PTAA the values are: t_{cm}=2 hours, a_m=0.15 mA/cm^2, t_{cg}=42 hours, a_g= 0.3 mA/cm^2. The dependent current source in the proposed equivalent circuit model takes this degradation in short-circuit current density. The magnitude of this dependent current source is given by,

$$I_i(t) = I_{sc,t=0} \left[a_m \left(1 - e^{-\frac{t}{t_{cm}}} \right) + a_g \left(1 - e^{-\frac{t}{t_{cg}}} \right) \right] \qquad (4)$$

B. Change in Open-circuit voltage:

There are two components which play a role in evolution of open-circuit voltage. First, increase in open-circuit voltage due to migration of ions from interfaces to bulk perovskite. Second, decrease in open-circuit voltage due to increase in non-radiative recombination. At thermal equilibrium, ions near the contact layers create an electric field opposing the built-in electric field. Thus, reduces the net electric filed and reduces the open-circuit voltage. Here, the parameter V_d is defined as the difference in open circuit voltage if there are no ions at thermal equilibrium ($V_{oc,0}$) and the actual open circuit voltage measured at time t=0 ($V_{oc,t=0}$, before exposure). The V_d for NiO is 0.07 V and for PTAA is 0.01 V. At the onset of photo-degradation

these ions start moving from the perovskite-contact layer interfaces towards the neutral bulk region and so, the open circuit voltage starts to increase towards the value if there were no ions present at thermal equilibrium with a time constant t_{cm}=2 hours which is consistent with the time constant obtained from degradation in current. This is first component behind the change in open circuit voltage. So, the change in open-circuit voltage due to ion migration is given by,

$$\Delta V_{oc,i}(t) = V_d \left(1 - e^{-\frac{t}{t_{cm}}}\right); \; V_d = V_{oc,0} - V_{oc,t=0} \tag{5}$$

$$V_{oc,0} = \frac{nkT}{q} ln\left(\frac{J_l}{J_0} + 1\right) \tag{6}$$

As ions are generated during exposure, these ions recombine with the generated electron hole pairs and there is an increase in non-radiative recombination. Due to increase in recombination the lifetime of electrons and holes will decrease. Thus, the open circuit voltage will decrease. The expression of open circuit voltage considering non-radiative recombination, but no ion migration is given by [4],

$$V_{oc,r} = \frac{kT}{q} ln(\frac{N_B J_{sc}\tau}{q n_i^2 W}) \tag{7}$$

The expression for decrease in open-circuit voltage due to increase in non-radiative recombination can be derived as equation (8),

$$\Delta V_{oc,r}(t) = V_{oc,r,t=0} - V_{oc,r,t=t} = 3\frac{kT}{q} ln(\frac{J_{sc,t=0}}{J_{sc,t=t}}) \tag{8}$$

The total change in open-circuit voltage during photon-induced degradation can be given by equation (10),

$$\Delta V_{oc}(t) = V_{oc,t=t} - V_{oc,t=0} = \Delta V_{oc,i}(t) - \Delta V_{oc,r}(t) \tag{9}$$

$$\Delta V_{oc}(t) = V_d \left(1 - e^{-\frac{t}{t_{cm}}}\right) - 3\frac{kT}{q} ln(\frac{J_{sc,t=0}}{J_{sc,t=t}}) \tag{10}$$

This change in open-circuit voltage can be incorporated in the equivalent circuit in figure

3 as a dependent voltage source in series with the diode. The magnitude of which can be given by,

$$V_i(t) = V_d(1 - e^{-\frac{t}{t_{cm}}}) - 3\frac{kT}{q}\ln(\frac{J_{sc,t=0}}{J_{sc,t=t}}) \tag{11}$$
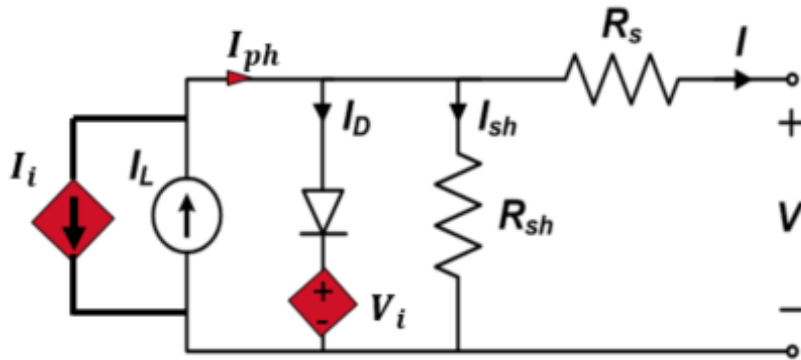
Fig. 3. Proposed modified equivalent circuit model for perovskite solar cells

The total current extracted from the circuit is given by,

$$I = I_L - I_i - I_0\left[\exp\left(\frac{q(V-V_i)}{nkT}\right) - 1\right] - \frac{V+IR_s}{R_{sh}} \tag{12}$$
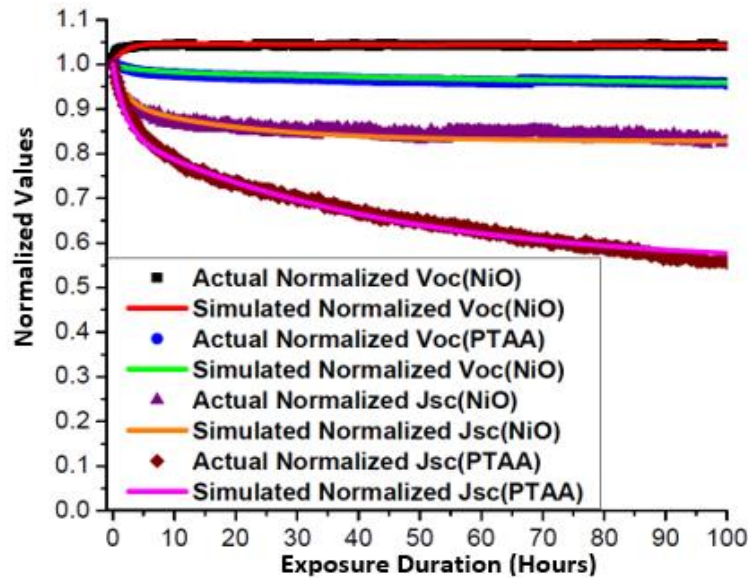
Fig. 4. Comparison of normalized change in open-circuit voltage and short-circuit current degradation between experimental and simulated result obtained from our model.
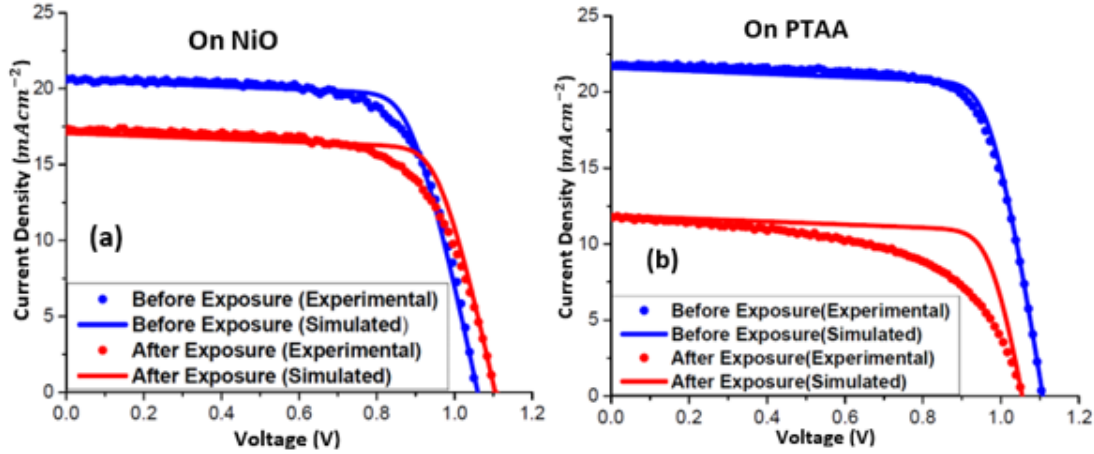
Fig. 5. Comparison of Light IV curves simulated using the equivalent circuit model (Fig. 3) before and after degradation for 100 hours at one-sun intensity with the experimental Light IV curves (a) on NiO (b) on PTAA

Fig.4 shows the comparison between experimental and simulated results over 100 hours of photon-induced degradation for normalized open-circuit voltage and short-circuit current. Fig. 5 shows the simulated light IV using the equivalent circuit diagram in Fig. 3 before and after degradation along with the experimental results obtained on the p-i-n solar cell. The mismatch in light IV after degradation between actual and simulated result comes from the degradation in series and shunt resistance which we ignored in our equivalent circuit model.

Finally, we have developed a comprehensive model based on device physics which explains quantitatively the influence of ion-induced recombination and migration of ions from the interfaces into the middle of the device. The experimental data on both current and voltage degradation perfectly match the model. We have also showed how different interfaces affect stability and show that this phenomenon can also be described by using the universal model that we have developed.

Conclusion

Both generation and migration of ions contribute to the photon-induced degradation of perovskite solar cells. The degradation in short-circuit current density can be modeled using a double-exponential model which explains both migration and generation of ions. The change in open-circuit voltage can be explained by two opposing components: open-circuit voltage increases due to migration from ions from perovskite-transport layers' interfaces towards bulk perovskite and decreases with increase in non-radiative recombination. These factors can be considered with a dependent current source in parallel with the photo-generated current source and a dependent voltage source in series with the diode to have complete equivalent circuit for perovskite solar cells. The perovskite-HTL interface also plays a significant role in photon-induced degradation of perovskite solar cells.

Acknowledgement

References

[1]   Pranav H. Joshi, Liang Zhang, Istiaque M. Hossain, Hisham A. Abbas, Ranjith Kottokkaran, Satyapal P. Nehra, Mahendra Dhaka, Max Noack, and Vikram L. Dalal, in AIP Advances 6, 115114 (2016).

[2]   Hisham A. Abbas, Ranjith Kottokkaran, Balaji Ganapathy, Mehran Samiee, Liang Zhang, Andrew Kitahara, Max Noack and Vikram L. Dalal, in APL materials, 3, 016105 (2015).

[3]   Namyoung Ahn, Dae-Yong Son, In-Hyuk Jang, Seong Min Kang, Mansoo Choi, and Nam-Gyu Park, in J. Am. Chem. Soc. 137, 8696−8699 (2015).

[4]   Ronald A. Sinton, in Applied Physics Letters, 69, 2510 (1996).

[5]   Woon Seok Yang, Byung-Wook Park, Eui Hyuk Jung, Nam Joong Jeon, Young Chan Kim, Dong Uk Lee, Seong Sik Shin, Jangwon Seo, Eun Kyu Kim, Jun Hong Noh, Sang Il Seok, in Science, Vol. 356, Issue 6345, pp. 1376-1379 (2017).

[6]   Pranav Joshi, Liang Zhang, Ranjith Kottokkaran, Hisham Abbas, Istiaque Hossain, Satyapal Nehra, Mahendra Dhaka, Max Noack

APPENDIX B.   CdS:In/ZnO:Al AS BUFFER ELECTRON TRANSPORT LAYERS FOR INPROVEMENT IN ENVIRONMENTAL STABILITY AND DARK RECOVERY AFTER PHOTON-INDUCED DEGRADATION OF PEROVSKITE SOLAR CELLS

A paper to be submitted

Istiaque Hossain, Liang Zhang, Ranjith Kottokkaran, Hisham Abdussamad-Abbas, Max Noack and Vikram L. Dalal

Iowa State University, Ames, Iowa, 50010, USA

Abstract

Photon-induced degradation in power conversion efficiency of perovskite solar cells is a very well-known phenomenon. In this work, we report that Indium doped CdS and Aluminum doped ZnO as electron transport layers improve the dark recovery after photon-induced degradation as they act as buffer layers to protect the aluminum contacts from mobile iodine ions. It also improves the stability in presence of moisture by encapsulation of perovskite. We also report the highest efficiency (18.4%) of p-i-n structured perovskite solar cells on PTAA using single solution process.

Introduction

Organolead trihalide perovskite (OTP) as a light absorbing material has already showed huge potential in photovoltaic applications. More than 20% efficiency has already been reported by several groups. Some research groups have already reported high diffusion length [1,2,3,4], high carrier lifetime [3], and large absorption coefficient [5] etc. as attributes towards high power conversion efficiency. Despite of this tremendous light conversion efficiency they show some very interesting electronic characteristics. Some research groups have reported that these perovskite-based devices show transient behavior [6] which might be responsible for

dependence of light IV measurement on scan direction, scan speed, and light and voltage preconditions before light IV measurement [6,7,8]. Light IV hysteresis and voltage evolution also showed dependence on device structure and contact layers (Electron and hole transport layers). Photon-induced degradation is also challenging problem which needs to be solved before making perovskite commercially viable. But the encouraging sign is that some of these devices show complete recovery in dark after photon induced degradation which proves that this degradation is reversible [11,12]. To make perovskite solar cells reliable for commercialization, we need to find the proper device structure with suitable transport layers. In this report we will demonstrate that using both CdS and ZnO we can improve the ambient stability of perovskite solar cells.

Device Fabrication

We have used ITO Coated glass substrate and spin coated 2.18 mg/mL PTAA solution in toluene at 6000 rpm for 40 secs which gives a thickness of about 20nm. Then annealed at 150°C for 10 mins. We have pre-wetted the PTAA substrate with DMF before spin-coating perovskite which reduces the surface energy and enhances the spread-ability of perovskite solution. Then, about 1.6 M perovskite solution, contains CH_3NH_3I, PbI_2, DMSO in DMF with molar ratio of 1:1.05:1, was spin coated at 4000 rpm for 25 seconds with drop cast chlorobenzene on 10 seconds' delay. This gives about 600nm of perovskite layer thickness. Then it was annealed at 60°C for 1 minute followed by 100°C for 5 minutes. Then 20 mg/mL $PC_{60}BM$ in chlorobenzene solution was spin coated at 2000 rpm for 40 seconds. Then the whole structure was annealed at 100°C for 15 minutes. Indium doped CdS (about 25nm) was deposited using thermal evaporator and Aluminum doped ZnO (about 280nm) was deposited

using sputtering. Both CdS and ZnO layers serve as buffer layers which enhances stability of these devices. Finally, about 100 nm of Aluminum was deposited using thermal evaporator. FIG. 2 shows the light IV characteristics of those two devices.
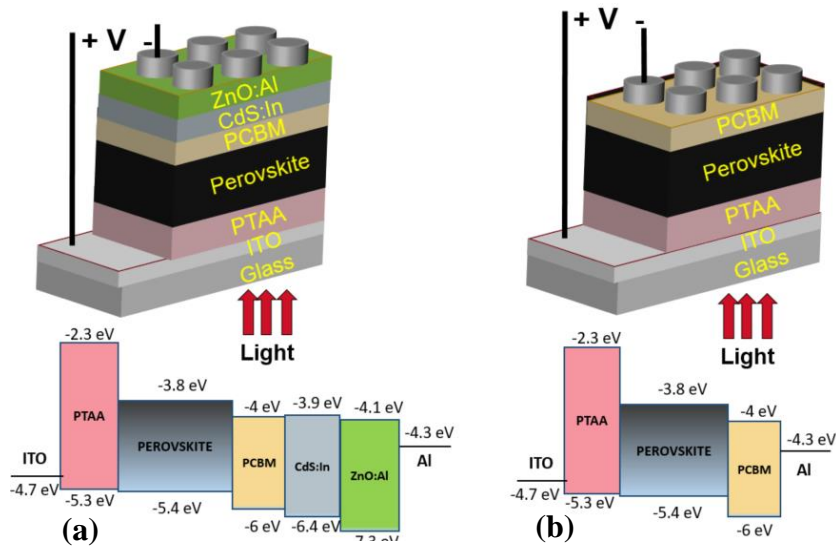
FIG 1: Device structures with corresponding band edges used in this experiment (a) With CdS/ZnO as buffer layers (b) With no buffer layers
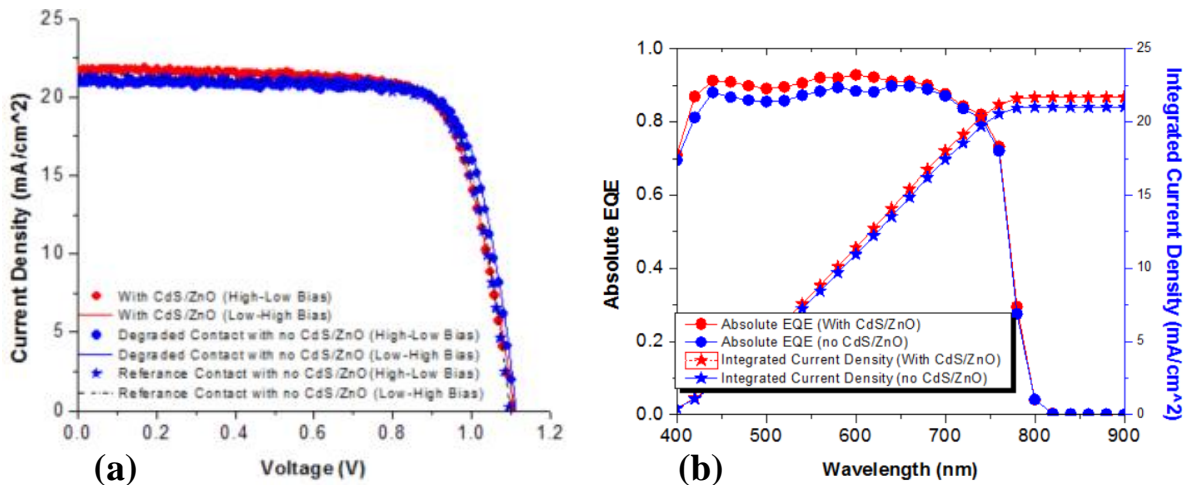
FIG 2: (a) Light IV measurements before photon-induced degradation (b) Absolute external quantum efficiency and integrated current density for both devices before photon-induced degradation; Red represents Light IV for device with CdS/ZnO as buffer layers, Blue represents Light IV for device with no buffer layers

FIG. 1 shows the device structure and corresponding band edges which are being compared for this photo-degradation study. One of them (FIG. 1a) has two extra layers Indium

doped Cadmium Sulfide and Aluminum doped Zinc Oxide which work as buffer layers. The other device (FIG. 1b) doesn't have these two extra layers. Both the devices showed above have similar efficiencies to start with. The device with CdS/ZnO as buffer layer has a starting power conversion efficiency of 18.4% and the control device had power conversion efficiency of about 17.8%. To make sure that all the changes are due to photon-induced degradation we have a reference contact with similar efficiency which doesn't show any degradation over time in dark. The photovoltaic parameters of these three devices before any degradation has been reported in Table 1. None of the devices showed any hysteresis in light IV measurements. FIG. 2 shows the initial light IV measurement before photon-induced degradation and absolute external quantum efficiency measurements of these devices.

Table 1: Photovoltaic parameters for perovskite solar cells before photon induced degradation

Device Structure	$V_{oc}(V)$	$J_{sc}(mA/cm^2)$	FF(%)	PCE (%)
With CdS/ZnO as buffer layers	1.11	21.7	76	18.4
No buffer layers-Degraded contact	1.11	21.3	75	17.8
No buffer layers-Reference contact	1.11	21	76	17.7

Results

The photo-degradation comparison for these two devices has been measured at open-circuit condition for 100 hours at one-sun intensity (AM1.5). FIG. 3 shows that both degraded almost similarly over 100 hours. Table 2 shows that degradation of all the photovoltaic parameters are comparable after 100 hours of photon-induced degradation.
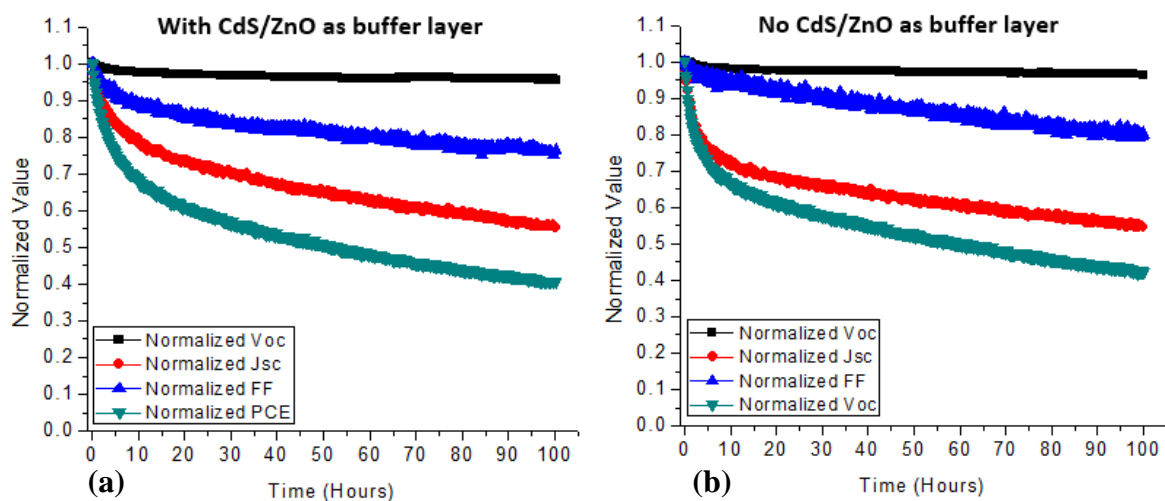
FIG. 3: Photo-degradation summary for 100 hours at one-sun intensity (AM1.5) (a) Device with CdS/ZnO as buffer layer (b) Device with no buffer layers

Table 2: Photon-induced degradation (in percentage) of photovoltaic parameters after exposing for 100 hours at 1 sun intensity in open-circuit condition

Device Structure	$V_{oc}(V)$	$J_{sc}(mA/cm^2)$	FF(%)	PCE (%)
With CdS/ZnO as buffer layers	4%	45%	24%	58%
No buffer layers-Reference contact	4%	45%	20%	57%

*Note: All the parameters decrease with time during photon induced degradation

The interesting factor is that the device which had CdS and ZnO as buffer layers has completely recovered after kept in dark for 43 hours [FIG. 4(a)]. But the device which didn't have CdS and ZnO as buffer layers didn't recover even after 43 hours in dark [FIG. 4(b)]. But the reference device in FIG. 5 shows no change during this period which proves that all these changes are due to photon-induced degradation only. The photovoltaic parameters of these devices before degradation, after degradation and after recovery in dark have been reported in Table 3.
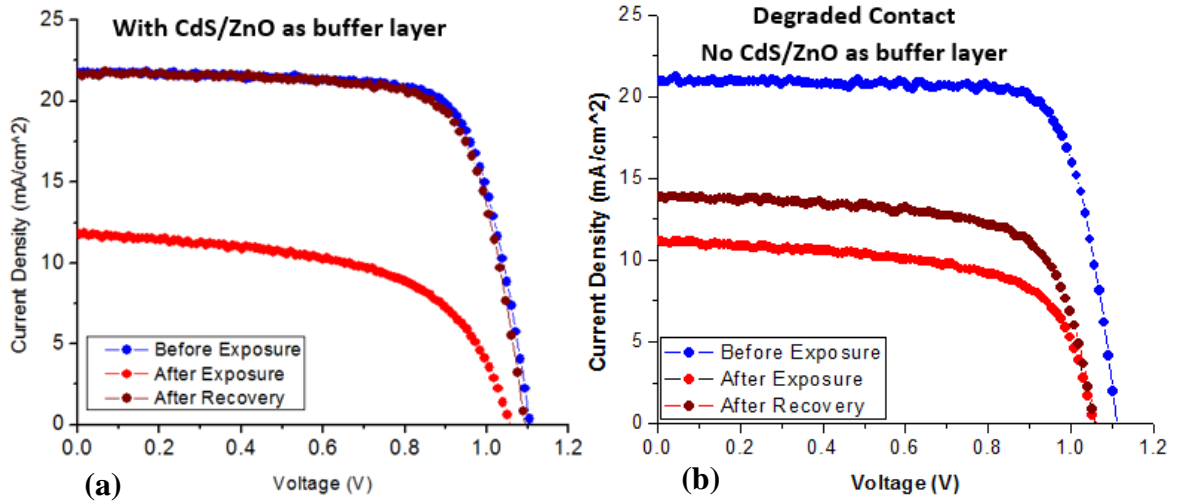
FIG. 4: Light IV recovery in dark after photon-induced degradation for 100 hours at one-sun intensity (AM1.5) (a) Device with CdS/ZnO as buffer layers (b) Device with no buffer layers

Table 3: Photovoltaic parameters comparison for perovskite solar cells before and after degradation along with after recovery

Device Structure		$V_{oc}(V)$	$J_{sc}(mA/cm^2)$	$FF(\%)$	PCE (%)
With CdS/ZnO as buffer layers	Before Degradation	1.11	21.7	76	18.3
	After Degradation	1.06	12.1	59	7.6
	After Recovery	1.10	21.7	75	17.9
No buffer layers-Degraded contact	Before Degradation	1.11	21.3	75	17.8
	After Degradation	1.07	11.7	61	7.6
	After Recovery	1.07	14	69	10.3
No buffer layers-Reference contact	Before Degradation	1.11	21	76	17.7
	After Degradation	1.11	20.8	76	17.6
	After Recovery	1.11	20.5	77	17.5

FIG. 5: Light IV characteristics of the reference device which shows no change during this period
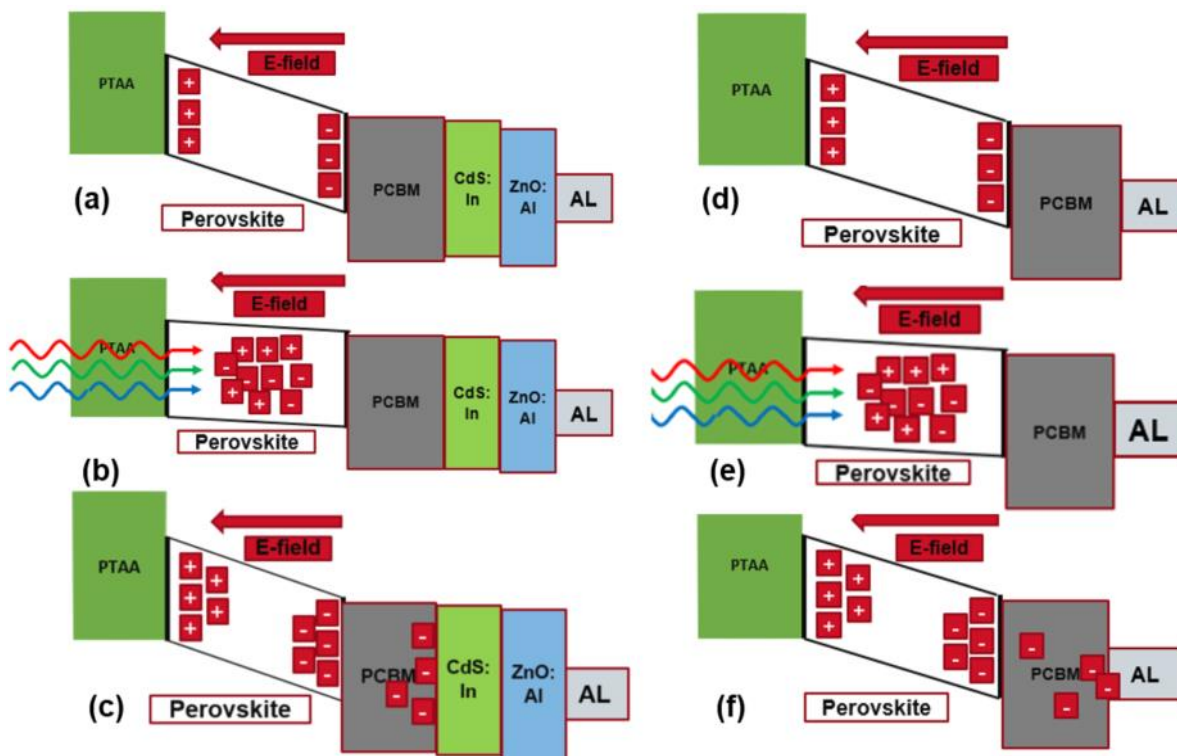
FIG. 6: Band diagrams to explain recovery in dark after photo-degradation (a),(b),(c) migration and generation of ions during photo-degradation followed by recovery in dark where CdS/ZnO as blocking layer which helps the device to recover completely even after photo-degradation for 100 hours at one-sun intensity (d),(e),(f) migration and generation of ions during photo-degradation followed by recovery in dark where there is no CdS/ZnO buffer layer. During recovery, the Aluminum contact is contaminated by iodine ions as they migrate through PCBM layer. Thus, the device doesn't recover after photo-degradation for 100 hours at one-sun intensity

These photo-degradation and recovery results can be explained by the simplified band-diagrams showed in FIG. 6 and using the explanation by Lee et al. that iodine ions can contaminate the metal contacts leading to a permanent degradation for these devices (Ref 9). This figure explains the recovery in dark after photo-degradation for devices with and without CdS/ZnO as blocking layers. At thermal equilibrium, due to built-in E-filed positive ions go towards hole transport layer (HTL) and negative ions go towards electron transport layer (ETL) [FIG. 6 (a) and (d)]. So, we have net electric field inside the active layer. Due to high electric field at the interfaces these ions do not recombine with generated electron-hole pairs. During exposure in open-circuit condition, due to decrease in internal E-field these ions migrate towards the intrinsic active layer. And in addition to that more ions are generated by high energy photons [FIG. 6 (d) and (e)]. The generated electron hole pairs recombine with the ions to contribute to current loss.

Just after exposure [FIG. 6 (c) and (f)] there are more mobile ions present inside bulk perovskite. During recovery, there is sudden increase in electric field from the ETL to HTL inside bulk perovskite. And as the activation energy of migration for iodine ions is lowest (ref 10) and so they are very easy to migrate. During recovery, suddenly the negative ions' concentration at Perovskite-PCBM interface increases. These ions have high enough energy to punch through PCBM and react with Aluminum [FIG. 6 (f)]. As these iodine ions contaminate Aluminum contact permanently, the series resistance and short circuit current don't recover. But in case of the device with CdS and ZnO, these iodine ions are blocked by these buffer layers [FIG. 6 (c)]. Consequently, this device completely recovers as the Aluminum contact doesn't get contaminated by iodine ions.
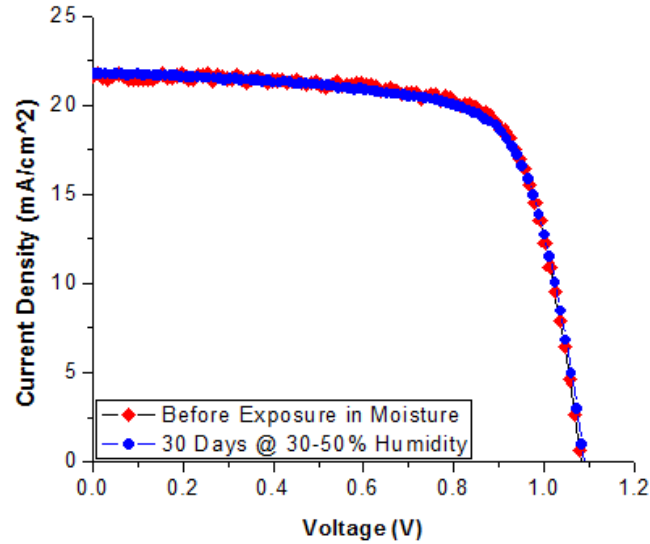
FIG. 7: Light IV response of perovskite solar cell with CdS/ZnO as buffer layers (i) Just after fabrication (ii) After device was kept in 30-50% humidity for 30 days.

CdS and ZnO as buffer layers also help to improve the stability of these devices in presence of moisture. FIG. 7 shows the light IV comparison of perovskite solar cell with CdS/ZnO as buffer layers before exposure in moisture (pristine device), and measured after it was kept at 30-50% humidity outside glovebox for 30 days. Perovskite solar cells with no CdS/ZnO as buffer layer degrades immediately after exposure to moisture but adding CdS/ZnO as buffer layer improves the device stability in ambient environment for more than 30 days. Table 4 shows the photovoltaic parameters of this device before and after exposure in moisture.

Table 4: Photovoltaic parameters for a device with CdS/ZnO as buffer layers before and after exposure in moisture

Condition	$V_{oc}(V)$	$J_{sc}(mA/cm^2)$	FF(%)	PCE (%)
Before Exposure in Moisture	1.09	21.6	74	17.4%
After 30 days @30-50% Humidity	1.09	21.5	71	16.7%

References

1. Zhi Guo, JS Manser, Y Wan, PV Kamat & L Huang, Nature communications, 6, 7471 (2015)

2. Samuel D. Stranks, Giles E. Eperon, Giulia Grancini, Christopher Menelaou, Marcelo J. P. Alcocer, Tomas Leijtens, Laura M. Herz, Annamaria Petrozza & Henry J. Snaith, Science, 342, pp. 341-344 (2013)

3. C Wehrenfennig, GE Eperon, MB Johnston, Henry J. Snaith & Laura M. Herz, Advanced Materials, DOI: 10.1002 (2013)

4. Guichuan Xing, Nripan Mathews, Shuangyong Sun, Swee Sien Lim, Yeng Ming Lam, Michael Grätzel, Subodh Mhaisalkar & Tze Chien Sum, Science, 342, pp. 344-347 (2013)

5. MA Green, A Ho-Baillie & HJ Snaith, Nature photonics, 8, pp. 506-509 (2014)

6. E. L. Unger, E. T. Hoke, C. D. Bailie, W. H. Nguyen, A. R. Bowring, T. Heumüller, M. G. Christoforo and M. D. McGehee, Energy Environ Science, 7, 3690-3698 (2014)

7. W. Tress, N. Marinova, T. Moehl, S. M. Zakeeruddin, Mohammad Khaja Nazeeruddin and

M. Grätzel, Energy Environ Science, 8, 995-1004 (2015)

8. Hui-Seon Kim and Nam-Gyu Park, J. Physical Chemistry Letters, 5 (17), pp 2927–2934 (2014)

9. Hyungcheol Back,a Geunjin Kim,a Junghwan Kim,a Jaemin Kong,a Tae Kyun Kim,a Hongkyu Kang,a Heejoo Kim,a Jinho Lee,b Seongyu Leeb and Kwanghee Lee, Energy Environ. Sci., 9, 1258-1263 (2016)

10. Christopher Eames, Jarvist M. Frost, Piers R. F. Barnes, Brian C. O'Regan, Aron Walsh & M. Saiful Islam, Nature Communications 6, Article number: 7497 (2015)

11. Pranav H. Joshi, Liang Zhang, Istiaque M. Hossain, Hisham A. Abbas, Ranjith Kottokkaran, Satyapal P. Nehra, Mahendra Dhaka, Max Noack, and Vikram L. Dalal, AIP Advances 6, 115114 (2016)

12. Pranav Joshi, Liang Zhang, Ranjith Kottokkaran, Hisham Abbas, Istiaque Hossain, Satyapal Nehra, Mahendra Dhaka, Max Noack, Vikram Dalal, Photovoltaic Specialists Conference (PVSC), 2016 IEEE 43rd, pages 0242-0248

APPENDIX C.   UNDERSTANDING THE EFFECT OF STOICHIOMETRY IN PHOTON INDUCED DEGRADATION OF PEROVSKITE SOLAR CELLS

A paper to be submitted

Istiaque Hossain, Liang Zhang, Laila-Parvin Poly, Max Noack and Vikram L. Dalal

Iowa State University, Ames, Iowa, 50010, USA

Abstract

In this work, we investigate the effect of stoichiometry (PbI_2 to CH_3NH_3I $malor$ $ratio$) on photon induced degradation of p-i-n structured solution-processed perovskite ($CH_3NH_3PbI_3$) solar cells. We did comparative study with different molar ratio of PbI_2 to CH_3NH_3I (1, 1.025, 1.05, 1.075 & 1.10) on photon induced degradation for 100 hours under 1 sun intensity in open-circuit condition. We report the highest efficiency (18.5%) of p-i-n structured perovskite solar cells on PTAA using single solution process. We also showed that degradation in short-circuit current density can be fitted with two additive exponential terms which can be explained by both migration and generation of ions within bulk perovskite during photon-induced degradation.

Introduction

Organolead trihalide perovskite (OTP) as a light absorbing material has already showed huge potential in photovoltaic applications. There has already been a rapid increase in power conversion efficiency with maximum being 22.1% [1]. Already several groups have confirmed an efficiency > 20% [1,2]. Very high diffusion lengths of photo-generated carries have been reported by several research groups which enables these devices to have very good collection efficiencies [3,4,5,6]. People have also reported that perovskite as absorber layer shows high

carrier lifetime [5], and large absorption coefficient [7] etc. as attributes towards high power conversion efficiency. Despite of this tremendous light conversion efficiency they show some very interesting electronic characteristics [8,9,10,11,12]. Some research groups have reported that these perovskite-based devices have mobile ions present in the active layer and these ions show transient behavior with applied electric field [6] which might be responsible for dependence of light IV measurement on scan direction, scan speed, and light and voltage pre-biasing conditions before light IV measurement [13,14,15,16]. Light IV hysteresis and voltage evolution also showed dependence on device structure and contact layers (Electron and hole transport layers). In this report, we will investigate the effect of stoichiometry (PbI_2 to CH_3NH_3I $malor$ $ratio$ in $perovskite$ $precusor$ $solution$) which affects the ion density inside bulk perovskite on photon-induced degradation.

Device Fabrication

We have used ITO Coated glass substrate and spin coated 2.18 mg/mL PTAA solution in toluene at 6000rpm for 40 seconds which gives a thickness of about 20nm. Then annealed at 150°C for 10 minutes. The perovskite precursor solution has high contact angle with the PTAA substrate. As a result, the precursor perovskite solution spreads very poorly on PTAA and leads to a lot of pin-holes in the perovskite film. Here we have prewetted the PTAA substrate with DMF which helps to reduce the surface energy and enhances spread-ability of perovskite precursor solution on PTAA substrate by increasing the contact angle at the interface [17]. So, we have pre-wetted the PTAA substrate with DMF before spin-coating perovskite which improves the film quality with almost no pin-holes. For our control device about 1.6 M perovskite solution, contains CH_3NH_3I, PbI_2, DMSO in DMF with molar ratio of

1:1.05:1, was spin coated at 4000rpm for 25 seconds with drop cast of chlorobenzene on 10 seconds' delay as showed in $FIG.$ 1 [18]. This gives about 600nm of perovskite layer thickness. Then it was annealed at 60°C for 1 minute followed by 100°C for 5 minutes. Then 20mg/mL PC60BM in chlorobenzene solution was spin coated at 2000 rpm for 40 seconds. Then the whole structure was annealed at 100°C for 15 minutes. Finally, about 100 nm of Aluminum was deposited using thermal evaporator. The highest power conversion efficiency of the control device recorded was 18.5% with average being 16.8±0.76%. For this study, solar cells were fabricated with different molar ratio between PbI_2 to CH_3NH_3I in the precursor perovskite solution for photon-induced degradation study. The device structure and power conversion efficiencies of perovskite solar cells with different molar ratio (1, 1.025, 1.05, 1.075 & 1.10) have been reported in FIG. 2 and Table 1.
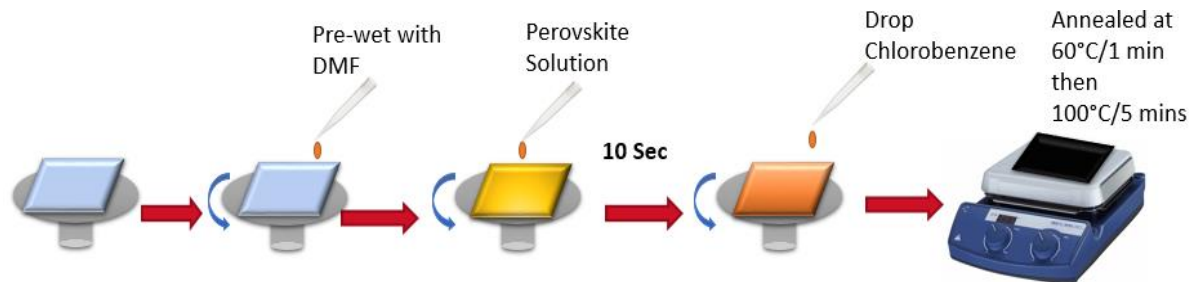
FIG. 1: Schematic of spin-coating of perovskite on PTAA substrate

Table 2: Photovoltaic parameters for perovskite solar cells fabricated with different stoichiometry

$[PbI_2]/[MAI]$	$V_{oc}(V)$	$J_{sc}(mA/cm^2)$	$FF(\%)$	PCE (%)
1*	1.07	21.6	68	15.7
1.025**	1.11	21.8	74	18.0
1.05	1.11	21.3	75	17.7
1.075	1.12	20.1	74	16.7
1.10**	1.11	22	75	18.4

*Note: **Measured *4 minutes & **2 minutes after exposing under 1X(AM1.5) intensity***

FIG. 2: (a) Device structure and band edges of perovskite solar cell, light IV along with power conversion efficiencies for devices fabricated with different PbI_2 to CH_3NH_3I molar ratio (b) $[PbI_2]/[MAI]=1$ (c) $[PbI_2]/[MAI]=1.025$ (d) $[PbI_2]/[MAI]=1.05$ (e) $[PbI_2]/[MAI]=1.075$ and (f) $[PbI_2]/[MAI]=1.10$. The solid line represents light IV scanned from low to high bias and dotted line represents light IV scanned from high to low bias. None of the light IV measurements show any hysteresis.

Results

We studied the photon-induced degradation of these devices for 100 hours under 1 sun intensity (AM1.5) in open-circuit condition. The photon-induced degradation and comparison among degradation in short-circuit current density over 100 hours have been reported in FIG. 3. The key take-away from this photon-induced degradation study is that the degradation decreases relative increase in PbI_2 before it reaches a minimum and then again increases with relative increase in PbI_2. The normalized degradation in short-circuit current density after 100 hours as a function of PbI_2 to CH_3NH_3I malor ratio has been reported in FIG. 4. The

degradation index has been calculated as,

$$Normalized\ J_{sc}\ degradation\ (t = 100\ Hours) = 1 - \frac{J_{sc,t=100\ hours}}{J_{sc,t=0}}$$

This photon-induced degradation has been repeated several times with different stoichiometry and the cumulative standard error of experiment for this degradation index was calculated as 0.016. This standard error has been used as error bar in FIG. 4. This result can be explained considering both migration and generation of ions during photon induced degradation [18,19]. The stoichiometry of perovskite precursor solution can affect the initial density of ions at perovskite-transport layer interfaces (FIG. 5). When we have used 1:1 molar ratio between $PbI_2\ and\ CH_3NH_3I$ there some positive MA^+ and negative I^- ions present inside bulk perovskite as according to Walsh et al. this kind of decomposition has lowest formation energy. Thus, the formation of perovskite along with formation of initial ions can be explained by the following chemical reaction:

$$a * MAI + \ a * PbI_2 \rightarrow \ y * (MA^+ + I^-) + z * MAPbI_3$$
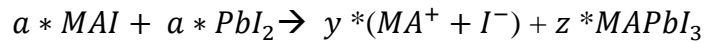
a, y and z are all constants.

In presence of internal electric-field the positive MA^+ ions migrate towards the perovskite-HTL interface and negative I^- ions migrate towards perovskite-ETL interface (FIG. 5). Because of very high electric field at the interface these ions do not recombine with photo-generated electron-hole pairs. Thus, the initial short-circuit current density before exposure is not affected by this interface trapped ions. But, during the photon-induced degradation in open-circuit condition these ions can migrate towards the neutral perovskite region. There are more ions generated by high energy photons. These ions in bulk perovskite act as recombination centers for photo-generated electron-hole pairs. Thus, the reduction in collection efficiency leads to the degradation in short-circuit current density.

Now, if we increase the relative concentration of PbI_2 in the perovskite precursor solution, these excess of PbI_2 can shift the chemical reaction to reduce initial ion densities by forming more perovskite atoms. This phenomenon can be explained by the following chemical reaction:

$$y*(MA^+ + I^-) + z*MAPbI_3 + x_1*PbI_2 \rightarrow y'*(MA^+ + I^-) + z'*MAPbI_3$$

Here, y, z, x_1, y' and z' are all constants. Also, $y' < y$ and $z < z'$. x_1 represents the excess of PbI_2.

Lower initial ion densities at the interfaces leads to lower degradation in short-circuit current density. As we have seen when the $PbI_2 \ to \ CH_3NH_3I$ molar ratio changes from 1 to 1.025 the normalized degradation in short-circuit current density decreases. If we keep increasing the relative concentration of PbI_2 at some point we can eliminate the initial densities of ions trapped at the interfaces and the degradation in short-circuit current density reaches minimum (FIG. 5). That chemical reaction can be illustrated from the following equation:
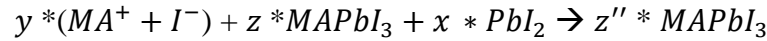
$$y*(MA^+ + I^-) + z*MAPbI_3 + x*PbI_2 \rightarrow z''*MAPbI_3$$

Here, y, z, x and z'' are all constants. Also, $z < z''$. x represents the excess of PbI_2.

If we keep increasing the relative concentration of PbI_2 then we are adding excess of PbI_2 which can easily decompose and introduce negative I^- ions (FIG. 5). Thus, the degradation in short-circuit current density will again increase as illustrated in FIG. 4.

In FIG. 6 we can show that the normalized degradations in short-circuit current density for different stoichiometry can be fitted with a double-exponential equation as,

$$J_{sc}(t) = J_{sc,t=0} - \Delta J_{sc} \tag{1}$$

$$\Delta J_{sc} = J_{sc,t=0}\left[a_m\left(1 - e^{-\frac{t}{t_{cm}}}\right) + a_g\left(1 - e^{-\frac{t}{t_{cg}}}\right)\right] \tag{2}$$

With boundary conditions,

$$(i)\ a_m + a_g = \frac{\Delta J_{sc}}{J_{sc,t=0}}\bigg|_{t\to\infty} \qquad (ii)\ \Delta J_{sc} = 0 \text{ at t=0}$$

FIG. 3: Photon-induced degradation for 100 hours at 1 sun intensity (AM1.5) in open circuit condition for devices fabricated with different PbI_2 to CH_3NH_3I molar ratio. Here all the values are normalized with respect to the values at time, t=0. (a) $[PbI_2]/[MAI]=1$ (b) $[PbI_2]/[MAI]=1.025$ (c) $[PbI_2]/[MAI]=1.05$ (d) $[PbI_2]/[MAI]=1.075$ and (e) $[PbI_2]/[MAI]=1.10$ (f) Comparison in short-circuit current degradation among devices with different PbI_2 to CH_3NH_3I malor ratio

Table 2 shows the value of coefficients that has been used to fit the normalized degradation in short-circuit current density. It is understandable why we need two exponentials to fit the short-circuit current degradation if we consider both migration and generation of ions contribute in this photon-induced degradation. We can consider the first exponential takes care of the migration of ions with a time constant of t_{cm} and a magnitude of a_m . And the second exponential models the generation of ions with a time constant of t_{cg} and a magnitude of a_g. As a_m is a function of initial ion densities it should have high correlation with degradation in

short-circuit current density of devices fabricated with different PbI_2 to CH_3NH_3I molar ratio. FIG. 6(c) shows the correlation between a_m and Normalized short-circuit current degradation after 100 hours. As the figure shows, they can be fitted with a straight line with $R^2 = 0.91$. This indicates that they have a very high correlation.

FIG. 4: Normalized short-circuit current degradation at t=100 hours as function of PbI_2 to CH_3NH_3I malor ratio
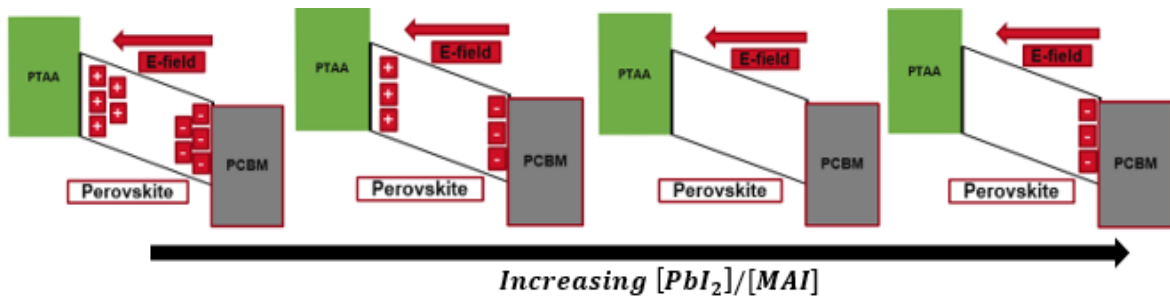
FIG. 5: Schematic illustration of change in interface charge densities with relative increase in PbI_2 with respect to CH_3NH_3I

Table 2: Parameters for fitting J_{sc} degradation with double-exponential model

$[PbI_2]/[MAI]$	a_m	$t_{cm}(minutes)$	a_g	$t_{cg}(minutes)$	R^2
1	0.53	120	0.10	2500	0.90
1.025	0.34	120	0.27	2500	0.97
1.05	0.15	120	0.30	2500	0.99
1.075	0.25	120	0.30	2500	0.99
1.10	0.35	120	0.25	2500	0.99

FIG. 6: Fitting J_{sc} degradation with double-exponential model (a) $[PbI_2]/$
$[MAI]=1,1.05,1.10$ (b) $[PbI_2]/[MAI]=1.025,1.075$. The solid lines represent fitted line with
double exponential and dotted lines represent experimental normalized J_{sc} degradation. (c)
The correlation plot between Ion migration coefficient (a_m) and Normalized J_{sc} degradation
after 100 hours

In summary, the stoichiometry of perovskite precursor solution can affect the photon-induced degradation as the ion densities at the interfaces is a dependent on PbI_2 to CH_3NH_3I molar ratio. We need to find the optimum value of this molar ratio which will minimize the degradation in short circuit current density.

References

1. Woon Seok Yang, Byung-Wook Park, Eui Hyuk Jung, Nam Joong Jeon, Young Chan Kim, Dong Uk Lee, Seong Sik Shin, Jangwon Seo, Eun Kyu Kim, Jun Hong Noh, Sang Il Seok, Science, 356(6345), 1376-1379 (2017)

2. Nam-Gyu Park, J. Physical chemistry letters, 4, 2423–2429 (2013)

3. Zhi Guo, JS Manser, Y Wan, PV Kamat & L Huang, Nature communications, 6, 7471 (2015)

4. Samuel D. Stranks, Giles E. Eperon, Giulia Grancini, Christopher Menelaou, Marcelo J. P. Alcocer, Tomas Leijtens, Laura M. Herz, Annamaria Petrozza & Henry J. Snaith, Science, 342, 341-344 (2013)

5. C Wehrenfennig, GE Eperon, MB Johnston, Henry J. Snaith & Laura M. Herz, Advanced Materials, 26(10), 1584-1589 (2014)

6. Guichuan Xing, Nripan Mathews, Shuangyong Sun, Swee Sien Lim, Yeng Ming Lam, Michael Grätzel, Subodh Mhaisalkar & Tze Chien Sum, Science, 342, 344-347 (2013)

7. MA Green, A Ho-Baillie & HJ Snaith, Nature photonics, 8, 506-509 (2014)

8. Mehran Samiee, Siva Konduri, Balaji Ganapathy, Ranjith Kottokkaran, Hisham A. Abbas, Andrew Kitahara, Pranav Joshi, Liang Zhang, Max Noack and Vikram Dalal, Applied Physics Letters, 105, 153502 (2014)

9. Henry J. Snaith, Antonio Abate, James M. Ball, Giles E. Eperon, Tomas Leijtens, Nakita K. Noel, Samuel D. Stranks, Jacob Tse-Wei Wang, Konrad Wojciechowski, and Wei Zhang, J. Physical Chemistry Letters, 5(9), 1511-1515 (2014)

10. Zhengguo Xiao, Yongbo Yuan, Yuchuan Shao, Qi Wang, Qingfeng Dong, Cheng Bi, Pankaj Sharma, Alexei Gruverman & Jinsong Huang, Nature materials, 14, 193-198 (2015)

11. Christopher Eames, Jarvist M. Frost, Piers R. F. Barnes, Brian C. O'Regan, Aron Walsh & M. Saiful Islam, Nature communications, 6, 7497 (2015)

12. Nam Joong Jeon, JH Noh, WS Yang, YC Kim, S Ryu, J Seo & Sang Il Seok, Nature, 517, 476–480 (2015)

13. E. L. Unger, E. T. Hoke, C. D. Bailie, W. H. Nguyen, A. R. Bowring, T. Heumüller, M. G. Christoforo and M. D. McGehee, Energy Environ Science, 7, 3690-3698 (2014)

14. W. Tress, N. Marinova, T. Moehl, S. M. Zakeeruddin, Mohammad Khaja Nazeeruddin and M. Grätzel, Energy Environ Science, 8, 995-1004 (2015)

15. Hisham A. Abbas, Ranjith Kottokkaran, Balaji Ganapathy, Mehran Samiee, Liang Zhang, Andrew Kitahara, Max Noack and Vikram L. Dalal, APL materials, 3, 016105 (2015)

16. Hui-Seon Kim and Nam-Gyu Park, J. Physical Chemistry Letters, 5 (17), 2927–2934 (2014)

17. Becker, H; Gärtner, Analytical and Bioanalytical Chemistry. 390(1) , 89–111 (2008)

18. Namyoung Ahn, Dae-Yong Son, In-Hyuk Jang, Seong Min Kang, Mansoo Choi, and Nam-Gyu Park, J. Am. Chem. Soc. 137, 8696−8699 (2015)

19. Pranav H. Joshi, Liang Zhang, Istiaque M. Hossain, Hisham A. Abbas, Ranjith Kottokkaran, Satyapal P. Nehra, Mahendra Dhaka, Max Noack, and Vikram L. Dalal, AIP Advances 6, 115114 (2016)

20. Pranav Joshi, Liang Zhang, Ranjith Kottokkaran, Hisham Abbas, Istiaque Hossain, Satyapal Nehra, Mahendra Dhaka, Max Noack, Vikram Dalal, Photovoltaic Specialists Conference (PVSC), IEEE 43rd, 0242-0248 (2016)

APPENDIX D.   UNDERSTANDING THE CONTRIBUTION OF HOLE TRANSPORT LAYERS IN PHOTON INDUCED DEGRADATION OF PEROVSKITE SOLAR CELLS

A paper to be submitted

Istiaque Hossain, Ranjith Kottokkaran, Liang Zhang, Laila-Parvin Poly, Max Noack and Vikram L. Dalal

Iowa State University, Ames, Iowa, 50010, USA

Abstract

In this work, we investigate on how different hole transport layers contribute to photon induced degradation of p-i-n structured perovskite ($CH_3NH_3PbI_3$) solar cells. NiO and PTAA as hole transport layers have been used for comparative study. We will also establish a mathematical relationship between Short circuit current degradation and open circuit voltage evolution. Finally, we will report that the experimental result matches well with the simulated result obtained from our model.

Introduction

The rapid increase in power conversion efficiency using organolead trihalide perovskite (OTP) as a light absorbing material has already showed huge potential in photovoltaic applications. Already several groups have confirmed an efficiency > 20% [3]. Some research groups have already reported high diffusion length [16,17,18,19] high carrier lifetime [18], and large absorption coefficient [15] etc. as attributes towards high power conversion efficiency. Despite of this tremendous light conversion efficiency they show some very interesting electronic characteristics [5,9,11,13,14]. Some research groups have reported that these perovskite-based devices show transient behavior [6] which might be responsible for dependence of light IV measurement on scan direction, scan speed, and light and voltage preconditions before light IV

measurement [6,7,8,10]. Light IV hysteresis and voltage evolution also showed dependence on device structure and contact layers (Electron and hole transport layers). To make perovskite solar cells reliable for commercialization, we need to find the appropriate device structure with suitable transport layers. In this report, we will investigate the effect of different transport layers (PTAA and NiO) on photon-induced degradation.

Device Fabrication

We have used ITO Coated glass substrate and spin coated 2.18 mg/mL PTAA solution in toluene at 6000rpm/40 secs which gives a thickness of about 20nm. Then annealed at 150°C for 10 mins. We have washed the PTAA substrate with DMF before spin-coating perovskite which reduces the surface energy and enhances the spread-ability of perovskite solution. In case of NiO (Thickness of about 30 nm), we have deposited using E-beam evaporator and then annealed at 200°C for 1 hour in ambient environment. About 1.6 M perovskite solution, contains CH_3NH_3I, PbI_2, DMSO in DMF with molar ratio of 1:1.05:1, was spin coated at 4000rpm for 25 seconds with drop cast of chlorobenzene on 10 seconds' delay [20]. This gives about 600nm of perovskite layer thickness. Then it was annealed at 60°C for 1 minute followed by 100°C for 5 minutes. Then 20mg/mL PC60BM in chlorobenzene solution was spin coated at 2000 rpm for 40 seconds. Then the whole structure was annealed at 100°C for 15 minutes. Indium doped CdS (about 25nm) was deposited using thermal evaporator and Aluminum doped ZnO (about 280nm) was deposited using sputtering. Both CdS and ZnO layers serve as buffer layers which enhances stability of these devices. Finally, about 100 nm of Aluminum was deposited using thermal evaporator.
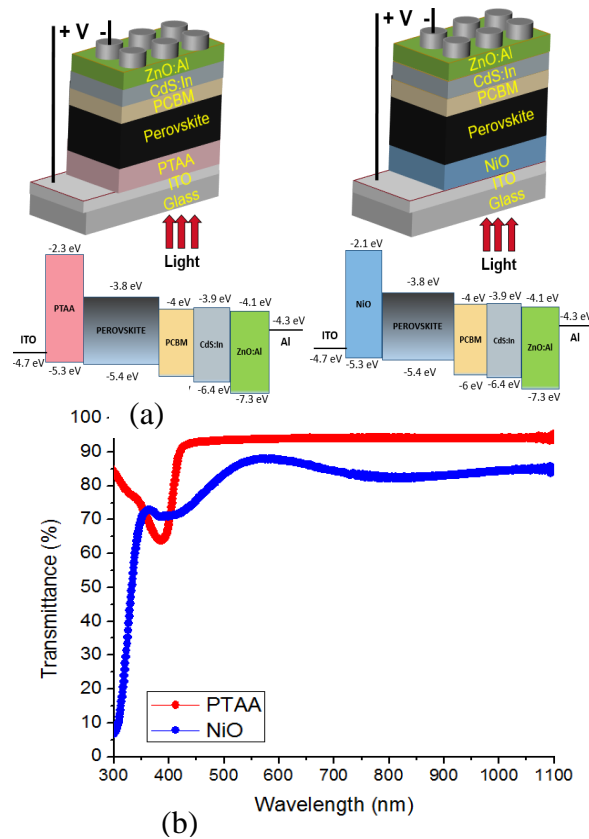
FIG. 1: (a) Device structure and corresponding band edges (b)Transmission of PTAA and NiO
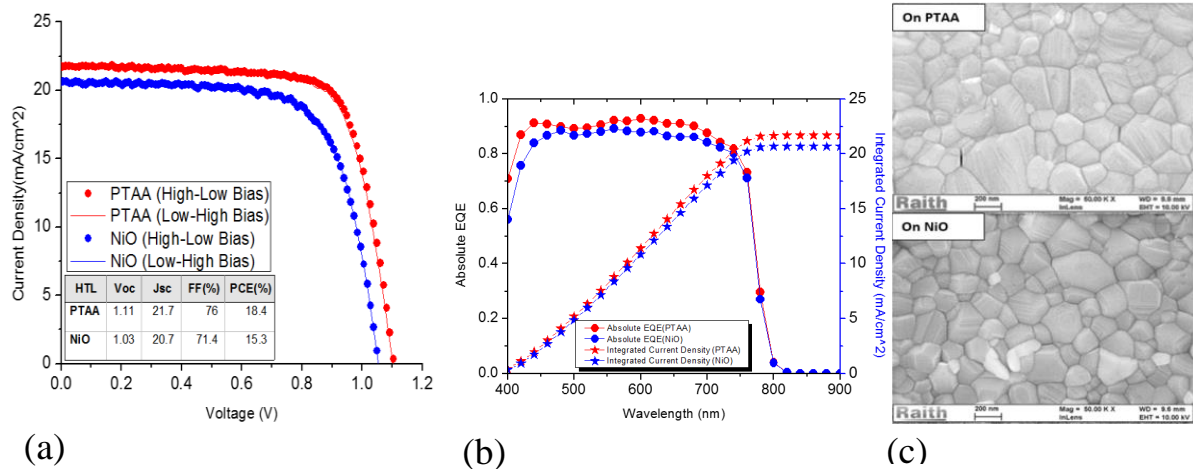
FIG. 2: (a) Light IV characteristics of devices fabricated on NiO and PTAA. Both didn't show any hysteresis (b) External quantum efficiency and integrated short-circuit current density (c) SEM images shows the topography of perovskite films deposited on PTAA and NiO

Figure 2(a) shows the light IV characteristics of those two devices. The photo conversion efficiency of the device fabricated on PTAA as hole transport layer is about 18.4% and on NiO as hole transport layer is about 15.5% before photon induced degradation. None of the devices showed any hysteresis in light IV measurement. Figure 2(b) shows the external quantum efficiency and integrated current density of these two p-i-n devices. PTAA has higher transmission [Figure 1(b)]. Thus, device fabricated on PTAA shows higher short-circuit current density than NiO. The SEM images in figure 2(c) which shows the topography of perovskite films fabricated on NiO and PTAA, suggests that there is no significant difference in grain size which can also play a role in photon induced degradation. Both have perovskite grain sizes in the range of about 200-400 nm.
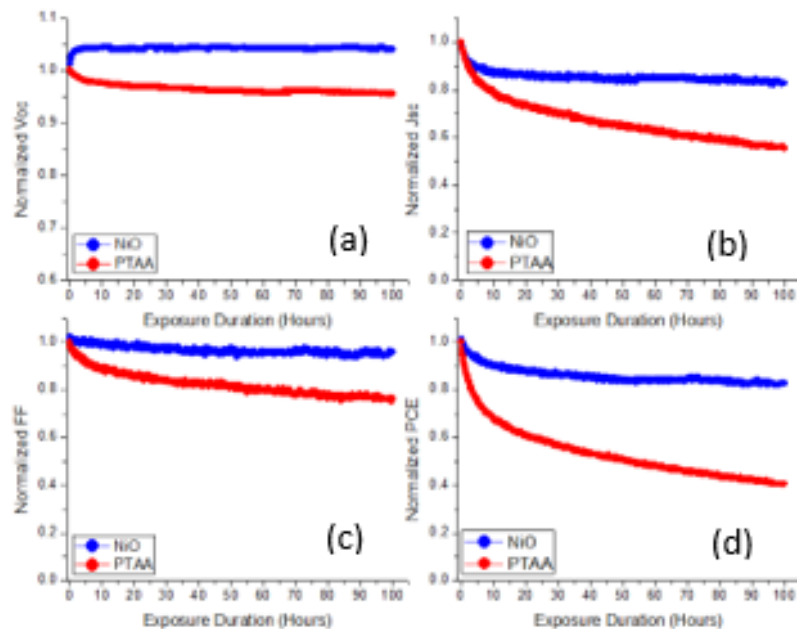
FIG. 3: Photon-induced degradation comparison of these two p-i-n devices under one-sun intensity (AM1.5) for 100 hours (a) Normalized open-circuit voltage degradation (b) Normalized short-circuit current degradation (c) Fill-factor degradation (d) Degradation in power conversion efficiency

Results

Then we measured photon-induced degradation on these two types of p-i-n devices in open circuit condition up to 100 hours under one-sun illumination with AM1.5 spectra for comparative study [figure 3]. The key features from this photon-induced degradation are: The open-circuit voltage for the solar cell on PTAA decreases over time under continuous illumination, while the open-circuit voltage increases for the cell fabricated on NiO, the short-circuit current and fill factor degrades more for the cell fabricated on PTAA compared to the cell fabricated on NiO. Thus, the power conversion efficiency degradation for the cell with PTAA as hole transport layer is much higher than power conversion efficiency degradation with NiO.

But, encouraging sign is that both devices, either on PTAA or NiO as hole transport layer has recovered in dark. The solar cell fabricated on PTAA has completely recovered in 43 hours at room temperature after light exposure for 100 hours at one sun intensity. And the device fabricated on NiO completely recovered after it was kept in dark for 13 hours at room temperature. The light IV characteristics of these devices before exposure, after exposure and after recovery has been showed in figure 4.

The photo-degradation can be explained by using the ion generation and migration theory during photo-exposure [1,12]. At thermal equilibrium, due to built-in E-filed positive ions go towards hole transport layer (HTL) and negative ions go towards electron transport layer (ETL). So, we have net electric field inside the active layer. Due to high electric field at the interfaces these ions do not recombine with generated electron-hole pairs. During exposure, due to decrease in internal E-field these ions migrate towards the intrinsic active layer. And in addition to that more ions are generated by photons. The generated electron hole pairs recombine

with the ions to contribute to current loss. Higher degradation in short circuit current on PTAA indicates that the generation of ions during photo-exposure is higher for the device with PTAA as hole transport layer compared to the device fabricated on NiO (figure 3).

(a)   (b)
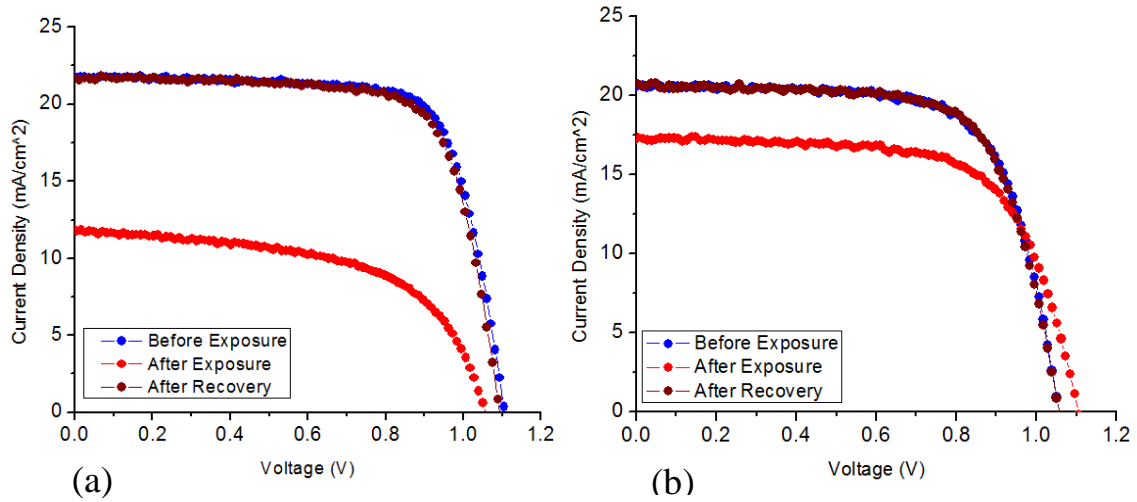
FIG. 4: Light IV degradation and recovery in dark (a) fabricated on PTAA as HTL (b) Fabricated on NiO as HTL

The degradations in short-circuit current density can be fitted with a double-exponential equation as,

$$J_{sc}(t) = J_{sc,t=0} - \Delta J_{sc} \tag{1}$$

$$\Delta J_{sc} = J_{sc,t=0}\left[a_m\left(1 - e^{-\frac{t}{t_{cm}}}\right) + a_g\left(1 - e^{-\frac{t}{t_{cg}}}\right)\right] \tag{2}$$

With boundary conditions,

$$(i)\ a_m + a_g = \frac{\Delta J_{sc}}{J_{sc,t=0}}\Big|_{t\to\infty} \qquad (ii)\Delta J_{sc} = 0 \text{ at t=0}$$

It is understandable why we need two exponentials to fit the short-circuit current degradation if we consider both migration and generation of ions contribute in this photon-induced degradation. We can consider the first exponential takes care of the migration of ions with a time constant of t_{cm} and a magnitude of a_m. And the second exponential models the

generation of ions with a time constant of t_{cg} and a magnitude of a_g. For NiO the values which can describe the short-circuit current degradation are: t_{cm}= 2 hours, a_m= 0.084 $mAcm^{-2}$, t_{cg}=20 hours, a_g=0.084 $mAcm^{-2}$. For PTAA the values which can describe the short-circuit current degradation are: t_{cm}= 2 hours, a_m= 0.15 $mAcm^{-2}$, t_{cg}= 42 hours, a_g=0.3 $mAcm^{-2}$.

The change in open circuit voltage can be explained by considering two components which play a role during light exposure. First, increase in open circuit voltage due to migration of ions from contact layers to the bulk which helps the open circuit voltage to increase during exposure because of increase in net built-in potential. Second, decrease in open circuit voltage due to increase in non-radiative recombination because of generation of ions during photo-exposure.

Just after the fabrication due to internal electric field the positive ions start moving towards the hole transport layer (HTL) and negative ions move towards Electron transport layer (ETL). At thermal equilibrium, these ions near the contact layers create an electric field opposing the built-in electric field. Thus, reduces the net electric filed and reduces the open-circuit voltage. Here, the parameter V_d is defined as the difference in open circuit voltage if there are no ions at thermal equilibrium ($V_{oc,0}$) and the actual open circuit voltage measured at time t=0 ($V_{oc,t=0}$, before exposure). At the onset of photo-degradation these ions start moving from the contact layers towards the neutral bulk region and so, the open circuit voltage starts to increase towards the value if there were no ions present at thermal equilibrium with a time constant τ_c. This is first component behind the change in open circuit voltage. So, the change in open-circuit voltage due to ion migration is given by [2],

$$\Delta V_{oc,i}(t) = V_d \left(1 - e^{-\frac{t}{\tau_c}}\right); \quad V_d = V_{oc,0} - V_{oc,t=0} \tag{3}$$

$$V_{oc,0} = \frac{nkT}{q} ln\left(\frac{J_l}{J_0} + 1\right) \tag{4}$$

As ions are generated during exposure, these ions recombine with the generated electron hole pairs and there is an increase in non-radiative recombination. Due to increase in recombination the lifetime of electrons and holes will decrease. Thus, the open circuit voltage will decrease. The expression of open circuit voltage considering non-radiative recombination, but no ion migration is given by [4],

$$V_{oc,r} = \frac{kT}{q} \ln\left(\frac{N_B J_{sc} \tau}{q n_i^2 W}\right) \tag{5}$$

Now, if we assume that lifetime of carriers and short circuit current at t=0 and t=t are $\tau_{t=0}$, $J_{sc,t=0}$ and $\tau_{t=t}$, $J_{sc,t=t}$ respectively. Change in open-circuit voltage due to increase in non-radiative recombination is given by,

$$\Delta V_{oc,r}(t) = V_{oc,r,t=0} - V_{oc,r,t=t} = \frac{kT}{q} \ln\left(\frac{J_{sc,t=0}\tau_{t=0}}{J_{sc,t=t}\tau_{t=t}}\right) \tag{6}$$

Assuming diffusion lengths of electron and hole are equal,

$$J_{sc} = 2qGL = 2qG\sqrt{D\tau} \tag{7}$$

The expression of ration between current densities between time t=0 to t=t becomes,

$$\frac{J_{sc,t=0}}{J_{sc,t=t}} = \sqrt{\frac{\tau_{t=0}}{\tau_{t=t}}} \tag{8}$$

$$\frac{\tau_{t=0}}{\tau_{t=t}} = \left(\frac{J_{sc,t=0}}{J_{sc,t=t}}\right)^2 \tag{9}$$

Substituting the expression of ratio between lifetimes in the equation of change in open circuit voltage,

$$\Delta V_{oc,r}(t) = V_{oc,r,t=0} - V_{oc,r,t=t} = 3\frac{kT}{q}\ln\left(\frac{J_{sc,t=0}}{J_{sc,t=t}}\right) \tag{10}$$

Total Change in V_{oc} at time t=t,

$$\Delta V_{oc}(t) = V_{oc,t=t} - V_{oc,t=0} = \Delta V_{oc,i}(t) - \Delta V_{oc,r}(t) \tag{11}$$

$$\Delta V_{oc}(t) = V_d \left(1 - e^{-\frac{t}{\tau_c}}\right) - 3\frac{kT}{q}\ln\left(\frac{J_{sc,t=0}}{J_{sc,t=t}}\right) \tag{12}$$

Figure 5 shows the comparison between experimental and simulation result for both devices. The simulated normalized change in open-circuit voltage and short-circuit current matches well with the experimental change in open-circuit voltage and short-circuit current.
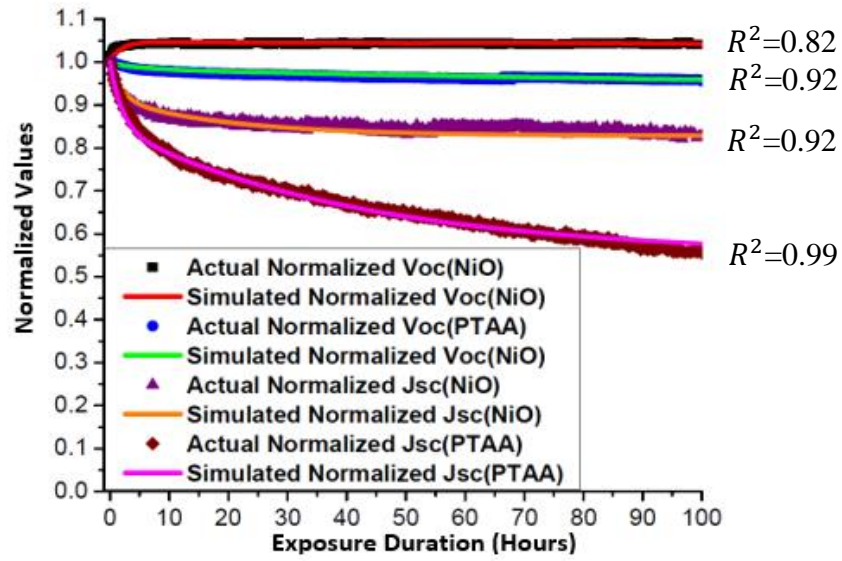
FIG. 5: Comparison of normalized change in open-circuit voltage and short-circuit current degradation between experimental and simulated result obtained from our model.

In summary, contact layers can play a significant role in photon-induced degradation of perovskite solar cells. The simulation results prove our explanation that both migration and generation of ions contribute to the photon-induced degradation of perovskite solar cells.

References

1. Pranav H. Joshi, Liang Zhang, Istiaque M. Hossain, Hisham A. Abbas, Ranjith Kottokkaran, Satyapal P. Nehra, Mahendra Dhaka, Max Noack, and Vikram L. Dalal, AIP Advances 6, 115114 (2016)

2. Ralf Widenhorn, Michael Fitzgibbons, and Erik Bodegomb, Journal of Applied Physics 96, 7379 (2004)

3. Nam-Gyu Park, J. Physical chemistry letters, 4, pp. 2423–2429 (2013)

4. Ronald A. Sinton, Applied Physics Letters, 69, 2510 (1996)

5. Mehran Samiee, Siva Konduri, Balaji Ganapathy, Ranjith Kottokkaran, Hisham A. Abbas, Andrew Kitahara, Pranav Joshi, Liang Zhang, Max Noack and Vikram Dalal, Applied Physics Letters, 105, 153502 (2014)

6. E. L. Unger, E. T. Hoke, C. D. Bailie, W. H. Nguyen, A. R. Bowring, T. Heumüller, M. G. Christoforo and M. D. McGehee, Energy Environ Science, 7, 3690-3698 (2014)

7. W. Tress, N. Marinova, T. Moehl, S. M. Zakeeruddin , Mohammad Khaja Nazeeruddin and M. Grätzel, Energy Environ Science, 8, 995-1004 (2015)

8. Hisham A. Abbas, Ranjith Kottokkaran, Balaji Ganapathy, Mehran Samiee, Liang Zhang, Andrew Kitahara, Max Noack and Vikram L. Dalal, APL materials, 3, 016105 (2015)

9. Henry J. Snaith, Antonio Abate, James M. Ball, Giles E. Eperon, Tomas Leijtens, Nakita K. Noel, Samuel D. Stranks, Jacob Tse-Wei Wang, Konrad Wojciechowski, and Wei Zhang, J. Physical Chemistry Letters, 5(9), pp 1511-1515 (2014)

10. Hui-Seon Kim and Nam-Gyu Park, J. Physical Chemistry Letters, 5 (17), pp 2927–2934 (2014)

11. Zhengguo Xiao, Yongbo Yuan, Yuchuan Shao, Qi Wang, Qingfeng Dong, Cheng Bi, Pankaj Sharma, Alexei Gruverman & Jinsong Huang, Nature materials, 14, 193-198 (2015)

12. Pranav Joshi, Liang Zhang, Ranjith Kottokkaran, Hisham Abbas, Istiaque Hossain, Satyapal Nehra, Mahendra Dhaka, Max Noack, Vikram Dalal, Photovoltaic Specialists Conference (PVSC), 2016 IEEE 43rd, pages 0242-0248

13. Christopher Eames, Jarvist M. Frost, Piers R. F. Barnes, Brian C. O'Regan, Aron Walsh & M. Saiful Islam, Nature communications, 6, 7497

14. Nam Joong Jeon, JH Noh, WS Yang, YC Kim, S Ryu, J Seo & Sang Il Seok, Nature, 517 (2015)

15. MA Green, A Ho-Baillie & HJ Snaith, Nature photonics, 8, pp. 506-509 (2014)

16. Zhi Guo, JS Manser, Y Wan, PV Kamat & L Huang , Nature communications, 6, 7471 (2015)

17. Samuel D. Stranks, Giles E. Eperon, Giulia Grancini, Christopher Menelaou, Marcelo J. P.

Alcocer, Tomas Leijtens, Laura M. Herz, Annamaria Petrozza & Henry J. Snaith, Science, 342, pp. 341-344 (2013)

18. C Wehrenfennig, GE Eperon, MB Johnston, Henry J. Snaith & Laura M. Herz, Advanced Materials, DOI: 10.1002 (2013)

19. Guichuan Xing, Nripan Mathews, Shuangyong Sun, Swee Sien Lim, Yeng Ming Lam, Michael Grätzel, Subodh Mhaisalkar & Tze Chien Sum, Science, 342, pp. 344-347 (2013)

20. Namyoung Ahn, Dae-Yong Son, In-Hyuk Jang, Seong Min Kang, Mansoo Choi, and Nam-Gyu Park, J. Am. Chem. Soc. 137, 8696−8699 (2015)

APPENDIX E.   DETERMINING THE OPTIMUM ELECTRIC FIELD REQUIRED FOR ION MIGRATION IN PEROVSKITE SOLAR CELL

A paper to be submitted

Istiaque Hossain and Vikram L. Dalal

Iowa State University, Ames, Iowa, 50010, USA

Abstract

Organolead trihalide perovskite (OTP) based solar cells are low cost and has given very high efficiency [12,3,45,8,15,20,21] in shorter length of research time but they show some interesting electronic behaviors such as voltage and efficiency evolution during light soaking [11,12] as well as hysteresis in current-voltage (IV) measurement [7,8,9,10,14]. Although the actual physics behind these interesting behaviors is still unknown, now-a-days ion migration [6,7,11,12,13] is the most accepted theory. Here we have documented a method to determine the optimum electric field (around $1V\ \mu m^{-1}$) that is required to initiate the ion migration in an n-i-p structure. Then we have discussed how this parameter plays a role in IV measurements.

Introduction

The rapid increase in power conversion efficiency using organolead trihalide perovskite (OTP) as a light absorbing material has already showed huge potential in photovoltaic applications. Already several groups have confirmed an efficiency > 20% [3]. Some research groups have already reported high diffusion length [16,17,18,19], high carrier lifetime [18], and large absorption coefficient [15] etc. as attributes towards high power conversion efficiency. Despite of this tremendous light conversion efficiency they show some very interesting electronic characteristics. Some research groups have reported that these

perovskite based devices show transient behavior [6] which might be responsible for dependence of light IV measurement on scan direction, scan speed, and light and voltage preconditions before light IV measurement [6,7,10]. Xiao et al. has showed that the direction of photocurrent can be reversed using an electric field around $1V\ \mu m^{-1}$ [11]. These devices also show a modification of built-in potential depending on different preset conditions [7]. Some research groups have reported significant improvement in open circuit voltage and photo conversion efficiency during light soaking over time [11,12]. Many groups have also reported hysteresis in light IV measurement [7,8,910,14]. Several theories such as field dependent orientation of methyl amine ions (MA^{+}) [22,23,24], ferroelectricity [9,24,25], lattice distortion which can affect the charge dynamics [22,23,24], conductivity of contact layers [26] and ion migration [6,7, 11,12,13] has been developed over the recent years to explain these behaviors. In recent times the ion migration theory has gained most popularity as it can explain most of these effects. In this letter we have discussed the mechanism of ion migration and determined the optimum electric field required to initiate the ion migration. We have also explained the reason behind significant evolution of open circuit voltage and efficiency during light soaking in open circuit condition [11,12] and related this optimum electric field with light IV measurements.

Results and Discussions

The device structure and the light IV characteristic that we have used during this experiment is shown in figure 1. This was a n-i-p structure device with compact TiO_x as an electron transport layer (ETL) and P_3HT as a hole transport layer (HTL). The efficiency of the device was 9% after 20 mins of light soaking in open circuit condition and the hysteresis is

also showed in figure 1. We have used three different thicknesses of the perovskite layer of around 400, 500 and 600 nm.
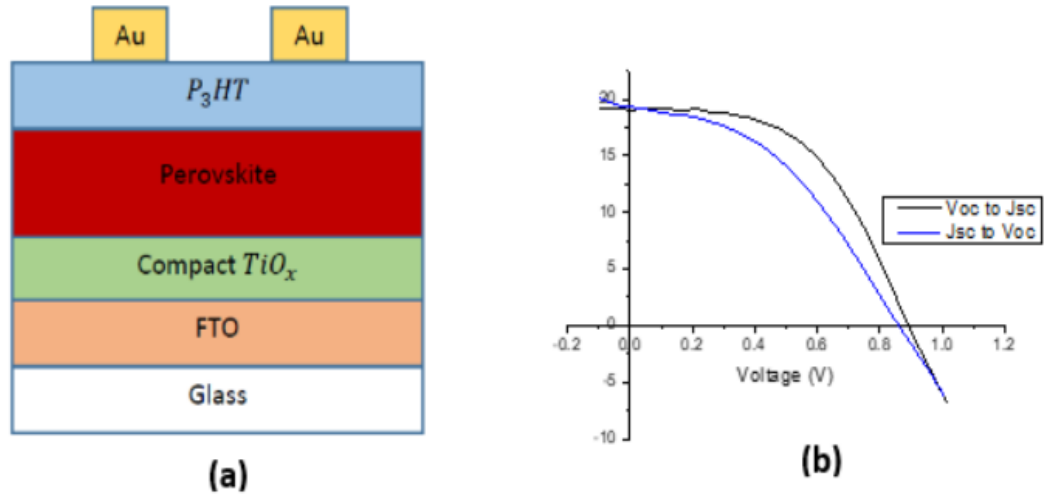
Figure 1: (a) Schematic diagram of the n-i-p perovskite device which is used for our measurements (b) The light IV characteristics (400 nm perovskite thickness) of that device after 20 minutes of light soaking in open circuit condition. The black line was scanned from high-bias to low-bias and the blue line was scanned from low-bias to high-bias.

In figure 2 the process of ion migration has been described. First in short circuit condition due to the built-in potential the positive ions move towards the hole transport layer (HTL) and forms a space charge region near the perovskite-HTL interface and that makes perovskite n-type doped near the HTL interface. Similarly, the negative ions move towards the electron transport layer (ETL) and forms a space charge region near the perovskite-ETL interface and that makes the perovskite p-type doped ETL interface. Then these two space charge regions create an electric field opposing the built-in electric field.

So now we have an effective built-in potential which is lower than original built-in electric field and given by,

$$V'_{bi} = V_{bi} - V_{ion} \qquad (1)$$

This process continues until the effective built-in field is large enough to move these ions and form space charge. So finally, it reaches a steady-state condition and there is a net electric field due to the effective built-in potential. Now if we apply forward bias these ions migrate in the opposite direction and finally reaches a steady state condition again. In this case to have significant ion migration we must apply forward bias more than a threshold voltage. We call this threshold voltage as onset of ion migration voltage (V_{onset}).
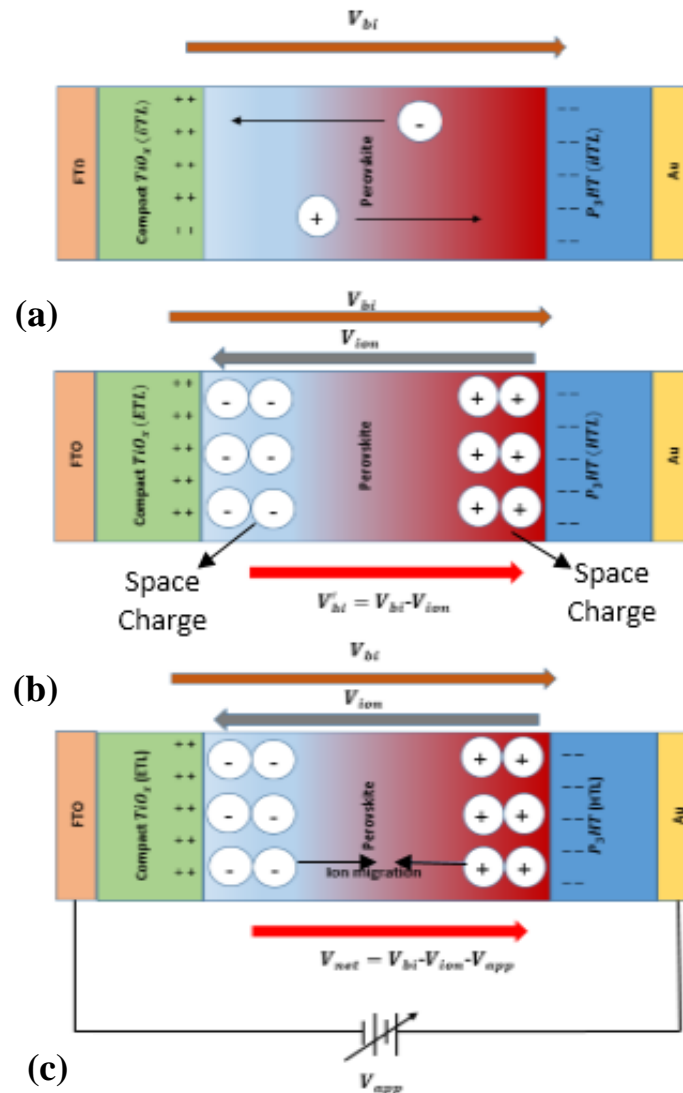

Figure 2: The process of ion migration (a) Due to the built-in potential the positive ions move towards the HTL and negative ions move towards ETL (b) The ions move towards the contact layers and form space charge regions which develops an electric field opposing the built-in electric field. The effective built-in potential is reduced to $V'_{bi} = V_{bi} - V_{ion}$ (c) If

The reason we must apply a minimum voltage to initiate this ion migration is that we must overcome the barrier due to the effective built-in potential and there might be some interface charge traps as well. Below this threshold voltage we might have some ion migration due to diffusion as the barrier lowers because of applying a small forward bias but above this threshold voltage ion migration due to drift dominates and we have observed a significant increase in migration of ions. In this section, I have showed a method to calculate this onset of ion migration voltage from capacitance vs time plot at different bias. The measured net capacitance can be expressed as,

$$C_{net} = \frac{dQ}{dV} \tag{2}$$

The capacitance that we measure at a given bias voltage has three charge components: the depletion charge due to the built in potential, the injection charge due to applied bias and the ion charge due to ion migration. So, total charge that contributes to the net capacitance can be expressed as,

$$Q = Q_{depl} + Q_{inj} + Q_{ion} \tag{3}$$

The net voltage (V) is effective on all three types of charges and so we can take derivative with respect to V on both sides of equation 3,

$$\frac{dQ}{dV} = \frac{dQ_{depl}}{dV} + \frac{dQ_{inj}}{dV} + \frac{dQ_{ion}}{dV} \tag{4}$$

Equation 4.10 can be expressed as three capacitance components,

$$C_{net} = C_{depl} + C_{inj} + C_{ion} \tag{5}$$

From equation 5, we can see that the measured net capacitance can be expressed as linear combination of depletion, injection and ion capacitance components. Thus, we can express the contribution of capacitance from migration of ions can be expressed as,

$$C_{ion} = C_{net} - \left(C_{depl} + C_{inj}\right) \qquad (6)$$

If we can find a way to determine the combination of depletion and injection capacitance ($C_{depl} + C_{inj}$), by subtracting this amount from the measured capacitance we can get the capacitance due to ion migration. From the parallel plate capacitance approximation, we can relate the amount of charges and the capacitance due to ion migration,

$$Q_{ion} = V C_{ion} \qquad (7)$$

We can express the rate of ion migration as a function of rate of change in capacitance. Figure 3(a) shows the ionic capacitance vs time curve for a n-i-p device with perovskite layer thickness of 400 nm. For this measurement before starting measurement at any bias we have kept the device at short circuit condition in dark to stabilize the capacitance and to ensure that the device is at similar initial condition before measuring at every bias. Then we have instantaneously changed the bias from short circuit condition to a specific biasing voltage. So, at time t=0 assuming there is no ion migration the capacitance we have measured indicates the combination of depletion and injection capacitance components. Then we have measured the capacitance at different time. If we deduct the capacitance at time t=0 from measured capacitance at time $t = t_1$, we can get the ionic capacitance due to ion migration. Then we have plotted this ionic capacitance as a function of time [figure 3(a)]. From this figure, we can see that initially the capacitance increases very quickly and finally reaches a linear or steady state condition. Another important thing to observe from this plot is that the slope of these curves at linear region increases with increasing bias voltage as the rate of ion migration is

higher at higher bias voltage. Thus, the slope of this linear region is a function of rate of ion migration. Then we have plotted the slope of steady state response as a function of bias voltage [figure 3(b)] which can be fitted as a straight line. The line has an intercept at x-axis of 0.45 V. This intercept shows that below 0.45 V the rate of ion migration is negligible and above 0.45 V we have significant ion migration. We call this threshold voltage as onset of ion migration voltage. We have also repeated the same procedure below 0.45 V (at 0.3 V and 0.35 V) to observe if there is any significant ion migration or not and we have observed that the change in ionic capacitance is not significant below this threshold voltage [figure 3(a)]. The onset of ion migration voltage will vary with change in perovskite layer thickness. So, we have calculated the optimum electric field (E_{opt}) that is required for ion migration which is independent of thickness and we have got a value of 1.13 V μm^{-1} for this 400nm device which is consistent with the result reported by Xiao et al. [11] and Deng et al. [12] where they have reported that to switch the photo-current direction from polling effect they had to apply an electric field of around 1V μm^{-1}. We have also repeated the same experiment for 500 nm and 600 nm thick perovskite layer devices and we have obtained this optimum electric field of 1.18 V μm^{-1} and 1.05 V μm^{-1} respectively.

Table 4.3: Optimum electric field required for ion migration at different perovskite layer thickness

Thickness (Perovskite)	$V_{onset}(V)$	E_{opt} (V μm^{-1})
400 nm	0.45	1.13
500 nm	0.59	1.18
600 nm	0.63	1.05

Figure 3: Calculation of onset of ion migration voltage and optimum electric field required for ion migration in a 400nm perovskite layer n-i-p device (a) Plot shows ionic capacitance as a function of time at different forward biasing conditions. The graph clearly shows the slope at linear region increases with increasing forward bias voltage. That signifies the rate of ion migration is higher at higher bias voltage. (b) Plot shows the slope of linear region at different bias voltage as a function of bias voltage. We can fit the data points by a straight line and the x-intercept gives the onset of ion migration voltage. From this voltage, we can calculate the optimum E-field required for ion migration.

Now there are several research groups who have reported the significant increase in open circuit voltage and efficiency during light soaking [11,12,27]. This behavior can be explained from ion migration. As we have showed in short circuit condition the ions move near the contact layers to form space charge regions and that reduces the effective built-in potential. As a result, the starting open circuit voltage is lower. When the device is illuminated the photo-voltage acts as forward bias and initiates ion migration which increases the effective built-in potential and so the open circuit voltage increases. The increased open circuit voltage further increases the ion migration and as a result increases the effective built-in potential as well as the open circuit voltage. This process continues until the open circuit voltage saturates as the drift and reverse diffusion of ions are balanced [12].
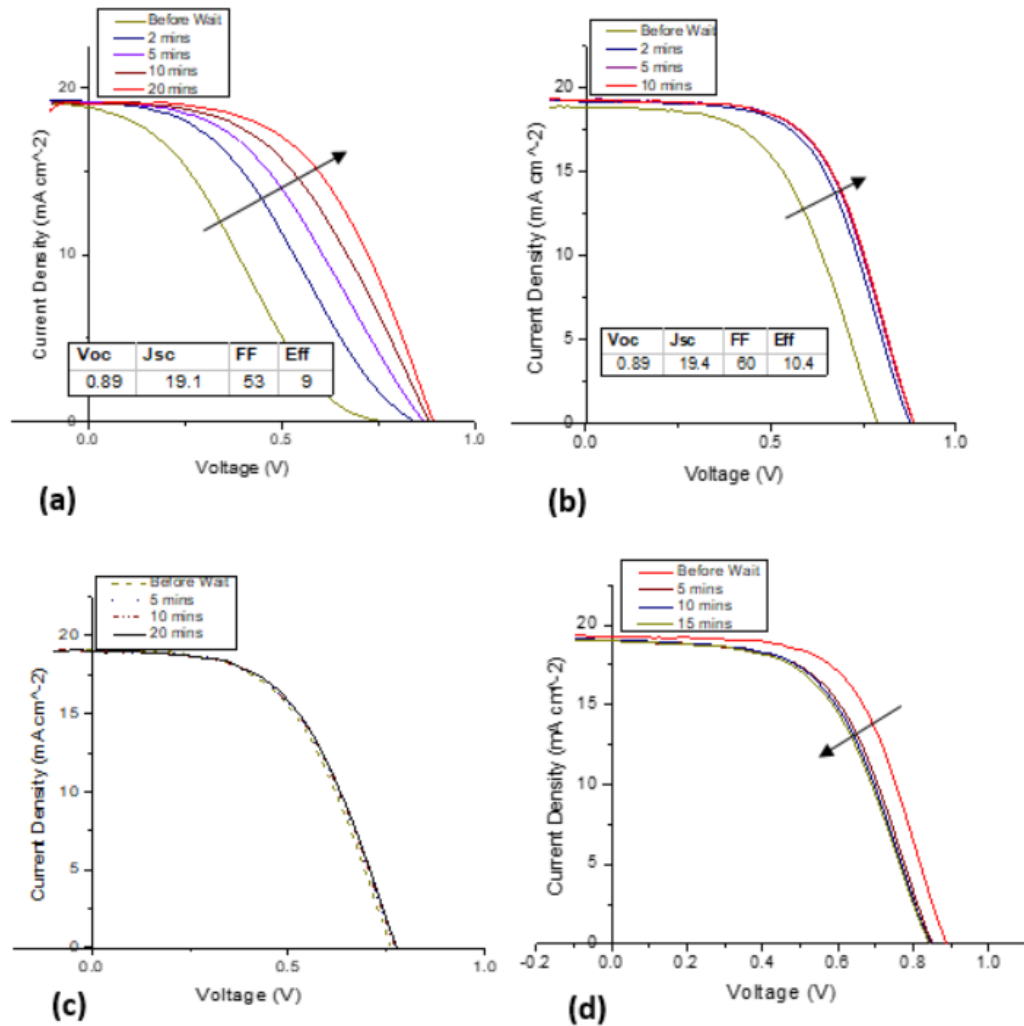
Figure 4: These plots show the comparison of light IV curves of 400 nm perovskite (n-i-p) solar cell at different biasing conditions before measurements (a) Shows the evolution of light IV curves during light soaking in open circuit condition for 20 minutes. We can clearly observe the evolution of open circuit voltage with time. The arrow shows the direction of evolution with increasing time. The efficiency showed on the graph is after 20 mins of light soaking. (b) Shows the evolution of light IV curves when it was kept in dark at forward bias with biasing voltage of 0.9 V which is greater than the onset of ion migration voltage of 0.45 V. We can clearly observe the evolution of open circuit voltage with time. Again, the arrow shows the direction of evolution with increasing time. The efficiency on the graph is after 10 mins of forward bias at 0.9 V in dark. (c) Shows the light IV curves when he device was kept in dark for 20 minutes in forward bias at biasing voltage of 0.3 V which in smaller than the onset of ion migration voltage of 0.45 V. As we have predicted that we don't have significant ion migration at this voltage, we don't have signification voltage evolution. (d) Shows the light IV curves when the device was kept in dark at reverse bias condition with biasing voltage of -0.5 V after the open-circuit voltage saturates at the maximum value. As we have expected the open circuit voltage decreases with increasing time. The arrow shows the direction of light IV characteristic change with time.
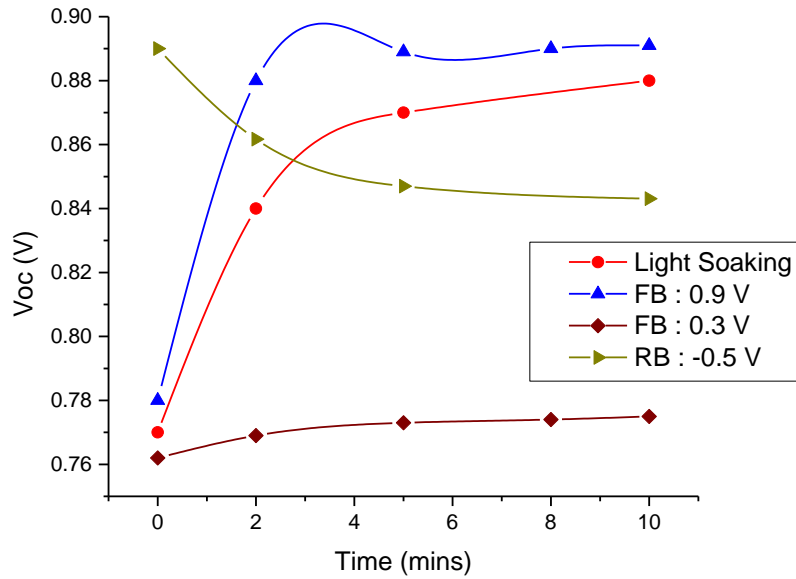
Figure 5: Shows the comparison of open circuit voltage evolution of 400 nm perovskite solar cell at different biasing conditions prior to measurement. Here in case of all the biasing conditions the device was kept in dark. We can clearly observe that at forward bias of 0.9 V in dark the open circuit voltage increases very rapidly as the rate of ion migration is very high at this bias. But in case of forward bias of 0.3 V in dark the open circuit voltage evolution is insignificant as we don't have any significant ion migration at this biasing voltage. There is very slight increase in open circuit voltage because of the exposure during measurement but that is not significant. At reverse bias in dark the open circuit voltage decreases with time as expected.

If our model is accurate, we should also observe the open circuit voltage evolution even when we apply a bias in forward direction in dark. And as we have discussed for the 400nm device if we apply forward bias more than 0.45 V we should observe voltage evolution as the ion migration is significant in this range. Similarly, if we apply a forward bias less than 0.45 V we should not observe any significant voltage evolution as we can neglect ion migration in this range. Also in reverse bias, the open circuit voltage should decrease as the ions move in opposite direction. From figure 4 we can see that the open circuit voltage saturates very quickly if we keep it in dark at forward bias voltage of 0.9 V [figure 4(b)] compared to light soaking

[figure 4(a)]. At a forward bias voltage of 0.3 V the open circuit voltage should not increase significantly [figure 4(c)] although we have seen very slight increase as the device was under illumination during the measurements. So, the results from light IV also matches with the result that we have got from the ionic capacitance vs time curves. In figure 5 the comparison of open circuit voltage evolution has been shown at different preconditions before measurement.

In summary we have measured the optimum electric field which is required for ion migration in perovskite based solar cells. And we have measured this value to be around $1\,V\,\mu m^{-1}$ and we have described a procedure to measure it. Also, we have showed that this result can explain some interesting behaviors that we observe in light IV measurement.

References

1.   Mingzhen Liu, Michael B. Johnston & Henry J. Snaith, Nature 501, 395 (2013)

2.   Nam Joong Jeon, Jun Hong Noh,   Woon Seok Yang, Young Chan Kim, Seungchan Ryu, Jangwon Seo & Sang Il Seok, Nature 517, 476 (2015)

3.   Nam-Gyu Park, J. Physical chemistry letters, 4, pp. 2423–2429 (2013)

4.   Wanyi Nie , Hsinhan Tsai , Reza Asadpour, Jean-Christophe Blancon, Amanda J. Neukirch, Gautam Gupta, Jared J. Crochet, Manish Chhowalla, Sergei Tretiak, Muhammad A. Alam, Hsing-Lin Wang & Aditya D. Mohite, Science, 347, 6221, pp. 522-525 (2015)

5.   Dianyi Liu & Timothy L. Kelly, Nature photonics, 8, 133-138 (2014)

6.   E. L. Unger, E. T. Hoke, C. D. Bailie, W. H. Nguyen, A. R. Bowring , T. Heumüller , M. G. Christoforo and M. D. McGehee, Energy Environ Science, 7, 3690-3698 (2014)

7.   W. Tress, N. Marinova , T. Moehl , S. M. Zakeeruddin , Mohammad Khaja Nazeeruddin and M. Grätzel, Energy Environ Science, 8, 995-1004 (2015)

8.   Hisham A. Abbas, Ranjith Kottokkaran, Balaji Ganapathy, Mehran Samiee, Liang Zhang, Andrew Kitahara, Max Noack and Vikram L. Dalal, APL materials, 3, 016105 (2015)

9.   Henry J. Snaith, Antonio Abate, James M. Ball, Giles E. Eperon, Tomas Leijtens, Nakita K. Noel, Samuel D. Stranks, Jacob Tse-Wei Wang, Konrad Wojciechowski, and Wei

Zhang, J. Physical Chemistry Letters, 5(9), pp 1511-1515 (2014)

10.   Hui-Seon Kim and Nam-Gyu Park, J. Physical Chemistry Letters, 5 (17), pp 2927–2934 (2014)

11.   Zhengguo Xiao,   Yongbo Yuan, Yuchuan Shao, Qi Wang, Qingfeng Dong, Cheng Bi, Pankaj Sharma, Alexei Gruverman & Jinsong Huang, Nature materials, 14, 193-198 (2015)

12.   Yehao Deng, Zhengguo Xiao & Jinsong Huang, Advanced Energy Materials, DOI 10.1002 (2015)

13.   Christopher Eames, Jarvist M. Frost, Piers R. F. Barnes, Brian C. O'Regan, Aron Walsh & M. Saiful Islam, Nature communications, 6, 7497

14.   Nam Joong Jeon, JH Noh, WS Yang, YC Kim, S Ryu, J Seo & Sang II Seok, Nature, 517 (2015)

15.   MA Green, A Ho-Baillie & HJ Snaith, Nature photonics, 8, pp. 506-509 (2014)

16.   Zhi Guo, JS Manser, Y Wan, PV Kamat & L Huang , Nature communications, 6, 7471 (2015)

17.   Samuel D. Stranks, Giles E. Eperon, Giulia Grancini, Christopher Menelaou, Marcelo J. P. Alcocer, Tomas Leijtens, Laura M. Herz, Annamaria Petrozza & Henry J. Snaith, Science, 342, pp. 341-344 (2013)

18.   C Wehrenfennig, GE Eperon, MB Johnston, Henry J. Snaith & Laura M. Herz, Advanced Materials, DOI: 10.1002 (2013)

19.   Guichuan Xing, Nripan Mathews, Shuangyong Sun, Swee Sien Lim, Yeng Ming Lam, Michael Grätzel, Subodh Mhaisalkar & Tze Chien Sum, Science, 342, pp. 344-347 (2013)

20.   Huanping Zhou, Qi Chen, Gang Li, Song Luo, Tze-bing Song, Hsin-Sheng Duan, Ziruo Hong, Jingbi You, Yongsheng Liu & Yang Yang, Science, 345, pp. 542-546 (2014)

21.   Chang-Wen Chen, Hao-Wei Kang, Sheng-Yi Hsiao, Po-Fan Yang, Kai-Ming Chiang & Hao-Wu   Lin, Advanced Materials, 26, 6647-6652 (2014)

22.   R. S. Sánchez, V. Gonzalez-Pedro, J.-W. Lee, N.-G. Park, Y. S. Kang, I. Mora-Sero and J. Bisquert, J. Physical Chemistry Letters, 5(13), 2357–2363 (2014)

23.   F. Brivio, A. Walker and A. Walsh, APL Materials, 1, 042111 (2013)

24.   C. C. Stoumpos, C. D. Malliakas and M. G. Kanatzidis, Inorganic Chemistry, 52, 9019–9038 (2013)

25.   A. Dualeh, T. Moehl, N. Tétreault, J. Teuscher, P. Gao, M. K. Nazeeruddin and M. Grätzel, ACS Nano, 8, 362–373 (2014)

26.   D. L. Staebler and C. R. Wronski, J. Applied Physics Letters, 51, 3262(1980)

27.   Pablo Docampo, James M. Ball, Mariam Darwich, Giles E. Eperon & Henry J. Snaith, Nature Communications, 4, 2761 (2013)